Stochastic approach to the problem of predictive power in the theoretical modeling of the mean-field

Irene Dedes Nonell

No. d'ordre

UNIVERSITÉ DE STRASBOURG

École Doctorale de Physique et Chimie-Physique

Institut Pluridisciplinaire Hubert Curien - UMR CNRS 7178

Département de Recherches Subatomiques

THÈSE présentée par :

Irene DEDES NONELL

soutenue le : **6 Octobre 2017**

pour obtenir le grade de : **Docteur de l'Université de Strasbourg**

Discipline/ Spécialité : Physique Théorique

Approche stochastique du problème du pouvoir prédictif dans la modélisation du champ moyen

THÈSE dirigée par :

M. DUDEK Jerzy	Professeur, Université de Strasbourg

RAPPORTEURS :

Mme. GULMINELLI Francesca	Professeur, Université de Caen Normandie
M. COLO Gianluca	Professeur, Università degli Studi di Milano (Italie)

AUTRES MEMBRES DU JURY :

M. GOZDZ Andrzej	Professeur, Université Marie Curie-Sklodowska (Pologne)
M. GALL Benoit	Professeur, Université de Strasbourg
M. FORNAL Bogdan	Professeur, Institue of Nuclear Physics, Polish Academy of Sciences (Pologne)

Contents

List of Figures

List of Tables

The Goals and Structure of the Present Document [Introductory Comments]

The present document describes the doctor-thesis research-project in the domain of theoretical nuclear physics – more precisely in the domain of theoretical nuclear structure. In this project we will present numerous results of the realistic calculations which can be – and will be – compared with the experimental data. However the main interest in this project will be *not so much* on

Reproducing the Existing Experimental Data

but rather

Reproducing the Existing Experimental Data
and first of all
Predicting as Reliably as Possible Results in the Unknown Zones.

Our starting point is an observation that all so far known realistic theoretical models of nuclear structure depend on adjustable parameters, and – as observations of some other authors indicate – quite a lot of attention has been focussed in the past literature on the developments of the *models themselves*, whereas much, much less attention has been payed to the role of the *parameter adjustment procedures*.

This second aspect is receiving quickly increasing attention in our domain of research following a very fast progress in the specialised domain of science devoted to this issue:

The Inverse-Problem Theory of *Applied Mathematics*.

Inverse-Problem Theory addresses generally the issues of mathematical modelling e.g. in sciences, economy or politics, developing the mathematical methods whose importance lies in the fact that they are independent of any practical realisations. Perhaps paradoxically, the methods of adjustment of parameters for the reliable modelling can today be seen as mathematically (often much) more involved than the physical models themselves.

Why so much attention payed in our domain of physics *now* – and why *so late*?

It has been very well known to those working on mathematical modelling, and this for long years that the uncontrolled, untested results of the parameter adjustment procedures such as minimisation of the χ^2-test are very likely meaningless[1]. The reasons will be discussed in this document in several places, but one of the principal ones is related to the

[1] In their introduction to the book-chapter *Modelling of Data*, the authors of *Numerical Recipes*, the book whose first editions date about 30 years back, [1] (p. 651), observe with sarcasm:

"Unfortunately, many practitioners of parameter estimation never proceed beyond determining the numerical values of the parameter fit. They deem a fit acceptable if a graph of data and model '*l o o k s g o o d*'.
This approach is known as chi-by-the-eye. Luckily, its practitioners get what they deserve."

[i.e. - what the authors of the book meant here is: *'They'* obtain a *meaningless result*.]

so-called ill-posed inverse problem and/or divergencies of the algorithms most often related to the parametric correlations in the modelling, cf. Chapter 1 of this document. It will also be shown in this document that the so-called good fit quality in some zone of interest and the extrapolation of the predictions to the other zones behave as (almost) uncorrelated data sets. In other words, especially in the case of problems with the algorithmic stability, the predictions addressing new zones may depend 'exponentially' on the details in the fitted area... implying *de facto* null predictive power.

It is being repeated today in an increasing number of publications that *after* performing the parameter adjustment the rudimentary applications of the very well known mathematical tools of the inverse problem theory are necessary – without them the predictions of the modelling 'nears playing with the random numbers'.

These were just a few comments related to the question: "Why so much attention[2] payed now?" Concerning the second one: "Why so late, in nuclear physics given the fact that the issue was quite hot in other domains of research?" – It is difficult and perhaps not very instructive to analyse the historical tendencies like this one, however, one mechanism is certainly measurable in terms of important amounts of the research budgets. Indeed, the majority of the present day experimental research in nuclear physics is performed in the world-unique centres where each experiment – before being accepted – undergoes a detailed scrutiny. It then follows that the reliable theoretical predictions are very precious in optimising the experimental conditions and in avoiding unnecessary loss of the beam time – where from a considerable increase of interest in the high quality modelling for the experimental applications.

Interests and Motivations of the Present Project

In the present project we will be interested in detecting and examining the mechanisms of destabilisation of the theory predictions for the nuclear structure applications. Importantly, we wish not only to be able to detect the problems of uncertainties of theory predictions but also learn about the efficient methods of countering their negative effects. With these goals in mind we will apply certain methods inspired by the Inverse-Problem Theory of applied mathematics, combined with the probability calculus and the Monte-Carlo simulation techniques. We will be able to illustrate the impact of the experimental errors and estimate for the first time in the present context the realistic sizes of the prediction uncertainties as well as the mechanism of their propagation (and the 'speed' of their increase) when the combination of the proton and neutron numbers of the studied nuclear species approach the exotic nuclear zones.

The present project has been conceived as an introductory contribution to a number of international collaborations aiming at the research of nuclei of increasing exoticity. As it is well known, when the difference between the neutron and the proton numbers approaches its extremes, the nuclear life-times decrease very quickly, approaching and quickly exceeding the present-day instrumental detection limits. The idea proposed[3] is to search, within

[2] Recently, there have been organised entire nuclear physics conferences devoted exclusively to the issue of parameter-determination, modelling uncertainties and the inverse-problem related issues, signifying the new important trend.

[3] The project along these lines has been formally proposed to one of the funding agencies and we have learned recently that the project has been accepted. This would allow to the team of 7 proponents participating in the project to realise it and we hope to be able to contribute with our information about the optimisation of the Hamiltonians to the implied large scale calculations of the new generation.

the specially optimised large scale calculations, for the nuclear isomers (long lived excited states) *living longer than the corresponding ground-states thanks to specific quantum symmetries*. Such configurations will very likely offer the new possibilities of populating and detecting the very exotic-nuclei 'in revolutionary (Z,N)-plane areas' – if the isomers in question live orders of magnitude longer than the respective ground-state configurations.

To be more precise: One class of isomers which are at the target of the discussed project are the so-called high-K isomers. Their long life-times are principally due to the presence of stable axial symmetry and the increasing total spins aligned with the symmetry axis. Another class are the so-called shape isomers. Their long life-times are expected to be caused either by the fact that an excited state may have a very different, hopefully higher fission barrier (as compared to the ground-state configuration) – or – by exotic symmetries such as octahedral and tetrahedral ones[4]. Indeed, the latter two symmetries are known to generate neither dipole nor quadruple moments, thus neither E2 nor E1 transitions what is expected to contribute to the nuclear stability by orders of magnitude.

> *As far as the future applications of the present project is concerned, we hope to contribute with various variants of the mean-field Hamiltonian parameters as well as estimates of the prediction uncertainties for the exotic-nuclear isomers in exotic nuclei.*

Even though the applications of the results of the present project to the mentioned large scale calculations of the isomeric properties are among important *motivations* of the present project – these calculations are expected to be advanced soon in the future.

> *As far as the accomplished chapters of the project are concerned, we were able to perform the systematic studies of the single-nucleon energy uncertainties and their impact on the predicted levels - in particular for a series of examples in the super-heavy nuclei. We succeeded in detecting, examining and eliminating the parametric correlation in our realistic nuclear mean-field approach with the help of the Monte-Carlo methods thus contributing to the stabilisation of the model for the large scale calculations.*

There are many other detailed groups of results which are presented case by case in this document; here we limited ourselves to a few strategical lines of the motivations.

[4]One possibility would be to follow up the results of the very recent article from our group: *"First Evidence for the Presence of Nuclear Octahedral and Tetrahedral Symmetries in a Rare Earths Nucleus"* by J. Dudek, D. Curien, I. Dedes, K. Mazurek, S. Tagami, Y. R. Shimizu and T. Bhattacharjee, July 2017, (submitted for publication).

The Structure of the Present Document

The present document is split into Chapters in each of which a series of correlated aspects, be it mathematical or in terms of the calculations results are collected together.

Chapter 1 is devoted to the description of some general features of the uncertainties in mathematical modelling. We introduce the Inverse Problem in the context of the quantum theories and combine its strategical notions with the elements of the probability calculus for the present nuclear context. We also discuss certain mathematical/technical aspects needed for the project which include the powerful Singular Value Decomposition theorem, Monte-Carlo simulation techniques and the efficient method of non-linear minimisation in the multi-dimensional spaces.

Chapter 2 is focussed on the relatively detailed description of our realisation of the realistic phenomenological nuclear mean-field theory. This includes the definition of various variants of the Hamiltonian as well as the description of the method of numerical solutions of the associated Schrödinger equation. For that purpose we present the spherical basis used to apply the diagonalisation solution-method and the way of calculating the matrix elements with arbitrary interactions of spherical symmetry. We present briefly how the experimental data for the mean-field single-nucleon energies are extracted from the raw experimental data. Finally we introduce an advanced Woods-Saxon Hamiltonian in which the most important, nuclear-structure dependent terms such as spin-orbit or tensor interaction terms are described in some details.

Chapter 3 presents the results of the calculations, the first part of which is based on the detailed analysis of the exact simulation model. With the help of this mathematical construction we present certain practical aspects of the mathematics of the inverse problem. We introduce an essential distinction between the intraneous and extraneous prediction regimes and discuss and illustrate the differences between the two. We devote some discussion to the specific notion of the so-called exact theories which, in the realistic cases (and if they exist – we do not know of any in the domain of the nuclear structure) are shown to possibly loose any significance - if the instrumental precision is not sufficient: This brings us to what we refer to as NO-GO property even-for-the-exact-theories. Finally we discuss the powerful notion of the *induced exact models* – which is a central tool for the realistic estimates of the prediction performance of the realistic models.

Chapter 4 shows our analysis of the detection and elimination of the parametric correlations using the Monte-Carlo method. These correlations in the realistic cases become strongly non-linear and may involve more than two parameters. We compare the results for the traditional Woods-Saxon Hamiltonian with the modernised version whose construction of the spin-orbit potential is based on the microscopic arguments. In this version the spin-orbit potential depends on the nucleonic densities and is calculated using the designed self-consistency algorithm. In this way, and in the spirit of the advanced phenomenological methods, we combine the parametric robustness of the central potential – discussed in the text – with the self-generated simplicity of the density-dependent spin-orbit term.

Chapter 5 illustrates the overall performance of the density-dependent version of the Woods-Saxon Hamiltonian which is expected to be used routinely in the large scale calculations of the nuclear isomeric properties mentioned above. We show in particular that the density-dependent spin-orbit potential, which depends formally on 4 parameters (two parameters less as compared to the traditional one) performs fully comparably to the original traditional variant. However we also demonstrate that the 4 coupling constants of the

density depended Hamiltonian are strongly (but linearly) correlated. These correlations can trivially be eliminated and we arrive at the conclusion that the density dependent spin-orbit potential with one free parameter performs comparably well, and occasionally better than the traditional, spin-orbit interaction potential depending on 6 parameters.

Chapter 6 gives some synthetic remarks about the FORTRAN programmes developed entirely for the purpose of this project; one part of the programming was devoted to the solution of the Schrödinger equation, whereas another one, based on the free distribution of the Xfig graphical system has been developed entirely by us for the graphical applications used in this document.

Chapter 1

Predictive Power and Inverse Problem in Quantum Theories

In this Chapter we begin by introducing the notion of *predictive power* of a physical theory. It will be explained that obtaining 'good' or 'bad' results not only depends on the uncertainties of the experimental information, but also on the physical model's errors. This brings us to the issue of 'parameter optimisation', and at the same time to the underlying mathematical theory known in the literature under the name of *inverse problem*. We will introduce all the mathematical framework around the inverse problem theory needed for this project, and the mathematical tools necessary for practical solutions. We will combine probability theory aspects together with the inverse problem, for a better description of the concept of Predictive Power in stochastic terms. This will finally lead us to formulating our realisation of the Monte-Carlo simulations techniques.

1.1 Predictive Power of a Mathematical Model

The issue of introducing and/or making precise the notion of *prediction uncertainties*, or – as formulated more colloquially – of *predictive power of mathematical modelling*, turns out to be a relatively complex one, as presented below with the help of a few examples. Summarised in a few words: It always has to do with trying to optimise a certain outcome of mathematical modelling – before testing, most often against some experimental data – usually *via* adjustment of some elements of the model (e.g. parameters) to the results of the already existing experiments.

Let us consider a few examples. Usually, in various domains of research or technology, we may wish to know something about the expected result before an empirical verification. For example, when exploring the oil fields in geophysics, it is important to know where to start drilling since installing one 'pump' may cost up to a billion of dollars. Consequently a modelling efforts will be necessary based on the geological structure of the area of interest. In political life of every state, candidates to the presidency wish to know who advances towards the victory before the actual day of vote. Therefore a careful (costly) collection, analysis and interpretation of the opinion pols, usually referred to as sampling, are of utmost importance. All the associated information treatment and related modelling methods usually involve application of advanced mathematical approach based on the theorems elaborated in the framework of *applied mathematics* (see below).

In physics, and in particular in nuclear physics – the research domain of the present thesis – we wish to learn how to approach in the most economical way "t h e unknown", for example completing the Chart of Nuclei with the very exotic, yet unknown nuclear species. For this, we would need to give certain indications about selected, particular structural properties of the poorly known or totally unknown nuclei so that the experimental conditions can be optimised – and this at the possibly lowest instrumental costs. Towards this goal, advanced theoretical modelling will be necessary and the optimisation of the model parameters will play the most crucial role so that the finally predicted result is trustworthy and as stable agains all sorts of uncertainties as only possible. Checking *ex-post* if the theoretical prediction is in agreement with the experimental information will provide the next step in the process of improving the completeness and reliability of the theoretical description and, more generally, the mathematical modelling.

When discussing theory's 'predictive power', one usually has not much doubt about what is meant. We often assume without saying (as it turns out also even without verifying) that the theory in question can predict and produce reliably the results, which usually address the experimentally unknown region. But as soon as we attempt posing more precise questions, serious difficulties are likely to arise, already at the semantic level. Below we will give some examples before addressing more precisely the issue of the definition of prediction uncertainties and predictive power.

Model Prediction – What Does It Mean: To Predict?

Consider a given mathematical model (or 'theory', as theorists prefer). Any calculation performed with this theory and addressing yet unknown information-range can be called a prediction. It is only after the corresponding experimental verification that we may say if the predicted result – and thus the prediction – is or is not acceptable, in other words: if it is a good or a poor prediction. Therefore, since performing any calculation before the actual experiments are performed can always be called *a prediction*, each prediction has always *a predictive power*. Therefore this term alone does not represent any particular feature and to become useful, it must be complemented with some qualifiers. For instance, we may need to specify what we call *good* predictive power. But being good for someone may not be good enough for someone else. Therefore, the discussed terminology (we avoid at this point the word 'definition') carries a dose of subjective judgement and arbitrariness. Consequently, we will need to approach the issue of some objective criteria or, if impossible, some relative criteria, which will allow to examine theory's prediction capacities, and thus predictive power, by minimising the effect of explicit or implicit subjective judgement. We will discuss this problem again after introducing some notions related to the issue of probability in the context of mathematical modelling.

1.1.1 About Uncertainties of Theoretical Modelling

All today known theories which address the structure of subatomic systems can be considered incomplete. Thus each of them usually addresses some fragments of the more complete set of data, a part of the full information at hand. This has to do with the fact that the present day knowledge of the nucleon-nucleon interaction, even though progressing in time, is still rather limited. Somewhat colloquially: In principle, what we aim at knowing is what is sometimes referred to as the 'full truth about the system'. Thus, ideally, we would wish to have a theory which perfectly and exactly describes the physical systems of

interest and therefore can give the full[1] information about all the observables we may be interested in. Along these lines of thinking, solving the 'true' Schrödinger equation within a given non-relativistic theory, based on the 'true' Hamiltonian, $\hat{H}^{\text{true}}$, will, by definition, precisely describe all the nuclear interactions – thus implied quantum mechanisms, states and transitions and, in particular, the exact energies of the system, e_n^{true}.

Let us follow this line of thinking by observing that physical theories, even though incomplete, evolve and improve with time, so that we could express this evolution by writing

$$\hat{H} = \hat{h}_1 + \hat{h}_2 + ... + \hat{h}_n + ... \tag{1.1}$$

Above, $\hat{H}$ represents our actual knowledge, $\hat{h}_i$ – with increasing index 'i' – represent, say, the newer and newer interaction terms found along the progress, and $\hat{h}_n$ represents the last one found so far. Therefore, since the 'full truth Hamiltonian' remains unknown, we can write our present-day knowledge Hamiltonian using the following symbolic form

$$\hat{H} = \hat{H}_{\text{true}} + \delta\hat{H}_{\text{ignor}} \;\leftrightarrow\; \hat{H}_{\text{true}} = \hat{H} - \delta\hat{H}_{\text{ignor}}, \tag{1.2}$$

where $\delta\hat{H}_{ignor}$ represents symbolically our ignorance, the lack of knowledge which as long as present, will always lead to the theoretical uncertainties, sometimes referred to as theoretical errors. Let us emphasise that this part of our discussion uses so far a rather descriptive/colloquial terminology involving such objects as 'operators $\hat{H}_{\text{true}}$ and $\delta\hat{H}_{\text{ignor}}$'; these terms are not uncommon in working discussions – but what are they when it comes to comparison with experiment?

In reality, what we have called so far 'operators $\hat{H}_{\text{true}}$ and $\delta\hat{H}_{\text{ignor}}$' are *de facto* abstract symbols, whose exact mathematical form remains unknown. The role of these symbols is to help us in guiding the *heuristic* discussions. In 'practice' we will never be able to act with these 'operators' on e.g. basis wave functions in order to calculate for instance the corresponding matrix elements. It becomes clear that, even if useful when deriving the final mathematical expressions – which will help us working on the prediction capacities of the modelling – the final results of such considerations, e.g. of the mathematical derivations, must not depend on any of them.

At this point let us make a few steps further towards a more precise meaning of such terms as 'exact theories' and 'exact Hamiltonians'. Since we have introduced already the symbol $\hat{H}_{\text{true}}$ - let us suppose, as the working hypothesis, that its precise mathematical form has been found. Two scenarios can be envisaged: Either this Hamiltonian depends on some *adjustable parameters*, say $\{p\} \equiv \{p_1, p_2, \ldots p_{n_p}\}$, often called *coupling constants* - or, conversely, depends on no parameter. Since all the most advanced theories we know of, belong to the first category, this is what we retain for the rest of the present discussion.

Let us begin with the observation that in order to be able to apply the exact theory in question, we will need to optimise its adjustable parameters. One might pose the question of "whether it makes sense to talk about exact theories which depend on adjustable parameters", to discuss the notions such as H_{true} or H_{ignor}" – or for that matter – if it makes sense to talk about exact theories *at all*? We believe that on the conceptual level the answer is strongly affirmative. Indeed, if we accept that the evolution represented symbolically by Eq. (1.1) is driven by some guide-line other than physicist's fantasy – such a guideline must represent an idea of following a steady improvement of our knowledge – the tendency whose limiting case some philosophers call *absolute truth*. We would not

[1] The term which first would need to be made precise.

defend at this place the idea that in nuclear structure physics the questions of this type have any practical solution in the foreseeable future, but we can be sure that if *we never formulate such questions even in abstract terms* - we will never have any chances to find an answer. This is usually done by trying to reproduce a representative set experimental data as well as possible, say, $\{f_k^{\rm exp} \pm \delta f_k^{\rm exp}\}$ where $\delta f_k^{\rm exp}$ refers to the experimental errors and $k = 1, 2, \ldots n$. As far as model parameters go, here, one may think of a set of a very few coupling constants, say κ_i, $i = 1, 2, \ldots n_p$, where n_p is a small integer number. These coupling constants are expected to describe nearly an infinity ($n \to \infty$) of all imaginable (or at least available) experimental data. Since the experimental data are, and will always be, biased due to experimental errors, from the point of view of mathematics they represent *random variables* which, as all random variables in probability calculus, are characterised by their respective probability distributions

$$P_k(f_k) = P_k(f_k;\, f_k^{\rm exp}, \delta f_k^{\rm exp}), \tag{1.3}$$

where, very often, probability distributions[2] P_k represent Gaussian (the so-called 'normal') distributions centred at $f_k^{\rm exp}$, with the 'sigma-value' related to the experimental error, in short: $\sigma_k \leftrightarrow \delta f_k^{\rm exp}$. The presence of the uncertainties of the experimental input, introduced to any parameter optimisation procedure will generally transmit the random variable character of the input to the final output result. Thus the deduced optimal parameters are in fact, from the mathematics point of view, random variables characterised by certain (derived) probability distributions. The resulting uncertainties of the deduced parameters can be expressed using the 'new generation' of probability distributions

$$\mathcal{P}_\kappa = \mathcal{P}_\kappa(p_\kappa) \;\; \text{or} \;\; \mathcal{P}_\kappa = \mathcal{P}_\kappa(p_1, p_2, \ldots p_{n_p}). \tag{1.4}$$

Therefore *de facto* each parameter of any theory must be considered as a random variable characterised by the corresponding probability distribution, here $\mathcal{P}_\kappa$. This implies that, whichever calculation we perform afterwards, all the calculated quantities, such as e.g. energies of the system, must also be seen as random variables accompanied by the probability distributions, for instance, for the eigen-energies

$$\Pi_\rho = \Pi_\rho(e_\rho), \tag{1.5}$$

in the simplest case [often the probability distributions of a given random variable will depend on other random variables]. Those latter probability distributions (as well as those given by eq. (1.4)) can often be determined as the by-products of the optimisation procedures: this and related problems will be in fact among the goals of the present work.

At this point we arrive at an important observation: even the so-called exact theories, which are expected to exactly reproduce the known experimental data and therefore generate no errors – simply do not exist. In the discussions related to "exact theories" it is easy to let oneself being driven by the tendencies of mixing the conceptual / purist level of the discussion, with kind of "practical connotations". For instance, by the very definition, the exact theory does not have any *theory errors* and even less "theory errors caused e.g. by the numerical methods applied in practice". In order to be able to produce

[2] By comparison with the standard Gaussian probability distribution,

$$P(x; \mu, \sigma) \propto \exp[-(x-\mu)^2/2\sigma] \;\; \text{where} \;\; \mu \equiv \langle x \rangle \equiv \bar{x},$$

let us observe the analogy between the so-called independent random variables, x and f_k as well as the symbols characterising the experimental results, $f_k^{\rm exp} \leftrightarrow \mu$ and $\delta f_k^{\rm exp} \leftrightarrow \sigma$.

such an exact result, we would need to know the exact i.e., errorless parameter values – but this, following the arguments around eqs. (1.3)-(1.4) will never be possible[3] since all our measurements are always biased by instrumental errors and uncertainties. Thus, unless we are able to construct the theory without any parameters (which could possibly become exact) - no other theoretical modelling will be able to satisfy the human expectations from the 'exact model'.

1.1.2 Mean-Field S.-P. Energies and Experimental Counterparts

In this document we use repetitively the notion with a rather long explicit name *mean-field single-particle (S.-P.) energies*. The long name emphasises the fact that the objects behind this concept exist in our theoretical considerations thanks to the existence of one of the most powerful and successful theory in nuclear structure physics: The Nuclear Mean Field Theory. The latter approximate theory uses as the starting-point the nucleon-nucleon interactions which, as the result of their complexity make finding effectively the solutions often impossible, almost impossible or very complex, especially for heavy nuclear systems. However, thanks to the introduction of a universal method which allows for an approximate elimination of the complex two-body nucleon-nucleon interactions and replacing them by a one-body effective potential, a number of efficient methods and concepts have been introduced. Among others, the concept of the mean-field single nucleon energies, fictitious theoretical constructions which turned out to render excellent services in many branches of theoretical physics and domains of physics, including the nuclear structure.

The concepts of the nuclear mean-field owe their great interest in nuclear structure physics to the fact that they allowed to construct, among others, the effective calculation schemes, which are very successful empirically. But they also allowed for introducing a number of simplifying notions, secondary concepts and ideas such as *nuclear surface* followed by the successful notions of the *nuclear shapes and deformations*. Those latter ones brought in the framework and the natural physical justification of other fruitful ideas such as the nuclear *collective motion theory*, the one which resulted in the Nobel Prize to A. Bohr, B. R. Mottelson and L. Rainwater in 1975.

> *One may be tempted to say that the nuclear mean-field theory gives not only the mathematical basis for the powerful computer codes which allow for the very effective nuclear structure calculations, successful interpretations of the numerous experimental results and predictions of many others thus accelerating the progress in nuclear structure physics.*
>
> *In parallel one may seek conceptual analogies between such domains of physics as thermodynamics and statistical physics and the nuclear mean field theory.*
>
> *Indeed, this was thermodynamics which allowed to leave the purely microscopic view of describing the gas particles in the container in terms of Avogadro-number Newtonian-trajectories and use derived notions addressing the averages. The new notions such as volume, pressure, temperature, entropy, free-energy of*

[3] The following idea may come to one's mind: If we cannot obtain the optimal parameters 'professionally' by using for this purpose the experimental information – perhaps we can just try to guess their values? After all, when we know those, the results of the exact theory with exact parameters are expected to be exact. This optimistic hope may need to be relativised: Since we looking for a single point in a multi-dimensional space of continuous variables (parameters), the probability of this to happen will be proportional to what is in topology referred to as measure of a single point – in the continuous space: zero.

the system etc. – it will be difficult to over-estimate how highly the description of the thermodynamic systems profited from them and helped 'imagining things'.

And yet:
These were human-constructed abstract notions – and we made them observable.

In the nuclear mean-field theory we introduce the notion of fictitious, abstract particles, whose motion is expected to resemble the motion of the real nucleons under the action of an average nuclear interaction... except that the real nucleons move under the action of all the real interactions which exist in the real nucleus. We call those fictitious human-constructed abstract notions mean-field nucleons: We calculate their energies according to the mean-field theory, with their help construct the hierarchy of the mean-field particle-hole excitations (thus in this sense fictitious numbers)... and compare very successfully with the really measured non-collective excitations. One is tempted to say:

And yet:
These were human-constructed abstract notions – and we made them observable.

The price to pay when working with the mean-field nucleon-energies is: No direct experimental data available since the single-nucleon energies are not observable – and in order to extract the 'experimental mean-field comparable nucleon-energies' specific extraction/averaging procedures have been designed. These can be considered very standard today in the nuclear physics literature and in the following part of this section we will briefly recapitulate how they are used.

As we have already mentioned, the experimental information which we have at our disposal and which we use to obtain the parameter values of the model, comes with errors. The present project focusses on selected properties of the so-called *doubly-magic* spherical nuclei. More precisely, we will analyse the properties of the nuclear mean-field single-nucleon energies using the available experimental information for the following nuclei:

$$^{16}_{8}\mathrm{O}_{8},\ ^{40}_{20}\mathrm{Ca}_{20},\ ^{48}_{20}\mathrm{Ca}_{28},\ ^{56}_{28}\mathrm{Ni}_{28},\ ^{90}_{40}\mathrm{Zr}_{50},\ ^{132}_{50}\mathrm{Sn}_{82},\ ^{146}_{64}\mathrm{Gd}_{82}\ \text{and}\ ^{208}_{82}\mathrm{Pb}_{126}. \tag{1.6}$$

As one of the realms of applications, we will examine the prediction uncertainties on the example of spherical super-heavy nuclei, later in this document.

Let us emphasise again (see the text in italic above) that in nuclear structure physics the so-called experimental single-nucleon energies are in fact complicated and model dependent objects, cf. Ref. [2]. This is because by the very definition, in experiment these objects represent certain mean values. Similarly as in the case of the nuclear modelling with the help of the nuclear structure *mean* field theories, the theoretical mean-field single-nucleon energies represent a result of a certain averaging (thus *mean*) of the nucleon-nucleon interactions. Therefore, even though the theory and experimental approaches are consistent at their conceptual starting points, since they both address certain mean values, the net result is that the central quantities of interest in this work, the mean-field single-nucleon energies, are not *directly* measurable. However, they are in permanent use in the nuclear structure theory and experiment as well as in many-many thousands of publications and we will use them in the present work in the same way as the other authors did in the past.

The single particle energies for spherical nuclei are deduced from one-nucleon transfer reactions, where the neighbouring nuclei with $A\pm1$ nucleons are populated or de-populated. These reactions provide the necessary information needed to extract the single-nucleon energies, i.e. the excitation energy, angular momentum and parity of the single particle or

single hole states of a given set of j^π quantum numbers. While any given mean-field single-nucleon level – always treated as an average – can be seen as coinciding with one nuclear level in some cases, there are often various levels of the same spin and parity (arising from excited core configurations) in the same energy region and these mix with the unperturbed mean-field model state. To recover its energy, one needs to compute the 'center of gravity' of the whole group by weighting the energy of each level in proportion to how strongly it is excited in the transfer reaction (i.e. by its spectroscopic factor $S(\kappa, i)E_i$) [2, 3]:

$$\varepsilon_\kappa = \sum_i S(\kappa, i)E_i, \tag{1.7}$$

where ε_κ is the mean-field single-particle energy we are looking for, E_i an actual energy level of odd nucleus populated in the transfer reaction, and $S(\kappa, i)$ is the spectroscopic factor, i.e. the probability that level i contains the single-particle κ. This procedure was justified by M. Baranger [3], from a theoretical point of view.

As it follows from the underlying formalism ([4], Vol. I, pg. 423; [5], pg. 59), one has to stress that the appropriate use of Eq. (1.7) to calculate the single-particle energy ε_κ requires that the spectroscopic factors must satisfy the normalisation condition

$$\sum_i S(\kappa, i) = 1, \tag{1.8}$$

usually referred to as 'sum rule'. This is a very helpful element of the information since it allows:

- To verify whether all the components 'i' (also called 'fragments') have been seen in any given experiment – and therefore whether the obtained information is sufficiently complete, and:
- To verify – taking into account the experimental errors – whether the $S(\kappa, i)$ values have been precisely determined, i.e. without any major bias.

Unfortunately, we do not always have the full experimental information needed to assure Eq.(1.8). The large values of spectroscopic factors usually extracted from transfer reactions using hadrons as projectiles are not always reliable. Nevertheless, they can be used, by virtue of an approximation, in the weighting procedure, provided that Eq. (1.7) is replaced by [2]

$$\varepsilon_\kappa = \frac{\sum_i S(\kappa, i)E_i}{\sum_i S(\kappa, i)}. \tag{1.9}$$

As it can be seen from Eq. (1.9), the uncertainties of the experimental single-particle energy estimates originate from two sources: The measured excitation energies E_i, whose uncertainties due to the instrumental reasons can be considered rather small and usually do not exceed a few keV – and the spectroscopic factors $S(\kappa, i)$. The first one depends on the energy resolution of the instrument, and is usually well controlled under each given experimental realisation. On the other hand, the spectroscopic factors are calculated using the measured and theoretical cross sections of the reaction, cf. [2], [5] (page 59)

$$\left.\frac{d\sigma}{d\Omega}(\theta, E_i)\right|_{exp} = S(\kappa, i) \times \left.\frac{d\sigma}{d\Omega}(\theta, E_\kappa)\right|_{th}, \tag{1.10}$$

where we assume for the theoretical calculation that the state is a pure particle- or hole-state. This means that, at the end, our 'experimental' single particle energies are in fact model dependent since, in particular, one has to take into account that the spectroscopic factors may change depending on the model used. Consequently, it is very important to have at one's disposal a large number of reaction data which allow for the cross-checking before obtaining a reliable result for the spectroscopic factor.

1.2 Inverse Problem Theory of Applied Mathematics

In this section we are going to discuss some selected aspects of the mathematical theory called *Inverse Problem Theory*[4] – a chapter of very actively developing sub-field in the domain of *Applied Mathematics*. We will establish links between this particular mathematical theory and the applications to the quantum theory of nuclear structure focussing on the modelling of the nuclear mean-fields.

Inverse Problem Theory is the sub-field of mathematics, which addresses generally the mathematical conditions of modelling certain properties, relations, effects or phenomena, irrespectively of the nature of their particular realisations. The central role in construction of this theory is played by the fact that the great majority of the models needed in numerous practical applications, in particular in theoretical physics, depend on parameters. Thus, accordingly, one says that:

> *Applying model M on the ensemble of its optimal parameters p^{opt} produces the results d called data. Introducing the corresponding operator, $\hat{M}$, one writes symbolically:*
>
> $$\boxed{\hat{M}p^{\mathrm{opt}} = d.}$$
>
> *This situation is referred to as solving the direct problem or solving the forward problem.*

However, since the optimal parameter values of any model are usually not known *a priori*, it is necessary to find them beforehand. For that purpose one should first:

> *Determine the optimal set of parameters by solving formally the inverse relation:*
>
> $$\boxed{\hat{M}^{-1}d = p^{\mathrm{opt}}}$$
>
> *– wherefrom the name solving the inverse problem for the above operation.*

[4] *Inverse Problem* is a mathematical method which has been intensively studied during the last few decades – mainly because of the existence of numerous applications. To give an idea about this recent activity we have performed a Google-test by comparing the number of hits when searching for the strings of characters 'Inverse Problem' on the one hand side and 'Nuclear Physics' on the other. The resulting hit-numbers are: 9,890,000 for Inverse Problem and 6,480,000 for Nuclear Physics. This should be confronted with the fact that the field of Nuclear Physics is much older than the field of the Inverse Problem, thus implying that the broadness and the level of activity in the former are very important. There exist specific journals devoted to this field of mathematics as well as numerous textbooks of varying scope and mathematical rigour, cf. e.g. references [1, 6–22].

One of the central issues faced by the inverse problem theory are the mathematical conditions of existence and stability of the inverse operator $\hat{M}^{-1}$ since, as it can be shown, in most of the cases of fundamental practical interest – such an operator simply does not exist and alternative methods of finding the effective optimal parameter sets must be sought. Yet, the knowledge of the inverse problem theory gives an important guidance also in such cases and the related discussion will be followed in the next sections.

The problems of parameter optimisations caused by a possible non-existence of the inverse operator are complicated further by the fact that the optimisation methods must use the experimental data which, strictly speaking, are not 'just numbers' but random variables as pointed out earlier. This implies the necessity of taking into account the probability (or, more adequately:) uncertainty probability-distributions related to the experimental data which form the input to the optimisation procedures. Solutions to this problem are very important and can be obtained using the Monte-Carlo methods, one of the central aspects of the present work.

According to the inverse problem theory, each construction of the solutions of the inverse problem (read: optimisation of the model parameters) must take into account the following aspects simultaneously:

- We must construct the model itself, i.e., to start with, select or derive the formalism. For instance, in the case of the non-relativistic nuclear structure problems, the natural approach will consists in using the Schrödinger equation with appropriately defined interaction potential, the latter depending on a number of parameters whose optimal values will need to be found.
- Having prepared the formalism appropriately, we will need to adequately select and prepare the experimental information. This fragment of the full procedure is referred to as 'sampling'. The accepted data should be representative for the studied problem and preference to the precise measurements should be given.
- The method of solution of the parameter optimisation problem, should be verified as adequate for the undertaken research on both conceptual and numerical realisation levels. Furthermore: The mathematical inverse problem theory provides a number of mathematical theorems and criteria, which will allow to verify *ex post* whether the obtained solutions are meaningful or not. Without that step – as indicated in the literature – the solutions should by default be assumed meaningless[5].

Taking the above three points into account simultaneously is pivotal for meaningful parameter optimisation, possible detection of 'pathologies' such as missing experimental information, the presence of instabilities, and – very importantly as it will be discussed in this work – the presence of the parametric correlations.

[5] As quoted already: In their introduction to the book chapter *Modelling of Data*, the authors of *Numerical Recipes* [1] (p. 651), observe with sarcasm: *"Unfortunately, many practitioners of parameter estimation never proceed beyond determining the numerical values of the parameter fit. They deem a fit acceptable if a graph of data and model 'looks good'. This approach is known as chi-by-the-eye. Luckily, its practitioners get what they deserve."* [i.e. - what is meant here is: *they* obtain a *meaningless result*.]

1.2.1 A Particular Reference Case: Linear Inverse Problem

Let us begin by considering a model whose parametric dependence is linear, i.e., $M \to G$ maps a set of parameters p (causes) to a set of data d (effects) strictly linearly

$$Gp = d, \tag{1.11}$$

in which case the solution of the inverse problem reads

$$G^{-1}d = p, \tag{1.12}$$

under the condition that the numbers of parameters and data points are equal in which case G^{-1} is just an inverse matrix and the considered problem is strictly equivalent to a system of linear equations in matrix representation. [In what follows we avoid putting 'huts' over the operators, for simplicity.]

However, more generally, we will need to assume that p and d are two vectors of dimensions n_p and n_d, respectively. Therefore, G can be seen as a general $n_d \times n_p$ matrix. In the realistic cases we usually work with $n_p \ll n_d$ since the number of parameters is usually requested to be much smaller than the number of data points. In such cases we may take advantage of the fact that the product $G^T G$ is a $n_p \times n_p$ square matrix. Applying G^T to the left and right hand sides of Eq. (1.11) we obtain

$$\left(G^T G\right) p = G^T d. \tag{1.13}$$

From the above equation we can formally write the matrix equation that will allow us to calculate the optimal-parameter vector

$$p = \left(G^T G\right)^{-1} G^T d. \tag{1.14}$$

The Problem of Singularities: Ill-Posed Inverse Problems. At this stage, we may think that the problem is solved. However, the existence of the solution of Eq. (1.14) depends on whether $(G^T G)^{-1}$ exists or not. The problem usually arises when the rank of $G^T G$ (maximum number of linearly independent rows or columns) is not equal to n_p. If this happens, the determinant of the squared matrix is zero and therefore the underlying matrix is not invertible. The mathematical consequence of this fact is that there is no unique solution for any given input data vector.

> *We say that the underlying selection of data (sampling) does not constrain this particular model since, formally, in the considered case we may have an infinite number of solutions. We say that the original inverse problem is 'Ill Posed'.*

When this happens either the sampling of the data will need to be modified, or the model improved.

1.2.2 Least-Squares Problem

When the problem in Eq. (1.13) cannot be solved exactly, we may attempt by-passing this step by minimising the square of such a 'generalised distance' between data and the model result. For this, we need to introduce a new quantity, say S, which defines the difference between d and Gp

$$S = d - Gp. \tag{1.15}$$

The 'optimal' parameters will be found by minimising the square:

$$S^2 = (d - Gp)^T (d - Gp), \tag{1.16}$$

imposing that the partial derivatives over the corresponding parameters vanish:

$$\frac{\partial S^2}{\partial p_j} = 0, \qquad j = 1,... n_p . \tag{1.17}$$

It will be useful to express the above vanishing condition explicitly with the help of summations, i.e.:

$$S^2 = \sum_{i=1}^{n_d} \left(d_i - \sum_{j=1}^{n_p} G_{ij} p_j \right) \left(d_i - \sum_{k=1}^{n_p} G_{ik} p_k \right), \tag{1.18}$$

so that

$$\begin{aligned} 0 = \frac{\partial S^2}{\partial p_m} &= \sum_{i=1}^{n_d} \left(- \sum_{j=1}^{n_p} G_{ij} \frac{\partial p_j}{\partial p_m} \right) \left(d_i - \sum_{k=1}^{n_p} G_{ik} p_k \right) \\ &+ \sum_{i=1}^{n_d} \left(d_i - \sum_{j=1}^{n_p} G_{ij} p_j \right) \left(- \sum_{k=1}^{n_p} G_{ik} \frac{\partial p_k}{\partial p_m} \right) \\ &= - \sum_{i=1}^{n_d} G_{im} \left(d_i - \sum_{k=1}^{n_p} G_{ik} p_k \right) - \sum_{i=1}^{n_d} \left(d_i - \sum_{j=1}^{n_p} G_{ij} p_j \right) G_{im} \\ &= \sum_{k=1}^{n_p} \sum_{i=1}^{n_d} G^T_{mi} G_{ik} p_k - \sum_{i=1}^{n_d} G^T_{mi} d_i + \sum_{j=1}^{n_p} \sum_{i=1}^{n_d} G^T_{mi} G_{ij} p_j - \sum_{i=1}^{n_d} G^T_{mi} d_i \\ &= 2 \sum_{k=1}^{n_p} \sum_{i=1}^{n_d} G^T_{mi} G_{ik} p_k - 2 \sum_{i=1}^{n_d} G^T_{mi} d_i. \end{aligned} \tag{1.19}$$

We can re-write the above expression in the matrix form as follows

$$\frac{\partial S^2}{\partial p_m} = 2 \left(G^T G\, p - G^T d \right)_m = 0, \tag{1.20}$$

which finally leads to

$$p = \left(G^T G \right)^{-1} G^T d. \tag{1.21}$$

A Formal Analogy: Distance Minimisation vs. Linear Inverse Problem. Let us observe that Eq. (1.14) is formally the same as the just derived Eq. (1.21), which means that the first equation is the solution of the linear inverse problem and at the same time of the least-squares problem. Above, the problem of the existence of the solutions of the actual least-squares problem (or not) has been transformed into the problem of the existence or not if the inverse matrix $(G^T G)^{-1}$ and will need to be studied on the case by case basis.

1.2.3 Non-Linear Inverse Problem

In the case of the linear models we are able to arrive at an explicit expression for the optimal model-parameters since we can identify separately the three elements: the matrices G or $G^T G$ acting directly on the parameters p represented by a single vector and the vector of data d, even though the existence of the solution was not always guaranteed.

In the case of the non-linear model, we cannot separate the operator from the parameters with the help of the elementary algebraic operations (matrix multiplications) as we did in the previous section; but we will show how to by-pass this difficulty soon.

Let us continue by introducing the characteristic features of the non-linearity. Thus, for the non-linear model, we rather explicitly use the parentheses, '(' and ')', in the same way as to express a functional dependence, $f = f(x)$, and write

$$M \to G; \;\; Gp = d \;\; \to \;\; G(p) = d. \tag{1.22}$$

Next we will obtain the solutions analogous to the one in Eq. (1.14) by generalising the *least-squares* approach introduced earlier into the form known as χ^2-*minimisation*. Let us remind the reader at this point that the minimisation of the χ^2-test corresponds conceptually to the minimisation, in multidimensional spaces, of a generalised distance between a point representing the experimental data and the results of the modelling representing the same physical quantities. Since one demonstrates in topology that there exist an infinite number of manners of defining the distance in multidimensional spaces - it becomes clear that selecting one of those cannot be in general considered as equivalent to solving the inverse problem $M^{-1}d = p^{\rm opt}$.

The non-linear problems are of central importance for us in the present project since we are going to work with the Schrödinger equation which connects the parameters with the results/data in a strongly non-linear manner. [We will soon abandon the use of the term *data* for the results of the model, even though this way of expressing can be considered standard in the jargon in the inverse problem theory domain.]

Nuclear Mean-Field Theory in the Context of the Inverse Problem. Consider a given realisation of the nuclear mean-field theory. The latter is equivalent to saying that the interaction potential, say $\hat{V}$, which generally depends on a number of parameters $p \equiv \{p_1, p_2, ... p_{n_p}\}$ is known – so is the related Hamiltonian:

$$\hat{V} = \hat{V}(p) \;\; \to \;\; \hat{H}(p) = \hat{t} + \hat{V}(p). \tag{1.23}$$

Solving the implied Schrödinger equation for each given set of parameters,

$$\hat{H}(p)\psi_n = e_n^{th}(p)\,\psi_n, \tag{1.24}$$

allows to obtain its solutions as functions of the model parameters. Even though both the energies and the wave-functions depend on these parameters, we do not introduce this dependence into ψ_n explicitly, not to complicate the notation. The dependence of the energies on the parameters will be needed explicitly below but we will slightly modify the notation as follows:

$$e_n^{th} \equiv f_n(p), \tag{1.25}$$

where $f_n(p)$ are continuous differentiable functions. Our goal is to find the optimal values of the parameters of the Hamiltonian to assure the best description of the physical system. For this purpose we will use the known experimental data $d^{exp} \equiv \{d_1^{exp}, d_2^{exp}, ... d_{n_d}^{exp}\}$. We will employ the χ^2-minimisation and define for this purpose the measure of the distance between the data and the model results in the usual form

$$\chi^2(p) = \sum_{i=1}^{n_d} w_i \left[d_i^{exp} - f_i(p)\right]^2, \tag{1.26}$$

in which w_i, called the weight factors, are by definition non-negative – otherwise at the disposal of the physicist. The choice of the weights is totally subjective.

The minimum of the above function occurs when its gradient vanishes[6], therefore we impose

$$\frac{\partial \chi^2}{\partial p_j} = 0, \quad j = 1,... n_p \,. \tag{1.27}$$

In order to be able to construct a computer-programmable algorithm finding the solutions of the above equations we will introduce an iterative algorithm allowing to advance from the preceding iteration to the next,

$$p^{(k+1)} = p^{(k)} + \Delta p^{(k)}, \tag{1.28}$$

according to a certain prescription. The corresponding prescription will be based on the Taylor expansion and can be constructed as follows.

To start let us re-write Eq. (1.26) at the iteration number $(k+1)$:

$$\chi^2(p^{(k+1)}) = \sum_{i=1}^{n_d} w_i \left[d_i^{exp} - f_i(p^{(k+1)}) \right]^2 . \tag{1.29}$$

Taking advantage of the Taylor linearisation, write down

$$\begin{aligned} f_i(p^{(k+1)}) &= f_i(p^{(k)} + \Delta p^{(k)}) \\ &\approx f_i(p^{(k)}) + \sum_{j=1}^{n_p} \left. \frac{\partial f_i}{\partial p_j} \right|_{p=p_j^{(k)}} \underbrace{\left(p^{(k+1)} - p^{(k)} \right)}_{\Delta p^{(k)}} . \end{aligned} \tag{1.30}$$

We can simplify the last expression by introducing the short-hand notation for the Jacobian matrix at each iteration 'k' as follows

$$J_{ij}^{(k)} \equiv \left. \frac{\partial f_i}{\partial p_j} \right|_{p=p_j^{(k)}} \tag{1.31}$$

so that

$$f_i(p^{(k)} + \Delta p^{(k)}) \approx f_i(p^{(k)}) + \sum_{j=1}^{n_p} J_{ij}^{(k)} \times \left(p^{(k+1)} - p^{(k)} \right) . \tag{1.32}$$

Before continuing, let us define two more auxiliary objects which will simplify the notation:

$$b_i^{(k)} = \sqrt{w_i} \left[d_i^{exp} - f_i(p^{(k)}) \right] \tag{1.33}$$

and

$$\mathcal{J}_{ij}^{(k)} = \sqrt{w_i}\, J_{ij}^{(k)}. \tag{1.34}$$

Inserting Eq. (1.32) to Eq. (1.29) we obtain the linearised expression for χ^2 as follows

$$\begin{aligned} \chi^2(p^{(k+1)}) &= \sum_{i=1}^{n_d} w_i \left[d_i^{exp} - f_i(p^{(k+1)}) \right]^2 \\ &\approx \sum_{i=1}^{n_d} w_i \left[d_i^{exp} - f_i(p^{(k)}) - \sum_{j=1}^{n_p} J_{ij}^{(k)} \left(p_j^{(k+1)} - p_j^{(k)} \right) \right]^2 \end{aligned}$$

[6] At this point we do not complicate the discussion by introducing any distinction between two types of the extrema (minima vs. maxima) and the saddle points, all satisfying condition (1.27), even though they are considered in the programming.

$$= \sum_{i=1}^{n_d} \left[b_i^{(k)} - \sum_{j=1}^{n_p} \mathcal{J}_{ij}^{(k)} \Delta p_j^{(k)} \right]^2$$
$$= \sum_{i=1}^{n_d} \left[\sum_{j=1}^{n_p} \mathcal{J}_{ij}^{(k)} \Delta p_j^{(k)} - b_i^{(k)} \right]^2 . \tag{1.35}$$

As the next step we introduce the last result into the expression for the gradient. We have to take into account that when we derive over $p^{(k+1)}$, $p^{(k)}$ should be treated as constant, therefore

$$\begin{aligned}
\frac{\partial \chi^2}{\partial p_m} &= 2 \sum_{i=1}^{n_d} \left[\sum_{j=1}^{n_p} \mathcal{J}_{ij}^{(k)} \Delta p_j^{(k)} - b_i^{(k)} \right] \cdot \left[\sum_{j'=1}^{n_p} \mathcal{J}_{ij'}^{(k)} \frac{\partial \Delta p_{j'}^{(k)}}{\partial p_m} \right] \\
&= 2 \sum_{i=1}^{n_d} \left[\sum_{j=1}^{n_p} \mathcal{J}_{ij}^{(k)} \Delta p_j^{(k)} - b_i^{(k)} \right] \cdot \left[\sum_{j'=1}^{n_p} \mathcal{J}_{ij'}^{(k)} \frac{\partial p_{j'}^{(k+1)}}{\partial p_m} \right] \\
&= 2 \sum_{i=1}^{n_d} \left[\sum_{j=1}^{n_p} \mathcal{J}_{ij}^{(k)} \Delta p_j^{(k)} - b_i^{(k)} \right] \cdot \left[\sum_{j'=1}^{n_p} \mathcal{J}_{ij'}^{(k)} \delta_{j'm} \right] \\
&= 2 \sum_{i=1}^{n_d} \left[\sum_{j=1}^{n_p} \mathcal{J}_{ij}^{(k)} \Delta p_j^{(k)} - b_i^{(k)} \right] \cdot \mathcal{J}_{im}^{(k)} \\
&= 2 \sum_{j=1}^{n_p} \sum_{i=1}^{n_d} \left[\mathcal{J}_{im}^{(k)} \right]^T \cdot \left[\mathcal{J}_{ij}^{(k)} \Delta p_j^{(k)} - b_i^{(k)} \right],
\end{aligned} \tag{1.36}$$

and after simplifying the notation, we obtain

$$\left(\mathcal{J}^T \mathcal{J} \right)^{(k)} \left(p^{(k+1)} - p^{(k)} \right) - \left(\mathcal{J}^T \right)^{(k)} b^{(k)} = 0 \tag{1.37}$$

leading finally to the iterative algorithm

$$\boxed{p^{(k+1)} = p^{(k)} + \left[\left(\mathcal{J}^T \mathcal{J} \right)^{(k)} \right]^{-1} \left(\mathcal{J}^T \right)^{(k)} b^{(k)}.} \tag{1.38}$$

The last relation allows to construct the effective iteration algorithm which will be used in many application in the present project.

> *Let us emphasise that the application of the above algorithm to effectively obtain the solutions depends on the existence or not of the inverse of the product $\mathcal{J}^T \mathcal{J}$.*
>
> *It then becomes clear that the very existence of solutions, as well as the convergence properties of the algorithm depend critically on the properties of the Jacobian matrix.*

The discussion in the next section sheds some light on that subject.

1.3 Theorem about Singular Value Decomposition

Let us begin by rewriting Eq.(1.38) in an equivalent, short form

$$p = \mathcal{A}^{-1} y \quad \text{where} \quad p \equiv p^{(k+1)} - p^{(k)} \text{ and } y \equiv \left(\mathcal{J}^T \right)^{(k)} b^{(k)}, \tag{1.39}$$

and where $\mathcal{A} = \mathcal{J}^T\mathcal{J}$ represents the matrix whose properties will be examined.

Theorem: Singular Value Decomposition. *Any real matrix M of dimension $m \times n$ and rank $r \leq min(m, n)$ can be factorised as a product of three matrices as follows*

$$M = U\Lambda V^T, \tag{1.40}$$

where U and V are $m \times m$ and $n \times n$ orthogonal matrices, respectively, and Λ is a $m \times n$ diagonal matrix with all its entries being non-negative where r of them are strictly positive.

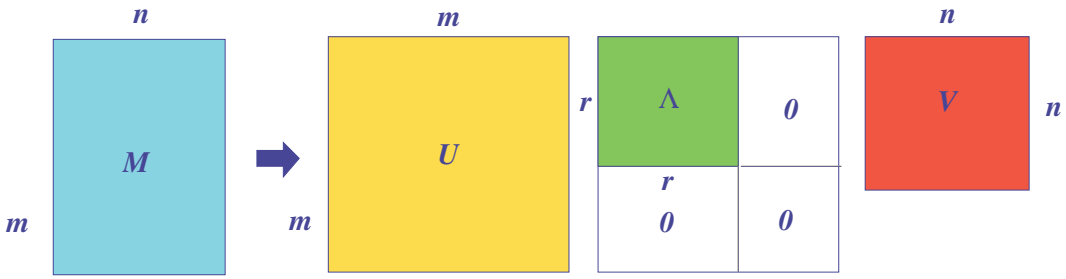

Figure 1.1 – A schematic representation of the structure of the singular value decomposition.

This diagonal matrix is usually represented in the literature in the compact form [12]:

$$\Lambda = \text{diag}\{\lambda_1, \lambda_2, ... \lambda_r, 0, 0, \ldots 0\}, \text{ cf. Figure 1.1}, \tag{1.41}$$

in which, by convention, $\lambda_1 > \lambda_2 > ... \lambda_r$. The λ_i matrix elements are called *singular values* of matrix M. In linear algebra, orthogonal matrices are square matrices which satisfy

$$UU^T = U^TU = \mathbb{1} \tag{1.42}$$

what implies that they also satisfy $U^T = U^{-1}$.

Coming back to Eq. (1.40), we can rewrite the matrix $\mathcal{A}$ by applying the previous theorem to the Jacobian, $\mathcal{J}$,

$$\mathcal{J} = U\Lambda V^T, \tag{1.43}$$

and consequently

$$\mathcal{J}^T = \left(U\Lambda V^T\right)^T = V\Lambda^T U^T = V\Lambda U^T. \tag{1.44}$$

These last two equations allow to write

$$\mathcal{J}^T\mathcal{J} = V\Lambda U^T U\Lambda V^T = V\Lambda^2 V^T \tag{1.45}$$

whereas inverting the last relation gives

$$\left(\mathcal{J}^T\mathcal{J}\right)^{-1} = \left(V\Lambda^2 V^T\right)^{-1} = V\Lambda^{-2}V^{-1} = V\Lambda^{-2}V^T. \tag{1.46}$$

Above we transformed the $\left(\mathcal{J}^T\mathcal{J}\right)^{-1}\mathcal{J}^T$ product as follows

$$\left(\mathcal{J}^T\mathcal{J}\right)^{-1}\mathcal{J}^T = V\Lambda^{-2}V^T V\Lambda U^T = V\Lambda^{-1}U^T, \tag{1.47}$$

which finally allows us to write

$$p^{(k+1)} = p^{(k)} + \left(V\Lambda^{-1}U^T\right)b^{(k)}. \tag{1.48}$$

We can identify

$$\mathcal{A} \equiv V\Lambda^{-1}U^T. \tag{1.49}$$

Comments About the Singular Values in the Context of Ill-Posedness. The new expression for the optimal parametric solution tells us that the solution exists unless one or more entries of matrix Λ are zero or close to it. Indeed, taking into account Eq. (1.49), let us write (1.48) using the explicit summation format

$$[p^{(k+1)} - p^{(k)}]_j = \sum_{\ell=1}^{n} V_{j\ell} \frac{1}{\lambda_\ell} \sum_{i=1}^{m} U_{\ell k}^T b_i^{(k)}. \tag{1.50}$$

The last summation can be performed since all the elements there are known at an iteration no^k; we can introduce an abbreviated notation

$$B_\ell \equiv \sum_{i=1}^{m} U_{\ell k}^T b_i^{(k)} \tag{1.51}$$

which allows us to write

$$\boxed{[\boldsymbol{p^{(k+1)} - p^{(k)}}]_j = \sum_{\ell=1}^{n} \boldsymbol{V_{j\ell}} \frac{\mathbf{1}}{\boldsymbol{\lambda_\ell}} \boldsymbol{B_\ell},} \tag{1.52}$$

from where we can easily see the role of the vanishing eigenvalues λ_ℓ. It becomes clear that even if one only among the λ_ℓ in the diagonal matrix is zero, the summation in Eq. (1.52) diverges and consequently we cannot find the solution of our problem because the confidence intervals for all the parameters are divergent too.

> *Let us observe an apparently paradoxical functioning of these transformations: In Eq. (1.43) and Eq. (1.44) which underlie our considerations, the possible zero eigenvalues of the matrix Λ cause that some columns of the matrix U in the case of calculating $\mathcal{J}$ and some columns of the matrix V when calculating $\mathcal{J}^T$ will not contribute. Consider more closely the case of $\mathcal{J}^T$; if, say, $\lambda_{\ell=5} = 0$ the column V_{j5} should disappear from our considerations. Considering the last expression Eq (1.52), we conclude that, paradoxically, the column with the index corresponding to vanishing eigen-values λ_ℓ (and thus infinity for the fraction $\frac{1}{\lambda_\ell}$) simply do not contribute to the summations and, more precisely, the corresponding columns of the matrix V viz. $V_{j\ell}$ should in fact disappear from our considerations*[7].

Strict Divergences vs. 'Just' Destabilising the Computer Algorithm. Let us emphasise that even though Eq. (1.50)–Eq. (1.52) indicate the presence of the singularity very precisely as the 'yes/no' condition, in practical numerical algorithms the situation is much more complicated. This is because one of the λ-values may approach 0 gradually from one iteration to another with the result that the strong divergence arises within the algorithm without necessarily dividing by zero! It may then happen that the 'optimal parameters' approach the borders of acceptable ranges not because of the properties of the

[7] In this case we arrive at a new situation in which it is not so much the parametric correlations which perturb the algorithm but rather a parameter is demonstrated not to be a justified part of the model ? at the given sampling which is considered predefined.

experimental data – but rather as the result of the 'poorly controlled, numerically small values in the denominators'.

Trying To Quantify the Divergence Level: Condition Number. In applied mathematics one introduces an indicator of ill-posedness in the form of the parameter called *condition number* [6, 12]. The latter is defined as the ratio between the biggest and the smallest eigenvalues $\{\lambda_i\}$:

$$\mathrm{cond}(\mathcal{A}) = \frac{\max(\{\lambda_i\})}{\min(\{\lambda_i\})}\,. \tag{1.53}$$

If $\mathrm{cond}(\mathcal{A})$ is very large, the problem is considered ill-conditioned/ill-posed. Defining the exact limits between the 'large' and the 'small' is somehow arbitrary in this context. For instance, for linear problems, $\mathrm{cond}(\mathcal{A}) \simeq 1$ is considered as a sign of the well-posed problem. On the other hand, if $\mathrm{cond}(\mathcal{A}) >> 1$, the problem is considered ill-posed. Condition number of the order of some thousands can already be of concern. If $\min(\{\lambda_i\}) \to 0$, the quotient in Eq. (1.53) tends to infinity.

Parametric Correlations within the Algorithm. One of the very powerful methods in approaching the ill-posedness and possibly counteracting its negative effects is related to the mechanism of *parametric correlations* mentioned above. As noticed earlier, if two or more columns of $\mathcal{A}$ are linearly dependent, it follows that $\mathcal{A}$ is singular. But this information translates into the condition of the type

$$p_j = f(p_i) \tag{1.54}$$

for a given i and j. The presence of such correlations can be detected using the Monte-Carlo methods as it will be presented later in this work. This can be used as an alternative sign of ill-posedness, which can be investigated with the help of Eqs. (1.53). Let us remind the reader that that the parametric correlation in the form of Eq. (1.54) is manifested by the flat-bottom valleys on the plane (p_i, p_j) and the two facts represent alternative manifestations of the same.

1.4 'Good Looking' Results – Possibly Insignificant

In relation to the ill-posedness and, more generally, the possible physical in-significance of the 'optimal parameters' obtained via χ^2-minimisation, we will need to investigate a number of related issues:

- Routinely verify the sequence of the singular values and analyse the consequences of some nearly vanishing; identify the condition number;
- Using the automated minimum search – How can we be sure that we arrived at the absolute-minimum solution and not at a local minimum with the very close χ^2-value? – and/or whether the 'optimum' is not the result of an instability, Eqs. (1.52)-(1.53)-(1.54)?
- How can we profit from the detection of the parametric correlations in the initial variant of the problem, in order to reformulate it via elimination of such correlations thus arriving at the stable new, but equivalent, formulation?
- How to influence the sampling of the experimental data in order to diminish the chances of ill-posedness?

We will formulate our answers these questions in the next sections and chapters of this document.

1.5 Inverse Problem and Probability Considerations

In the preceding sections we have introduced the notion of the Inverse Problem and discussed the role of the underlying mathematical theory in optimisation of the parameterisations of the models. Let us emphasise that in all the cases in which the inverse of the operator $\hat{M}$ in the formal position of the problem,

$$\hat{M}(p) = d, \tag{1.55}$$

is not known or - even worse - does not exist, the physicists usually bypass the problem rather than solving it: instead of attempting the impossible, i.e. $p = \hat{M}^{-1}d$, one rather minimises the generalised distance between experiment and theory. One of the infinitely many realisations of this idea is the minimisation of the χ^2-test, the latter having in itself an infinite number of realisations since the weight factors in its definition remain arbitrary. This type of 'generally accepted' arbitrariness adds to the uncertainties of the final result of the optimisation procedures which employ the bypassing of the possibly unique solution of the inverse problem via minimisation. Let us remind the reader at this point that *the minimisation of the χ^2-test* corresponds conceptually to the minimisation, in multidimensional spaces, of a generalised distance between a point representing the experimental data and the results of the modelling representing the same physical quantities. Since one demonstrates in topology that there exist an infinite number of manners of defining the distance in multidimensional spaces - it becomes clear that selecting one of those cannot be in general considered as equivalent to solving the inverse problem $M^{-1}d = p^{\text{opt}}$.

The presence of the arbitrariness in the approach is equivalent to saying that there exist numerous alternative hypotheses. We may be justified to ask the questions about the relative viability / probability of one vs. another possible hypothesis. By introducing the relative probability hypotheses we parametrise our ignorance. In other words, we may formulate the general approach / method which focuses on finding the relative probabilities of what we think the right answers are.

Under such considerations, theory parameters p and experimentally known data d are treated as random variables with their corresponding probability distributions. In this context let us begin by recalling some useful concepts which will allow to advance towards more and more precision – in accordance with the methods developed within *applied mathematics*.

1.5.1 Sampling: Degree of Freedom in Inverse Problem Theory

The term *sample* in the inverse problem theory is applied to any set of data representing experiment. Any sub-sets of a sample is also called sample. In particular, a sample can be composed of one single datum.

The term *sampling* refers to the ensemble of procedures which are applied to prepare and select the data points which will compose the sample(s).

The importance of these notions in the inverse problem theory consists in the fact that the solutions of the inverse problem as well as their very existence depends not only on the

model itself but, on the equal footing, on the sample employed. In other words: the same mathematical algorithm may lead to an ill-posed or well-posed inverse problem depending on the choice of the data sampling.

1.5.2 Random Variables and Probability Density

In probability theory a *random variable* is a variable whose possible values are the numerical outcomes of a random phenomenon. It is usually represented by X. Different results of experiments are used to code numbers $x_1, x_2, \ldots x_n$, which are called realisations of variable X.

Once we know all the realisations of the random variable, we can construct the occurrence frequency histograms. For this purpose we consider a stretch of the x-axis and dividing it into n_{hist} intervals of length Δx_i, we attribute the numbers of occurrences, f_i, to each interval. The corresponding normalisation condition reads

$$\sum_{i=1}^{n_{hist}} f_i \Delta x_i \equiv \sum_{i=1}^{n_{hist}} P_i = 1, \tag{1.56}$$

where P_i is called the occurrence probability of each interval 'i': $[x_i, x_i + \Delta x_i]$. As $n \to +\infty$ and $\Delta x_i \to 0$, the constructed histograms tends to a smooth profile which allows defining the *probability density* $f(x)$. In this case the size of the interval is infinitesimal $\Delta x \equiv dx$, therefore the probability of finding one realisation value of X in the interval $[x, x + dx]$ is

$$dP(x) = f(x)dx \tag{1.57}$$

and, in analogy to Eq.(1.56):

$$\int_{-\infty}^{+\infty} dP(x) = \int_{-\infty}^{+\infty} f(x)dx = 1. \tag{1.58}$$

It is important to notice that $f(x)$ is always non-negative since it originates from the occurrence-counting and consequently after normalisation $0 \leq f(x) \leq 1$.

Expected Value. The *mean value* or *expected value*, μ, of a random variable X is defined using the probability density as

$$\mu \equiv E[X] = \int_{-\infty}^{+\infty} x f(x)dx. \tag{1.59}$$

It can be interpreted as a weighted average, where each realisation value is multiplied by its occurrence probability. Equation (1.59) refers to the continuous case, but we can of course define it for the discrete case as well. Then we may write in analogy:

$$\mu = \sum_{i=1}^{n} x_i P_i, \tag{1.60}$$

as long as Eq. (1.56) is satisfied, otherwise one may need to normalise the discrete distribution by $\sum_i P_i = 1$. In the case of all the points being equiprobable, we may define μ as the *arithmetical mean value*

$$\mu = \frac{1}{n} \sum_{i=1}^{n} x_i. \tag{1.61}$$

Variance vs. Standard Deviation. In probability theory, *variance* σ^2 measures, in an abstract way, the distance between the running variable and the expectation value. It is defined using the probability density as follows

$$\sigma^2 = E[(X-\mu)^2] = \int_{-\infty}^{+\infty}(x-\mu)^2 f(x)dx, \tag{1.62}$$

where μ is defined by Eq.(1.59). The *standard deviation* σ is then defined as the square root of the variance

$$\sigma = \sqrt{\sigma^2}. \tag{1.63}$$

We can also define variance and standard deviation for discrete distributions. In such a case, we have

$$\sigma^2 = \sum_{i=1}^{n} P_i(x_i-\mu)^2, \tag{1.64}$$

where μ is given by Eq.(1.60). In the particular case of equiprobable distributions, the above expression takes the form

$$\sigma^2 = \frac{1}{n}\sum_{i=1}^{n}(x_i-\mu)^2. \tag{1.65}$$

It turns out that the broader the data distribution, the bigger the variance of the standard deviation. Conversely, the narrower the distributions, the more precise the final result.

1.5.3 Covariance Matrix - A Linear-Correlation Test

In Section 1.2 we discussed the ill-posedness of the inverse problem possibly arising from the parametric correlations among the parameters of the model. Consequently, it will be important to construct the method which helps detecting these correlations. The tool used to detect correlation between two different random variables X and Y is the special function called covariance, defined as

$$cov(X,Y) \equiv E[(X-E(X))(Y-E(Y))]. \tag{1.66}$$

Continuous variables. In the case of continuous random variables, following the previous definition in Eq.(1.59) we obtain

$$[cov\boldsymbol{X}]_{ij} = cov(X_i,X_j) = \int (x_i-\mu_i)(x_j-\mu_j)f(\boldsymbol{x})d\boldsymbol{x}. \tag{1.67}$$

Discrete variables. Here, following definition in Eq.(1.61):

$$[cov\boldsymbol{X}]_{ij} = cov(X_i,X_j) = \frac{1}{n}\sum_{k=1}^{n}(x_i^{(k)}-\mu_i)(x_j^{(k)}-\mu_j). \tag{1.68}$$

In both cases, we can construct the full $N \times N$ covariance matrix for all the elements of $\boldsymbol{X}$. Consider now the non-diagonal elements of this matrix, $[cov\boldsymbol{X}]_{ij}$ for $i \neq j$. One shows that for the uncorrelated variables $[cov\boldsymbol{X}]_{ij} \to 0$.

The diagonal elements of the covariance matrix are equal to the variances of each of the $\boldsymbol{X}$ vector elements

$$[cov\boldsymbol{X}]_{ii} = cov(X_i, X_i) = \frac{1}{n}\sum_{k=1}^{n}(x_i^{(k)} - \mu_i)^2 = \sigma_i^2. \tag{1.69}$$

Covariance Matrix and the Inverse Problem. Let us consider the linear form of the inverse problem (equivalent to Eq.(1.12)), where the vector of parameters $p \in \mathbb{R}^{n_p}$ can be found from the data $d \in \mathbb{R}^{n_d}$ with the help of the $n_p \times n_d$ matrix M

$$p = M^{-1}d. \tag{1.70}$$

Suppose that the measurement of d has been performed $\mathcal{K}$ times, allowing to calculate the mean value $\bar{d}$ for each vector element and consequently $\bar{p}$. Therefore we can calculate the covariance matrix for the data vector

$$[cov\,\boldsymbol{d}]_{ij} = cov(d_i, d_j) = \frac{1}{\mathcal{K}}\sum_{k=1}^{\mathcal{K}}(d_i^{(k)} - \bar{d}_i)(d_j^{(k)} - \bar{d}_j), \tag{1.71}$$

where $i, j = 1, \dots n_d$. For the parameter vector we can also construct the covariance matrix

$$[cov\,\boldsymbol{p}]_{ij} = cov(p_i, p_j) = \frac{1}{\mathcal{K}}\sum_{k=1}^{\mathcal{K}}(p_i^{(k)} - \bar{p}_i)(p_j^{(k)} - \bar{p}_j), \tag{1.72}$$

recalling that $i, j = 1, \dots n_p$. Using Eq.(1.70) we can combine Eq.(1.71) and (1.72) as follows

$$\begin{aligned}
[cov\,\boldsymbol{p}]_{ij} &= \frac{1}{\mathcal{K}}\sum_{k=1}^{\mathcal{K}}\left[(Md)_i^{(k)} - (\overline{Md})_i\right]\left[(Md)_j^{(k)} - (\overline{Md})_j\right] \\
&= \frac{1}{\mathcal{K}}\sum_{k=1}^{\mathcal{K}}\left[\sum_{\ell=1}^{n_d} M_{i\ell}\left(d_i^{(k)} - \bar{d}_i\right)\right]\left[\sum_{m=1}^{n_d} M_{jm}\left(d_j^{(k)} - \bar{d}_j\right)\right] \\
&= \frac{1}{\mathcal{K}}\sum_{k=1}^{\mathcal{K}}\left[\sum_{\ell=1}^{n_d} M_{i\ell}\left(d_i^{(k)} - \bar{d}_i\right)\right]\left[\sum_{m=1}^{n_d}\left(d_j^{(k)} - \bar{d}_j\right) M_{mj}^T\right] \\
&= \sum_{\ell=1}^{n_d}\sum_{m=1}^{n_d} M_{i\ell}\left[\frac{1}{\mathcal{K}}\sum_{k=1}^{\mathcal{K}}\left(d_i^{(k)} - \bar{d}_i\right)\left(d_j^{(k)} - \bar{d}_j\right)\right] M_{mj}^T \\
&= \sum_{\ell=1}^{n_d}\sum_{m=1}^{n_d} M_{i\ell}\,[cov\,d]_{lm}\,M_{mj}^T
\end{aligned} \tag{1.73}$$

we find

$$[cov\,\boldsymbol{p}]_{ij} = M\,[cov\,\boldsymbol{d}]_{ij}\,M^T. \tag{1.74}$$

In the case of independent measurements, we can expect that the data are not correlated, which means that in Eq.(1.74) the only non-zero matrix elements of $[cov\,\boldsymbol{d}]_{ij}$ are the diagonal terms. Keeping this in mind and taking also into account Eq.(1.69) in the most simplified case where we assume that all the data have the same standard deviation σ_d, we can write

$$[cov\,\boldsymbol{d}]_{ij} = \sigma_d^2\mathbb{1}. \tag{1.75}$$

Thus, Eq.(1.74) transforms to

$$[cov\,\boldsymbol{p}]_{ij} = \sigma_d^2 MM^T. \tag{1.76}$$

Finally, we can relate the above with the result in Eq.(1.38)

$$M \equiv (\mathcal{J}^T \mathcal{J})^{-1}, \tag{1.77}$$

and therefore

$$[cov\, \boldsymbol{p}]_{ij} = \sigma_d^2 M M^T = \sigma_d^2 (\mathcal{J}^T \mathcal{J})^{-1} \left[(\mathcal{J}^T \mathcal{J})^{-1} \right]^T = \sigma_d^2 (\mathcal{J}^T \mathcal{J})^{-2}. \tag{1.78}$$

Correlation Matrix – Pearson Coefficients. We arrived at the expression for the covariance matrix for the parameters. However, since each parameter has its own units and each model has its own parameters, it is more useful to normalise the last expression and obtain the *parameter correlation coefficients* also called *Pearson coeffcients*:

$$r_{ij} = \frac{[cov\, \boldsymbol{p}]_{ij}}{\sigma_i\, \sigma_j}, \tag{1.79}$$

which are the matrix elements of the *correlation matrix*. The advantage of this normalisation is that $-1 \leq r_{ij} \leq 1$ for whichever parameter units and model selected. In this way, we can compare the matrix elements, for the same model or comparing models and identify the one that has more or less correlations between its parameters. How to interpret the elements of this matrix will be explained later.

1.6 Minimisation – Levenberg-Marquart Method

The direct solving of the inverse problem will not be possible in this project since the inverse of the operator M does not exist – or at least it is not known. We will work with the nuclear mean-field methods employing the model Hamiltonians based on the non-linear interaction potentials – the parameter optimisation will be based on the non-linear least-squares approach. For the minimisation we will use the so-called Levenberg-Marquart algorithm (LMA), also known as Damped Least-Squares (DLS). It is more robust that the Gaussian-Newton algorithm, because LMA can find the minimum even if the initial guess was far from the final solution.

To explain how it works, recall Eq.(1.38) as the starting point to pose the minimisation problem:

$$\left(\mathcal{J}^T \mathcal{J}\right) \Delta p = \mathcal{J}^T [d - f(p)], \tag{1.80}$$

and remember that $\Delta p = p^{(k+1)} - p^{(k)}$, where (k) stands for the iteration number. As observed earlier, if the Jacobian matrix is not full-rank, we cannot find the solution to our problem since the underlying matrix is not invertible. For this reason, Levenberg added [23] a diagonal contribution to $\mathcal{J}^T \mathcal{J}$ to avoid the singularity of the Jacobian matrix

$$\left(\mathcal{J}^T \mathcal{J} + \lambda \mathbb{1}\right) \Delta p = \mathcal{J}^T [d - f(p)]. \tag{1.81}$$

The *damping factor* λ is non-negative and modified at each iteration. The disadvantage of this proposition is that for large values of λ

$$\left(\mathcal{J}^T \mathcal{J} + \lambda \mathbb{1}\right) \approx \lambda \mathbb{1} \tag{1.82}$$

and therefore the information from $\mathcal{J}^T \mathcal{J}$ is not used at all. For this reason, Marquardt ref. [24], suggested to replace the identity matrix in front of λ by the diagonal matrix composed of eigen-values of the matrix $\mathcal{J}^T \mathcal{J}$, resulting with

$$\left[\mathcal{J}^T \mathcal{J} + \lambda\, \mathrm{diag}(\mathcal{J}^{\mathrm{T}} \mathcal{J})\right] \Delta p = \mathcal{J}^T [d - f(p)], \tag{1.83}$$

the central defining-relation for the Levenberg-Marquardt algorithm. If we are far from the minimum, the damping factor λ will be increased to help the algorithm to find the right path. Conversely, if we are close to the minimum, λ is decreased thus, giving more importance to $\mathcal{J}^T\mathcal{J}$.

Our minimisation programs in various variants are all based on the application of the Levenberg-Marquardt algorithm.

1.7 Introductory Comments of the χ^2-Test Definition for the Present Project

As it is known from topology, a *distance* $d(a, b)$ between two points in an n-diensional space (under some extra conditions making precise certain mathematical aspect) is an arbitrary function which

- is non-negative, $d(a, b) \geq 0$;
- is symmetric, $d(a, b) = d(b, a)$;
- satisfies the rule of the triangle, $d(a, c) \leq d(a, b) + d(b, c)$

Keeping this in mind, the χ^2-function chosen for the present thesis can be seen a *a very special choice among an infifnite number of mathematically acceptable possibilities*. Its non-normalised version is taken in the form

$$\boldsymbol{\chi^2 = \sum_{i=1}^{n_d} w_i [e_i^{exp} - e_i^{th}(p)]^2} \tag{1.84}$$

where e_i^{exp} and e_i^{th} are the experimental and theoretical single particle energies, respectively. Here, it becomes clear that the choice of the quantity inside the square-brackets are standard elements of the definition, however w_i stays under subjective choice. In this case, since the spherical since the spherical single particle levels appear with degeneracies $(2j + 1)$ degeneracy, we naturally chose

$$\boldsymbol{w_i = 2j_i + 1} \tag{1.85}$$

At this point, the reader is referred to Chapter 7 for more details.

Let us add in passing that certain experimental fitting algorithms include another arbitrary choice of the weight factors containing some measure of the experimental uncertainty in the denominators – according to the principle "the bigger the error the smaller the weight factor", for instance $w \propto 1/\sigma^2$. We do not enter into this type of considerations given the fact that this would bias our considerations in a manner difficult to control. Indeed, the estimates of the experimental values of various mean-field nucleonic levels coming form different types of experiments, different groups of physicists and different subjective choices within each individual analysis would possibly combine incomparable error estimates.

1.8 Monte-Carlo Simulation Techniques

The Monte-Carlo simulation techniques are based on the repetitive algorithms which allow performing a given estimate under changing certain conditions, e.g. minimisation of

a χ^2-test a big number of times, say N_{MC}. Each repetition can be viewed as a test of a new hypothesis following a certain protocol, for instance testing the experimental input data according to the numerically generated probability distribution; at this point the Monte-Carlo methods use the numerical random number generators allowing to model any given probability distribution needed. For instance, one may be able to use the Monte Carlo methods to simulate e.g. the Gaussian uncertainty distributions of the experimental data and study the propagation of the information represented by such an input distribution down to the resulting probability distributions of the resulting final 'optimal' parameters.

In the case of simulating the experimental data uncertainty distributions we employ the Gaussian (also called normal) probability distributions; they are characterised by the random variable, say x, and two parameters usually denoted μ, the mean value and σ, the width parameter:

$$\mathcal{G}(x;\mu,\sigma_{exp}) = \frac{1}{\sqrt{2\pi\sigma^2_{exp}}} \exp\left[-(x-\mu)^2/(2\sigma^2_{exp})\right]; \tag{1.86}$$

these distributions are peaked at $\mu \equiv d_{exp}$.

After having generated the normal-distributed data set N_{MC} times, we proceed with the χ^2 minimisation to obtain the corresponding N_{MC} sets of the resulting parameters with the help of which we can construct their histograms of probability distributions, the Pearson correlation matrix, correlation 'dot-plots' which are discussed in the next section, etc.

1.8.1 Parametric Correlation Analysis

The success of the Monte-Carlo methods depends on statistics of computer-generated output, usually the bigger the statistics the better. Having sufficient statics allows us to introduce certain standard analysis tools detecting the presence of the parametric correlation – such as Pearson Correlation-Matrix introduced earlier. The normalised correlation coef-

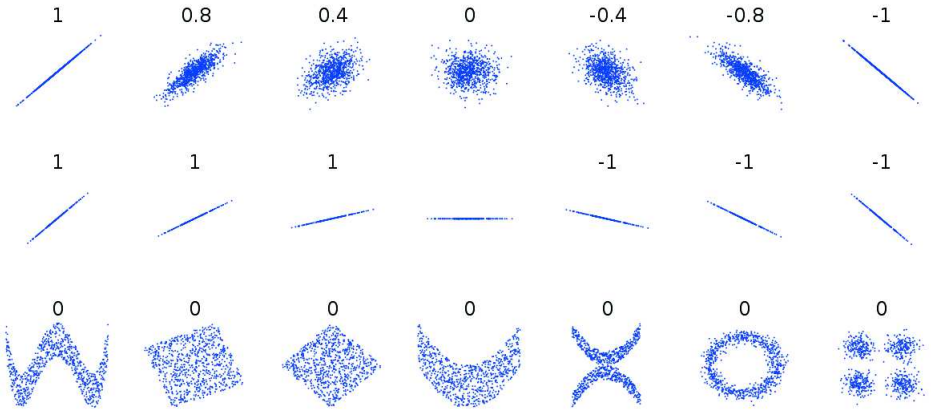

Figure 1.2 – Examples of two-dimensional (x, y) distributions of data-points with their corresponding values of Pearson coefficient. The bottom row results show correlated distributions which give $r_{ij} \approx 0$. The distributions in the upper row are the closest to what we will obtain in the realistic simulations related to the present project. *From Wikipedia* https://en.wikipedia.org/wiki/Pearson_correlation_coefficient.

ficient r_{ij}, cf. discussion around Eq.(1.79), can take the values between -1 to 1. Obtaining

$r_{ij} = \pm 1$ means a total positive or negative linear correlation between parameters p_i and p_j, for illustration cf. middle row of Figure 1.2. In other words, the more r_{ij} approaches the limits ± 1 the stronger the linear correlation between the corresponding parameters, cf. the first row of the figure. On the other hand, $r_{ij} \to 0$ means only that there is no linear correlation between the parameters p_i and p_j; in other words, the possible information about the non-linear correlations must be sought using different means. The appropriately adapted Monte-Carlo techniques provide one of the most powerful tools in this respect; these will be the diagrams which we refer in jargon as *dot-plots*, examples of which are given in Figure 1.2.

The *dot-plots* are two-dimensional distributions obtained from the Monte Carlo simulation results projected on the (p_i, p_j)-plane, where the axes represent the p_i and p_j parameters, respectively. To illustrate the functioning of such a Monte-Carlo technique, suppose we are optimising a model which depends on n_p parameters. We assume that the uncertainty distributions of each of the original experimental data points are known. With the help of the random number generator we generate a big number, say $N_{MC} \sim 10^6$, of experimental datas sets according to these known probability distributions (such procedures will also be presented in details later on in this document). Performing N_{MC} runs of minimisation, we generate N_{MC} sets of parameters (more precisely, n_p-tuplets of parameters i.e. $\{p_1, p_2, \ldots p_{n_p}\}_k$ for $k = 1, 2, \ldots N_{MC}$). To construct the (i, j)-*dot-plot* we place a dot on the (p_i, p_j)-projection plane for all the two-dimensional points with the coordinates $\{p_i, p_j\}_k$ from the set of N_{MC} n_p-tuplets. In other words, *dot-plots* represent two-dimensional probability distributions in the parameter space.

Some examples of these type of diagrams are shown in Figure 1.2. Let us note that in the bottom row of Figure 1.2 we can only find out about the existence of parametric correlations from the dot-plots since r_{ij} is zero in all those cases.

> *The discussed illustration should alert the reader about the (very) limited usefulness of the correlation matrix tests in the non-linear problems which dominate in the physics applications.*

Yet, as it seems, many authors let themselves being satisfied with the discussion of the possible uncertainties in their work limiting the discussion to the properties of the Pearson matrix.

Special comment should be made concerning Figure 1.2: contributor to Wikipedia took care that the points in the bottom row of the picture are distributed around central gravity point, therefore giving $r_{ij} \approx 0$ as indicated in the figure.

1.8.2 Pseudo-experimental Data and Possibly Exact Testing

The experimental data which we have at our disposal and which we use for adjusting the values of the model parameters are limited and usually not sufficient for various kinds of test-considerations. For this reason, one may introduce the concept of *pseudo-experimental data*. The basic principle of this idea is as follows. To start with, we use the best existing set of experimental data to adjust the optimal set of what we refer to as *reference-parameters*. Such a set assures that the model performs closely to its best limits which one can expect with the given limited experimental input. With the reference parameters known, we calculate the full set of theory results e.g. all the single-particle energy levels which can be provided by the model, generally much more than what is known experimentally.

After these preliminaries the real experimental data can be replaced by the calculated pseudo-experimental ones. The latter can be used to perform various tests. For instance, since the pseudo-experimental data reproduce the model reference-parameters exactly, they can be used for an exact modelling with the performance properties close to what is needed in order to describe the *real* data. This would allow testing the stability of the predictions of the model when arbitrarily increasing (decreasing) the number of data points or to perform the extra tests with varying data uncertainties. In particular: With this construction we can apply / develop the Monte Carlo techniques, testing the Gaussian-noise effects on the pseudo-experimental data. We can profit from the fact that with the pseudo-experimental data we cover the information range for the whole system and not only for a part of it – as in the case of the real experimental data. In this way we can detect which data-points are the most relevant for the most stable functioning of the parameter optimisation procedures or – to the contrary – are the most 'passive'. This type of information is very useful for optimising the new-experiment conditions for the usually 'overbooked' experimental facilities and are very useful in theory-experiment collaboration projects.

Chapter 2

Spherical Nuclear Mean-Field Model

Let us recall that the present project is focussed on examining the stability properties of the parameter adjustment procedures together with the related predictive power. We also aim at exploring certain aspects of the underlying inverse problem theory by employing, among others, the Monte-Carlo methods. Consequently, to an extent, the exact form of the Schrödinger equation and/or the interaction potential can be seen as playing a secondary role – under the condition that they can be considered realistic in the description of the physical observables of interest for us. Since we will be primarily interested in the mean-field single-nucleon energies, the possible choice could lie between the realistic phenomenological mean-field Hamiltonian in the Woods-Saxon form or the more microscopic form of e.g. the Skyrme Hartree-Fock type.

In arriving at the final decision we used the experience gained within the preceding PhD thesis completed in our group, B. Szpak [25]. In this latter thesis it has been shown that the choice of the Hamiltonian in the form of the spherical Skyrme-Hartree-Fock approach leads to a 'pathologically complex' mechanism of parametric correlations. Indeed, it is fair to say, as B. Szpak has shown, that in many situations Skyrme Hamiltonian leads to the parametric correlations in the form 'everyone with everyone', cf. Figure 2.1. Selecting this type of the Hamiltonian would bring us to the perspective of working on the parametric correlation removal [read: learning how to construct and implement parameter removal techniques] for the Hamiltonian which depends on up to 12 constants (in the considered realisation) where *de facto* only two or three among these parameters can be considered independent. This would mean a very challenging task - since the removal of the parametric correlations is in the literature either treated by what is considered as standard prescriptions[1] or not at all. Therefore we were tempted to opt for a less complex inverse problem context, not too complicated by the possibly highest degree of parametric correlations. This 'highest degree of parametric correlations' may be considered as a somewhat pathological property specifically of the Skyrme interactions, which are based on the expansions of the zero-range interactions having at their roots the Dirac δ-distribution. We thought that the ideal test ground for this kind of the project will be a model Hamiltonian with possibly a few two-parameter correlations of the p_i vs. p_j type, preferably. Let us emphasise that the possible ill-posedeness of the inverse problem depends on both the model itself and the sampling of the data. It goes without saying that enlarging the sampling by adding the new experimental data, e.g. new-measured mean-field energies or nuclear radii, possibly

[1] This means using the so-called *regularisation methods*; the latter consist in replacing the original problem by another 'similarly looking' problem and solving that one, hoping that the results of the original one and the replacement one are 'nearly the same' - or at least similar. Our approach is by decision different.

taking into account explicitly the coupling between the nuclear single-particle levels and the nuclear collective surface vibrations may in principle influence the form and even the presence of parametric correlations – and requires case by case analysis. However for the Hamiltonians in which visibly the majority of the parameters are correlated – and not necessarily only in the form of the binary relations as it is the case for the Skyrme effective Hamiltonians – the manipulations with the sampling is unlikely to be sufficiently effective to modify the parametric correlations in any qualitatively noticeable fashion.

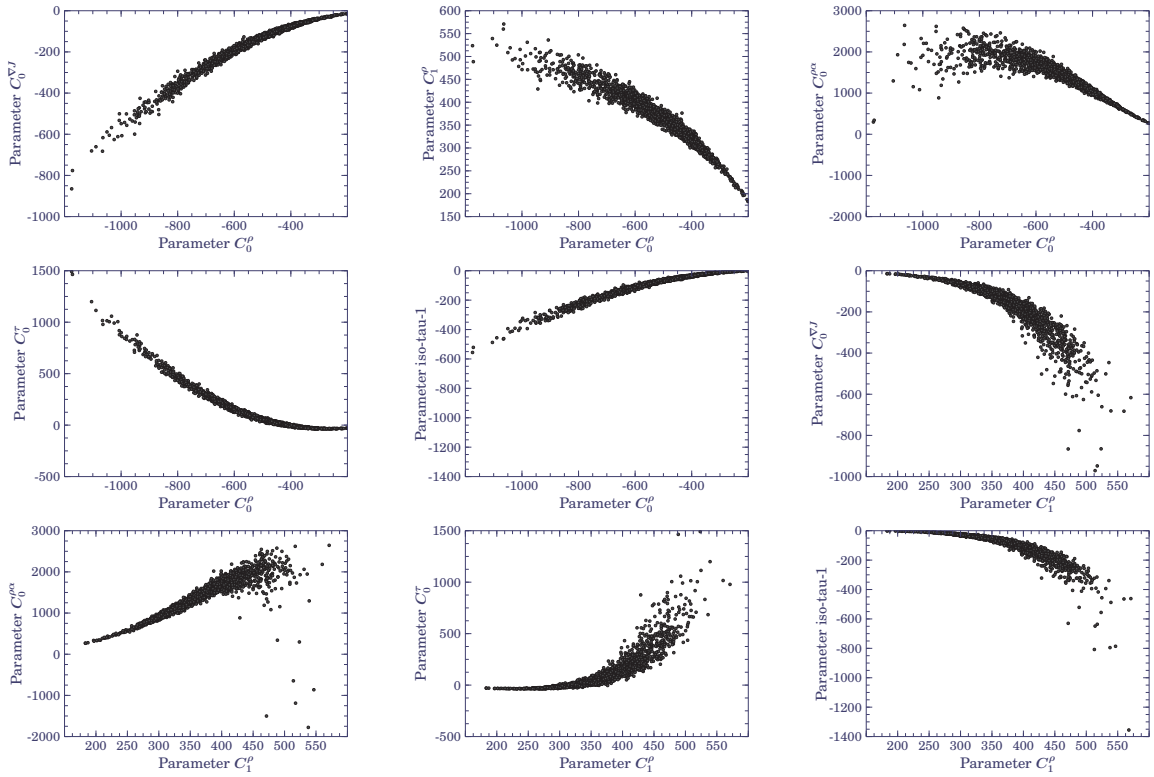

Figure 2.1 – Illustration from B. Szpak PhD Project (unpublished). The parameters of the Skyrme-HF SIII-Scheme Hamiltonian were fitted to ^{208}Pb mean-field single-particle energies. Illustration shows various correlations between the parameters of the Skyrme-Hamiltonian suggesting that there are rather very few independent parameters.

In the present project we wished to implement and test the powerful Monte-Carlo algorithms to detect and remove parametric correlations. For that, the ultra-short c.p.u.-execution times of the Schrödinger equation algorithms are primordial. We therefore decided to use the phenomenological realisation of the mean-field algorithm with the Woods-Saxon Hamiltonian, especially since B. Szpak has demonstrated the existence of occasional and non-trivial convergence problems of the self-consistent Skyrme-Hartree-Fock code. These would have most probably slowed down the collection of the Monte-Carlo results due to the causes inessential from the point of view of the principal goals here.

In this chapter the presentation of the nuclear mean field model used in the present document will be given. We focus on the spherical doubly magic nuclei, therefore we will consider a scalar, spherically symmetric potential when constructing the Schrödinger equation. We will employ the numerical method of solution with the help of the diagonalisation technique. This implies the convenience of using the spherical harmonic oscillator basis with the corresponding wave functions in the form of the generalised Laguerre polynomials and the spherical harmonics – in a spherical coordinate system.

2.1 Spherical Woods-Saxon Hamiltonian

Let us begin by introducing the Hamiltonian which will be used to describe the mean-field single-nucleon energies in this project. The general structure of the Hamiltonian considered here has the form

$$\hat{H}(\vec{r}) = \hat{t} + \hat{V}_C(\vec{r}) + \hat{V}_{SO}(\vec{r}) + \left[\hat{V}_E(\vec{r}) \leftrightarrow \text{electrostatic potential for protons}\right], \tag{2.1}$$

where $\vec{r}$ is the position-vector of a nucleon and $\hat{t}$, the nucleon kinetic energy operator defined as

$$\hat{t} = -\frac{\hbar^2}{2m}\nabla^2. \tag{2.2}$$

The Laplace operator, ∇^2, takes the following well known expression in spherical coordinates

$$\nabla^2 = \frac{1}{r^2}\left[\frac{\partial}{\partial r}\left(r^2\frac{\partial}{\partial r}\right) + \frac{1}{\sin\vartheta}\frac{\partial}{\partial\vartheta}\left(\sin\vartheta\frac{\partial}{\partial\vartheta}\right) + \frac{1}{\sin^2\vartheta}\frac{\partial^2}{\partial\varphi^2}\right]. \tag{2.3}$$

The so-called central potential, $\hat{V}_C(\vec{r}) \to \hat{V}_C(r)$, has been chosen in the Woods-Saxon form

$$\hat{V}_C(r) = \frac{V^c}{1+\exp[(r-R^c)/a^c]} \tag{2.4}$$

where V^c is the depth-parameter of the potential well, r^c in $R^c = r^c A^{1/3}$ is the radius-, and a^c-, the diffuseness parameters. The third term on the right-hand side in Eq. (2.1) represents the spin-orbit potential. In its traditional representation – in contrast to the density-dependent self-consistent realisation, which will be introduce later – it has the form:

$$\hat{V}_{SO}(\vec{r}) \to \hat{V}_{SO}(r) = \frac{1}{r}\frac{dv_{so}(r)}{dr}\,\vec{\ell}\cdot\vec{s} \tag{2.5}$$

where by definition

$$v_{so}(r) \stackrel{df.}{=} \frac{\lambda^{so}}{1+\exp\left[(r-R^{so})/a^{so}\right]}. \tag{2.6}$$

In analogy to V^c in the central potential, λ^{so} represents the strength of the spin-orbit phenomenological interaction, r^{so} in $R^{so} = r^{so}A^{1/3}$ is the spin-orbit radius parameter and a^{so}, the spin-orbit diffuseness parameter.

The operators of spin $\vec{s}$ and of orbital angular-momentum $\vec{\ell}$ couple to the combined total angular momentum operator $\vec{j}$ given by

$$\vec{s} + \vec{\ell} = \vec{j}. \tag{2.7}$$

Taking the square of the latter expression, the product $\vec{\ell}\cdot\vec{s}$ can be expressed as

$$\vec{\ell}\cdot\vec{s} = \frac{1}{2}(\vec{j}^{\,2} - \vec{s}^{\,2} - \vec{\ell}^{\,2}), \tag{2.8}$$

which, when acting on the eigenstates of $\hat{j}^2$, $\hat{\ell}^2$ and $\hat{s}^2$, transforms the latter into

$$\vec{\ell}\cdot\vec{s} \equiv \frac{1}{2}\left[j(j+1) - \ell(\ell+1) - s(s+1)\right]. \tag{2.9}$$

Finally, the last term in the Hamiltonian of Eq. (2.1) is the electrostatic Coulomb potential acting only at the protons. For the uniform charge density it takes the form:

$$\hat{V}_E(\vec{r}) \to \hat{V}_E(r) = \hbar c\alpha(Z-1)\begin{cases}\frac{3-(r/R^{coul})^2}{2R^{coul}}, & \text{for } r \le R^{coul},\\ \frac{1}{r}, & \text{for } r > R^{coul},\end{cases} \tag{2.10}$$

where c is the speed of light, α is the fine-structure constant and, as in the cases of the central and spin-orbit potential, $R^{coul} = r^{coul}A^{1/3}$ is the Coulomb radius parameter. In the present work we assume that the Coulomb radius is proportional to the central one:

$$r^{coul} = f_c \cdot r^c, \tag{2.11}$$

where f_c is a positive constant. However, in what follows we work most of the time with the approximation $f_c = 1$, leaving possible refinements for later.

The central potential depth and the spin-orbit strength can be defined separately for each nucleus and type of particles, however here we chose to parametrize them in terms of the proton Z and neutron N numbers and introduce two auxiliary parameters, for each of them. Thus, for the central potential depth we have

$$V^c = V_o \left(1 \pm \kappa_c \frac{N-Z}{N+Z}\right), \tag{2.12}$$

and for the spin-orbit strength

$$\lambda^{so} = \lambda_o \left(1 \pm \kappa_{so} \frac{N-Z}{N+Z}\right). \tag{2.13}$$

In both cases, the plus sign $(+)$ stands for protons and the minus sign $(-)$ for the neutrons.

At this point, we have completely defined our Hamiltonian which depends on twelve parameters, six for the protons and six for the neutrons:

$$\{V_o, \kappa_c, r^c_{\pi,\nu}, a^c_{\pi,\nu}, \lambda_o, \kappa_{so}, r^{so}_{\pi,\nu}, a^{so}_{\pi,\nu}\}. \tag{2.14}$$

The subscripts π, ν refer to proton and neutron parameter sets, respectively.

2.2 Solving the Schrödinger Equation

We can proceed to solve the Schrödinger equation

$$\hat{H}\Psi_n = e_n \Psi_n, \tag{2.15}$$

to obtain the single particle energies and wave functions of the individual nucleons. To be able to employ the diagonalisation method, we will need to introduce the harmonic oscillator basis wave functions $\{\Phi_k\}$; they will be specified in the following section. With the help of these wave functions we may express the so far unknown solutions of the Schrödinger equation, Ψ_n, as

$$\Psi_n = \sum_n c_{nk}\Phi_k, \tag{2.16}$$

where c_{nk} are some unknown coefficients and Φ_k denotes a given set of orthonormal basis vectors (basis wave-functions). We can introduce Eq. (2.16) into Eq. (2.15) obtaining

$$\hat{H}\sum_n c_{nk}\Phi_k = e_n \sum_n c_{nk}\Phi_k. \tag{2.17}$$

Multiplying both sides of the last equations by $\Phi^*_{k'}$ and integrating over the whole space we obtain

$$\sum_k c_{nk} \int dV \Phi^*_{k'} \hat{H} \Phi_k = \sum_k c_{nk} e_n \delta_{kk'}, \tag{2.18}$$

where we have used the orthonormality of the basis. The results of the integration are the matrix elements of our Hamiltonian. Using the standard 'bra-ket' notation, we write

$$\langle k'|\hat{H}|k\rangle = \int dV \Phi^*_{k'} \hat{H} \Phi_k. \tag{2.19}$$

With the above notation we can rewrite Eq. (2.18) in the following form:

$$\sum_k c_{nk} \left(\langle k'|\hat{H}|k\rangle - e_n \delta_{kk'} \right) = 0. \tag{2.20}$$

It represents a system of linear equations for the unknown coefficients c_{nk}. This system has the non-trivial solutions if and only if

$$\det \left(\langle k'|\hat{H}|k\rangle - e_n \delta_{kk'} \right) = 0. \tag{2.21}$$

In this way we arrived at the diagonalisation problem for the Hamiltonian matrix

$$H_{kk'} = \langle k'|\hat{H}|k\rangle. \tag{2.22}$$

In the following sections we will present the methods used in this work in order to find effectively the numerical solutions of the Schrödinger equation of interest.

2.3 Spherical Basis

Since this work addresses selected properties of the spherical nuclei, we will use the harmonic oscillator basis in the spherical coordinates. To begin with, consider a spinless particle moving in the spherically-symmetric harmonic oscillator potential. We will introduce the separation of the radial and angular variables as follows [26]

$$\phi_{n\ell m_\ell}(r, \vartheta, \varphi) = f_{n\ell}(r)\, Y_{\ell m_\ell}(\vartheta, \varphi), \tag{2.23}$$

where n, ℓ and m_ℓ are certain integer numbers. The radial functions $f_{n\ell}(r)$ are defined by

$$f_{n\ell}(r) = \frac{R_{n\ell}(r)}{r}, \tag{2.24}$$

where $R_{n\ell}(r)$ takes the form

$$R_{n\ell}(r) = \mathcal{N}_{n\ell}\, e^{-\frac{1}{2}\left(\frac{r}{a}\right)^2} \left(\frac{r}{a}\right)^{(\ell+1)} L_n^{(\ell+\frac{1}{2})}\left[\left(\frac{r}{a}\right)^2\right], \tag{2.25}$$

and where $L_n^{(\ell+\frac{1}{2})}$ are the generalised Laguerre polynomials, Ref. [27], Eq. No. (22.3.9). After the same reference, the normalisation constant, $\mathcal{N}_{n\ell}$, is given by

$$\mathcal{N}_{n\ell} = \sqrt{\frac{2^{\,n+\ell+2}\, n!}{a(2n+2\ell+1)!!\sqrt{\pi}}} \tag{2.26}$$

assuring the normalisation condition

$$\int_0^\infty r^2 f^2_{n\ell}(r) dr = \int_0^\infty R^2_{n\ell}(r) dr = 1. \tag{2.27}$$

Finally 'a' is the so-called stretching factor

$$a = \sqrt{\frac{\hbar}{m\omega}}. \tag{2.28}$$

The angular components in Eq. (2.23) are the spherical harmonics, whose standard expression is

$$Y_{\ell m_\ell}(\vartheta, \varphi) = \sqrt{\frac{2\ell+1}{4\pi}\frac{(\ell-m_\ell)!}{(\ell+m_\ell)!}}\, P_\ell^{m_\ell}(\cos\vartheta)\, e^{i\, m_\ell\, \varphi}. \tag{2.29}$$

The above form shows explicitly the separate dependence on ϑ and φ, cf. Ref. [28], Eq. No. (1), p. 133. Above, $P_\ell^{m_\ell}$ are the associated Legendre polynomials and we have

$$-\ell \leq m_\ell \leq +\ell. \tag{2.30}$$

To take into account that the nucleons are $s = 1/2$ spinors we will introduce the corresponding spinor wave functions, χ_{sm_s},

$$\chi_+ \equiv \chi_{\frac{1}{2}+\frac{1}{2}} = \begin{pmatrix} 1 \\ 0 \end{pmatrix} \qquad \chi_- \equiv \chi_{\frac{1}{2}-\frac{1}{2}} = \begin{pmatrix} 0 \\ 1 \end{pmatrix}. \tag{2.31}$$

They are eigenfunctions of the operators $\vec{s}^{\,2}$ and s_z,

Next we will need to construct wave-functions which are eigenstates of the operators $\vec{j}^{\,2}$, $\vec{\ell}^{\,2}$ and $\vec{s}^{\,2}$ simultaneously. This can be achieved using the Clebsch-Gordan coupling and the Clebsch-Gordan coefficients $C\,(\ell m_\ell; s, m_s | j m_j)$. Combining this information with Eq. (2.23) we obtain

$$\Phi_{n;jm_j,ls}(r) = \sum_{m_\ell m_s} C\,(\ell m_\ell; s, m_s | j m_j)\, \phi_{n\ell m_\ell}(r, \vartheta, \varphi)\chi_{sm_s}; \tag{2.32}$$

the expression in which the conservation condition

$$m_\ell + m_s = m_j \tag{2.33}$$

must be satisfied.

For spin $s = 1/2$ particles, in Eq. (2.32) the only two non-zero terms are the ones which correspond to the two possible values of m_s, i.e. $-1/2$ and $+1/2$. This means that for each value of ℓ we have two possible values for the total angular momentum $j = \ell + 1/2$ and $j = \ell - 1/2$. Therefore, the corresponding Clebsch-Gordan coefficients are, cf. Ref.[28], table 8.1, p. 271:

For $j = \ell + \frac{1}{2}$ and fixed m_j:

$$\mathcal{C}^{++}_{\ell m_j} \equiv C(\ell,\, m_\ell = m_j + \tfrac{1}{2}; s, m_s = +\tfrac{1}{2} | j = \ell + \tfrac{1}{2},\, m_j) = +\sqrt{\tfrac{\ell + m_j + \frac{1}{2}}{2\ell+1}}\,, \tag{2.34}$$

$$\mathcal{C}^{+-}_{\ell m_j} \equiv C(\ell,\, m'_\ell = m_j - \tfrac{1}{2}; s, m'_s = -\tfrac{1}{2} | j = \ell + \tfrac{1}{2},\, m_j) = +\sqrt{\tfrac{\ell - m_j + \frac{1}{2}}{2\ell+1}}\,. \tag{2.35}$$

For $j = \ell - \frac{1}{2}$ and fixed m_j:

$$\mathcal{C}^{-+}_{\ell m_j} \equiv C(\ell,\, m_\ell = m_j + \tfrac{1}{2}; s, m_s = +\tfrac{1}{2} | j = \ell - \tfrac{1}{2},\, m_j) = -\sqrt{\tfrac{\ell + m_j + \frac{1}{2}}{2\ell+1}}\,, \tag{2.36}$$

$$\mathcal{C}^{--}_{\ell m_j} \equiv C(\ell,\, m'_\ell = m_j - \tfrac{1}{2}; s, m'_s = -\tfrac{1}{2} | j = \ell - \tfrac{1}{2},\, m_j) = +\sqrt{\tfrac{\ell - m_j + \frac{1}{2}}{2\ell+1}}\,, \tag{2.37}$$

where we have introduced the extra short-hand notation in terms of the coefficients $\mathcal{C}^{++}_{\ell m_j}$, $\mathcal{C}^{+-}_{\ell m_j}$, $\mathcal{C}^{-+}_{\ell m_j}$ and $\mathcal{C}^{--}_{\ell m_j}$. Shortening even more the notation we write down the new forms of the wave-functions as

$$\phi^{+}_{n;\, jm_j, ls} \equiv \phi_{n\ell; m_j + \frac{1}{2}} \chi_{\frac{1}{2}+\frac{1}{2}} \quad \text{and} \quad \phi^{-}_{n;\, jm_j, ls} \equiv \phi_{n\ell; m_j - \frac{1}{2}} \chi_{\frac{1}{2}-\frac{1}{2}}, \tag{2.38}$$

with the help of which the wave functions in Eq. (2.32) take the following final form:

$$\begin{cases} j = \ell + \frac{1}{2}: & \Phi_{n;\, jm_j, \ell s}(r) = \mathcal{C}^{++}_{\ell m_j} \phi^{+}_{n;\, jm_j, ls} + \mathcal{C}^{+-}_{\ell m_j} \phi^{-}_{n;\, jm_j, ls}\,, \\ j = \ell - \frac{1}{2}: & \Phi_{n;\, jm_j, \ell s}(r) = \mathcal{C}^{-+}_{\ell m_j} \phi^{+}_{n;\, jm_j, ls} + \mathcal{C}^{--}_{\ell m_j} \phi^{-}_{n;\, jm_j, ls}\,. \end{cases} \tag{2.39}$$

2.4 Matrix Elements of the Hamiltonian

With the basis functions defined, we can proceed to calculate the matrix elements of the Hamiltonian matrix $H_{kk'} = \langle k' | \hat{H} | k \rangle$. To begin with, let us explicitly write down the wave functions of our new basis with the help of the ensemble of the relevant quantum numbers:

$$k \equiv \{n;\, jm_j, \ell s\} \quad \text{and} \quad k' = \{n';\, j' m'_j, \ell' s'\}. \tag{2.40}$$

The Hamiltonian considered depends on spin only through $\vec{s}^{\,2}$ and this implies that it is diagonal in terms of the spin wave functions $\chi_{\frac{1}{2},+\frac{1}{2}}$ and $\chi_{\frac{1}{2},-\frac{1}{2}}$. Therefore the matrix elements have the following structure

$$\begin{aligned} j = \ell + \tfrac{1}{2}: \quad \langle k' | \hat{H} | k \rangle &= \mathcal{C}^{++}_{\ell' m'_j} \mathcal{C}^{++}_{\ell m_j} \int dr\, (\phi^{+}_{n';\, j' m'_j, \ell' s'})^* \, \hat{H}\, \phi^{+}_{n;\, jm_j, ls} \\ &\quad + \mathcal{C}^{+-}_{\ell' m'_j} \mathcal{C}^{+-}_{\ell m_j} \int dr\, (\phi^{-}_{n';\, j' m'_j, \ell' s'})^* \, \hat{H}\, \phi^{-}_{n;\, jm_j, \ell s} \end{aligned} \tag{2.41}$$

and

$$\begin{aligned} j = \ell - \tfrac{1}{2}: \quad \langle k' | \hat{H} | k \rangle &= \mathcal{C}^{-+}_{\ell' m'_j} \mathcal{C}^{-+}_{\ell m_j} \int dr\, (\phi^{+}_{n';\, j' m'_j, \ell' s'})^* \, \hat{H}\, \phi^{+}_{n;\, jm_j, ls} \\ &\quad + \mathcal{C}^{--}_{\ell' m'_j} \mathcal{C}^{--}_{\ell m_j} \int dr\, (\phi^{-}_{n';\, j' m'_j, \ell' s'})^* \, \hat{H}\, \phi^{-}_{n;\, jm_j, ls}. \end{aligned} \tag{2.42}$$

The basis is composed of the wave functions which are eigenstates of all the operators the Hamiltonian commutes with, i.e. $\vec{j}^{\,2}$, $\vec{\ell}^{\,2}$ and $\vec{s}^{\,2}$. Because of this fact, the above matrix elements vanish unless $\ell' = \ell$, $m'_j = m_j$ and $s' = s$. Therefore, we can rewrite the latter expressions in the form

$$\begin{aligned} \int dr\, (\phi^{+}_{n';\, j' m'_j, \ell' s'})^* \, \hat{H}\, \phi^{+}_{n;\, jm_j, ls} &= \int dr\, (\phi^{-}_{n';\, j' m'_j, \ell' s'})^* \, \hat{H}\, \phi^{-}_{n;\, jm_j, ls} \\ &= \delta_{\ell\ell'}\, \delta_{ss'}\, \delta_{jj'}\, \delta_{m_j m'_j}\, \langle n'\ell' | \hat{H} | n\ell \rangle, \end{aligned} \tag{2.43}$$

where

$$\langle n'\ell' | \hat{H} | n\ell \rangle \equiv \int_0^\infty R^*_{n'\ell'}(r) \hat{H} R_{n\ell}(r)\, dr. \tag{2.44}$$

As the final step, we will obtain the explicit expressions for the matrix elements of the Hamiltonian, treating the kinetic energy operator and the central and spin-orbit interactions separately.

It will be convenient to replace formally the Hamiltonian in Eq. (2.44) by a generic symbol, say operator $\hat{\mathcal{O}}$:

$$\langle n'\ell'|\hat{H}|n\ell\rangle \rightarrow \langle n'\ell'|\hat{\mathcal{O}}|n\ell\rangle \equiv \int_0^\infty R_{n'\ell'}(r)\hat{\mathcal{O}}R_{n\ell}(r)\,dr. \tag{2.45}$$

Recall that the $R_{n\ell}(r)$ depend on the Laguerre polynomials and on the argument $(r/a)^2$. To calculate the implied integrals it will be convenient to introduce the following change of variables

$$z \equiv \frac{r^2}{a^2} \quad \rightarrow \quad r = a\sqrt{z} \quad \rightarrow \quad dr = \frac{a}{2}\frac{dz}{\sqrt{z}}. \tag{2.46}$$

Introducing the latter form into Eq. (2.45) and combining with Eq. (2.24) we find out that the non-zero matrix elements have the form

$$\langle n'\ell|\hat{\mathcal{O}}|n\ell\rangle = \frac{a}{2}\mathcal{N}_{n'\ell}\mathcal{N}_{n\ell}\int_0^\infty dz\, e^{-z} z^{\ell+\frac{1}{2}}\, L_{n'}^{(\ell+\frac{1}{2})}(z)\,\hat{\mathcal{O}}(a\sqrt{z})\,L_n^{(\ell+\frac{1}{2})}(z)\,. \tag{2.47}$$

From Eq. (2.47) the kinetic energy matrix elements can be expressed using the following analytical result

$$\begin{aligned}\langle n'\ell|\hat{T}|n\ell\rangle = a\,\hbar\omega\,\mathcal{N}_{n'\ell}\mathcal{N}_{n\ell}\int_0^\infty dz\, e^{-z}\, z^{\ell-\frac{1}{2}}\left\{\left[\frac{1}{2}(\ell+1-z)L_{n'}^{\ell+\frac{1}{2}}(z) + z\frac{dL_{n'}^{\ell+\frac{1}{2}}}{dz}\right]\right.\\ \left.\left[\frac{1}{2}(\ell+1-z)L_n^{\ell+\frac{1}{2}}(z) + z\frac{dL_n^{\ell+\frac{1}{2}}}{dz}\right] + \frac{\ell(\ell+1)}{4}L_{n'}^{\ell+\frac{1}{2}}(z)L_n^{\ell+\frac{1}{2}}(z)\right\},\end{aligned} \tag{2.48}$$

whereas the interaction terms need numerical integration procedures.

2.5 Density Dependent Spin-Orbit Potential

The spin-orbit interaction introduced in Eq. (2.5) is a pure phenomenological construction and it does not take into account explicitly any nucleon-nucleon interactions which take place in the nucleus. In this section we present an alternative choice of the definition of the spin-orbit potential, using the Hartree-Fock approach formalism. Following the 'microscopic generalisation of the WS-Universal' in [29], we will obtain a generalised Woods-Saxon approach with the density-dependent spin-orbit interaction which will involve a self-consistency condition in its algorithm.

2.5.1 Derivation of the Density-Dependent Spin-Orbit Potential

Let us consider the mean-field interaction $V(\vec{r})$ originating from a two-body, interaction, say $\hat{v}_{N-N}$:

$$V(\vec{r}) \sim \sum_i \int \Psi_i^*(\vec{r}\,')\hat{v}_{N-N}(\vec{r}-\vec{r}\,')\Psi_i(\vec{r}\,')\,d^3\vec{r}\,'. \tag{2.49}$$

In what follows we will use the isospin-conservation property, which allows to represent the full nucleonic density as a sum of the proton and neutron contributions

$$\rho(\vec{r}) \rightarrow \rho\,(r) = \sum_i |\Psi_i(r)|^2 = \rho_\pi(r) + \rho_\nu(r). \tag{2.50}$$

Above, Ψ_i are the single-nucleonic wave-functions labelled with the help of the quantum numbers $\{i\} = \{n, j, m_j; \ell\}$, and $\rho_{\pi/\nu}(r)$ refer to the proton/neutron density functions, respectively. It will be convenient to introduce the Taylor expansion in the form

$$\rho(r') \simeq \rho(r) + (r - r') \cdot \nabla\rho|_{r=r'}. \tag{2.51}$$

It is out of the scope of this document to give all the details of the derivation of the density dependent spin-orbit interaction. Further details of the entire 'step-by-step' mathematical derivation can be found in [29]. The corresponding new form of the spin-orbit interaction is [29]

$$\hat{V}_{SO}(r) = \lambda \frac{1}{r} \frac{d\rho(r)}{dr} \vec{\ell} \cdot \vec{s}, \tag{2.52}$$

where λ is the strength parameter. Since the nucleonic density is the sum of the proton and neutron contributions, it will be instructive to introduce the isospin dependence into the previous expression. We obtain the following form of the spin-orbit potential – the one acting on the protons:

$$\hat{V}^{\pi}_{SO}(r) = \frac{1}{r} \left[\lambda_{\pi\pi} \frac{d\rho_{\pi}(r)}{dr} + \lambda_{\pi\nu} \frac{d\rho_{\nu}(r)}{dr} \right] \vec{\ell} \cdot \vec{s}, \tag{2.53}$$

and the one acting on the neutrons:

$$\hat{V}^{\nu}_{SO}(r) = \frac{1}{r} \left[\lambda_{\nu\pi} \frac{d\rho_{\pi}(r)}{dr} + \lambda_{\nu\nu} \frac{d\rho_{\nu}(r)}{dr} \right] \vec{\ell} \cdot \vec{s}. \tag{2.54}$$

With this new formulation we describe the spin-orbit potential with 4 parameters for protons and neutrons $\{\lambda_{\pi\pi}, \lambda_{\pi\nu}, \lambda_{\nu\nu}, \lambda_{\nu\pi}\}$, instead of 6 parameters within the traditional formulation.

2.5.2 Interpretation and Comments

The newly introduced form of the spin-orbit potential has some evident structural differences as compared to its traditional formulation in Eq. (2.5), in that it is free from all the geometrical parameters such as the diffuseness a^{so} or the radius r^{so}. It will be shown that the traditional formulation of the spin-orbit potential presents the parametric correlations which, as already discussed in Chapter 1 of this document, generally destabilise the capacities of predictions of any model. Therefore, decreasing the total number of spin orbit parameters from 6 for the traditional definition to 4 for the present, microscopic one, may help to stabilise the parametrisation and consequently make the predictions with the underlying Hamiltonian more reliable.

On the one hand this may be seen as a very welcome feature, since we are interested in predicting the nuclear structure of exotic and very exotic and/or super-heavy nuclei, the properties of which are not always known nowadays with the certainty one may wish to have. Since the spin-orbit potential with six correlated parameters may not extrapolate reliably from the fitting region into far-away lying regions on the (Z, N)-plane, any alternative form, in particular based on the more microscopic considerations – in principle opens new possibilities.

On the other hand, we have to be sure that this important modification of the structure of the modelling and the expected improvements is not only apparent. We know that the central potential parameters determine to first order the whole spatial distribution of the

nucleons in the nucleus. Moreover, it turns out that the central potential parameters are the ones which extrapolate most reliably far away from the fitting range. Indeed:

- From electron scattering on nuclei we deduce, that the diffusivity can be considered independent on the nuclear mass and/or size of the nucleus, allowing to fix a^c to a constant value for all the nuclei, without taking into account neither Z nor N dependence;
- The hadron scattering experiments tell us that the nuclear effective mass distribution radius $R^c \sim A^{1/3}$ with a very good precision, what allows to extrapolate the information about the central radii of nuclei in a rather certain way with $R^c = r^c A^{1/3}$, with a single constant r^c;
- From the nucleonic-binding systematics we know that the effective depth of the central potential is almost constant with the first order modification term proportional to the neutron excess the latter defined by $(N - Z)/(N + Z)$. Consequently, the central depth taken as a function of two parameters as already shown in Eq. (2.12) is considered as a very reliable form.

Taking into account these facts, we may therefore expect that the spatial nucleonic density distributions are well described with the help of the six geometric central potential parameters (three for the protons and three for the neutrons). Consequently, expressing the spin-orbit interaction as functionally dependent on the densities promises an evolution into the right direction. We will show that this is indeed the case later in this document.

2.5.3 Nucleonic Density Functions

The general expression of the nuclear density has already been given in Eq. (2.50) above. Since it will be important for us to program explicitly the corresponding expressions to be able to perform the effective calculations of the matrix elements of the Hamiltonian, in this section we will explicitly give the corresponding form in terms of the basis wave functions.

In order to calculate the density-dependent spin-orbit matrix elements, we need first of all to calculate the density, and this can only be done once we know the eigen-functions $\Psi(r)$. This leads to a self-consistent procedure to compute the nuclear density: We first diagonalise the Hamiltonian using the traditional form of the Wood-Saxon spin-orbit. Then we introduce the so obtained solutions to construct the density functions and next we begin iterating the diagonalisation with the new spin-orbit potential until the differences between the n^{th} and $(n+1)^{st}$ iteration are negligible.

The particle density is defined as the sum of all the individual probabilities:

$$\rho(r) = \sum_{occup} \rho_{nlj}(r), \tag{2.55}$$

where $\sum_{occup}$ means summation over the occupied states. Let us focus first on the density for a certain main quantum number N and total angular momentum j:

$$\rho_j^N(r) = \sum_{m_j=-j}^{j} \left|\Psi_{N;jm_j,\ell}(r)\right|^2 \tag{2.56}$$

with

$$\Psi_{N;\,jm_j,\ell}(r) = \sum_n c^N_{j\ell n}\Phi_{n;\,jm_j,\ell s}(r), \tag{2.57}$$

where the wave functions $\Phi_{n;\,jm_j,\ell s}(r)$ are already given by Eq. (2.39). Since the product $\Psi^*_{N;\,jm_j,\ell}\Psi_{N;\,jm_j,\ell}$ is the same for both projections given by $j = \ell \pm 1/2$, let us introduce the following notation for simplicity

$$\mathcal{C}^+_{jm_j} \equiv \mathcal{C}^{\pm+}_{\ell m_j} \quad \text{and} \quad \mathcal{C}^-_{jm_j} \equiv \mathcal{C}^{\pm-}_{\ell m_j}. \tag{2.58}$$

Now, using the full notation of the wave function, the density function in Eq. (2.56) reads

$$\begin{aligned}\rho^N_j(r) = \sum_{m_j=-j}^{j}\sum_{n_1} c^N_{j\ell n_1}\left(\mathcal{C}^+_{jm_j} f^*_{n_1\ell}Y^*_{\ell;m_j-\frac{1}{2}}\langle\chi_+| + \mathcal{C}^-_{jm_j} f^*_{n_1\ell}Y^*_{\ell;m_j+\frac{1}{2}}\langle\chi_-|\right)\\ \cdot \sum_{n_2} c^N_{j\ell n_2}\left(\mathcal{C}^+_{jm_j} f_{n_2\ell}Y_{\ell;m_j-\frac{1}{2}}|\chi_+\rangle + \mathcal{C}^-_{jm_j} f_{n_2\ell}Y_{\ell;m_j+\frac{1}{2}}|\chi_-\rangle\right).\end{aligned} \tag{2.59}$$

The above multiplication gives four terms, however only two are non-zero since $\langle\chi_+|\chi_-\rangle$ and $\langle\chi_-|\chi_+\rangle$ vanish and therefore the summation can be simplified to

$$\rho^N_j(r) = \sum_{n_1,n_2} c^N_{j\ell n_1}c^N_{j\ell n_2}f_{n_1\ell}f_{n_2\ell}\left[\sum_{m_j=-j}^{j}\left(\mathcal{C}^+_{jm_j}\right)^2\left|Y_{\ell;m_j-\frac{1}{2}}\right|^2 + \sum_{m_j=-j}^{j}\left(\mathcal{C}^-_{jm_j}\right)^2\left|Y_{\ell;m_j+\frac{1}{2}}\right|^2\right]. \tag{2.60}$$

It can easily be shown that both terms in Eq. (2.60) give the same result since they do not depend on the alignment of the angular momentum $\vec{\ell}$ and spin $\vec{s}$. In what follows we will derive the explicit expression for $j = \ell + 1/2$ and $m_j = m_\ell + 1/2$, the first step being to change the summation index

$$\sum_{m_j=-j}^{j}\left(\mathcal{C}^+_{jm_j}\right)^2\left|Y_{\ell;m_j-\frac{1}{2}}\right|^2 = \sum_{m_\ell=-\ell-1}^{\ell}\frac{\ell+m_\ell+1}{2\ell+1}\left|Y_{\ell m_\ell}\right|^2 = \sum_{m_\ell=-\ell}^{\ell}\frac{\ell+m_\ell+1}{2\ell+1}\left|Y_{\ell m_\ell}\right|^2. \tag{2.61}$$

In [28], p. 150, Eq. (1) and (2) we find

$$\sum_{m_\ell=-\ell}^{\ell}\left|Y_{\ell m_\ell}\right|^2 = \frac{2\ell+1}{4\pi} \quad \text{and} \quad \sum_{m_\ell=-\ell}^{\ell} m_\ell\left|Y_{\ell m_\ell}\right|^2 = 0, \tag{2.62}$$

which simplifies Eq. (2.61) to

$$\sum_{m_j=-j}^{j}\left(\mathcal{C}^+_{jm_j}\right)^2\left|Y_{\ell;m_j-\frac{1}{2}}\right|^2 = \frac{1}{4\pi}\left(j+\frac{1}{2}\right). \tag{2.63}$$

Introducing the previous result into Eq. (2.60) we obtain the following expression for the partial particle density

$$\rho^N_j(r) = \frac{2j+1}{4\pi}\sum_{n_1,n_2} c^N_{j\ell n_1}c^N_{j\ell n_2}f_{n_1\ell}(r)f_{n_2\ell}(r). \tag{2.64}$$

Next, we can perform the summation over all the occupied states, just taking into account that we can replace the summation over j by the one over ℓ,

$$\rho\,(r) = \sum_{N,\ell,n_1,n_2}\frac{1}{2\pi}f_{n_1\ell}(r)f_{n_2\ell}(r)\left[(\ell+1)c^N_{\ell+\frac{1}{2}n_1}c^N_{\ell+\frac{1}{2}n_2} + \ell\; c^N_{\ell-\frac{1}{2}n_1}c^N_{\ell-\frac{1}{2}n_2}\right]. \tag{2.65}$$

It is important to notice that the latter expression has no dependence on the angles, in accordance with the spherical symmetry of the system, and moreover it takes into account the 'magnetic' degeneracy of the states.

2.5.4 Gradient of the Density Function

The new spin-orbit interaction depends on the gradient of the density, therefore it will be necessary to obtain the explicit expression for it. The final expression of the density depends only on r via the product of the two radial functions $(f_{n_1\ell} f_{n_2\ell})$, consequently:

$$\begin{aligned}\frac{d}{dr}\left(f_{n_1\ell} f_{n_2\ell}\right) &= \frac{d}{dr}\left(\frac{1}{r^2} R_{n_1\ell} R_{n_2\ell}\right) \\ &= -\frac{2}{r^3} R_{n_1\ell} R_{n_2\ell} + \frac{1}{r^2}\left(\frac{dR_{n_1\ell}}{dr} R_{n_2\ell} + R_{n_1\ell}\frac{dR_{n_2\ell}}{dr}\right),\end{aligned} \tag{2.66}$$

where we used Eq. (2.23). Using again the change of variables introduced in Eq. (2.46) we can rewrite the above equation in terms of z:

$$\frac{d}{dr}\left(f_{n_1\ell} f_{n_2\ell}\right) = -\frac{2}{(a\sqrt{z})^3} R_{n_1\ell} R_{n_2\ell} + \frac{2}{a^3\sqrt{z}}\left(\frac{dR_{n_1\ell}}{dz} R_{n_2\ell} + R_{n_1\ell}\frac{dR_{n_2\ell}}{dz}\right). \tag{2.67}$$

Recall, that the radial function $R_{n\ell}$ treated as a function of z, has the form

$$R_{n\ell}\Big(z\Big) = \mathcal{N}_{n\ell}\, e^{-\frac{z}{2}} z^{\frac{1}{2}(\ell+1)}\, L_n^{(\ell+\frac{1}{2})}(z), \tag{2.68}$$

and therefore its derivative with respect to z takes the form

$$\frac{dR_{n\ell}(z)}{dz} = \mathcal{N}_{n\ell}\, e^{-z/2} z^{\frac{1}{2}(\ell-1)}\left[\frac{1}{2}(\ell+1-z) L_n^{\ell+\frac{1}{2}}(z) + z\frac{dL_n^{\ell+\frac{1}{2}}(z)}{dz}\right]. \tag{2.69}$$

Inserting Eq. (2.68) and (2.69) into Eq. (2.67) and simplifying, one obtains

$$\begin{aligned}\frac{d}{dr}\left(f_{n_1\ell} f_{n_2\ell}\right) = \frac{2}{a^3\sqrt{z}} &\mathcal{N}_{n_1\ell}\mathcal{N}_{n_2\ell}\, e^{-z} z^{\ell} \\ &\cdot \left[(\ell - z) L_{n_1}^{\ell+\frac{1}{2}} L_{n_2}^{\ell+\frac{1}{2}} + z\left(\frac{dL_{n_1}^{\ell+\frac{1}{2}}}{dz} L_{n_2}^{\ell+\frac{1}{2}} + L_{n_1}^{\ell+\frac{1}{2}}\frac{dL_{n_2}^{\ell+\frac{1}{2}}}{dz}\right)\right].\end{aligned} \tag{2.70}$$

Finally, we can write the full expression for the density function gradient

$$\begin{aligned}\frac{1}{r}\frac{d\rho}{dr} = \frac{1}{\pi a^4} \sum_{N,\ell,n_1,n_2} \Bigg\{ &\mathcal{N}_{n_1\ell}\mathcal{N}_{n_2\ell}\, e^{-z} z^{\ell-1} \\ &\cdot \left[(\ell+1) c^N_{\ell+\frac{1}{2}n_1} c^N_{\ell+\frac{1}{2}n_2} + \ell\; c^N_{\ell-\frac{1}{2}n_1} c^N_{\ell-\frac{1}{2}n_2}\right] \\ &\cdot \left[(\ell - z) L_{n_1}^{\ell+\frac{1}{2}} L_{n_2}^{\ell+\frac{1}{2}} + z\left(\frac{dL_{n_1}^{\ell+\frac{1}{2}}}{dz} L_{n_2}^{\ell+\frac{1}{2}} + L_{n_1}^{\ell+\frac{1}{2}}\frac{dL_{n_2}^{\ell+\frac{1}{2}}}{dz}\right)\right]\Bigg\}.\end{aligned} \tag{2.71}$$

The latter expressions have been programmed to be able to construct the mixed proton-neutron expressions necessary according to Eqs. (2.53) and (2.54).

2.5.5 Tensor Interaction Term

The spin-orbit and tensor nucleon-nucleon interactions play an important role in the elementary theory of the nuclear interactions; both these terms exist on their own footing

and application of the Hartree or Hartree-Fock formalisms leads to the implied one-body mean-field potentials. This property applies also to the Skyrme-Hartree-Fock formalism [30],[31],[32] and references therein. The tensor force is one of the most important components in the nucleon-nucleon interaction, being associated with the exchange of the lightest meson between the two nucleon, viz. the pion. Again it would be out of the scope of the present document to present a very detailed analysis of the mentioned formalism; instead we would like to present only the basic concepts to show how we introduced the tensor interaction into our problem.

Let us begin by introducing the Skyrme interaction in space configuration, defined with a zero-range (local) δ-function and as a sum of a 2-body interaction plus a 3-body interaction [30], if $\alpha = 1$ and for only the ground-state of the even-even nuclei,

$$\begin{aligned} v_{12} &= t_0(1 + x_0\hat{P}_\sigma)\delta(\vec{r}_{12}) \\ &+ \tfrac{1}{2}t_1(1 + x_1\hat{P}_\sigma)[\vec{k}'^2\delta(\vec{r}_{12}) + \delta(\vec{r}_{12})\vec{k}^2] \\ &+ t_2(1 + x_2\hat{P}_\sigma)\vec{k}'\delta(\vec{r}_{12})\vec{k} \\ &+ \tfrac{1}{6}t_3(1 + x_3\hat{P}_\sigma)\rho^\alpha\left(\tfrac{r_1+r_2}{2}\right)\delta(\vec{r}_{12})\vec{k} \\ &+ iW_0(\vec{\sigma}_1 + \vec{\sigma}_2)\vec{k}' \times \delta(\vec{r}_{12})\vec{k} \\ &+ v^t(r), \end{aligned} \tag{2.72}$$

where $\vec{r}_{12} \equiv \vec{r}_1 - \vec{r}_2$ is the relative distance between two particles, $\vec{k}$ and $\vec{k}'$ are the relative momentum operators defined by

$$\vec{k} = +\frac{1}{2i}(\vec{\nabla}_1 - \vec{\nabla}_2) \quad \text{acting on the right, and} \tag{2.73}$$

$$\vec{k}' = -\frac{1}{2i}(\vec{\nabla}'_1 - \vec{\nabla}'_2) \quad \text{acting on the left.} \tag{2.74}$$

In Eq. (2.72), the first 3 terms and the last two correspond to the 2-body interaction and the fourth one stands for the 3-body interaction, which has been transformed to a 2-body interaction by averaging over one of the particles. The tensor contribution $v^t(r)$ reads [32]

$$\begin{aligned} v^t(r) = \tfrac{1}{2}t_e\Big\{ &\left[3(\vec{\sigma}_1 \cdot \vec{k}')(\vec{\sigma}_2 \cdot \vec{k}') - (\vec{\sigma}_1 \cdot \vec{\sigma}_2)\vec{k}'^2\right]\delta(\vec{r}_{12}) \\ &+ \delta(\vec{r}_{12})\left[3(\vec{\sigma}_1 \cdot \vec{k}\,)(\vec{\sigma}_2 \cdot \vec{k}\,) - (\vec{\sigma}_1 \cdot \vec{\sigma}_2)\vec{k}^2\right]\Big\} \\ + t_o\Big[&3(\vec{\sigma}_1 \cdot \vec{k}')\delta(r)(\vec{\sigma}_2 \cdot \vec{k}) - (\vec{\sigma}_1 \cdot \vec{\sigma}_2)\vec{k}' \cdot \delta(\vec{r}_{12})\vec{k}\Big]. \end{aligned} \tag{2.75}$$

Let us remark in passing that the notation of the tensor interaction is not unique, the differences among authors lie in their definitions of the parameters t_e and t_o. From the interaction in Eq.(2.72) one can construct the Hamiltonian. It turns out that the central and the tensor interactions introduce a correction to the spin-orbit interaction. In [30], Vautherin and Brink only considered the central one, whereas in [33], [32] both contributions are considered. Therefore, the spin-orbit correction due to tensor component reads

$$\Delta\vec{W}_q(\vec{r}) = \alpha\vec{J}_q(\vec{r}) + \beta\vec{J}_{q'}(\vec{r}), \tag{2.76}$$

where q and q' stand for protons, p, or neutrons, n, and $q' \neq q$. The new constants introduced, α and β, are both sums of the central and tensor contributions, *viz.*:

$$\alpha = \alpha_c + \alpha_t \qquad \text{and} \qquad \beta = \beta_c + \beta_t, \tag{2.77}$$

where the constants with subscript c come from the central-interaction contribution, and the ones with subscript t come from the tensor contribution.

In Eq. (2.76) we introduce a new quantity, $\vec{J}_q(\vec{r})$, known as spin-density or spin-current. It is defined as follows

$$\vec{J}_q(\vec{r}) = (-i) \sum_{i,\sigma,\sigma'} \phi_i^*(\vec{r},\sigma,q) \left[\vec{\nabla}\phi_i(\vec{r},\sigma',q) \times \langle\sigma|\vec{\sigma}|\sigma'\rangle\right], \tag{2.78}$$

where the summation runs only over all the occupied states. The wave functions ϕ_i represent the single particle states, as defined in Eq. (2.31), which we copy for convenience below:

$$\phi_i(\vec{r},\sigma,q) = \frac{R_\gamma(r)}{r} \sum_{m_\ell m_s} C\left(\ell m_\ell; s, m_s | j m_j\right) Y_{\ell m_\ell}(\vartheta,\varphi)\chi_{s m_s}(\sigma)\chi_q(\tau). \tag{2.79}$$

Above, $i = \{q, n, \ell, j, m_j\}$ and $\gamma = \{q, n, \ell, j\}$, whereas q denotes the particle charge. Since we are working with doubly-magic spherical nuclei, it can be shown [30] that the spin-density $\vec{J}_q(\vec{r})$ can be written down as

$$\vec{J}(\vec{r}) = \frac{\vec{r}}{r} J(r), \tag{2.80}$$

where

$$J(r) = \sum_\kappa J_\kappa(r); \tag{2.81}$$

again summation extends over all the occupied states. The one-single-particle state spin-density $J_{n\ell j}$, with $\kappa = \{n\ell j\}$, is

$$J_\kappa(r) = \frac{(2j_\kappa + 1)}{4\pi r^3} g(\ell_\kappa, j_\kappa) \tilde{R}_\kappa^2(r), \tag{2.82}$$

where subscript nlj defines the spectroscopic label and $g(\ell, j)$ is given by

$$\begin{aligned} g(\ell, j) &= j(j+1) - \ell(\ell+1) - s(s+1) \\ &= j(j+1) - \ell(\ell+1) - \frac{3}{4}, \end{aligned} \tag{2.83}$$

since we are considering $s = 1/2$ particles. The meaning of $\tilde{R}_i(r)$ will be defined in the next section. Considering the imposed spherical symmetry, the spin-correction in Eq. (2.76) can be rewritten to take the form

$$\Delta W_q(r) = \alpha J_q(r) + \beta J_{q'}(r). \tag{2.84}$$

At this point, we can write the full expression of the spin-orbit potential, following our approach:

$$\begin{aligned} \hat{V}_{SO}^q(r) &= \frac{1}{r}\left[\lambda_{qq}\frac{d\rho_q(r)}{dr} + \lambda_{qq'}\frac{d\rho_{q'}(r)}{dr} + \Delta W_q(r)\right]\vec{\ell}\cdot\vec{s} \\ &= \frac{1}{r}\left[\lambda_{qq}\frac{d\rho_q(r)}{dr} + \lambda_{qq'}\frac{d\rho_{q'}(r)}{dr} + \lambda_{qq}^{(t)} J_q(r) + \lambda_{qq'}^{(t)} J_{q'}(r)\right]\vec{\ell}\cdot\vec{s}, \end{aligned} \tag{2.85}$$

where superscript (t) stands for tensor.

2.5.6 Spin-Density Function

Similarly to the presentation in Section 2.5.4 we will explicitly write down the expression for the spin-density function $J_q(r)$. Let us begin by defining $\tilde{R}_{n\ell}$ appearing in Eq. (2.82):

$$\tilde{R}_i(r) \equiv c^N_{n\ell j} R_{n\ell}(r), \tag{2.86}$$

where coefficients c^N_{nlj} are obtained through the Hamiltonian diagonalisation and they are the same as those in Eq.(2.57). Introducing the above definition to Eq. (2.81) we arrive at

$$J(r) = \frac{1}{4\pi r^3} \sum_{N\ell j n_1 n_2} (2j+1) \left[j(j+1) - \ell(\ell+1) - \frac{3}{4} \right] c^N_{n_1\ell j} c^N_{n_2\ell j} R_{n_1\ell}(r) R_{n_2\ell}(r). \tag{2.87}$$

The above square bracket can be calculated for parallel and anti-parallel spin configuration separately as

$$j = \ell + \frac{1}{2} \quad \longrightarrow \quad (2j+1) \left[j(j+1) - \ell(\ell+1) - \frac{3}{4} \right] = +2\ell(\ell+1), \tag{2.88}$$

$$j = \ell - \frac{1}{2} \quad \longrightarrow \quad (2j+1) \left[j(j+1) - \ell(\ell+1) - \frac{3}{4} \right] = -2\ell(\ell+1). \tag{2.89}$$

Taking them into account, allows to rewrite Eq. (2.87) without summation over j:

$$J(r) = \frac{1}{2\pi r} \sum_{N\ell n_1 n_2} \ell(\ell+1) \left(c^N_{n_1\ell+\frac{1}{2}} c^N_{n_2\ell+\frac{1}{2}} - c^N_{n_1\ell-\frac{1}{2}} c^N_{n_2\ell-\frac{1}{2}} \right) f_{n_1\ell}(r) f_{n_2\ell}(r), \tag{2.90}$$

where we used the definition

$$f_{n\ell}(r) = \frac{R_{n\ell}(r)}{r}. \tag{2.91}$$

Since in Eq. (2.84) we are interested in the product $J_q(r)/r$, it is more convenient to calculate the following expression

$$\frac{1}{r^2} f_{n_1\ell}(r) f_{n_2\ell}(r)\,. \tag{2.92}$$

Remembering that

$$R_{n\ell}(z) = \mathcal{N}_{n\ell}\, e^{-\frac{z}{2}}\, z^{\frac{1}{2}(\ell+1)} L_n^{(\ell+\frac{1}{2})}(z) \tag{2.93}$$

and taking into account the change of variables $r \to z$ as introduced in Eq.(2.45) we obtain

$$\frac{1}{r^2} f_{n_1\ell}(r) f_{n_2\ell}(r) = \frac{1}{a^4} \mathcal{N}_{n_1\ell} \mathcal{N}_{n_2\ell}\, e^z\, z^{(\ell-1)} L_{n_1}^{(\ell+\frac{1}{2})}(z)\, L_{n_2}^{(\ell+\frac{1}{2})}(z). \tag{2.94}$$

The result in Eq. (2.94) can be finally introduced into Eq. (2.89) and we arrive at:

$$\frac{1}{r} J(r) = \frac{1}{2\pi a^4} \sum_{N\ell n_1 n_2} \Bigg[\mathcal{N}_{n_1\ell} \mathcal{N}_{n_2\ell}\, e^z\, z^{(\ell-1)} L_{n_1}^{(\ell+\frac{1}{2})}(z)\, L_{n_2}^{(\ell+\frac{1}{2})}(z) \cdot \ell(\ell+1) \left(c^N_{n_1\ell+\frac{1}{2}} c^N_{n_2\ell+\frac{1}{2}} - c^N_{n_1\ell-\frac{1}{2}} c^N_{n_2\ell-\frac{1}{2}} \right) \Bigg]. \tag{2.95}$$

This is the generic expression for the proton or neutron contributions which have been presented in Eq. (2.85) and were used for computer code programming.

2.6 Experimental Data for Spherical Nuclei

The experimental data used to constrain our spherical mean-field Hamiltonian parameters are the mean-field correspondent single-particle energies of the following 8 spherical doubly-magic nuclei

$$^{16}_{8}\mathrm{O}_{8},\ ^{40}_{20}\mathrm{Ca}_{20},\ ^{48}_{20}\mathrm{Ca}_{28},\ ^{56}_{28}\mathrm{Ni}_{28},\ ^{90}_{40}\mathrm{Zr}_{50},\ ^{132}_{50}\mathrm{Sn}_{82},\ ^{146}_{64}\mathrm{Gd}_{82}\ \text{and}\ ^{208}_{82}\mathrm{Pb}_{126}\,. \tag{2.96}$$

As we already mentioned in Section 1.1.2, the single nucleon energies are not directly observable. They are deduced from the measurements of the single-particle transfer reactions involving the single particle or single-hole states in the neighbouring nuclei with $Z \pm 1$ and $N \pm 1$. In order to illustrate the nucleon mean-field energy extraction procedures we will focus on ^{208}Pb nucleus, one of the best studied in this domain of nuclear structure.

In Section 1.1.2 and in particular in Eq. (1.9) we have introduced the expressions involving the mean energy ε_κ of all the measured fragments of the states with same spin and parity. This, combined with the nucleon separation energies of the neighbouring nuclei, defines the sought single particle energies in the considered nucleus:

$$e_\kappa = -|S_q| - |\varepsilon_\kappa| \tag{2.97}$$

for a state κ measured in a $A-1$ nucleus, and

$$e_\kappa = -|S_q| + |\varepsilon_\kappa| \tag{2.98}$$

for a state κ measured in a $A+1$ nucleus. In both cases S_q denotes the nucleon separation energy, q indicating the type of particle: protons, p, or neutrons, n. Table 2.1 shows the neutron and proton separation energies for ^{208}Pb nucleus [2].

To extract the single particle energies of ^{208}Pb which has $Z = 82$ protons and $N = 126$ neutrons, we need the information about:

- The neutron single-hole states of ^{207}Pb;
- The neutron single-particle states of ^{209}Pb,
- The proton single-hole states of ^{207}Tl, and:
- The proton single-particle states of ^{209}Bi.

In the case of extracting the neutron single particle energies, the range of the excitation energies was rather small and some states were considered pure [2]. The results for the ^{208}Pb single particle energies can be found in Tables 2.2 and 2.3 for neutrons and protons, respectively.

$S_n(^{208}\mathrm{Pb})$ [keV]	$S_n(^{209}\mathrm{Pb})$ [keV]	$S_p(^{208}\mathrm{Pb})$ [keV]	$S_p(^{209}\mathrm{Bi})$ [keV]
7367.87 (0.05)	3937.4 (1.3)	8004(5)	3799.0 (0.8)

Table 2.1 – Neutron and proton separation energies in ^{208}Pb, for the 126$^{\text{th}}$ and 127$^{\text{th}}$ neutrons and 82$^{\text{nd}}$ and 83$^{\text{rd}}$ protons [34].

In what follows, Tables 2.4 and 2.5 show the results for the single particle energies adopted for the nuclei considered in the present thesis.

	Neutron State κ	No.Frag [ref]	ε_κ [MeV]	e_κ [MeV]
^{209}Pb	$\nu d_{3/2}$	1	2.54	−1.40
	$\nu g_{7/2}$	1	2.49	−1.45
	$\nu s_{1/2}$	1	2.03	−1.91
	$\nu d_{5/2}$	1	1.57	−2.37
	$\nu i_{11/2}$	1	0.78	−3.16
	$\nu g_{9/2}$	1	0.00	−3.94
GAP $N = 126$				3.43
^{207}Pb	$\nu p_{1/2}$	1	0.00	−7.37
	$\nu f_{5/2}$	1	0.57	−7.94
	$\nu p_{3/2}$	1	0.89	−8.27
	$\nu i_{13/2}$	9 [35]	2.40	−9.80
	$\nu f_{7/2}$	4 [36]	3.00	−10.40

Table 2.2 – Values of the neutron single particle levels e_κ located around the neutron Fermi level of ^{208}Pb measured in ^{209}Pb and ^{207}Pb, as shown in the first column. The second column indicates the neutron orbitals, the third one contains the information about how many fragments were taken into account to calculate the mean energy given the fourth column. Finally, the fifth column presents the binding energies for each state, adopted as single particle energies.

	Proton State κ	No.Frag [ref]	ε_κ [MeV]	e_κ [MeV]
^{209}Bi	$\pi f_{5/2}$	5 [37]	3.44	−0.36
	$\pi i_{13/2}$	5 [37]	1.97	−1.83
	$\pi f_{7/2}$	2 [37]	1.31	−2.49
	$\pi h_{9/2}$	1 [37]	0.00	−3.80
GAP $Z = 82$				4.30
^{207}Tl	$\pi s_{1/2}$	3 [38]	0.10	−8.10
	$\pi d_{3/2}$	1 [38]	0.35	−8.35
	$\pi h_{11/2}$	2 [38]	1.35	−9.35

Table 2.3 – Values of the proton single particle levels e_κ located around the proton fermi level of ^{208}Pb measured in ^{209}Bi and ^{207}Tl. The second column indicates the proton orbital, the third one gives the number of fragments [and the references] one had to take into account to calculate the mean energy value in the third column. Finally, the fifth column indicates the binding energies for each state, adopted as single particle energies.

$^{16}_{8}O_{8}$			
Proton orbital	ε_κ [MeV]	Neutron orbital	ε_κ [MeV]
$\pi d_{3/2}$	5.51	$\nu d_{3/2}$	1.60
$\pi s_{1/2}$	−0.10	$\nu s_{1/2}$	−3.27
$\pi d_{5/2}$	−0.60	$\nu d_{5/2}$	−4.14
GAP $Z = 8$	8.44	GAP $N = 8$	8.23
$\pi p_{1/2}$	−9.04	$\nu p_{1/2}$	−12.37
$\pi p_{3/2}$	−15.36	$\nu p_{3/2}$	−18.55
$^{40}_{20}Ca_{20}$			
Proton orbital	ε_κ [MeV]	Neutron orbital	ε_κ [MeV]
		$\nu f_{5/2}$	−1.38
$\pi p_{1/2}$	2.42	$\nu p_{1/2}$	−4.20
$\pi p_{3/2}$	0.71	$\nu p_{3/2}$	−5.86
$\pi f_{7/2}$	−1.09	$\nu f_{7/2}$	−8.36
GAP $Z = 20$	5.32	GAP $N = 20$	5.25
$\pi d_{3/2}$	−6.41	$\nu d_{3/2}$	−13.61
$\pi s_{1/2}$	−9.14	$\nu s_{1/2}$	−16.26
		$\nu d_{5/2}$	−21.50
$^{48}_{20}Ca_{28}$			
Proton orbital	ε_κ [MeV]	Neutron orbital	ε_κ [MeV]
$\pi f_{5/2}$	−3.90	$\nu f_{5/2}$	−1.20
$\pi p_{3/2}$	−5.20	$\nu p_{1/2}$	−2.86
$\pi f_{7/2}$	−9.23	$\nu p_{3/2}$	−4.62
GAP $Z = 20$	7.15	GAP $N = 28$	5.34
$\pi s_{1/2}$	−16.38	$\nu f_{7/2}$	−9.95
$\pi d_{3/2}$	−16.67	$\nu d_{3/2}$	−12.52
		$\nu s_{1/2}$	−12.60
$^{56}_{28}Ni_{28}$			
Proton orbital	ε_κ [MeV]	Neutron orbital	ε_κ [MeV]
$\pi g_{9/2}$	2.80	$\nu g_{9/2}$	−6.50
$\pi p_{1/2}$	0.40	$\nu p_{1/2}$	−9.10
$\pi f_{5/2}$	0.30	$\nu f_{5/2}$	−9.50
$\pi p_{3/2}$	−0.70	$\nu p_{3/2}$	−10.20
GAP $Z = 28$	7.15	GAP $N = 28$	5.34
$\pi f_{7/2}$	−5.00	$\nu f_{7/2}$	−14.60
$\pi s_{1/2}$	−7.90	$\nu s_{1/2}$	−17.80
$\pi d_{3/2}$	−8.50	$\nu d_{3/2}$	−18.40

Table 2.4 – Experimental values of the single particle energies for ^{16}O, ^{40}Ca, ^{48}Ca, ^{56}Ni.

$^{90}_{40}\mathrm{Zr}_{50}$			
Proton orbital	ε_κ [MeV]	Neutron orbital	ε_κ [MeV]
		$\nu d_{3/2}$	-4.60
$\pi g_{7/2}$	0.40	$\nu g_{7/2}$	-4.40
$\pi d_{5/2}$	-1.30	$\nu s_{1/2}$	-5.63
$\pi g_{9/2}$	-5.15	$\nu d_{5/2}$	-7.15
GAP $Z = 40$	3.20	GAP $N = 50$	4.85
$\pi p_{1/2}$	-8.35	$\nu g_{9/2}$	-12.00
$\pi p_{3/2}$	-9.86	$\nu p_{1/2}$	-12.60
$\pi f_{5/2}$	-10.09	$\nu p_{3/2}$	-13.00
		$\nu f_{5/2}$	-13.50

$^{132}_{50}\mathrm{Sn}_{82}$			
Proton orbital	ε_κ [MeV]	Neutron orbital	ε_κ [MeV]
		$\nu f_{5/2}$	-0.397
		$\nu h_{9/2}$	-0.841
$\pi d_{3/2}$	-7.228	$\nu p_{1/2}$	-1.039
$\pi d_{5/2}$	-8.706	$\nu p_{3/2}$	-1.548
$\pi g_{7/2}$	-9.668	$\nu f_{7/2}$	-2.402
GAP $Z = 50$	6.139	GAP $N = 82$	5.006
$\pi g_{9/2}$	-15.807	$\nu h_{11/2}$	-7.408
$\pi p_{1/2}$	-16.109	$\nu d_{3/2}$	-7.343
		$\nu s_{1/2}$	-7.675
		$\nu d_{5/2}$	-8.998
		$\nu g_{7/2}$	-9.770

$^{146}_{64}\mathrm{Gd}_{82}$			
Proton orbital	ε_κ [MeV]	Neutron orbital	ε_κ [MeV]
$\pi d_{3/2}$	-1.70	$\nu h_{9/2}$	-5.80
$\pi h_{11/2}$	-1.90	$\nu p_{3/2}$	-6.20
$\pi s_{1/2}$	-1.95	$\nu f_{7/2}$	-7.34
GAP $Z = 64$	3.43	GAP $N = 82$	3.90
$\pi d_{5/2}$	-5.38	$\nu s_{1/2}$	-11.24
$\pi g_{7/2}$	-5.71	$\nu d_{3/2}$	-11.26
		$\nu h_{11/2}$	-11.99

Table 2.5 – Experimental values of the single particle energies for ^{90}Zr, ^{132}Sn, ^{146}Gd.

Chapter 3

Uncertainties of Theory Predictions

In this chapter we present the conceptual framework and mathematical properties related to the solution of the inverse problem in view of the optimisation and stabilisation of the parameter adjustment procedures – via direct illustrations. Even though we are aiming at modelling of the realistic nuclear mean-field properties focussing on the single-nucleon energies, we wish to present first the rather complex procedures and properties using a simple exactly soluble model.

One may say, roughly, that the leading line of this section is this: in modern physics or for that matter in any other research domain, to present the theory result 'by giving just a number', strictly speaking has no meaning for a specialist – as emphasised by the explicit requests by certain Publishers [39], the latter reference demanding that the theory *prediction uncertainties* are *routinely tested*[1] before accepting the publication. The present chapter will be devoted to the illustrations of certain practical aspects of what publishers begin requesting, first using the mathematical toy model and next in a realistic context.

Let us complete this short introduction with some comments about a possible abuse of the language and, perhaps, an abuse in typography by allowing for a relatively frequent presence of quotation marks (' '). They will often be employed in this chapter with the purpose of diminishing the arrival and the impact of likely misunderstandings. Indeed, we will be confronted with what may turn out to be a severe semantical problem, in that several words used currently in the discussions and literature - strictly speaking cannot be interpreted according to their exact meaning throughout several discussions or comments which follow. To give a few examples, beginning with nearly trivial: If a sequence of numbers were just generated by us with the computer, but they serve in the role of *experimental data* - we will refer to them as 'experimental' data. Next: Suppose we need the term *optimal parameters* - but we demonstrated earlier that the applied adjustment procedures may have infinitely many different, non-equivalent definitions/realisations. It follows that any calculations will necessarily involve the personal judgement of a physicist, wherefrom the term *optimisation* should in fact refer rather to *optimisation by Mme A. B.*, alternatively *Mr X. Y.*, and cannot be associated with any exact notion in mathematical sense. In such a context we will write: 'optimal' parameters. Knowing that a frequent use of the quotation marks may be sometimes received as slightly irritating... – we will use those symbols only when really an alert will be needed.

[1] It is more and more evident from the progress in the publication trends that 'changing a parameter at the input and looking at the modification on the output' is not considered as any valid test of the model uncertainties. Instead, application of the standard theorems of the Inverse Problem theory of Applied Mathematics is more and more often expected.

3.1 Inverse Problem Seen Through an Exact Model

Let us begin by certain semantical issues first: In this text, the term *exact model*, refers to a model capable of reproducing the data of a predefined class exactly. In other words: for an exact model there must exist at least one set of parameters "for which the modelling curve passes through the data points of the class mentioned".

It turns out that nearly all mechanisms and properties of mathematical modelling, which may be needed by a physicists within the inverse problem theory, can be tested and illustrated down to an arbitrary detail before applying them in a realistic physical context. For the sake of illustration, in this section we will discuss an exactly soluble four-parameter toy model. It presents practically all the features of interest in this work when trying to learn about any more advanced, realistic physical theory, from the point of view of the parameter determination procedures, their limitations and advantages.

Mathematical Model and Its 'Experimental' Data Sampling. Let us begin the presentation of the soluble model in question, whose certain elementary features were introduced in Ref. [40], by defining the sampling: the set of numbers which will be used in the role of the experimental data. For this purpose we will introduce a generating function denoted $f_{\rm g}(x)$ as a continuous function of its real argument x. The numbers which further on will be called *experimental data* will be generated by defining a certain sequence of *reference x-arguments* denoted $\{x_1, x_2, \ldots, x_{n_d}\}$. The generating function can be defined arbitrarily but for the present realisation of the modelling it will be convenient to set it as a simple exponential:

$$f_{\rm g}(x) = \exp(x). \tag{3.1}$$

To advance in the construction of our illustrative model, we will let ourselves being guided by various steps we usually follow, when constructing our physical theories. With this goal in mind let us introduce our 'reference experimental data' as

$$f_i^{\rm exp} \equiv f_{\rm g}(x_i) = \exp(x_i), \text{ for } i = 1, 2, \ldots n_d. \tag{3.2}$$

Here, reference x_i-values will be selected to be of the order of unity, to fix the attention. From now on the experimental data are considered to be known.

The Issue of 'Experimental' Errors. To stay as much realistic as possible we will also simulate the presence of the experimental errors since we are interested in studying the impact of those errors on the final results, such as the parameter-, and prediction uncertainties. For this purpose we introduce a new set of numbers, say $\{\delta f_i^{exp}\}$, playing the role of the experimental errors. Thus the reference experimental data transform into a new sequence in accordance with the usual requirements, when presenting the experimental result:

$$f_1^{exp} \to f_1^{exp} \pm \delta f_1^{exp},\ f_2^{exp} \to f_2^{exp} \pm \delta f_2^{exp},\ \ldots\ f_{n_d}^{exp} \to f_{n_d}^{exp} \pm \delta f_{n_d}^{exp}. \tag{3.3}$$

Constructing an Heuristic Model with Parameters: Employing Symmetries I. We assume that the 'new theory' behind the 'new phenomenon' represented by the data in (3.2)-(3.3) needs to be constructed 'from scratch[2]'. Thus the first step will be to analyse the

[2]Let us emphasise that, quite generally, we construct our theories 'from scratch' on a case by case basis. Here we made our selection in trying to be pedagogical without pretending being general. Even though the details will change from case to case, possibly from physicist to physicist, what will be the most important goal at this stage is to arrive at the mathematical model expression(s) which contain the best-adapted model-parameters at this step of the construction. The mathematical model will be represented a few lines below with the help of a *model-generating function* $G_{\rm g}$, see below.

asymptotic behaviour: What are the 'phenomenological model expressions' which describe the new data at the smallest and at the largest value-limits?

Knowing the form of the data-generating function, $f_{\rm g}(x)$, it comes as no surprise *to us* that the un-alerted physicist will still arrive at her/his 'asymptotic phenomenological model description at the low-value limit' with the linear structure of the modelling so that she/he would write:

$$f_i^{exp} \approx A + Bx_i \approx \exp(x_i), \text{ for small } x_i, \tag{3.4}$$

where A and B are *parameters of the model* under construction. Here we have explicitly introduced the *approximately equal* sign ($\approx$) because of the use of the data in the presence of the error-bars. Indeed, the latter could be big, small and/or varying irregularly, and make the exact deductions impossible at this point.

Analysing briefly the symmetries of the model we can conjecture that it is composed of two terms of opposite parities, one even (a constant A) and one odd (the one which is linear in x_i).

Constructing an Heuristic Model with Parameters: Employing Symmetries II. Similarly we may extend the simple analysis of the experimental data in terms of the few-parameter phenomenological-expressions to the large value limit, and since we might expect now that the data represent a combination of an even and an odd symmetry terms, it is not impossible, perhaps even very likely, that our imaginary physicist *Mme A. B* (*Mr X. Y*) arrives at the following expression:

$$\text{Large value asymptotic limit}: \ f_i^{\rm exp} \approx C\sinh(x_i) + D\cosh(x_i), \tag{3.5}$$

From an Asymptotic to the Global Description: Constructing the Model. Still in the process of constructing and improving our phenomenological few-parameter model, we can combine the last two equations to construct the hypothetical, more complete version with the new, four-parameter model-expression, as the new working hypothesis:

$$\text{Heuristic Proposition}: \ f_i^{\rm exp} \approx A + Bx_i + C\sinh(x_i) + D\cosh(x_i). \tag{3.6}$$

It will be convenient to introduce, for the sake of the following development, a *model generating-function*, say $F_{\rm g}(x)$, analogous to the data generating-function $f_{\rm g}(x)$ in Eq. (3.1) in the form

$$F_{\rm g}(x; A, B, C, D) \equiv A + Bx + C\sinh(x) + D\cosh(x). \tag{3.7}$$

Optimal Parameters: χ^2-Minimisation Rather Than Solving Inverse Problem. We may say that at this point we have at our disposal both the experimental data set, $\{f_i^{\rm exp}\}$, with the corresponding errors, and the theoretical model represented by the model-generating function $F_{\rm g}(x; A, B, C, D)$. The next logical step is to determine the "optimal[3]" values of the parameters $\{A, B, C, D\}$, on which our model depends. For this purpose we may choose applying the minimisation of the χ^2-test function given by

$$\begin{aligned}\chi^2(A, B, C, D) &\stackrel{df}{=} \sum_{i=1}^{n_d} [f_i^{\rm exp} - F_{\rm g}(x_i; A, B, C, D)]^2 \\ &= \sum_{i=1}^{n_d} \{\exp(x_i) - [A + Bx_i + C\sinh(x_i) + D\cosh(x_i)]\}^2 .\end{aligned} \tag{3.8}$$

[3]We use the double quotation marks at this particular point to underly the results of our discussion in Chapter 1, which has led us to the conclusion that the method of minimising the generalised distance between experimental data and the model results is highly, since (∞^2), non-unique. The physicist may and perhaps even should keep this permanently in mind when developing new theories 'from scratch'.

Let us remark in passing that the above definition does not address at this point such issues as e.g. calculation of the root-mean-square deviations of the considered quantities and the issue of the normalisation of the above expression is left apart as inessential here.

Our Construction Defines In Fact an Exact Model! Let us emphasise, that our construction presented so far has all the features of an exact theory. Indeed, in the absence of errors, we obtain the exact solution by setting

$$A = 0, \quad B = 0, \quad C = 1 \quad \text{and} \quad D = 1, \tag{3.9}$$

since then

$$A + Bx_i + C\sinh(x_i) + D\cosh(x_i) \to \sinh(x_i) + \cosh(x_i) = \exp(x_i) = f_{\rm g}(x_i), \tag{3.10}$$

the relation which reproduces exactly the toy-model experimental-data by construction. However, we know and we need to keep in mind that the experiment is never error-less, and therefore we will never obtain the exact solution after the parameter optimisation. Therefore, even though the model allows to study the *exact theories* we better emphasise here the abstract sense of this term in the great majority of realistic applications – some of those realistic ones will be of principal interest in this project.

Monte-Carlo Approach and the Experimental Data Treatment. Since, as discussed earlier in this document, the experimental data represent, from the mathematics point of view, some random variables characterised by their probability distributions, we will generate those distributions numerically using the random-number generator. For that purpose we introduce the Gaussian distributions $\mathcal{N}(\mu_i, \sigma_i)$, centred at $\mu_i = \exp(x_i)$, with the standard deviations denoted σ_i, the latter defined uniquely by f_i^{exp}. Thus the errors of the reference experimental data define the Gaussian characteristics

$$f_i^{exp} \pm \delta f_i^{exp} \;\leftrightarrow\; \{\mu_i, \sigma_i\}. \tag{3.11}$$

Once we have defined all the errors in Eq. (3.11) we may generate, according to the usual principles of the Monte-Carlo approach, the sequence of N_{MC} Gaussian distributed experimental data sets $\{f_1^{\rm exp}, f_2^{\rm exp}, \dots f_{n_d}^{\rm exp}, \}_k$ for $k = 1, 2, \dots N_{MC}$. The index 'MC' stands for Monte-Carlo, and the values of N_{MC} are of the order of 10^5 or more.

Probability Distributions for the Model Parameters: Histograming Technique. To obtain the probability distributions of the model parameters, we repeat the adjustments and find, for $k = 1, 2, \dots N_{MC}$, all the sets of parameters $\{A, B, C, D\}_k$. These results will allow us to construct the occurrence-probability histograms for each parameter, and determine, among others, their most probable values. As the next step in the applications, knowing the probability distributions for the parameters (also referred to as parameter uncertainty distributions) we will be able to analyse the prediction results together with their probability distributions – thus uncertainties. All these aspects will be illustrated in detail below in this section.

The Notion of Intraneous and Extraneous Prediction Ranges and Predictions. The considered model depends on $n_p = 4$ parameters. To allow for relatively simple and pedagogical illustrations, while preserving all the mathematical/algebraic rigour and all features of the parameter adjustment analysis, we will use the smallest non-trivial choice for the number of input data points: $n_d = 5 > n_p$. Furthermore, to fix some numbers for the numerical applications we arbitrarily selected

$$x_i \in [0.0, 0.4] \;\to\; f_i^{\rm exp} = \exp(x_i),\; i = 1, 2, 3, 4, 5\,. \tag{3.12}$$

Definition of the above set of experimental data will allow to introduce an important notion of what we refer to as *intraneous* and *extraneous* prediction zones. More precisely: We will fit the optimal parameters using the n_d data points, $\{f_1^{\exp}, \ldots f_{n_d=5}^{\exp}\}$. All calculations with the model-generating function $F_{\rm g}(x; A, B, C, D)$ for $x \neq x_i$ will be our model predictions.

As it turns out, we have in fact two zones with clearly distinct asymptotic-behaviour prediction-properties (for continuous parametric behaviour models) as illustrated below: The one lying inside of the fitting area for which

$$f_1^{\exp} < f_{\rm g}(x) < f_{n_d}^{\exp}; \;\; \text{zone called Intraneous,} \tag{3.13}$$

and the one for which

$$f_{\rm g}(x) < f_1^{\exp} \text{ and } f_{n_d}^{\exp} < f_{\rm g}(x); \;\; \text{zone called Extraneous.} \tag{3.14}$$

Thus the predictions made for the points lying among $\{f_1^{\exp}, \ldots f_5^{\exp}\}$ will be called *intraneous predictions*.

Let us mention as a kind of alert message, that some authors use for the same two situations, not quite correctly, the terms *interpolations* and *extrapolations*, respectively. [Recall: In mathematics, the term e.g. interpolation refers to "passing a curve of an *a priori* given definition, for instance polynomial type, through a given sequence of points" – a property which almost never applies in case of the fitting].

The Final Numerical Input-Details Before Modelling and Illustrating. To prepare the model for the extraneous prediction calculations we will introduce an auxiliary interval analogous to the one in eq. (3.12):

$$X_j \in [1.0, 2.0], \tag{3.15}$$

which will be used to perform the calculations, among others, of the predictions and their uncertainties in the extraneous zone.

Let us put together the numerical information necessary to run the calculations with the present model. For the sampling points (model reference values) we set arbitrarily

$$x_1^r = 0.0, \;\; x_2^r = 0.1, \;\; x_3^r = 0.2, \;\; x_4^r = 0.3 \text{ and } x_5^r = 0.4, \tag{3.16}$$

the sequence, which defines our reference experimental data (three digit precision) using Eq. (3.1):

$$f_1^r = 1.0, \;\; f_2^r \approx 1.11, \;\; f_3^r \approx 1.22, \;\; f_4^r \approx 1.35 \text{ and } f_5^r \approx 1.49. \tag{3.17}$$

Taking into account Eq. (3.12) and Eq. (3.13), for the intraneous predictions we define the following three reference argument-values

$$x_1^{in} = 0.15, \;\; x_2^{in} = 0.25 \text{ and } x_3^{in} = 0.35, \tag{3.18}$$

corresponding to the exact (again three digit precision) 'measurement-result' values

$$f_1^{in} \approx 1.16, \;\; f_2^{in} \approx 1.28, \;\; f_3^{in} \approx 1.42. \tag{3.19}$$

Concerning the extraneous predictions we arbitrarily define the following reference argument-values:

$$X_1 = 1.2, \;\; X_2 = 1.4, \;\; X_3 = 1.6, \;\; X_4 = 1.8 \text{ and } X_5 = 2.0, \tag{3.20}$$

from where, applying again Eq.(3.1), one finds that the corresponding exact 'predicted measurement' values are:

$$F_1 \approx 3.32, \;\; F_2 \approx 4.06, \;\; F_3 \approx 4.95, \;\; F_4 \approx 6.06 \text{ and } F_5 \approx 7.39. \tag{3.21}$$

Final Remarks about the Error Probability Distributions. Since our goal from now on will be to study and analyse the impact of the experimental errors on the 'optimal' parameter-values as well as prediction and their probability (or: uncertainty) distributions, in what follows we will introduce the simple working hypothesis of the common, i.e. i-independent, constant uncertainty, $\sigma_i \to \sigma_{exp}$, for all the 'experimental' input data – at any given test-run. By switching from one error hypothesis to another we will repeat the ensemble of necessary calculations for another value, say σ'_{exp}, but again common for all the 'experimental' data points.

Moreover, we will use the same sets of 'experimental' data with fixed σ_{exp} to make predictions either *inside* the fitting range, which for that reason are called *intraneous predictions*, or outside of the fitting zone, called therefore *extraneous predictions* – the terms defined earlier in this section.

3.1.1 Parametric Uncertainty Distributions: First Illustrations

Let us begin by emphasising again that even though the discussed model is by construction exact, thus capable of reproducing the mathematical truth exactly, the latter situation will never be achieved outside of the purely mathematical considerations since there do not exist error-less experimental data. At the same time, increasingly poor quality of the data will generally lead to exceeding any maximum prediction-uncertainty *allowed by the constructor of the model/theory* within her/his given context, for instance: "the uncertainty of at least one of the predicted observables F_j must not exceed one (or two? or three?) standard deviation(s)". This will bring us to the paradoxical property of:

Uselessness of even of the exact models under realistic instrumental conditions.

We will refer to this feature as *NO-GO property of an exact model* - as discussed below.

Uncertainty Distributions of 'Optimal' Model Parameters. Figure 3.1 together with Table 3.1 illustrate the properties of the (uncertainty) probability distributions for the model parameters. These distributions are obtained using the combined technique of constructing the occurrence-histograms, which are then complemented by the fitted Gaussian curves illustrated in the Figure. The four diagrams illustrate $\{A, B, C, D\}$-parameter occurrence distributions obtained with the help of the Monte Carlo simulations using $\sigma_{exp} = 0.0005$, 0.001, 0.005 and 0.01, respectively.

The results are summarised in Table 3.1, which shows for each case the most probable value and the corresponding confidence interval for each parameter obtained by employing the calculated distributions. Notice a quick increase of the width of the distributions implied by the increasing error bars of the 'experimental' data. At the largest σ_{exp} considered we arrive at the situation of a near overlapping of the peaks which correspond to the exact-model exact-solutions $A = B = 0$ and $C = D = 1$, cf. in particular right-bottom panel of Figure 3.1.

Let us notice that the presented calculation results correspond to an exact model in which we have introduced the Gaussian-parameterised, thus symmetric, error distributions. Consequently the peak positions of the distributions are always at the right (exact) original positions. This implies that in the imposed variant of our model, the experimental errors with symmetric error-bars will not perturb the *expected value* of each parameter. Let us mention furthermore that the approach discussed has more freedom (not exploited at this

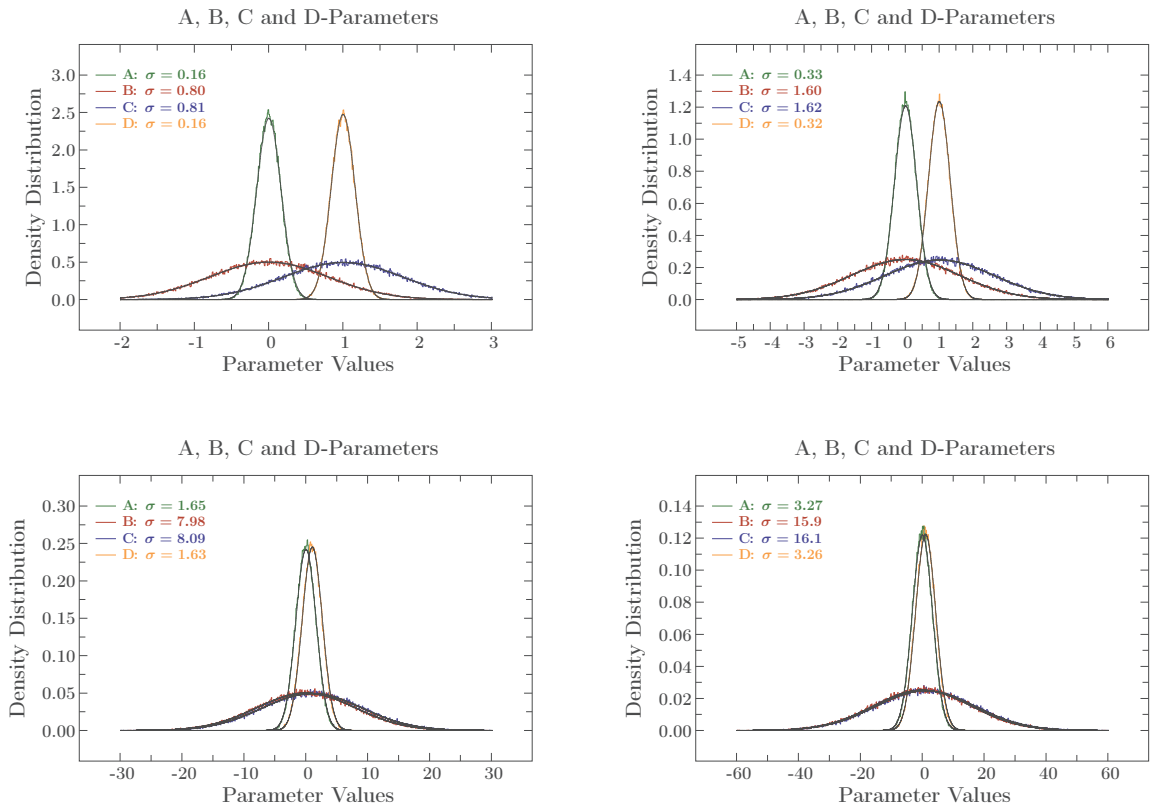

Figure 3.1 – Probability (uncertainty) distributions of parameters A, B, C and D for the increasing experimental errors parameterised with $\sigma_{exp} = 0.0005,\ 0.001,\ 0.005,\ 0.01$. Top left: $\sigma_{exp} = 0.0005$; top right: $\sigma_{exp} = 0.001$; bottom left: $\sigma_{exp} = 0.005$; bottom right: $\sigma_{exp} = 0.01$. The simulations performed with 5 sampling points, given by Eqs. (3.16)-(3.17). The surface under each curve is normalised to 1. It needs emphasising that even though the curves might look similar the units on the horizontal axis are very different and thus the figure illustrates a variation which is extremely strong.

point) allowing for more advanced modelling. Indeed, referring to Eq. (3.11), we may notice that σ_{exp}, whose variation was employed here, influences exclusively the error bars, δf_i^{exp}, whereas f_i^{exp} remained untouched. One could envisage an extension allowing to vary this element stochastically as well, but this variant will not be discussed here.

Possible Correlation Between Terms of the Same Symmetry. Another specific feature which attracts attention is the behaviour of the parameter adjustment algorithm with respect to the symmetries of various terms – even if the final expression does not obey any particular symmetry. Indeed, on the one hand side our exact model, cf. Eqs. (3.6)-(3.7), is the sum of two even terms

$$A + D\cosh(x) \tag{3.22}$$

and two odd terms

$$Bx + C\sinh(x), \tag{3.23}$$

whereas, on the other hand side, the underlying model-generating function $\exp(x)$ is neither odd nor even. It turns out that the standard deviations of the same symmetry terms are very similar: A as compared to D and for B as compared to C.

Comments About the Stochastic Significance. Let us slow down for commenting about some specific features which are perhaps not clearly discernible from the graphical

σ_{exp}	$A \pm \sigma_A$	$B \pm \sigma_B$	$C \pm \sigma_C$	$D \pm \sigma_C$
0.0005	0.00 ± 0.16	0.00 ± 0.79	1.00 ± 0.81	1.00 ± 0.16
0.0010	0.00 ± 0.32	0.00 ± 1.59	1.00 ± 1.61	1.00 ± 0.32
0.0020	0.00 ± 0.64	0.00 ± 3.16	1.00 ± 3.21	1.00 ± 0.64
0.0050	0.00 ± 1.60	0.00 ± 7.91	1.00 ± 8.02	1.00 ± 1.60
0.0100	0.00 ± 3.24	0.00 ± 15.9	1.00 ± 16.2	1.00 ± 3.24
0.0200	0.00 ± 6.45	0.00 ± 31.8	1.00 ± 32.2	1.00 ± 6.45

Table 3.1 – The uncertainty ranges of the exact $\{A = 0, B = 0, C = 1, D = 1\}$ parameter values with their standard-deviations obtained using increasing values of σ_{exp}. Observe that the exact model in (3.6)-(3.7) has been chosen as a sum of even $[A + D\cosh(x)]$ and odd $[Bx + C\sinh(x)]$ terms modelling $\exp(x)$, which is neither even nor odd. It turns out that the standard deviations for the even-symmetry terms, A and D, are approximately equal (similar can be said about the odd-symmetry terms B and C). This latter observation may have instructive consequences for practitioners developing their modelling methods for any new experimental information. Observe that within this particular model, σ_A, σ_B, σ_C and σ_D increase essentially proportionally to σ_{exp}.

illustration in Figure 3.1. For that purpose let us focus on the last illustration in Figure 3.1, corresponding to $\sigma_{exp} = 0.01$, and observe that the exact values of B and C parameters, which are of the order of unity, are predicted to lie within the h u g e interval whose length measured in terms of $\pm 3\sigma$ is of almost ~ 96 units. In this context, the following Figure 3.2, presents a short reminder for a quick reference.

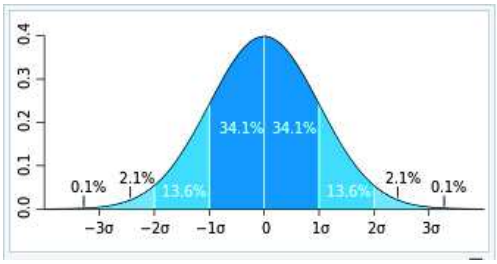

Figure 3.2 – From Wikipedia: A reminder about the standard deviation σ and the stochastic meaning $\pm 2\sigma$ and $\pm 3\sigma$ intervals [To be used when interpreting the results in Figure 3.1]. Recall: 68% of the data lie within 1 standard deviation, 95% within 2 and 99.7% within 3.

In particular, the Full Width at Half Maximum (FWHM) which is used in the literature as a standard characteristic of the width of the probability distribution curves, among others for the Gaussian distributions is given by

$$\text{FWHM} = 2\sqrt{2\ln 2}\,\sigma \approx 2.355\,\sigma. \tag{3.24}$$

Referring in this context to Eqs. (3.6) or (3.7) which determine the variation of the model-generating function we notice an extremely high uncertainty which bypasses by orders of magnitude the exact values of the parameters in this model.

Globalising the Perspective: Recall, that when constructing exact models for the inverse problem simulations and for modelling prediction uncertainties of the type we constructed here, it is up to a physicist to control the global performance

of the model via generating functions, $f_g(x)$ and $F_g(x)$, cf. Eqs. (3.1) and (3.7) which remain an element of a subjective decision. This adds to the qualities of the approach, which in this way takes the format of an even more elastic and powerful tool. By choosing a strongly varying, exponential generating function, we do hope being able to discover all possible 'surprises' or forms of what at first glance may seem as unexpected[4] mathematical feature(s), but could remain 'hidden' otherwise.

Such a strong impact of the experimental errors on a quick increase of the uncertainty widths of the resulting parameter values – one could think – will have dramatic effect on the predictions of the model. It will therefore be instructive to examine the error propagation to the intraneous and extraneous prediction regimes. These results are shown in the following sections.

3.1.2 Uncertainty Distributions: Extraneous Prediction Regime

Let us begin by showing the results for the extraneous predictions. The diagrams in Figure 3.3 show the results obtained, as before, for the increasing experimental data uncertainness $\sigma_{exp} = 0.0005$, 0.001, 0.005 and 0.01 , for the extraneous-prediction values:

$$F_1 \approx 3.32,\ F_2 \approx 4.06,\ F_3 \approx 4.95,\ F_4 \approx 6.06 \text{ and } F_5 \approx 7.39\,. \text{ [cf. Eq. (3.21)]} \qquad (3.25)$$

Let us observe, as already noticed in the case of the parametric uncertainty distributions, that the confidence intervals of each F_j increase with increasing σ_{exp} very quickly; the corresponding values are given within the field of each figure with the colour codes corresponding to the curves. In the discussed illustration, as in the case of the preceding one, the units on the x-axis increase very quickly so that the diagrams are very similar looking, whereas in reality they are not at all. To be more specific, we recall, with the help of Figure 3.2, that even when considering only the one standard deviation interval $[\mu - \sigma, \mu + \sigma]$ which contains 68% of the 'data' (here: cases of interest) the uncertainties may become unacceptably large. Whereas in some cases this may be immediately evident, e.g. if the observable in question is by definition positive, whereas stochastic estimate of the uncertainties allows for a large proportion of the negative values, in some other cases a more detailed analysis may be necessary. Table 3.2 summarises the results of our simulations.

Two characteristic observations can be made on the basis of the information in the Table. Firstly, and rather naturally, the standard deviation uncertainties for the extraneous predictions shown here increase with increasing 'experimental' error, σ_{exp}, in a certain rate which reflects the variation of σ_{exp} chosen by us. But secondly, and more importantly, the character (or 'speed') of this tendency changes very quickly, when the prediction zone gets *farther and farther away* from the fitting zone (intraneous zone) – cf. results in columns 2 and 6. Consequently (for the sake of this example we take the 5th line in the Table) whereas predictions represented by $F_1 = 3.32 \pm 2.68$ may look not very certain but almost

[4]Indeed, for instance the totally different behaviour of the modelling in terms of the intraneous and extraneous performance of predicting was, in its extreme, surprising even for members of our team. But on this occasion we have discovered that many authors confuse the 'acceptable behaviour of the fit – thus intraneous prediction – with the powerful extraneous predictions'. The modelling discussed here shows that these two can be generally considered nearly independent, as illustrated in the following sections. However this property has decisive consequences for the applications in nuclear structure, first of all for the very exotic and super-heavy nuclei international research programs.

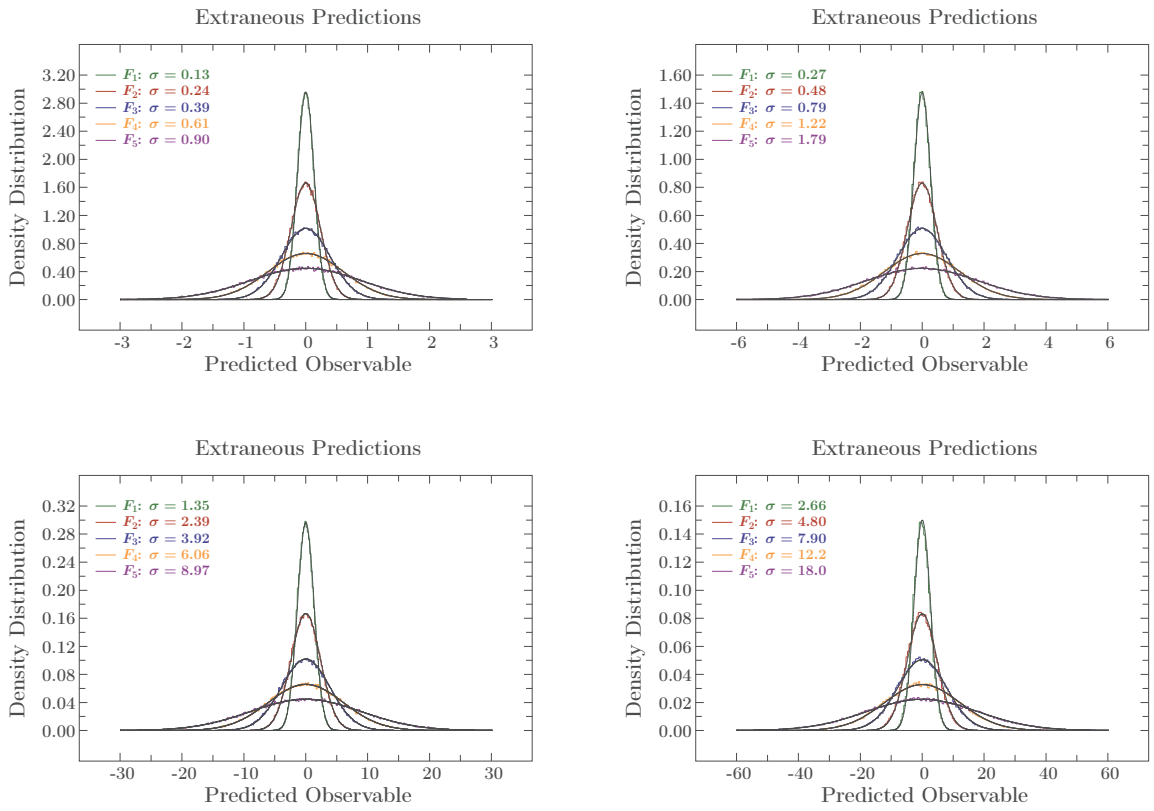

Figure 3.3 – Uncertainty probability distributions of the calculated extraneous predictions, cf. Eq. (3.25), obtained using the Monte Carlo results for parametric uncertainties in Figure 3.1. Top left: $\sigma_{exp} = 0.0005$; top right: $\sigma_{exp} = 0.001$; bottom left: $\sigma_{exp} = 0.005$; bottom right: $\sigma_{exp} = 0.01$. In each figure, the histograms have been shifted to 0 in the x-axis scale for easier comparison. Again, the surface under each curve is equal to 1.

acceptable in many contexts, the prediction $F_5 = 7.39 \pm 17.9$ will most likely be considered unacceptable, in many cases.

A Working Conclusion at this Stage of the Discussion. We believe that the most important observation at this stage can be formulated as certain warnings. They could have been considered ... nearly trivial ... will it not be for the numerous publications, which violate their essence. Remarks in the role of the warnings:

- The uncertainties of the extraneous predictions may grow very quickly with the distance form the fit-zone and may become fully unacceptable;

- Thus the validity of conclusions – including verification whether the prediction uncertainties lie within the zone of acceptability in the physics context – especially those which involve extraneous predicting, must be tested;

- Can such testing be done routinely in every physical case of interest and using 'professional' mathematical tools?

The answer to the last question is affirmative, such test can be performed nearly always using the concept of pseudo experimental data and an associated notion of 'induced exact modelling'; these concepts will be presented, illustrated and discussed in detail later on in this document.

σ_{exp}	$F_1 \pm \sigma_{F_1}$	$F_2 \pm \sigma_{F_2}$	$F_3 \pm \sigma_{F_3}$	$F_4 \pm \sigma_{F_4}$	$F_5 \pm \sigma_{F_5}$
0.0005	3.32 ± 0.13	4.06 ± 0.24	4.95 ± 0.39	6.06 ± 0.61	7.39 ± 0.90
0.0010	3.32 ± 0.27	4.06 ± 0.48	4.95 ± 0.78	6.06 ± 1.21	7.39 ± 1.79
0.0020	3.32 ± 0.53	4.06 ± 0.95	4.95 ± 1.56	6.06 ± 2.41	7.39 ± 3.56
0.0050	3.32 ± 1.34	4.06 ± 2.39	4.95 ± 3.91	6.06 ± 6.04	7.39 ± 8.92
0.0100	3.32 ± 2.68	4.06 ± 4.81	4.95 ± 7.87	6.06 ± 12.2	7.39 ± 17.9
0.0200	3.32 ± 5.39	4.06 ± 9.60	4.95 ± 15.7	6.06 ± 24.3	7.39 ± 35.8

Table 3.2 – By construction, F_i are the exact values of the extraneous predictions. Their standard-deviation uncertainties σ_i are calculated using Monte-Carlo approach as discussed in the text, for various σ_{exp}, the latter mimicking experimental errors. It is up to physicist to decide which value of the prediction confidence interval is still acceptable in the context. For the experimental errors which lead to exceeding that value, the exact model in question is unacceptable (read: useless in the context!) – the situation which we refer to as NO-GO property.

Let us emphasise that depending on the details of the modelling-algorithm the extraneous predictions may deteriorate in a more or less dramatic rate – and this is not the main point of the present working conclusions. The main point is to say that not verifying this aspect in every case studied makes the predictions resembling slightly a poker-game: Nothing certain can be said about the quality of the extraneous predictions of such a model

The results of the simulations, here addressing the extraneous predictions, have shown the importance of two elements as far as the quality of the final result is concerned. Thus not only:

- An acceptable, possibly the best root-mean-square deviations and verified(!) as stable as possible a performance in the fitting zone, but also:
- The effective distance between the extraneous prediction zone and the actual fit area.

Having established these properties we will compare our conclusions with the analogous ones for the intraneous predictions in the following section.

3.1.3 Uncertainty Distributions: Intraneous Prediction Regime

It may come as a surprise that the results in this section differ, should one say: dramatically[5] – from the results in the previous section. Indeed, the 4 diagrams in Figure 3.4 show the results analogous to those in the preceding section, but for the intraneous range, i.e. the predictions lie in between the reference points, cf. Eq. (3.17). As it can be observed, despite the very wide confidence intervals obtained in the case of the extraneous predictions, the predictions for f_i are very precise giving confidence intervals even smaller than the input error σ_{exp}.

Let us emphasise at this point, that the uncertainty distributions for the parameters A, B, C and D are common for the modelling in the two prediction zones, intraneous and extraneous, i.e., for $\{f_i\}$ and $\{F_j\}$. Therefore, the 'good-results' for the intraneous predictions need to be confronted with the 'disastrously poor' confidence intervals for the

[5] A number of comments which relativise the results of certain observations presented in this section will still be given slightly below.

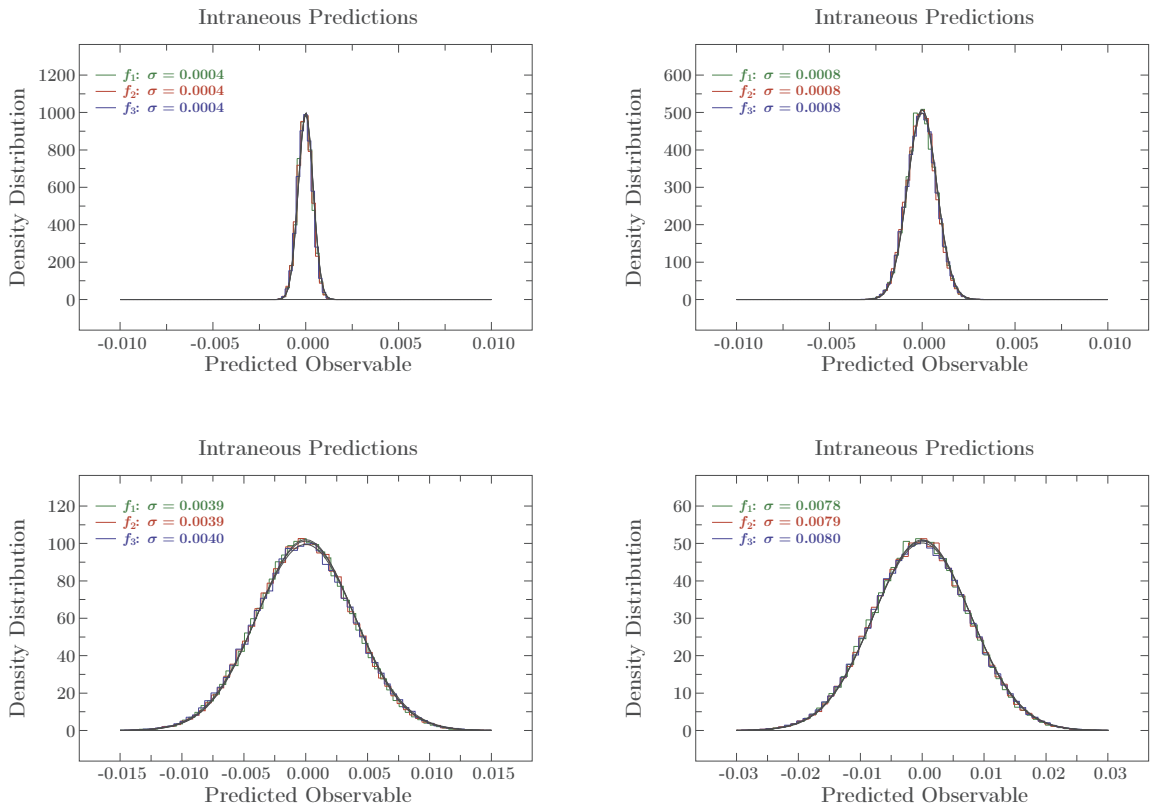

Figure 3.4 – Probability uncertainty distributions of intraneous predictions in Eq. (3.14) obtained from the Monte Carlo results of Figure 3.1. Top left: $\sigma_{exp} = 0.0005$; top right: $\sigma_{exp} = 0.001$; bottom left: $\sigma_{exp} = 0.005$; bottom right: $\sigma_{exp} = 0.01$. In each figure, the histograms have been shifted to 0 in the x-axis scale for better comparing the results and show that the distributions have nearly the same width for each f_i. The surface under each curve is equal 1.

parametric distributions in Table 3.1, at least for some σ_{exp}-values and comparably bad results for some extraneous predictions. One may conclude that, primarily, the same quality parameter uncertainty-distributions may lead to (very) good or (very) bad prediction uncertainty distributions, depending on whether one is considering the intraneous or the extraneous prediction intervals.

σ_{exp}	$f_1 \pm \sigma_{f_1}$	$f_2 \pm \sigma_{f_2}$	$f_3 \pm \sigma_{f_3}$
0.0005	1.1618 ± 0.0004	1.2840 ± 0.0004	1.4191 ± 0.0004
0.0010	1.1618 ± 0.0008	1.2840 ± 0.0008	1.4191 ± 0.0008
0.0020	1.1618 ± 0.0016	1.2840 ± 0.0016	1.4191 ± 0.0016
0.0050	1.1618 ± 0.0039	1.2840 ± 0.0040	1.4191 ± 0.0040
0.0100	1.1618 ± 0.0078	1.2840 ± 0.0079	1.4191 ± 0.0080
0.0200	1.1618 ± 0.0158	1.2840 ± 0.0158	1.4191 ± 0.0160

Table 3.3 – Results analogous to those in Table 3.2 with which they should be compared, but for intraneous predictions; for details – see the text.

Table 3.3 shows the confidence intervals for the intraneous predictions of the model. The incomparably better performance in terms of the stochastic description of uncertainties deserves noticing, given the fact that the confidence intervals are down to 5 orders of

magnitude (!) better in this case. Comparison of these results with the preceding one allows us to formulate a few synthetic comments which follow.

> *Uncertainties: Parameters, Intraneous and Extraneous Predictions. Let us put together, in the from of concluding observations, the results indicating that the excellent intraneous zone predictions, Table 3.3, are obtained with parameters which are very uncertain stochastically, Table 3.1 – the same parameters, which have led to the extraneous predictions … dominantly unacceptable, cf. Table 3.2.*
>
> *A physicist may choose to retain at this point that, even though the detailed performance of the model may depend on the particular context, that generally one must accept as mater of the rule that the quality of the fit and that of the intraneous predictions might have not much in common with the quality of the extraneous predictions, usually those latter ones which are in the center of attention.*
>
> *Finally, let us emphasise that the very notion of intraneous and extraneous prediction zones introduced in Ref. [40] plays a central role in formulating the distinction between the two concepts and the implied very different performance of the model in both cases.*

As a by-product of the preceding discussion one arrives at yet another feature which will help to use the semantics more appropriately: The notion of 'useless exact theories' and the so called NO-GO Property, or, more colloquially: NO-GO Command.

3.1.4 The NO-GO Command: Even for the Best, Exact Models

After having presented the above title let us simplify one of the already obtained results, shortened to one phrase:

> "The farther away the extraneous prediction zone from the fitting region,
> the broader the uncertainty distribution of the extraneous prediction."

Combining this with another affirmation

> "There do not exist error-less experimental data",

we arrive at the series permanent potential conflicts between the two restrictions, which, from the practitioner's perspective, can be formulated like this:

> *No matter how hard (or: how long time) we work on deriving the complex mathematical expressions behind an exact*[6] *theory in physics, it will be strictly*

[6] In Chapter 1, we have already commented on the semantical limitations, or surprises, in the context of the notion of an 'exact theory', and in particular we alerted the reader that our discussion of that aspect is limited to theories depending on adjustable parameters. We believe, despite all the alerts formulated here and related to the limitations of the use of exact theories (we do not know of any in nuclear physics), that such constructions, once achieved – will play an important role *no matter* the limitations related to stochastic significance of the associated solutions of the inverse problem and, most evidently, they will give a strong motivation for the unprecedented technological developments.

speaking 'useless in the context', as long as the instrumental capacities do not allow for obtaining a sufficiently constraining precision for theory's parameters.

The same affirmation can be presented in an alternative formulation: If for one reason or another, theory predictions are needed with an a priori prescribed precision, whereas the knowledge of the parameters – because of the present-day instrumental limitations – is not sufficiently precise, even an exact theory becomes 'useless in the context'.

Since the sizes of the extraneous-prediction uncertainty-distributions grow quickly with the distance form the fitting area (read: from the present-day knowledge) there will always exist a risk that at the sufficiently large distance from the fitting zone, the extraneous predictions will become meaningless and the model – 'useless in the context'.

Last but not least – Final clarifying statements: Above we refer to the exact theoretical models, whose parameter-adjustment stability as well as the stochastic significance of the final result have been verified using established methods of applied mathematics. We encountered numerous situations in this project, in which the acceptable description of the data has been achieved employing the parameter values lying in the unphysical ranges: Thus the agreement with the data as well as 'all model predictions' can, under these circumstances, be interpreted as equivalent to employing random numbers to compare with the data.

Some (or one) of above alerts may motivate a physicist to declare, that even an exact model cannot be used in her/his pre-defined context. We nick-name this mechanism the **NO-GO** property of an exact modelling. Needless to say, similar conclusions apply to the a priori *inexact* modelling, even though very likely in a less 'spectacular' general framing.

3.1.5 A Summary and Preliminary Conclusions

One of the most important implications of the simulations presented in the previous sections is that one *must not* conclude about the quality of the extraneous predictions from the quality of the intraneous ones. As we have illustrated using a simplified model – and some other authors arrived at similar conclusions using different methods – the so-to-speak good r.m.s. results in the intraneous zone do not translate at all into any similar r.m.s. quality in the extraneous zone – the property, information which seemingly still only rather a few authors are aware of.

All these properties must be studied separately on the case by case basis.

Let us emphasise that precisely this particular feature leads to serious misunderstandings and lies at the origin of inconsistent predictions or conclusions in the literature. In Figure 3.5 we try illustrates this mechanism by showing the quickly increasing standard deviation (equivalently: uncertainty of predictions) while increasing the distance between the fitted, intraneous zone, and the extraneous zone for two different values of σ_{exp}. The five black open circles in this Figure indicate the reference points (fitting zone) taken for the minimisation.

In order to obtain the results presented in Figure 3.5 we have calculated the standard deviation for the curves $F_{\rm g}(x)$ in Eq. (3.7) with the help the N_{MC} Monte-Carlo parameter sets $\{A, B, C, D\}$. The formula for the standard deviation has been given in Eq. (1.61) and

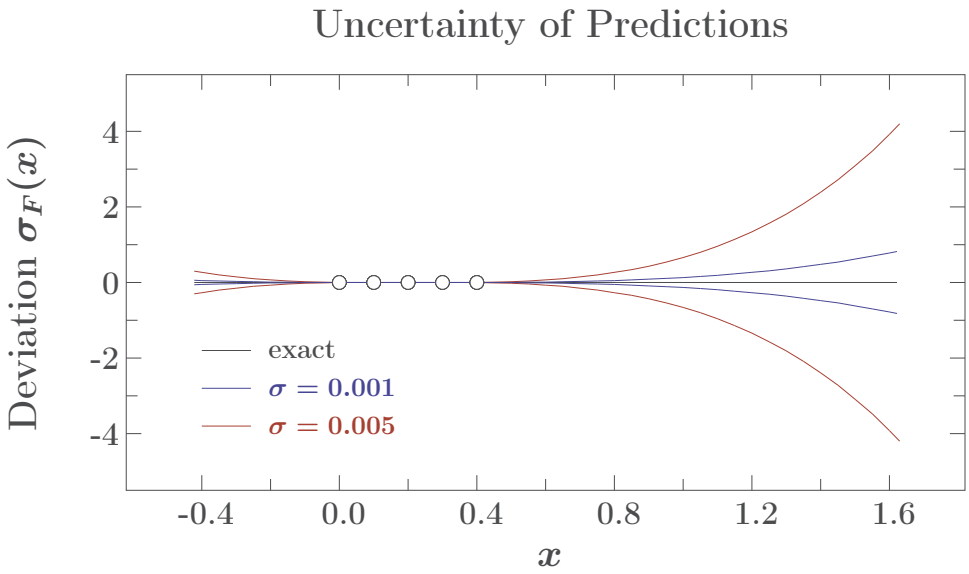

Figure 3.5 – Dependence of the standard deviation of the predictions as function of the generating parameter x, here relative to the exact result, the latter normalised to give horizontal straight line. In this illustration, increasing x beyond the last open-circle position measures the increasing distance of the actual prediction area from the fitting zone. The solid red line and the blue dashed line have been obtained using Eqs. (3.26) and (3.27) with the help of the Monte Carlo results with $\sigma_{exp} = 0.005$ and $\sigma_{exp} = 0.001$, respectively. The five open circles represent the reference values, (x_i^r, f_i^r), cf. Eqs. (3.16) and (3.17) used for the fitting.

Eq. (1.63). With the help of the cited expressions, we define the mean deviation at each x value as

$$\mu_F(x) = \frac{1}{N_{MC}} \sum_{i=1}^{N_{MC}} [A_i + B_i\, x + C_i \sinh(x) + D_i \cosh(x) - \exp(x)]. \tag{3.26}$$

It follows that the standard deviation as a function of x takes the form

$$\sigma_F(x) = \left\{ \frac{1}{N_{MC}} \sum_{i=1}^{N_{MC}} [\Delta F_i(x) - \mu_F(x)]^2 \right\}^{1/2} \tag{3.27}$$

where we defined

$$\Delta F_i(x) = A_i + B_i\, x + C_i \sinh(x) + D_i \cosh(x) - \exp(x). \tag{3.28}$$

To illustrate the varying uncertainty of the prediction we then employ the standard deviation – equivalently: confidence interval – by plotting in Figure 3.5 the two corresponding curves, $+\sigma_F(x)$ and $-\sigma_F(x)$, given by Eq. (3.27).

Let us have a practical look at the illustration in the Figure. If the user decides for her/his mathematical and/or physical reasons that e.g. $\sigma_F(x) > 2$ is not allowed for the model to be of practical use in the given context, then the results described by (e.g.) the red curve can not be considered useful for $x > 1.2$. Let us emphasise that both σ_F-curves presented in Figure 3.5 behave almost perfectly in the intraneous regime.

In what follows we will perform an analogous simulation but for the realistic case, using a realistic mean-field Hamiltonian in place of a toy-model formula.

3.2 Realistic Modelling: Introductory Elements

Having introduced in the preceding sections the main features of the exact mathematical approach, which allows for examining various features of the Inverse Problem down to all the details which a physicist may need, we will turn to the realistic applications in the nuclear mean-field theory context. To this end, we will introduce the mean-field Hamiltonian presented in Eq. (2.1) in its so-called traditional Woods-Saxon representation with the expression of the spin-orbit in the form of Eq. (2.5). With this choice we will be working with the modelling dependent on two sets of 6 parameters,

$$\{V^c, r^c, a^c, \lambda^{so}, r^{so}, a^{so}\}_{\pi,\nu} \tag{3.29}$$

one for the protons, π, and the other for the neutrons, ν. Since the primary goal at this time is to construct the uncertainty probability distributions for the single particle energies for doubly-magic spherical nuclei, the idea is to profit from the experience with the toy model discussed so far. Following this strategy we will: introduce a Gaussian noise for the sampling points (in this case, experimental single particle level energies), proceed with adjustment of parameters, calculate the energy spectra obtained with the optimal parameters and, following the Monte-Carlo *Ansatz*, repeat this procedure a reasonably big number of times, $N_{MC} \sim 10^5$. With the so obtained results we will be able to construct the occurrence histograms for parameters and single particle energy levels and by studying and analysing the widths and the obtained histograms we will be able to discuss the prediction capacities of the studied model.

In in order to provide a direct analogy with the previous case of the exact model, we will construct what we refer to as an *induced exact model* via the concept of *pseudo-experimental data*, introduced in Section 1.8.2. Following the prescription given there, we first adjust the parameters in Eq. (3.29) by performing the χ^2-fit to the experimentally known energy levels of ^{208}Pb, cf. Table 2.2 and 2.3. In this way we construct what we refer to as the *reference parameter set*, which is presented in Table 3.4.

Recall that the role of the *induced exact model* is to provide the test-ground environment – an algorithm for which the exact optimal solutions of the parameters are known – under the conditions that, apart from small deviations in terms of the actual parameter values, the performance of the *induced exact model* is very similar to the performance of the original one. Since the parametric details do not matter for the undertaken-test purposes, we decided to fix $a^c_\pi = a^c_\nu = 0.75$ fm and $a^{so}_\pi = a^{so}_\nu = 0.70$ fm, as the values close to the so-called WS-Universal parameter values [41–46]. The impact of this particular limiting choice on the calculated mean-field energies is minimal. Indeed, the central diffuseness value is very close to its universal value a^c_{univ}, which has been used as optimal by many authors within the last 30 years or so, and varying it within the range of $a^c_{\text{univ}} \pm 0.1$ fm makes the single particle energy levels move nearly parallel with only a small fraction of relative variations. Concerning the choice of the spin-orbit diffuseness, it will always be compensated by the spin-orbit strength parameter, as discussed in more detail in Section 4.2.2. Figure 3.6 shows the structure of the theoretical levels, as compared to the experimental ones, using the parameter values given in Table 3.4.

To construct the Monte-Carlo modelling of the experimental uncertainties, Gaussian uncertainty-distributions have been introduced to the exact pseudo-experimental energies, thus simulating in such a way the experimental errors in the framework of the induced exact model. In this first approach we decided to apply the same Gaussian noise to all the input data. For this purpose we use a common parameter, say $\sigma_{\text{ref.}}$, which is an analogue

	V^c (MeV)	r^c (fm)	a^c (fm)	f_c	λ^{so} (MeV fm$^2/\hbar^2$)	r^{so} (fm)	a^{so} (fm)
protons	−67.59	1.19	0.75	0.82	24.52	1.05	0.70
neutrons	−39.32	1.38	0.75	–	31.82	0.99	0.70

Table 3.4 – Reference central and spin-orbit potential parameters for protons and neutrons used to construct the values of the pseudo-experimental single particle energies for ^{208}Pb.

of σ_{exp} used in the case of the toy model presented in the previous sections of this chapter.

Let us introduce some auxiliary quantities which will be practical in the rest of this discussion. First of all, we will introduce the root-mean-square deviation for just one nucleus defined by

$$\text{r.m.s.}_1 = \left\{ \frac{\sum_i \left[(2j_i+1)(e_i^{\text{exp}} - e_i^{\text{th}})^2\right]}{\sum_i (2j_i+1)} \right\}^{1/2} , \tag{3.30}$$

where j refers to the single-nucleon orbital angular-momentum. Next, let us introduce an analogous quantity for $\mathcal{N}$ nuclei, when considered simultaneously in the parameter adjustment

$$\text{r.m.s.}_{\mathcal{N}} = \left\{ \frac{\sum_{k=1}^{\mathcal{N}} \sum_{i=1}^{n_k} \left[(2j_{i,k}+1)(e_{i,k}^{\text{exp}} - e_{i,k}^{\text{th}})^2\right]}{\sum_k \sum_i (2j_{i,k}+1)} \right\}^{1/2} . \tag{3.31}$$

Finally we will define the root-mean-square deviation (calculated with any set of parameters obtained under all possible varying circumstances, e.g. obtained with any one single-nucleus fit, or a few nuclei fit) calculated using the energies of the eight spherical nuclei considered in this document (^{16}O, ^{40}Ca, ^{48}Ca, ^{56}Ni, ^{90}Zr, ^{132}Sn, ^{146}Gd and ^{208}Pb):

$$\text{R.M.S.} = \left\{ \frac{\sum_{k=1}^{8} \sum_{i=1}^{n_k} \left[(2j_{i,k}+1)(e_{i,k}^{\text{exp}} - e_{i,k}^{\text{th}})^2\right]}{\sum_k \sum_i (2j_{i,k}+1)} \right\}^{1/2} . \tag{3.32}$$

As it can immediately be seen form the above definition, R.M.S. describes an average quality of the parametric fit tested with all the doubly-magic spherical-nuclei for which we have the experimental data at our disposal. Let us remark in passing, that when considering only one nucleus for the fitting, i.e. $\mathcal{N} = 1$, the results of Eq. (3.30) and Eq. (3.31) coincide. Similarly, when taking all the nuclei for the fitting, thus for $\mathcal{N} = 8$, Eqs. (3.31) and (3.32) give the same result.

To estimate a 'reasonable' test-value of $\sigma_{\text{ref.}}$ for the realistic calculations, we have calculated the R.M.S. deviation while fitting the parameters to the eight spherical nuclei considered. The result is close to 600 keV and this value was retained as the reference error value in the following discussion of the Monte-Carlo simulations.

After comparing the values of the deviations, r.m.s., R.M.S. and maximum absolute error Mx-abs., of Figures 3.6 and 3.7, we confirm that setting $\sigma_{\text{ref.}} = 600$ keV is a reasonable order of magnitude for simulating the experimental uncertainties. With this decision, one

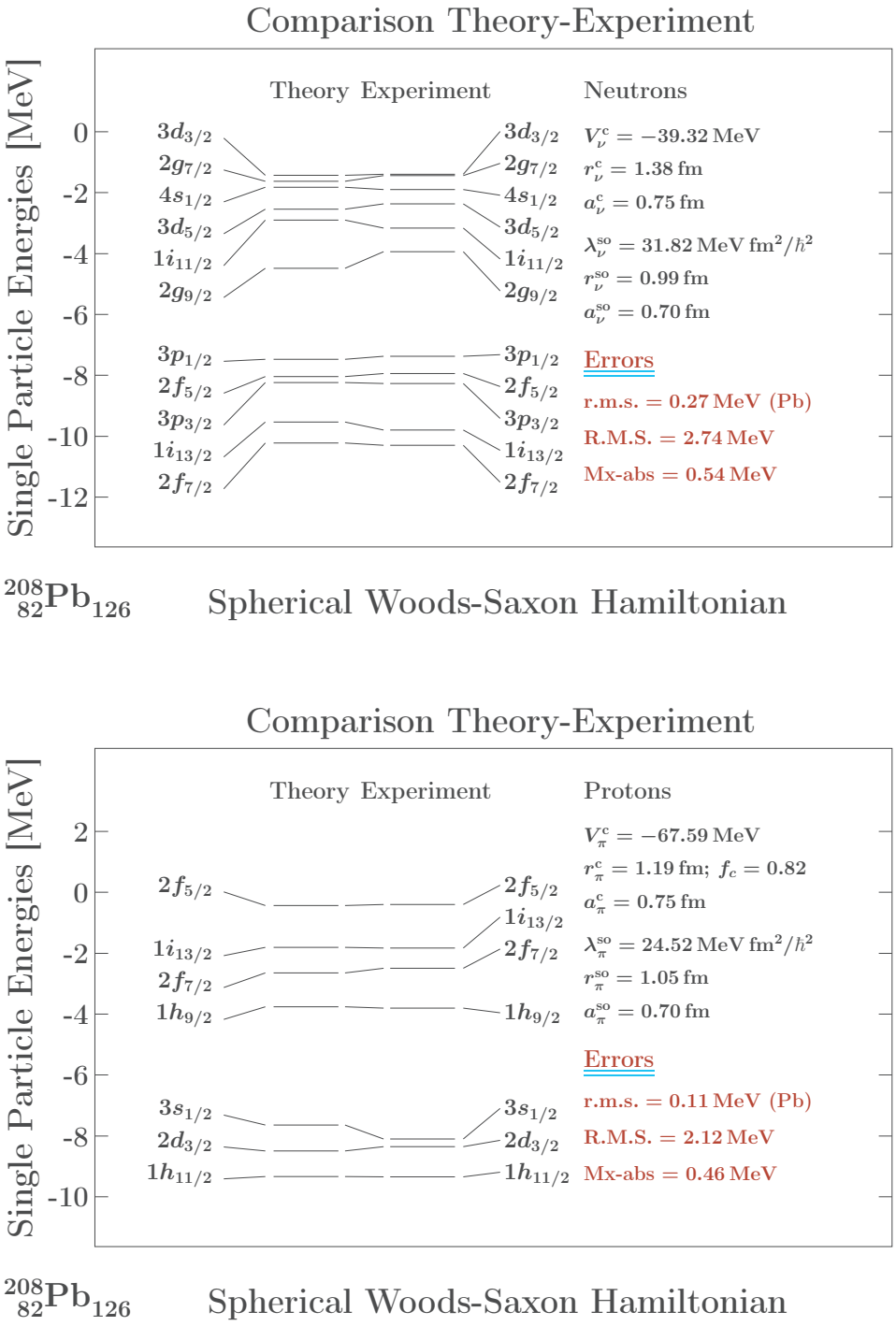

Figure 3.6 – Comparison of theoretical and experimental single nucleon energies for ^{208}Pb: Neutrons (upper panel) and protons (lower panel) obtained using the parameters presented in Table 3.4. The theoretical results have been used as pseudo-experimental values to construct the *induced exact realistic model*. The parameter values and the errors associated with the plotted spectra are given in the fields of the figures. The quantity r.m.s. has been calculated using Eq. (3.29), considering only the ^{208}Pb energies; the quantity R.M.S. originates from Eq. (3.32). Finally, Mx-abs stands for the maximum absolute error between the left and right columns of each panel.

can proceed to construct what it is usually referred to as 'noisy' data. In this case, we generated $N_{MC} = 20\,000$ random Gaussian-distributed sets of reference data, which we

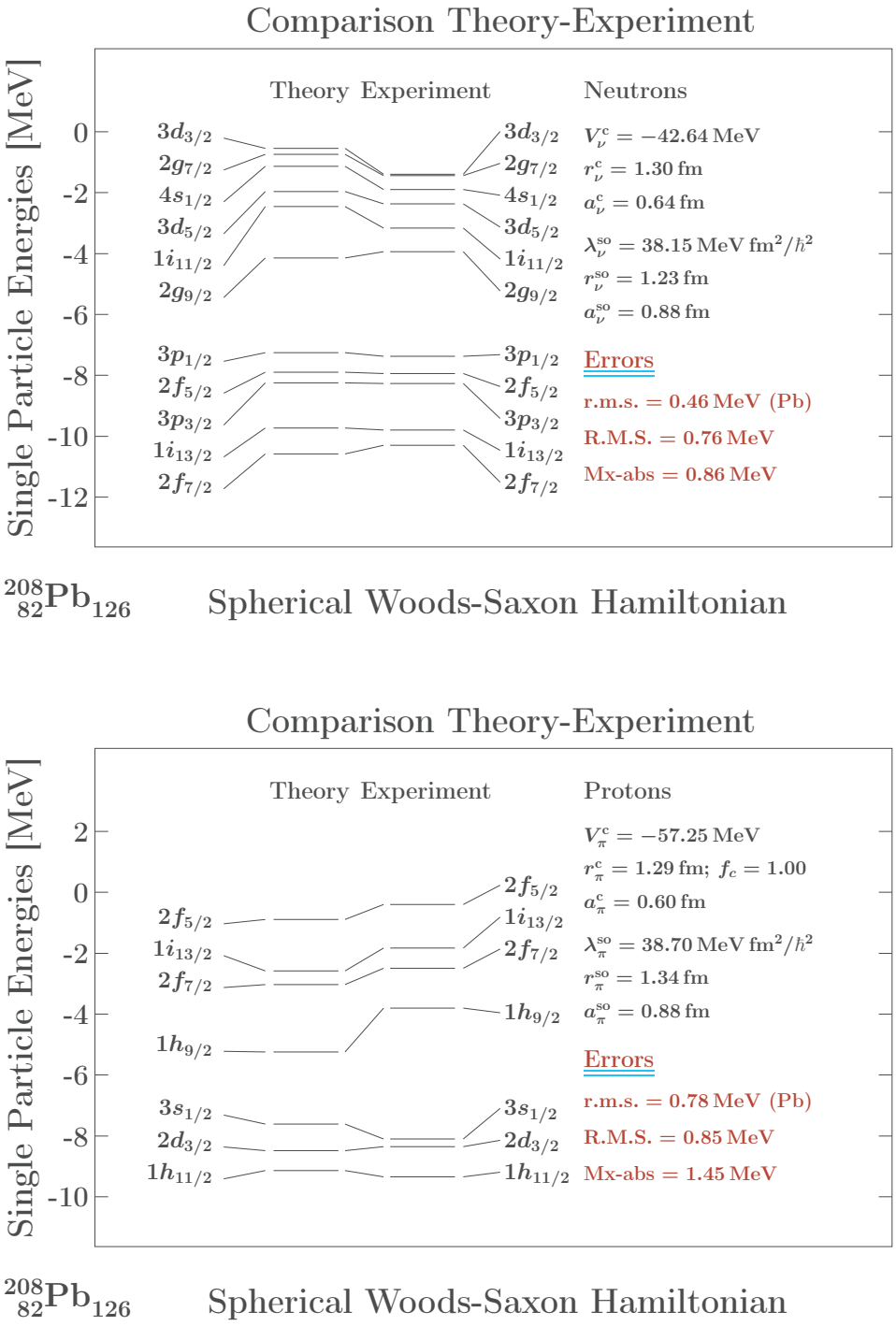

Figure 3.7 – Comparison between the theoretical and experimental single nucleon energies for ^{208}Pb: Neutrons (upper panel) and protons (lower panel). These results have been obtained fitting the WS-Hamiltonian parameters, Eq. (3.29), to the energies of ^{16}O, ^{40}Ca, ^{48}Ca, ^{56}Ni, ^{90}Zr, ^{132}Sn, ^{146}Gd and ^{208}Pb – simultaneously. The parameter values and the errors associated with the illustrated spectra are given in the fields of the figures. The quantity r.m.s. has been calculated using Eq. (3.29), considering only the ^{208}Pb energies; the quantity R.M.S. was obtained using Eq. (3.32). Finally, Mx-abs stands for the maximum absolute error between the left and right columns of each panel.

used to fit the parameters, obtaining in this way N_{MC} sets of parameters $\{p_{MC}\}$. They serve to calculate the corresponding N_{MC} single particle energy sets $\{e_{MC}\}$ for ^{208}Pb, allowing finally to construct the occurrence histograms.

Let us notice that even though the fit for the single ^{208}Pb case may be considered excellent given very low r.m.s. values, cf. Figure 3.6, the resulting parameters do *not* allow for acceptable predictions for the whole nuclear range as it can be deduced from the huge R.M.S. values. This is certainly not a (qualitatively) surprising an observation - but we give the precise indications here based on the real data.

> *Working Conclusion 1: We may now pose the question of the physicist's optimal choice* relative *to her/his context. In the case of the* intraneous *predictions, which in present context translate into the calculations for ^{208}Pb nucleus itself and/or some of its neighbours, the choice would clearly be: Use the local fit.*

3.2.1 Simulating the Level Uncertainty Distributions

Figure 3.8 shows the results for the smooth histograms obtained from the Monte-Carlo simulations as explained above. More precisely, these are the results for the neutron single particle energies of the main shell-closures $N_{\text{main}} = 5$ and $N_{\text{main}} = 6$. After the construction of the histograms and the corresponding normalisation so that the surface under each distribution is equal to one, a Gaussian distribution was fitted to each one,

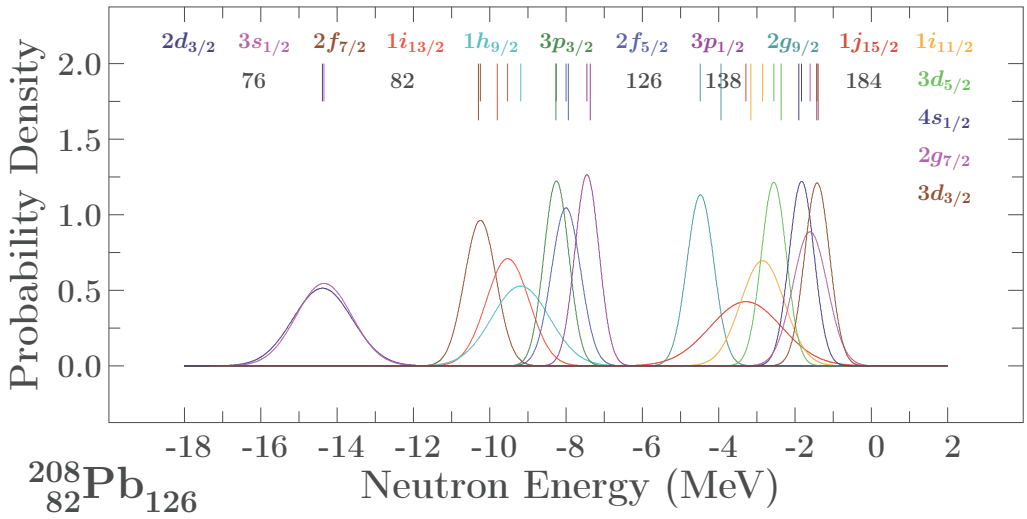

Figure 3.8 – Normalised, smoothed histograms showing the Monte-Carlo simulated probability density distributions of uncertainties for the neutron single particle energies within $N_{\text{main}} = 5$ and $N_{\text{main}} = 6$ main-shells and $2d_{3/2}$ and $3s_{1/2}$ corresponding to $N_{\text{main}} = 4$; nucleus ^{208}Pb. The short thick bars indicate the peak position of each distribution; the long thin bars represent the experimental values of the energies, cf. Table 2.2. The numbers printed between the bars indicate the occupation particle numbers in that energy region. The assumed experimental uncertainty common for all the levels is $\sigma_{\text{ref.}} = 600$ keV (see text). The normalisation is such that the surface under each curve is equal to 1. The values of the FWHM for each level can be found in the first row of Table 3.5.

and we checked that the position of the maximum and the full width at half maximum of the 'raw histogram' and the fitted Gaussian were the same and this is how the smoothed

probability density distributions in Figure 3.8 were obtained. In Figure 3.9, we show the analogous results but for the proton single particle energies corresponding to the $N = 4$ and $N = 5$ main-shells. In both figures, the thick short bars and thin long bars represent the distribution peak positions and the experimental values of the levels (where known), respectively.

Competition-Winning Experimentally-Known Orbitals. Let us emphasise that in cases in which a level is *not* known experimentally, which means that it was not considered for the parameter adjustment, its uncertainty distribution is on the average broader than in the case where the level is known experimentally. In the case of neutrons in Figure 3.8 and also Table 3.5, the uncertainty distributions of levels $1h_{9/2}$ and $1j_{15/2}$, which are not known experimentally, and therefore not taken into account in the minimisation procedure, happen to be twice as broad as the average of the others in the lightest isotopes, i.e. the closest to the fitting area. Observe that in the same figure, the next broadest distributions correspond to big-ℓ orbitals, $1i_{13/2}$ and $1i_{11/2}$.

Regarding the proton case in Figure 3.9 and Table 3.6, the same effects can be signalled. Observe that the FWHM for $1g_{7/2}$ level, again not known experimentally, is bigger than the ones known experimentally and of those which has lower ℓ values as $2d_{5/2}$, $3p_{3/2}$ or $3p_{1/2}$.

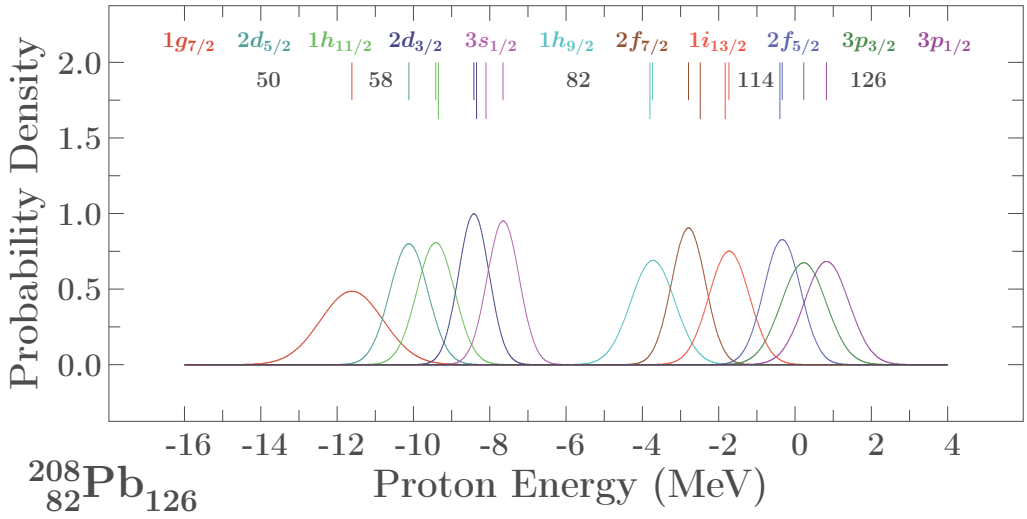

Figure 3.9 – Similar to the preceding one but for the protons. The values of the FWHM for each level can be found in the first row of Table 3.6.

The Richer the Sampling the Narrower the Uncertainty Distribution. The fact that for ^{208}Pb case studied, on the average, the neutrons have narrower uncertainty distributions than the protons, may be caused by the fact that the number of levels considered in the fitting procedure was bigger in the case of neutrons, i.e. 11 levels, whereas we have only 7 levels for the protons. This difference implies that the neutron parametrisation may be considered better constrained than the one of the protons and therefore the resulting final uncertainty distributions obtained are narrower. This statement could be considered as an argument in favour of intensifying experimental efforts to find more information about the experimental mean-field single-nucleon levels.

Let us notice that the gap $Z = 114$ for protons comes from a direct extrapolation of the information on the mean-field single-particle levels from ^{208}Pb, cf. Figure 3.9. In other

		$N_{\text{main}} = 5$						$N_{\text{main}} = 6$						
Z	N	$2f_{7/2}$	$1i_{13/2}$	$1h_{9/2}$	$3p_{3/2}$	$2f_{5/2}$	$3p_{1/2}$	$2g_{9/2}$	$1j_{15/2}$	$1i_{11/2}$	$3d_{5/2}$	$4s_{1/2}$	$2g_{7/2}$	$3d_{3/2}$
82	126	0.96*	1.33*	1.76	0.76*	0.90*	0.74*	0.83*	2.20	1.36*	0.77*	0.77*	1.05*	0.78*
114	164	1.30	1.46	2.22	1.03	1.19	1.00	0.87	1.77	1.64	0.73	0.74	1.01	0.78
114	170	1.47	1.44	2.33	1.19	1.34	1.15	0.79	1.52	1.59	0.58	0.59	0.88	0.62
114	172	1.55	1.46	2.39	1.27	1.42	1.23	0.81	1.46	1.60	0.58	0.59	0.88	0.61
114	180	1.92	1.67	2.66	1.64	1.78	1.59	1.06	1.35	1.75	0.81	0.79	1.04	0.80
114	184	2.12	1.83	2.81	1.84	1.98	1.80	1.24	1.38	1.87	0.99	0.95	1.19	0.96
114	196	2.74	2.38	3.34	2.46	2.60	2.42	1.83	1.71	2.35	1.56	1.49	1.74	1.51
114	214	3.64	3.28	4.15	3.35	3.50	3.29	2.71	2.49	3.14	2.38	2.26	2.57	2.30
114	228	4.28	3.94	4.76	3.97	4.14	3.92	3.33	3.12	3.74	2.95	2.79	3.16	2.84

Table 3.5 – Realistic Monte-Carlo calculation results of the FWHM values [in MeV] of the neutron single particle levels covering the nuclear main shells $N_{\text{main}} = 5$ and 6 for the ${}^{278-342}_{114}\text{Fl}_{164-228}$ super-heavy isotopes indicated. The ^{208}Pb results have been extracted from the curves in Figure 3.7; they show strong variations depending on the quantum characteristics of each individual state. The asterisk indicates that the level is known experimentally, i.e. taken for the parameter adjustment.

		$N_{\text{main}} = 4$					$N_{\text{main}} = 5$					
Z	N	$1g_{7/2}$	$2d_{5/2}$	$1h_{11/2}$	$2d_{3/2}$	$3s_{1/2}$	$1h_{9/2}$	$2f_{7/2}$	$1i_{13/2}$	$2f_{5/2}$	$3p_{3/2}$	$3p_{1/2}$
82	126	1.93	1.17	1.16*	0.94*	0.99*	1.36*	1.04*	1.25*	1.13*	1.39	1.37
114	164	1.79	1.01	1.20	0.88	0.92	1.38	1.08	1.22	1.19	1.41	1.45
114	170	1.99	1.18	1.31	0.99	1.00	1.36	0.92	1.05	0.99	1.19	1.20
114	172	2.07	1.27	1.38	1.06	1.06	1.38	0.90	1.02	0.88	1.14	1.14
114	180	2.45	1.66	1.70	1.44	1.40	1.60	1.02	1.07	0.85	1.07	1.01
114	184	2.66	1.88	1.89	1.66	1.60	1.77	1.16	1.18	0.95	1.12	1.04
114	196	3.30	2.55	2.50	2.34	2.26	2.36	1.72	1.68	1.47	1.50	1.39
114	214	4.28	3.54	3.44	3.36	3.25	3.33	2.65	2.57	2.41	2.33	2.23
114	228	5.01	4.27	4.14	4.11	3.98	4.07	3.36	3.26	3.14	3.02	2.92

Table 3.6 – Realistic Monte-Carlo calculation results of the FWHM values [in MeV] of the proton single particle levels covering the nuclear main shells $N_{\text{main}} = 4$ and 5 for ${}^{278-342}_{114}\text{Fl}_{164-228}$ superheavy isotopes indicated. The ^{208}Pb results have been extracted from the curves in Figure 3.7; they show strong variations depending on the quantum characteristics of each individual state. The asterisk indicates that the level is known experimentally, i.e., the corresponding energies were taken for the parameter adjustment.

words, in order to constrain better the underlying uncertainties some more experimental data on the single particle energies would be helpful – be it about the levels in ^{208}Pb, or – even better – on the light-super-heavy nuclei. Here one could envisage the experiment-theory collaboration which would aim at constructing the data basis which would allow the analysis of the gap evolution with increasing the neutron number - in analogy with the studies of the proton gaps in e.g. the Nickel isotopes showing a strong dependence of this gap on the neutron numbers

3.2.2 Focus on Super-Heavy Nuclei

Recall that one of the main goals of the present project is to evaluate the predictions for the unknown nuclear regimes. Such predictions must be obtained using the data on the nuclear areas known experimentally today. In particular, we would like to study the spectroscopic properties of the mean-field single-nucleon energies in the super-heavy nuclei. In this case, and as an analogy to the procedure engaged with the toy model in the previous sections, we would like to show/detect the point where one can no more use the realistic model for predicting mean-field single-nucleon properties far from the fitting range. For this reason, taking the parameters obtained in the Monte-Carlo simulations which have been used to produce the energy distributions of Figures 3.8 and 3.9, we predict the energy level distributions for some $_{114}$Fl-isotopes. The results of the FWHM of the isotopes studied are given in Tables 3.5 and 3.6 for neutrons and protons, respectively.

Nuclear Structure Effects: Non-Monotonic Variations. Let us observe that in general, when increasing the number of neutrons in the Fl-nucleus, thus considering heavier and heavier isotopes, the uncertainty widths of the studied distributions keep increasing, as well. However, the distributions do not change monotonically, neither as functions of the neutron number N, nor as functions of the angular momentum ℓ. The average tendencies can be summarised as follows. First of all, one may note that on the average the confidence intervals increase by a factor of ~ 3 when the neutron level moves from $N = 126$ to $N = 228$.

Deeply-Bound States in the Role of Extraneous Prediction Zones. Another systematic tendency visible from the presented results is that the uncertainties increase when the energy of individual nucleons moves away from the fitted zone, which can be seen as extraneous predictions within a given nucleus. This is visible for the deeply bound levels, whose distribution widths rapidly increase up to ~ 8 MeV (!), cf. Tables 3.7 and 3.8 for neutrons and protons, respectively.

Perspectives: How To Diminish the Uncertainties of Predictions? At this point, one may ask what can be done in order to diminish the uncertainties the predicted levels – in other words: to stabilise the modelling. One suggestion will be related to counteracting the parametric correlations, the mechanism introduced in Chapter 1, which will be followed in the next Chapters of this project. Another suggestion, based on the observations in this section, will be to improve the experimental constraints via increased number of good quality experimental data points. These aspects will be discussed in the next chapters as well.

		$N_{\text{main}} = 0$	$N_{\text{main}} = 1$		$N_{\text{main}} = 2$			$N_{\text{main}} = 3$					$N_{\text{main}} = 4$				
Z	N	$1s_{1/2}$	$1p_{3/2}$	$1p_{1/2}$	$1d_{5/2}$	$2s_{1/2}$	$1d_{3/2}$	$1f_{7/2}$	$2p_{3/2}$	$1f_{5/2}$	$1g_{9/2}$	$2p_{1/2}$	$1h_{11/2}$	$2d_{5/2}$	$1g_{7/2}$	$2d_{3/2}$	$3s_{1/2}$
82	126	6.11	5.34	5.32	4.49	4.11	4.54	3.56	3.01	3.70	2.57	2.96	1.63	1.93	2.75	1.82	1.72
114	164	5.79	5.15	5.12	4.44	4.09	4.45	3.67	3.13	3.76	2.84	3.10	2.01	2.18	3.01	2.09	1.97
114	170	6.05	5.42	5.39	4.70	4.36	4.71	3.92	3.40	4.00	3.06	3.36	2.17	2.42	3.20	2.33	2.21
114	172	6.14	5.51	5.48	4.79	4.45	4.80	4.01	3.49	4.08	3.14	3.45	2.24	2.51	3.27	2.42	2.30
114	180	6.51	5.88	5.86	5.17	4.84	5.17	4.38	3.87	4.43	3.50	3.84	2.56	2.89	3.60	2.80	2.68
114	184	6.70	6.07	6.05	5.36	5.03	5.36	4.57	4.07	4.62	3.69	4.04	2.75	3.09	3.77	3.00	2.88
114	196	7.26	6.64	6.62	5.94	5.62	5.94	5.15	4.68	5.18	4.28	4.64	3.33	3.71	4.32	3.62	3.50
114	214	8.07	7.47	7.46	6.78	6.48	6.78	6.01	5.56	6.02	5.15	5.51	4.22	4.60	5.14	4.51	4.39
114	228	8.67	8.08	8.08	7.40	7.11	7.41	6.64	6.20	6.64	5.79	6.15	4.88	5.25	5.76	5.15	5.03

Table 3.7 – Realistic Monte-Carlo calculation results of the FWHM values [in MeV] of the low-energy (deeply bound) neutron single particle levels covering the nuclear main shells $N_{\text{main}} = 0$ to 4 for ^{208}Pb and $_{114}$Fl super-heavy isotopes indicated.

		$N_{\text{main}} = 0$	$N_{\text{main}} = 1$		$N_{\text{main}} = 2$			$N_{\text{main}} = 3$				
Z	N	$1s_{1/2}$	$1p_{3/2}$	$1p_{1/2}$	$1d_{5/2}$	$1d_{3/2}$	$1f_{7/2}$	$2s_{1/2}$	$1f_{5/2}$	$1g_{9/2}$	$2p_{3/2}$	$2p_{1/2}$
82	126	5.16	4.52	4.59	3.79	3.85	2.96	3.22	2.93	2.04	2.15	1.99
114	164	4.16	3.70	3.77	3.14	3.21	2.51	2.59	2.52	1.82	1.74	1.61
114	170	4.49	4.01	4.09	3.44	3.51	2.79	2.90	2.78	2.05	2.02	1.89
114	172	4.60	4.12	4.19	3.55	3.61	2.89	3.01	2.88	2.14	2.12	1.99
114	180	5.04	4.56	4.63	3.97	4.04	3.29	3.46	3.29	2.53	2.56	2.43
114	184	5.26	4.78	4.85	4.19	4.25	3.51	3.69	3.51	2.73	2.79	2.66
114	196	5.92	5.43	5.50	4.83	4.90	4.14	4.36	4.16	3.36	3.47	3.35
114	214	6.86	6.38	6.44	5.77	5.85	5.08	5.34	5.12	4.30	4.45	4.36
114	228	7.55	7.06	7.13	6.46	6.55	5.77	6.06	5.83	4.99	5.18	5.09

Table 3.8 – Realistic Monte-Carlo calculation results of the FWHM values [in MeV] of the low-energy (deeply bound) proton single particle levels covering the nuclear main shells $N_{\text{main}} = 0$ to 3 for ^{208}Pb and $_{114}$Fl super-heavy isotopes indicated.

Chapter 4

Detecting Model Instabilities and Stabilising Predictions of Modelling

In the first chapter of this document, we presented the arguments suggesting that a presence of parametric correlations within the mathematical model destabilises the results of the parameter optimisation procedures leading at the end to the loss of reliability of the model predictions. In such cases, a small variation of the input data may cause dramatic changes in the obtained results for the optimal parameters. Therefore, being able to detect and control the parametric correlations within the model is a prerequisite for possibly improving the predictive power of any theory.

> *In this Chapter we present a systematic overview of the realistic numerical calculations which employ Monte-Carlo techniques and allow for discovering the typical mechanisms and their relative importance – a kind of* who is who? *– in the creation of the parametric correlations and their role as modelling-destabilisation factors.*

In what follows we will also discuss a selection of our solutions based on a phenomenological but realistic nuclear mean field approach aiming at a systematic improvement of the *stochastic quality* of the parameter optimisation procedures and, as an implication, of the quality of the theoretical predictions.

4.1 Parametric Correlations

An undesired consequence of the presence of parametric correlations is that, depending on their precise form, they may turn the inverse problem into an ill-posed inverse problem, i.e. either the solution is not unique (if it exists at all) or it does not continuously change with the modification of the input sampling. In other words – in the best case, i.e., if a solution can be obtained at all – any small change in the input may cause a very strong variation in the final results. There exist various ways of detecting the ill-posedness and its 'degree of intensity'. In this section we will focus on the detection of the presence of parametric correlations and examine Monte-Carlo based methods of their elimination.

4.1.1 Detecting Ill-Posedness Using the S.V.D. Theorem

The Singular Value Decomposition (S.V.D.) theorem has been presented in Chapter 1 and will be used in what follows. To prepare the test-grounds we optimise the parameters of the traditional Woods-Saxon Hamiltonian, cf. Eq. (2.14) for a single nucleus: ^{208}Pb.

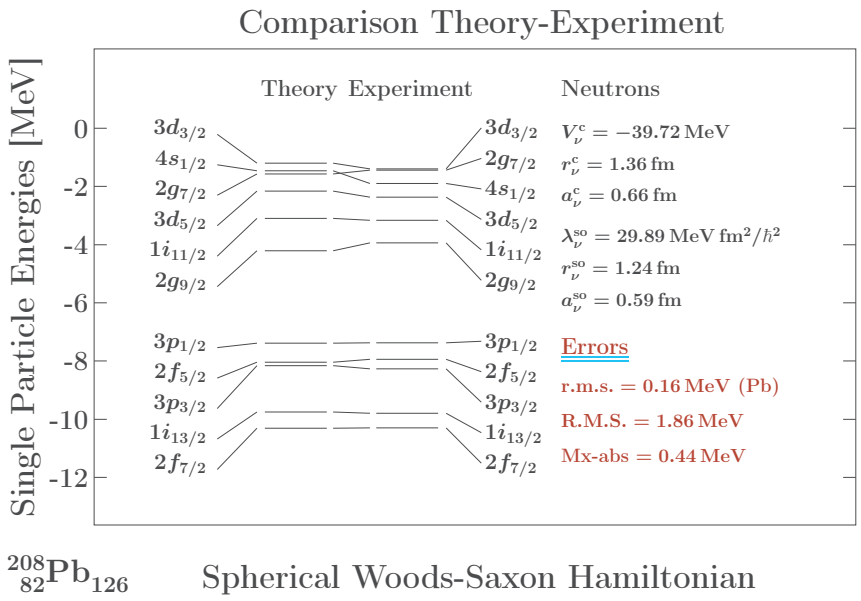

Figure 4.1 – Calculated ^{208}Pb neutron single particle energies, left column, resulting from the optimisation of parameters of the traditional-WS Hamiltonian. The experimental energies are given in the right column and the parameter values on the right side of the figure. One finds from top to bottom: r.m.s.-deviation from Eq. (3.30), R.M.S.-deviation from Eq. (3.32) and the maximum absolute error, Mx-abs. [Experimental data from Tables 2.2 and 2.3]

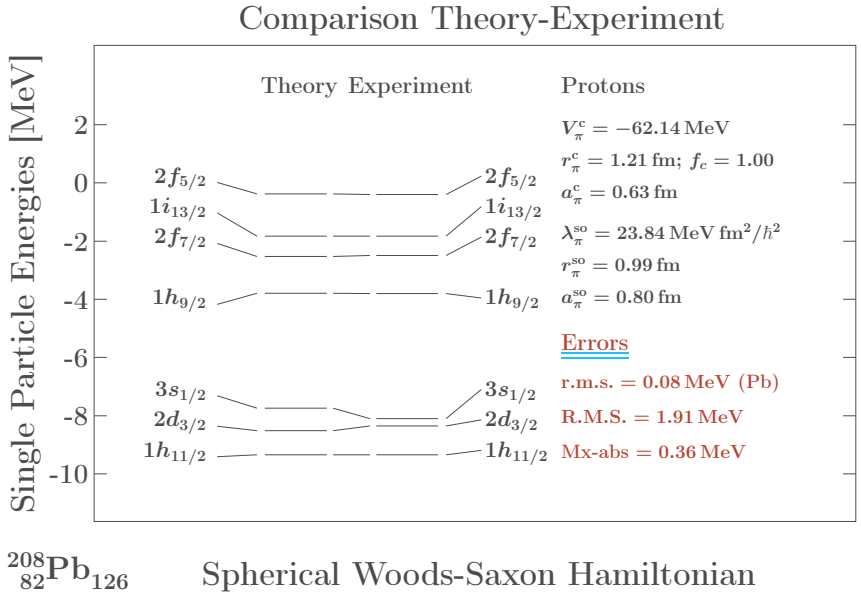

Figure 4.2 – The same as in Fig. 4.1 but for the protons.

Figures 4.1 and 4.2 show the results for the single nucleon energies in ^{208}Pb nucleus for neutrons and protons, respectively, together with the optimal-parameter values and various parameter-quality measures of the type of the root-mean-square deviation. Note the difference between the results in Figures 4.1 and 4.2 and those in Figure 3.6, where the parameters a^c and a^{so} were fixed. In the present case, Figures 4.1 and 4.2, all the six parameters are active in the χ^2-minimisation. We arrive at describing 11 neutron levels using 6 WS-parameters with the r.m.s.-deviation of 0.16 MeV and 7 proton levels with the r.m.s.-deviation of 0.08 MeV. However, the predictions for 8 doubly-spherical nuclei, Eq. (3.32), with the so-obtained parameters result in the R.M.S.-deviations not far from 2 MeV for both protons and neutrons, i.e. with the quality-estimate worse by more than an order of magnitude as compared to the single, central nucleus data. Such a big difference *may be* a sign of a 'pathological' behaviour of the model and/or its so-obtained 'optimal' parameters. It is therefore justified to ask why the description of the whole nuclear range looks so bad as compared to the one-nucleus description and what can one do to improve the performance of the modelling.

The first alarm-setting indicator of the ill-posedness (or ill-conditioning) in parameter-optimisation problems is the so-called condition number, which can be calculated using the Singular Value Decomposition theorem, cf. Eq. (1.53). We will employ this criterion separately for the neutrons and protons. The calculated condition number [recall: it is defined as the ratio of the biggest to the smallest eigen-value in the singular value decomposition] for the neutrons is

$$\mathrm{cond}(\mathcal{A})_\nu = \frac{312.99}{0.13} = 2.39 \times 10^3, \tag{4.1}$$

and for the protons

$$\mathrm{cond}(\mathcal{A})_\pi = \frac{505.76}{0.12} = 4.13 \times 10^3. \tag{4.2}$$

The results $\mathrm{cond}(\mathcal{A})_{\nu/\pi} \gtrsim 10^3$ tell us that our problem is indeed ill-posed [6, 12]. However, since these results do not tell us which parameters make our problem ill-conditioned, we will use the same Monte-Carlo techniques as in Chapter 3 to detect the parametric correlations and identify which parameters are correlated.

4.1.2 Detecting Parametric Correlations Using Pearson Matrix

In these exploratory simulations the experimental error-bars will be defined with the help of a single parameter σ_{exp} – fixed for all experimental levels. The dependence of the results on the a choice of this type will be tested later. We will begin tests for the presence/absence of parametric correlations, by employing the correlation matrix, Eq. (1.79) also referred to as Pearson matrix. We will show how the parametric-correlations depend on the actual σ_{exp} and on the size and type of the sampling in order to establish a quantitative link between the typical input to the inverse problem with the parameter optimisation output – in our framework of interest.

Sampling: ^{208}Pb Neutron Levels. We begin with the neutron levels and calculate the *Pearson correlation matrix* for the hypothesis $\sigma_{exp} = 600$ keV. Results in Tables 4.1 and 4.2 for the neutron and proton parameters, respectively, show that apart from the diagonal terms, only one non-diagonal matrix element in each table is close to 1, *viz.* the correlation coefficients (V^c, r^c) equal to 0.9902 for neutrons and 0.9705 for protons[1].

[1]Note that the correlation matrix is by construction symmetric.

It will be instructive to logically split the full (6×6) matrix in Tables 4.1 and 4.2 into four (symmetric) separate blocks which involve:

- Correlations between central-potential parameters alone;
- Correlations involving the spin-orbit potential parameters alone;
- Mixed correlations between the central-, and spin-orbit potential parameters.

	V_ν^c	r_ν^c	a_ν^c	λ_ν^{so}	r_ν^{so}	a_ν^{so}
V_ν^c	1.0000	0.9902	−0.0083	0.3786	0.3560	0.0726
r_ν^c	0.9902	1.0000	0.0401	0.3922	0.3602	0.0785
a_ν^c	−0.0083	0.0401	1.0000	0.2432	−0.2290	−0.1858
λ_ν^{so}	0.3786	0.3922	0.2432	1.0000	0.1157	0.4965
r_ν^{so}	0.3560	0.3602	−0.2290	0.1157	1.0000	0.1403
a_ν^{so}	0.0726	0.0785	−0.1858	0.4965	0.1403	1.0000

Table 4.1 – Correlation matrix between the neutron Hamiltonian parameters. Each Pearson matrix-element has been obtained using Eq. (1.70) from the Monte-Carlo simulations results, taking into account only the ^{208}Pb neutron levels and imposing $\sigma_{exp} = 600\,\text{keV}$.

	V_π^c	r_π^c	a_π^c	λ_π^{so}	r_π^{so}	a_π^{so}
V_π^c	1.0000	0.9705	0.1816	0.0017	0.1503	−0.0117
r_π^c	0.9705	1.0000	0.3888	0.0719	0.1382	−0.0194
a_π^c	0.1816	0.3888	1.0000	0.2895	0.0465	−0.1294
λ_π^{so}	0.0017	0.0719	0.2895	1.0000	0.5085	0.6100
r_π^{so}	0.1503	0.1382	0.0465	0.5085	1.0000	0.2469
a_π^{so}	−0.0117	−0.0194	−0.1294	0.6100	0.2469	1.0000

Table 4.2 – The same as in Table 4.1, but for the protons.

Observations and Discussion

1) In the 'central – central' block, only the potential depth and potential radius are strongly correlated, both for the neutrons and protons. The other non-diagonal matrix elements of this block are significantly smaller (close to zero) in the case of the neutrons.

In contrast, in the case of protons the radius and diffuseness parameters (r_π^c, a_π^c) are partially correlated in the present realisation of the modelling. This is most likely related to the presence of the Coulomb term, which in the present calculations was defined as the electrostatic potential generated by the uniform charge distribution and kept fixed without any adjustment. Such a term modifies rather strongly (and probably not in a very physical way) the effective diffusivity of the resulting final potential which is the sum of the nuclear and electrostatic contribution. An illustration of the corresponding geometrical relations involving the diffusivity effect will be shown later.

2) In the spin-orbit – spin-orbit block the protons and neutrons behave slightly differently. On the basis of the results in Table 4.1 one can deduce that the neutron spin-orbit potential parameters are not as strongly correlated as the central potential pair (V^c, r^c).

Indeed, the matrix elements involving the radius parameter $(\lambda_\nu^{so}, r_\nu^{so})$ and (r_ν^{so}, a_ν^{so}) are both close to 0.1, and only $(\lambda_\nu^{so}, a_\nu^{so})$ is close to 0.5 .

In the case of protons, all the three mentioned pair combinations lead to systematically bigger correlation coefficients. The third pair of this block $(\lambda_\nu^{so}, a_\nu^{so})$ deserves some extra comments. The corresponding values of the correlation coefficients are ≈ 0.5 for the neutrons and ≈ 0.6 for the protons. This correlation maybe expected and understood because of the form of the spin-orbit potential in Eq. (2.6). Indeed, calculating the derivative of the form-factor $v_{so}(r)$ analytically, one can easily see that the spin-orbit potential depends explicitly on the ratio (λ^{so}/a^{so}). It then follows that there must be an automatic compensation between variations of these two parameters during the process of minimisation implying their correlation.

3) In the 'non-diagonal central - spin-orbit' block we may observe that all the combinations lead to possibly only weakly correlated pairs with the absolute values of the Pearson matrix-elements all smaller than 0.4.

At this point, having analysed the results for the correlation matrix in Tables 4.1 and 4.2 one my be tempted to think that we know how the parameters of the Hamiltonian are correlated (de-correlated) and make the first conclusions. However, one should emphasise that the Pearson correlation-matrix coefficients, r_{ij}, contain the information only about the *linear* dependencies, which may exists between parameters, but not about other forms, cf. Figure 1.1. Therefore, it becomes important to continue with the two-dimensional correlation analysis. A preparatory discussion of the expected topological properties of such diagrams has been given in Chapter 1, where we introduced what we referred to as *dot-plots*.

4.2 Parametric Correlations and Monte-Carlo Method

Let us begin with a synthetic information about the illustrations of the Monte-Carlo simulations (the latter introduced earlier Chapter 1 and Chapter 3).

The Monte-Carlo results for all the possible correlations of central to central and spin-orbit to spin-orbit pairs of parameters are shown on Figures 4.3 - 4.14 for neutrons and protons. Each figure is composed of 4 different panels, showing the same correlation but for different values of σ_{exp}, defined as 50 keV, 200 keV, 400 keV and 600 keV. In this way one can oversee the evolution of the parametric correlations with increasing input error. Since the structure of the 'dot-plots' does not represent any universal/general pattern, in what follows we will proceed examining the results on the case-by-case basis.

4.2.1 Central-to-Central Potential Parameter-Correlations

Let us begin the discussion with the strongest correlations manifested by the relatively large values of the non-diagonal Pearson coefficients, $r_{ij} \sim 1$, in Tables 4.1 and 4.2, corresponding to the central potential depth, V^c-, and central potential radius, r^c- parameters. The corresponding dot-plots are shown in Figures 4.3 and 4.4 for neutrons and protons, respectively. Comparison clearly manifests that there is a quadratic ('parabolic') correlation between these two parameters. It has been demonstrated by a direct fit using the expression

$$r^c = \alpha \cdot (V^c)^2 + \beta \cdot V^c + \gamma \,. \tag{4.3}$$

Comparison of the results for different values of σ_{exp} shows that the parabolic correlations persist and the 'dot-plot lengths' of the obtained Monte-Carlo correlation curves increase with increasing σ_{exp}. Moreover, the Pearson coefficients denoted r_{xy} in the Figures remain nearly constant with $r_{xy} \approx 0.99$ for neutrons and $r_{xy} \approx 0.97$ for protons. This tells us that the presence of the correlation between V^c and r^c does not depend on the value of the experimental error.

Tables 4.3 and 4.4 present the values of the parabola coefficients after fitting according to Eq. (4.3). These numerical values correspond to the results presented graphically in Figures 4.3 and 4.4. Let us emphasise that except for some (insignificant) fluctuations, all the parabolas have approximately the same equation.

σ_{exp} [keV]	α_ν [fm Mev^{-2}]	β_ν [fm Mev^{-1}]	γ_ν [fm]
50	0.0003312	0.0471418	2.7147683
200	0.0004261	0.0546548	2.8635372
400	0.0004329	0.0553661	2.8814337
600	0.0004267	0.0549670	2.8757360

Table 4.3 – Neutrons: Fitted parabola-coefficients of Eq. (4.3) corresponding to the indicated values of σ_{exp}; for the graphical illustration, cf. Figure 4.3.

σ_{exp} [keV]	α_π [fm Mev^{-2}]	β_π [fm Mev^{-1}]	γ_π [fm]
50	0.0002467	0.0436343	2.9735560
200	0.0001917	0.0369053	2.7678581
400	0.0001684	0.0341338	2.6870053
600	0.0001971	0.0378265	2.8064431

Table 4.4 – Similar to Table 4.3 but for the protons.

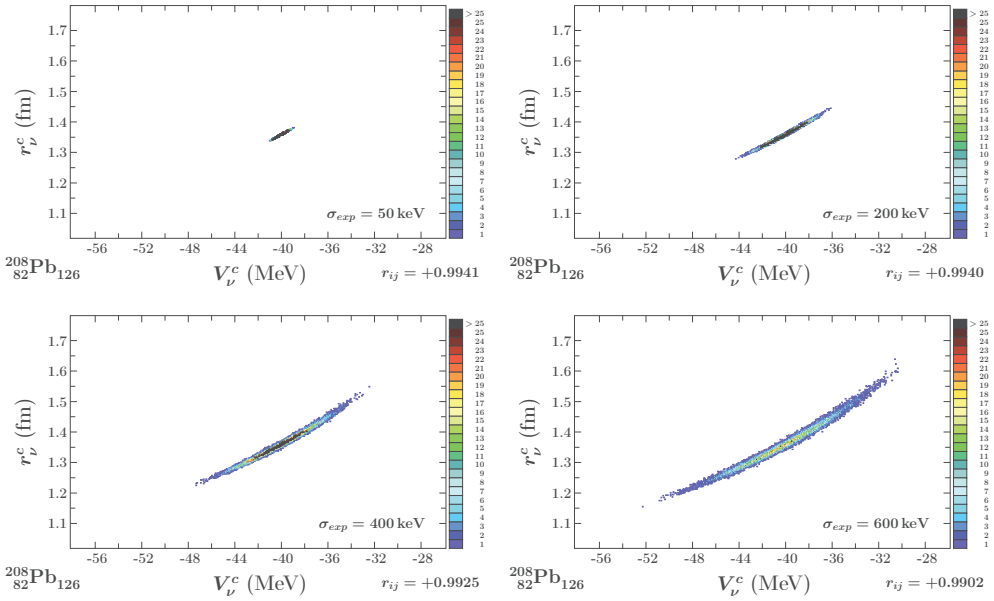

Figure 4.3 – Correlations between the neutron central potential depth parameter, V_ν^c, and the central potential radius parameter, r_ν^c, in ^{208}Pb, which turn out to be parabolic, see the text. As indicated in each panel: top left, $\sigma_{exp} = 50\,\mathrm{keV}$; top right $\sigma_{exp} = 200\,\mathrm{keV}$; bottom left $\sigma_{exp} = 400\,\mathrm{keV}$; bottom right $\sigma_{exp} = 600\,\mathrm{keV}$. Let us note that the Pearson coefficients r_{xy} shown at the bottom of each diagram stay approximately constant, independent of σ_{exp}.

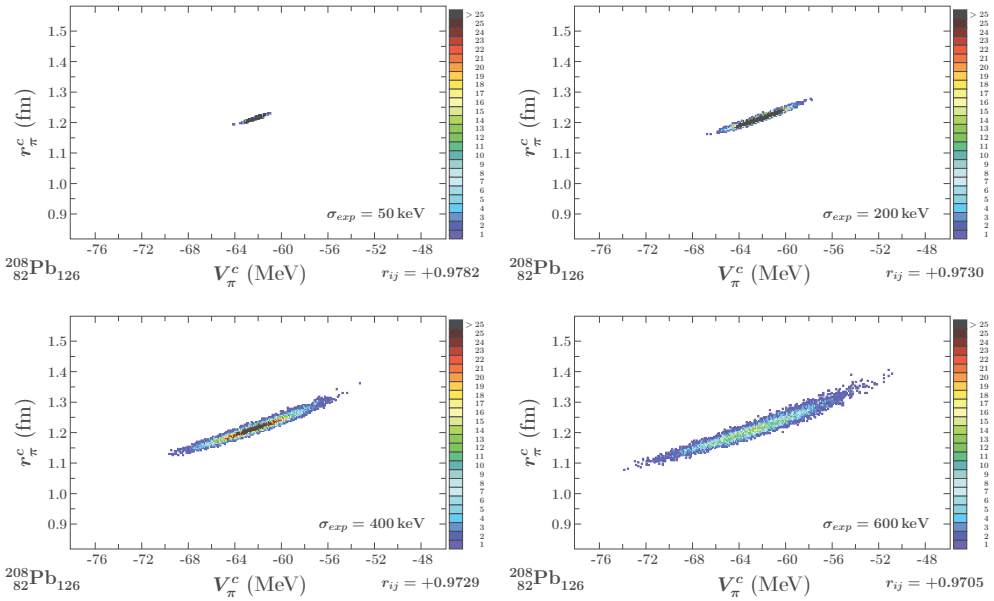

Figure 4.4 – The same as in Fig. 4.3 but for the protons in ^{208}Pb.

Figures 4.5 - 4.6 represent projections of the χ^2-minimisation results in the from of the 'dot-plots' onto the plane (V^c, a^c) for neutrons and protons. The fact that the shapes of the distributions manifest nearly radial symmetry together with the vanishing of the Pearson coefficient, suggests that the corresponding pairs of parameters can be considered uncorrelated.

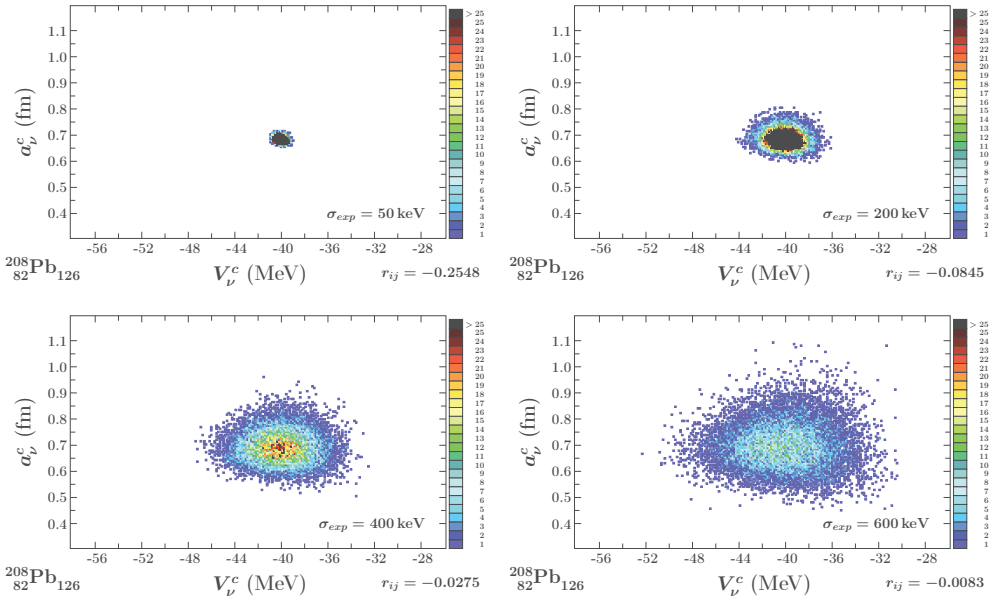

Figure 4.5 – Test for the parametric correlation between the neutron central depth V^c_ν and central diffuseness a^c_ν. Top left, $\sigma_{exp} = 50\,\mathrm{keV}$; top right $\sigma_{exp} = 200\,\mathrm{keV}$; bottom left $\sigma_{exp} = 400\,\mathrm{keV}$; bottom right $\sigma_{exp} = 600\,\mathrm{keV}$. Let us note that the r_{xy} coefficient changes with σ_{exp}, but its absolute value remains small. These results indicate the lack of parametric correlations between the two parameters indicated.

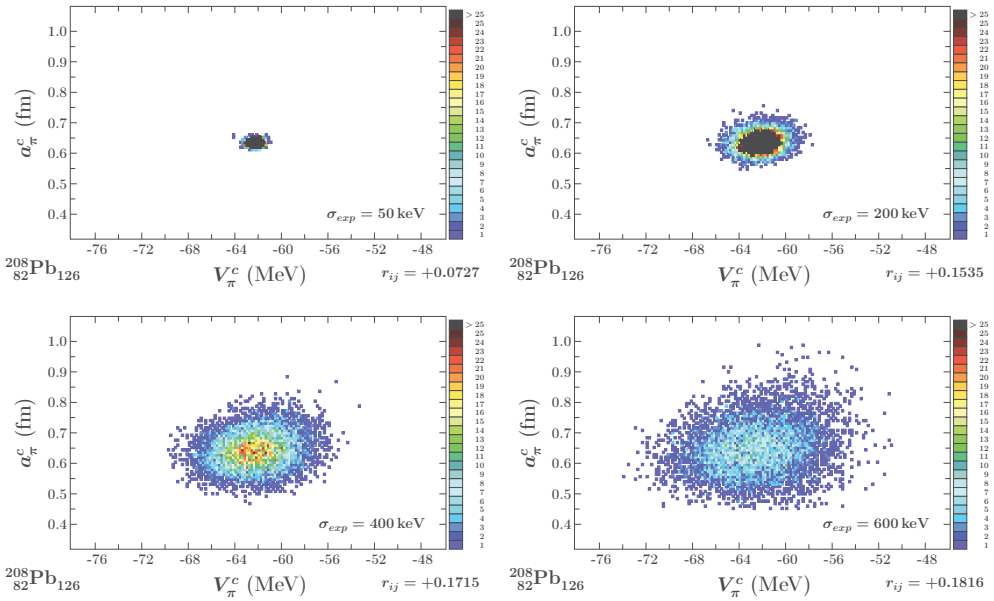

Figure 4.6 – Similar to Fig. 4.5 but for protons.

Figures 4.7 - 4.8 represent projections of the χ^2-minimisation results in the from of the 'dot-plots' onto the plane (r^c, a^c) for neutrons and protons. The fact that the Pearson coefficients are nearly zero and the shapes of the distributions manifest nearly radial symmetry, suggests that the corresponding pairs of parameters can be considered uncorrelated.

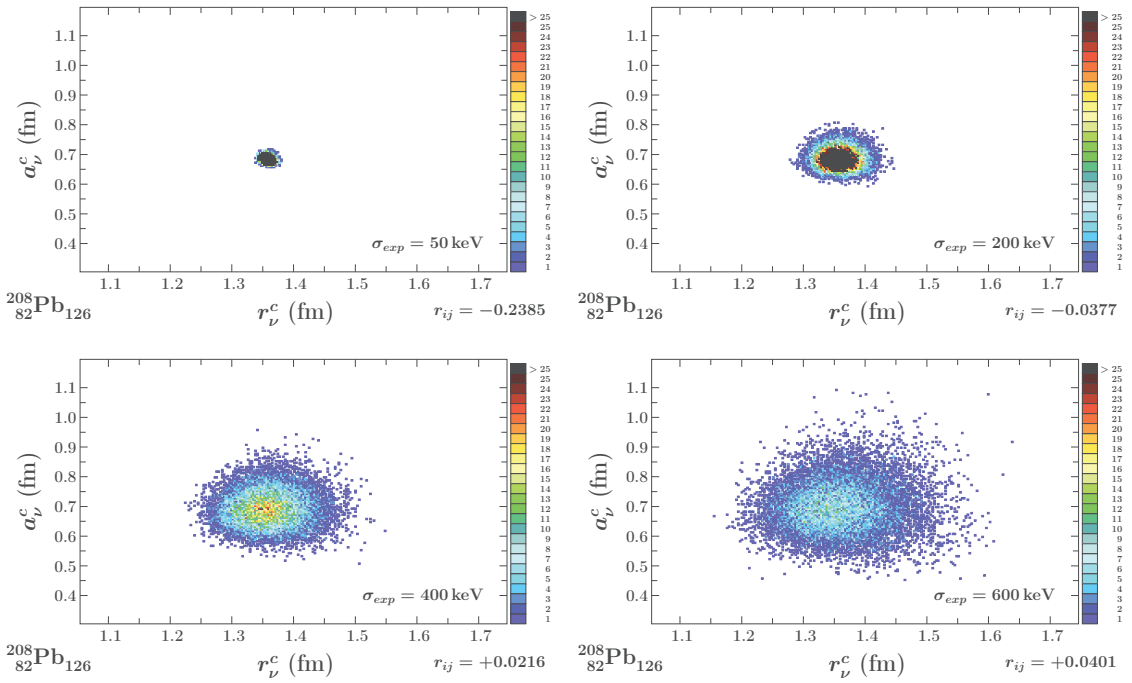

Figure 4.7 – Similar to the preceding one but for the neutron central radius r_ν^c and central diffuseness a_ν^c in ^{208}Pb. As before, the radial symmetry of the diagrams suggests that the parameters are uncorrelated and the small values of the Pearson coefficient confirm this.

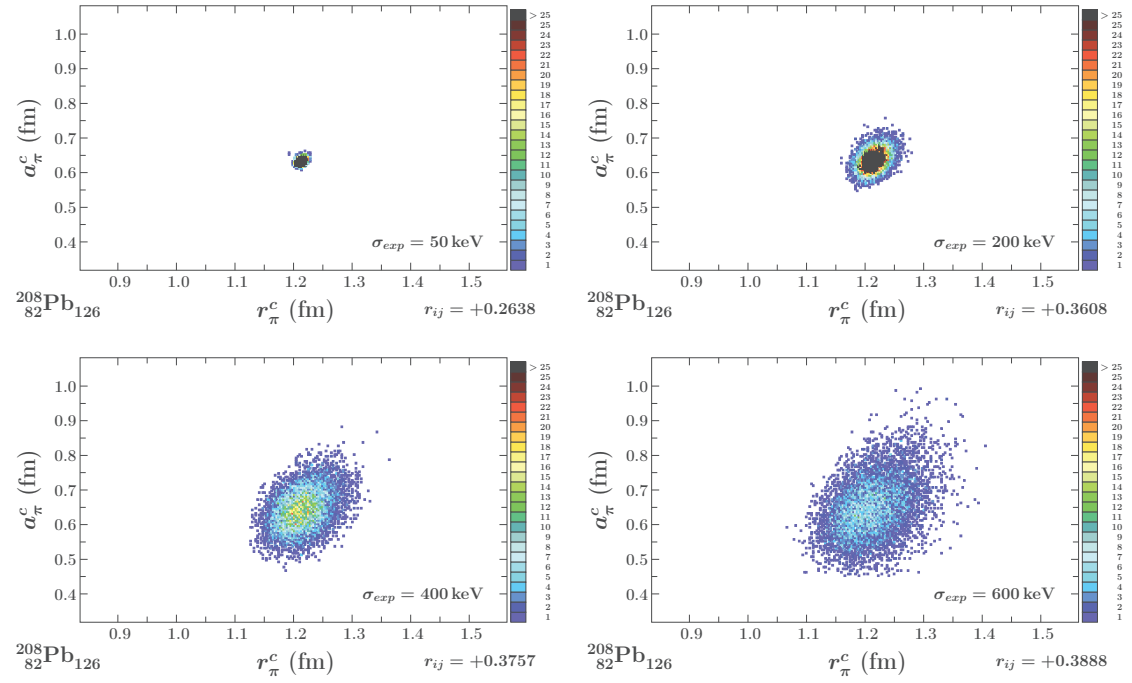

Figure 4.8 – Similar to that in Fig. 4.7 but for the protons.

4.2.2 Spin-Orbit – Spin-Orbit Parametric Correlations

Projections (λ^{so}, a^{so}). When analysing the correlation matrices in the preceding sections, we have noticed that the correlation of between (a^{so}, λ^{so}) can be justified analytically, because the spin-orbit potential depends explicitly on the fraction λ^{so}/a^{so}. Figures 4.9 and

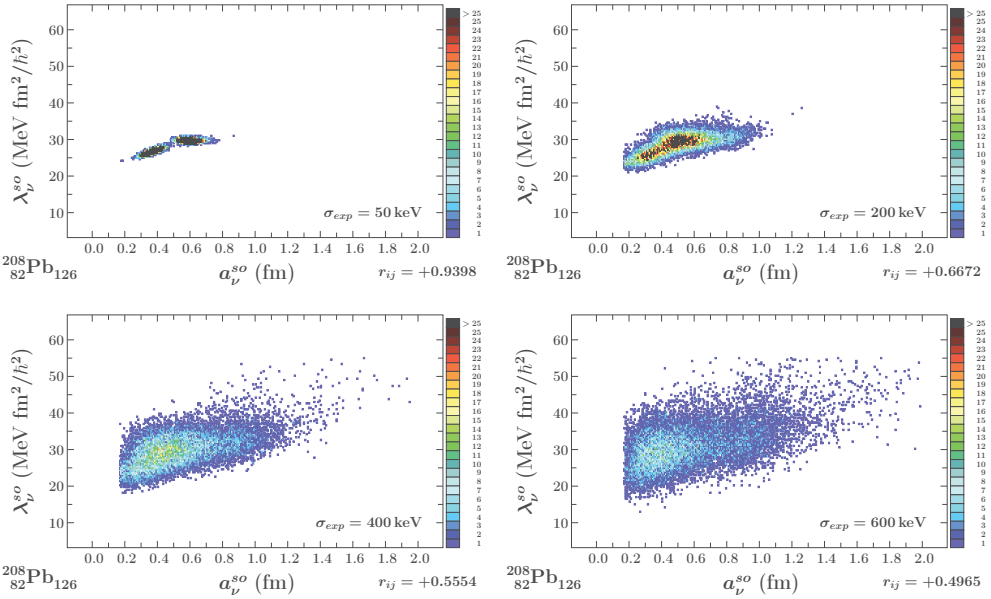

Figure 4.9 – Parametric correlation between the neutron spin-orbit diffuseness a_ν^{so} and spin-orbit strength λ_ν^{so} in ^{208}Pb. Top left, $\sigma_{exp} = 50$ keV; top right $\sigma_{exp} = 200$ keV; bottom left $\sigma_{exp} = 400$ keV; bottom right $\sigma_{exp} = 600$ keV.

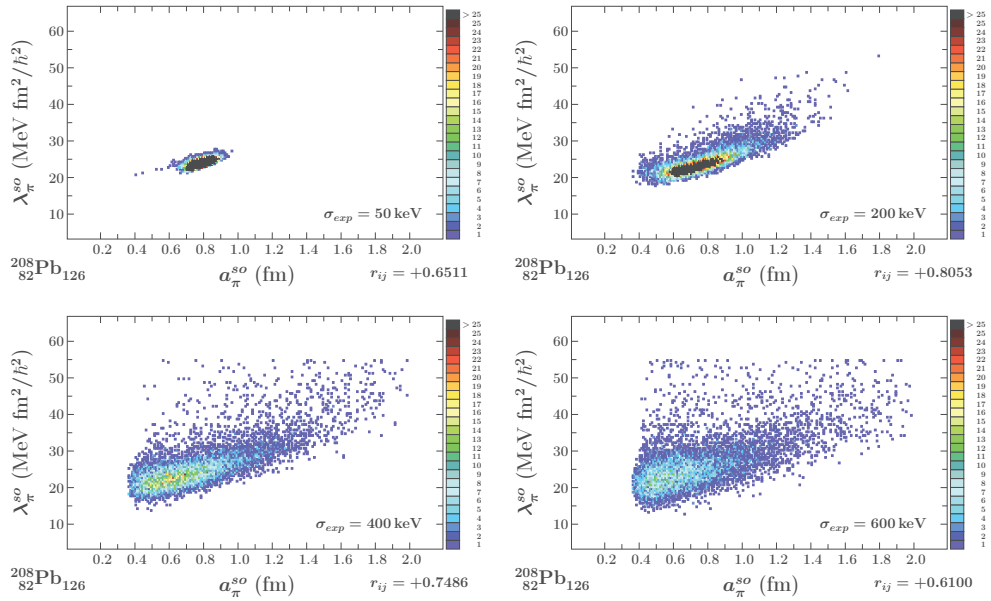

Figure 4.10 – Similar to the one in 4.9, but for the protons.

4.10 show the dot-plots for these correlations for neutrons and protons, respectively. Indeed, one may notice an approximate linear correlation tendency between these two parameters: As a^{so} increases, λ^{so} increases too. This tendency seems not to depend very much on the

value of σ_{exp}. For this reason, and analogously to the case of (V^c, r^c) projection-plots, in this case we fitted a straight line according to relation

$$\lambda^{so} = \mu\, a^{so} + \eta \tag{4.4}$$

whose coefficients can be found in Tables 4.5 and 4.6 for neutrons and protons, respectively.

σ_{exp} [keV]	μ_ν [MeV fm/$\hbar^2$]	η_ν [MeV fm^2/$\hbar^2$]
50	12.6003	22.2214
200	14.1110	22.0808
400	10.2562	24.3898
600	9.7807	25.5061

Table 4.5 – Fitted straight line coefficients of Eq. (4.4) for σ_{exp} indicated; here for the neutrons.

σ_{exp} [keV]	μ_π [MeV fm/$\hbar^2$]	η_π [MeV fm^2/$\hbar^2$]
50	13.7688	12.9248
200	13.5820	13.1520
400	16.3167	13.0680
600	14.2411	15.7030

Table 4.6 – Similar to Fig. 4.5 but for the protons.

Attention: In the case of the neutrons, a closer inspection of the diagrams (especially) for $\sigma_{exp} = 50$ keV and $\sigma_{exp} = 200$ keV, indicates that the points seem to center around two different values of a^{so}_ν. This suggests the necessity of further verifications. Therefore, one becomes even more motivated to test the characteristics of the projections of the distributions in question onto other projection planes and this strategy will be followed next.

Projections (r^{so}, a^{so}). Let us turn to the discussion of the (r^{so}, a^{so})-projections beginning with the neutrons. The distribution of points forms two 'bubbles' getting more and more

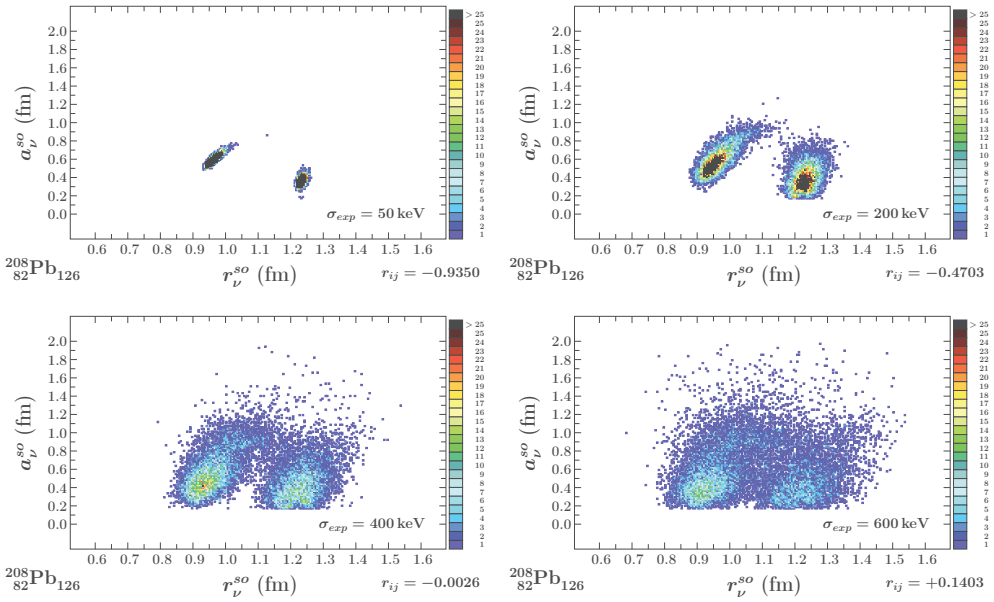

Figure 4.11 – Parametric correlation between the neutron spin-orbit radius, r_ν^{so}, and spin-orbit diffuseness, a_ν^{so}, in ^{208}Pb. Top left, $\sigma_{exp} = 50$ keV; top right $\sigma_{exp} = 200$ keV; bottom left $\sigma_{exp} = 400$ keV; bottom right $\sigma_{exp} = 600$ keV. Note a strong variation of Pearson coefficient r_{xy} with σ_{exp}. Observe the presence of two solutions manifested by the two-maximum structure of the diagrams. The first is referred to as compact (smaller value of the radius parameter) whereas the other one as non-compact (larger value of the radius parameter). Both are perfectly physical as discussed in the PhD project by N. Schunck, Ref. [47], who showed that the compact solution describes the rotational properties of nuclei systematically better.

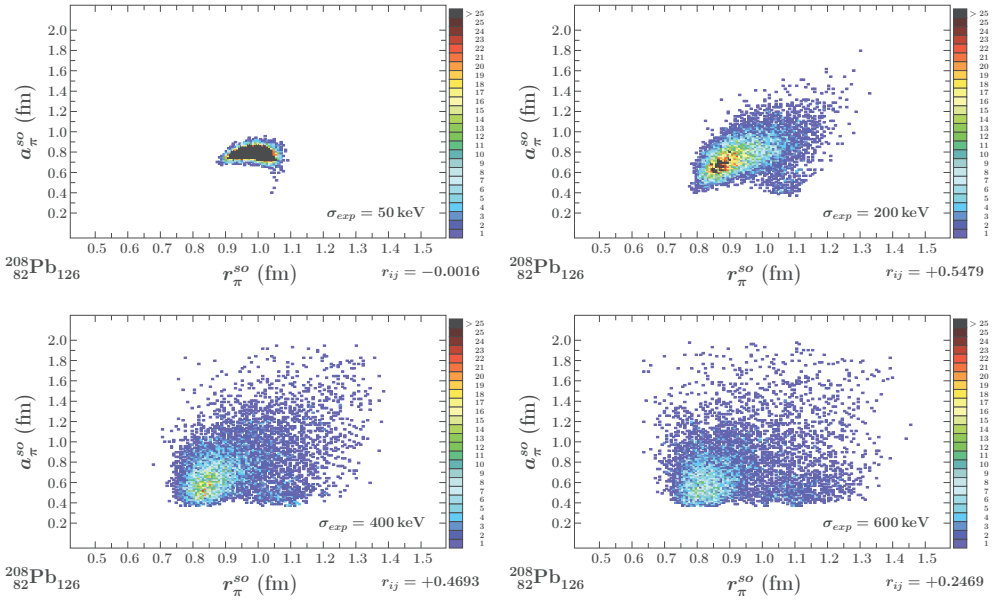

Figure 4.12 – Similar to the one in fig. 4.11, but for the protons.

separate when σ_{exp} decreases. It is instructive at this point to compare the values of the Pearson coefficient r_{xy}: For $\sigma_{exp} = 50$ keV, the Pearson coefficient is ~ -0.9, even though

the points do not form any clear-cut straight line correlation. It evolves towards zero when σ_{exp} increases.

A New Form of Parametric Correlations: Two Separate Distributions of Points. The non-linear correlation analysis seen from Figure 4.11 shows not only that the distribution is not linear but moreover, manifests a two-centre structure. The presence of the 'double-bubble' structure indicates that there exist two 'optimal solutions' for the spin-orbit radius. The smaller radius solution is called *compact configuration* and the bigger radius solution is called *non-compact configuration*. This effect has been already studied in the PhD Thesis of N. Schunk [47] and it was discussed and explained in terms of the specific form of the spin-orbit potential as proportional to the gradient of the Woods-Saxon potential, nearly constant inside of the nucleus, thus peaked at the surface.

In the case of protons, the clear 'double-bubble' structure is not present in our results. This has to do with the perturbations of the diffusivity properties of the full (nuclear plus Coulomb) potential via phenomenological and oversimplified representation of the Coulomb term, but we do not intend to examine this effects at this time. The more appropriate approach would be to generate the Coulomb potential using the calculated density distributions what goes beyond the scope of the present project.

Correlations (r^{so}, λ^{so}). Finally, let us turn to the (r^{so}, λ^{so})-projection in Figures 4.13 and 4.14, for neutrons and protons, respectively. In the case of the neutrons, the coexistence

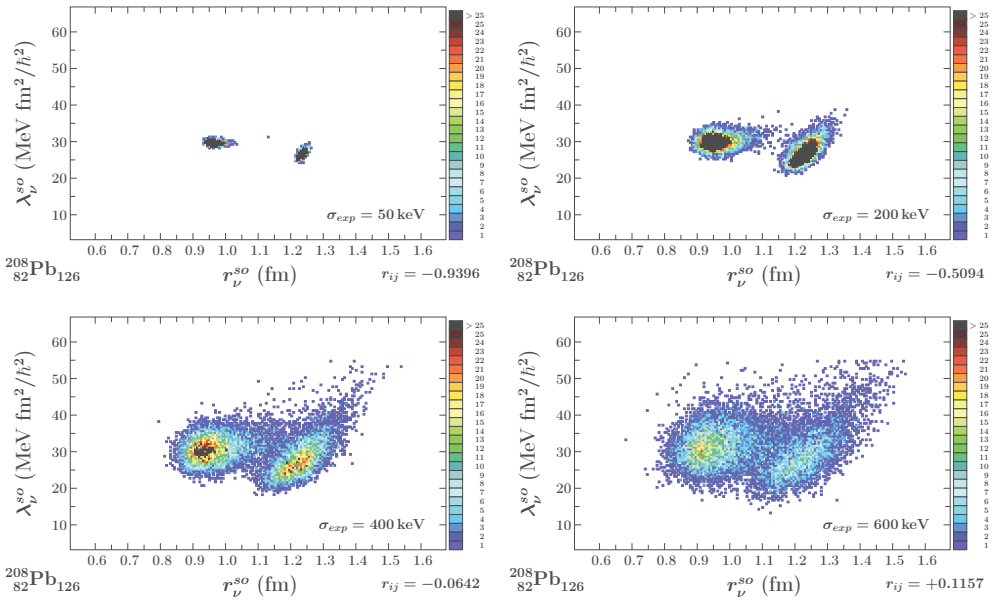

Figure 4.13 – Parametric correlation between the neutron spin-orbit radius r_ν^{so} and spin-orbit strength λ_ν^{so} in ^{208}Pb. Top left, $\sigma_{exp} = 50$ keV; top right $\sigma_{exp} = 200$ keV; bottom left $\sigma_{exp} = 400$ keV; bottom right $\sigma_{exp} = 600$ keV. Note again that the r_{xy} varies strongly with σ_{exp}.

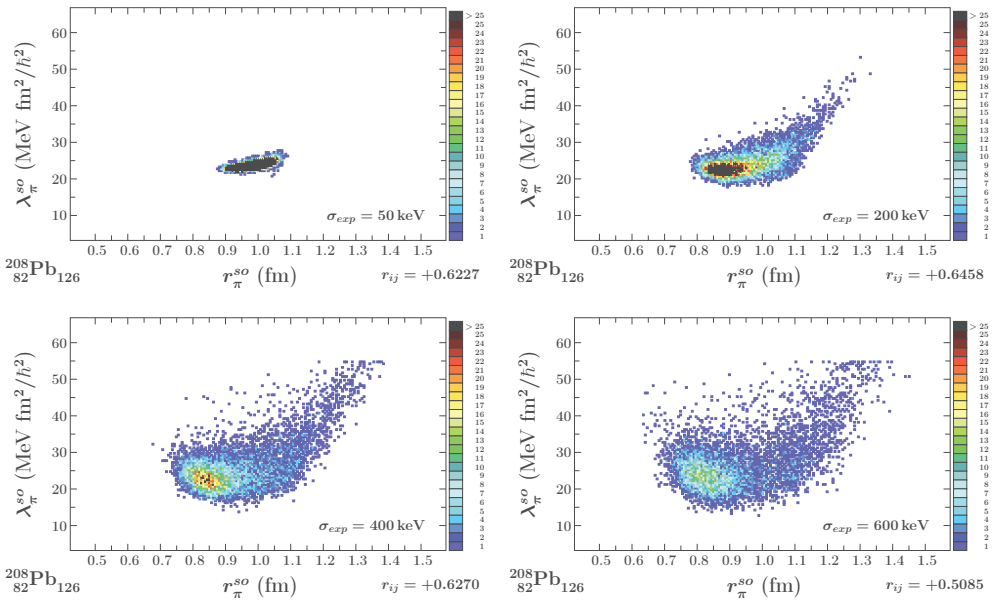

Figure 4.14 – Similar to the one in fig. 4.13, but for the protons.

between the spin-orbit compact and non-compact configurations in terms of r^{so} is again manifested. In the case of the two-centre distributions representing parametric correlation a 'phenomenological' way of 'removing correlations' will be to fix one of the two solutions, compact or non-compact, and treat them as two alternative solutions.

In the case of protons the clear-cut compact/non-compact coexistence is not present anymore. One may notice only some traces of it in the from of the tail seen at the limit of increasing r^{so} values.

4.3 Uncertainties of Nucleonic Energy Levels

In this section we will present the results of our Monte-Carlo study focussing on the uncertainties of the final predictions of the single-nucleon levels. We report on the results of eliminating the parametric correlations in order to examine the possible consequences in terms of the stabilisation of the result – equivalently: diminishing the final prediction uncertainties. We begin by presenting the uncertainty estimates in the presence of all the six parameters of the model treated as fully independent from one another when optimising the parametrisation. In other words we accept that some of them then may be correlated but we perform the calculations ignoring this mechanism at first.

This presentation will be followed by a discussion of the results of various variants of the predictions, each time removing – step by step – more and more parametric correlations.

4.3.1 Prediction-Uncertainties at Full Parametric Freedom

We begin by presenting the single-nucleon energy-uncertainty probability-distributions[2] for ^{208}Pb. They were obtained using the Monte-Carlo techniques in the preceding section when studying the properties of the Hamiltonian optimisation, cf. Figures 4.3 – 4.14.

Construction of the Uncertainty Probability Histograms. To construct the uncertainty probability histograms[3] also referred to as occurrence histograms, we divide the abscissa into small intervals and count the number of times that some value of our choice, for instance energy eigenvalue or the value of a given model-parameter, falls into so predefined interval. We obtain in this way a distribution in the form of a histogram (step-like function) which – after normalisation, cf. Eq. (1.56) – becomes uncertainty probability-distribution for a given nucleonic level or a model parameter. Finally, by fitting a continuous Gaussian distribution to each of the so obtained normalised histograms, we deduce the Gaussian characteristics μ and σ for each level or parameter.

[2] In what follows, the exact term – *single-nucleon energy-uncertainty probability-distributions* – will most of the time, when it does not cause ambiguities, be shortened to 'uncertainty distribution' or 'energy probability distribution'.

[3] Recall: These are the diagrams, which give a measure of the uncertainty of the model-quantities of our choice, e.g. energy eigen-values, and/or parameter uncertainty by associating with each value of the variable the corresponding occurrence probability. Since the normalised occurrence fractions lie in the interval [0,1], the maximum value 1 being excluded because of the finite errors of the input experimental data – no value is certain – what encourages us to use the term *uncertainty probability*.

The First Look at Uncertainty Probability Histograms: Neutrons. Figure 4.15 shows the Monte Carlo results for the probability distributions of the neutron single-particle energies in ^{208}Pb around the neutron occupation number $N = 126$. The Full Width at Half Maximum (FWHM) of each of those levels are given in Table 4.7.

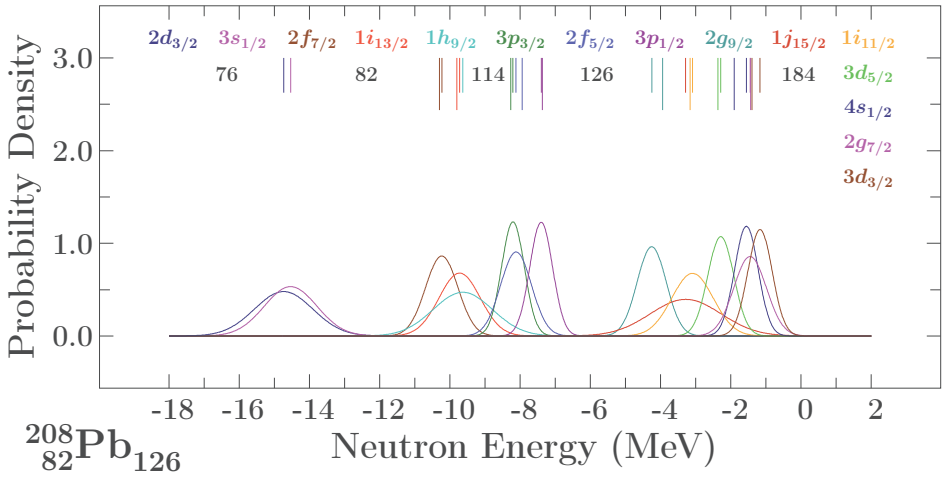

Figure 4.15 – Neutron-energy probability-density distributions for ^{208}Pb within the N_{main}=5 and $N_{\text{main}} = 6$ nuclear main-shells and $2d_{3/2}$ and $3s_{1/2}$ corresponding to $N_{\text{main}} = 4$. All the six Hamiltonian parameters are treated as independent from one another. The normalisation of the curves is such that the surface under each curve is equal to 1. The thick short vertical bars indicate the position of the distribution peaks. The thin long vertical bars represent the position of the experimental values for the known nuclear levels. The numbers between the short bars indicate the occupation. The assumed experimental error is $\sigma_{exp} = 600\,\text{keV}$ common for all the single-particle levels. The FWHM of each distribution can be found in Table 4.7. Observe the difference between the present illustration and the one in Figure 3.8, where the parameters were fitted to the *pseudo-experimental level energies*; in the present case the parameters are fitted to the experimental energies of ^{208}Pb.

		$N_{\text{main}} = 5$						$N_{\text{main}} = 6$						
Z	N	$2f_{7/2}$	$1i_{13/2}$	$1h_{9/2}$	$3p_{3/2}$	$2f_{5/2}$	$3p_{1/2}$	$2g_{9/2}$	$1j_{15/2}$	$1i_{11/2}$	$3d_{5/2}$	$4s_{1/2}$	$2g_{7/2}$	$3d_{3/2}$
82	126	1.09*	1.38*	1.99	0.76*	1.04*	0.77*	0.98*	2.37	1.39*	0.88*	0.79*	1.10*	0.82*
114	164	1.43	1.53	2.55	1.05	1.31	1.03	0.99	1.77	1.73	0.77	0.75	1.02	0.83
114	170	1.59	1.54	2.63	1.22	1.49	1.20	0.91	1.53	1.69	0.63	0.59	0.91	0.67
114	172	1.66	1.58	2.68	1.30	1.57	1.28	0.92	1.48	1.70	0.62	0.59	0.92	0.67
114	180	2.00	1.81	2.91	1.67	1.93	1.65	1.14	1.39	1.85	0.84	0.78	1.11	0.84
114	184	2.19	1.96	3.06	1.87	2.14	1.85	1.30	1.42	1.98	1.01	0.94	1.27	1.00
114	196	2.78	2.51	3.55	2.48	2.76	2.47	1.85	1.74	2.46	1.57	1.47	1.83	1.53
114	214	3.66	3.38	4.35	3.37	3.67	3.36	2.70	2.48	3.28	2.39	2.25	2.69	2.33
114	228	4.31	4.04	4.96	4.01	4.33	4.00	3.32	3.10	3.91	2.98	2.80	3.31	2.86

Table 4.7 – Realistic Monte-Carlo calculation results of the FWHM values [in MeV] of the neutron single particle levels within the nuclear main shells $N_{\text{main}} = 5$ and 6, for $_{114}$Fl super-heavy isotopes indicated. The ^{208}Pb results, first line, have been extracted from the curves in Figure 4.15. They show strong variations depending on the quantum characteristics of each individual state. The asterisk indicates that the corresponding level in ^{208}Pb is known experimentally and was taken for the parameter adjustment via χ^2-minimisation.

The First Look at the Uncertainty Probability Histograms: Protons. Figure 4.16 shows analogous results but for the case of protons, for the ^{208}Pb levels around the proton occupation number $Z = 82$. The Full Width at Half Maximum (FWHM) of each of those levels are given in Table 4.8.

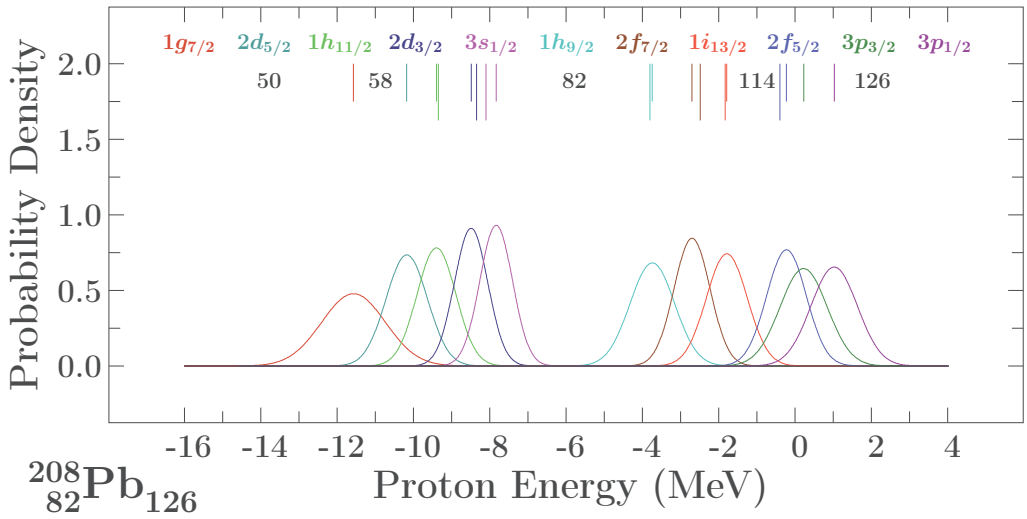

Figure 4.16 – Similar to Figure 4.15 but for the proton energy levels within the N_{main}=4 and $N_{\text{main}} = 5$ nuclear main-shells. The values of the FWHM of each distribution can be found in Table 4.8. Presented results correspond to the fit to the real experimental levels whereas those in the similar-looking Figure 3.9 were obtained using the pseudo-experimental data.

		$N_{\text{main}} = 4$					$N_{\text{main}} = 5$					
Z	N	$1g_{7/2}$	$2d_{5/2}$	$1h_{11/2}$	$2d_{3/2}$	$3s_{1/2}$	$1h_{9/2}$	$2f_{7/2}$	$1i_{13/2}$	$2f_{5/2}$	$3p_{3/2}$	$3p_{1/2}$
82	126	1.96	1.28	1.20*	1.03*	1.01*	1.38*	1.11*	1.26*	1.22*	1.46	1.43
114	164	1.82	1.14	1.24	0.99	0.95	1.38	1.10	1.20	1.21	1.40	1.41
114	170	2.02	1.34	1.37	1.11	1.06	1.33	0.96	1.02	0.98	1.20	1.17
114	172	2.10	1.43	1.44	1.18	1.13	1.35	0.96	0.99	0.94	1.17	1.11
114	180	2.49	1.82	1.79	1.56	1.50	1.57	1.10	1.07	0.95	1.08	1.03
114	184	2.70	2.04	1.98	1.77	1.71	1.74	1.25	1.20	1.06	1.14	1.08
114	196	3.37	2.71	2.61	2.46	2.37	2.36	1.82	1.73	1.59	1.55	1.48
114	214	4.38	3.69	3.55	3.48	3.37	3.37	2.76	2.65	2.55	2.40	2.35
114	228	5.12	4.42	4.25	4.23	4.10	4.14	3.47	3.35	3.28	3.09	3.05

Table 4.8 – The same as in table 4.7 but for the protons, covering the nuclear main shells $N_{\text{main}} = 4$ and 5, in $_{114}$Fl super-heavy isotopes indicated.

A Mini Summary

At this point we may attempt a first synthetic, semi-qualitative overview.

- Firstly, *on the average*, the uncertainties increase with increasing ℓ-quantum number of the level, however:
- Secondly – the *fluctuations* around this average trend are clearly visible, and:
- Thirdly, at this point only some symptoms of the mechanism can be signalled:

  > *Whenever the experimental information about a given level is* not *known, the uncertainty obtained via the Monte-Carlo testing seems to be bigger. Even though, "intuitively" one may consider this as "something to be expected", let us emphasise that there is no explicit mechanism (element in the algorithm) which could be identified as responsible for this type of correlations.*

  This trend will need to be verified later using better designed test-constructions.

- The results for the super-heavy nuclei given in the tables reveal a very quick increase in the uncertainties with an increase of the neutron number at the fixed proton number. However, the ℓ-dependence of the level widths shows its own tendencies.

4.3.2 Correlation: $r^c = f(V^c)$ – Its Impact on Uncertainties

After establishing the presence of parametric correlations between the central-depth and the central-radius parameters, which could be written in terms of a simple functional dependence of the form $r^c = f(V^c)$, happening to be parabolic, cf. Section 4.1.2, we will proceed to examining the consequences of its removal from the model. The parameter elimination in this case consists in expressing the central radius as a function of the central-depth $r^c = f(V^c)$ following Eq. (4.3) and Tables 4.3 and 4.4. In this way, r^c is no more considered as a minimisation parameter since its value is given by V^c, and instead of minimising the χ^2 over six parameters, we minimise it over five only, *viz.*:

$$\{V^c, a^c, \lambda^{so}, r^{so}, a^{so}\}_{\pi,\nu} \,. \tag{4.5}$$

We have re-run the Monte Carlo simulations under the above conditions with $\sigma_{exp} = 600\,\text{keV}$. The results for the neutrons and protons are summarised in Figures 4.17 - 4.19 and Tables 4.9 and 4.10.

Uncertainty Distributions for ^{208}Pb: Comparison for Neutron Levels. Let us observe, that for the low ℓ-values, comparison of the results in Tables 4.9 and 4.7 indicates systematically smaller width-values, when the parametric correlation is removed. For example for $3p_{3/2}$, after elimination, the width decreases more than 26%, from 0.76 MeV to 0.56 MeV. Similarly, in the case of levels $3p_{1/2}$, $2g_{9/2}$, $3d_{5/2}$, $4s_{1/2}$ and $3d_{3/2}$, the corresponding widths decrease by up to 43%. Concerning the big-ℓ levels we may note that,

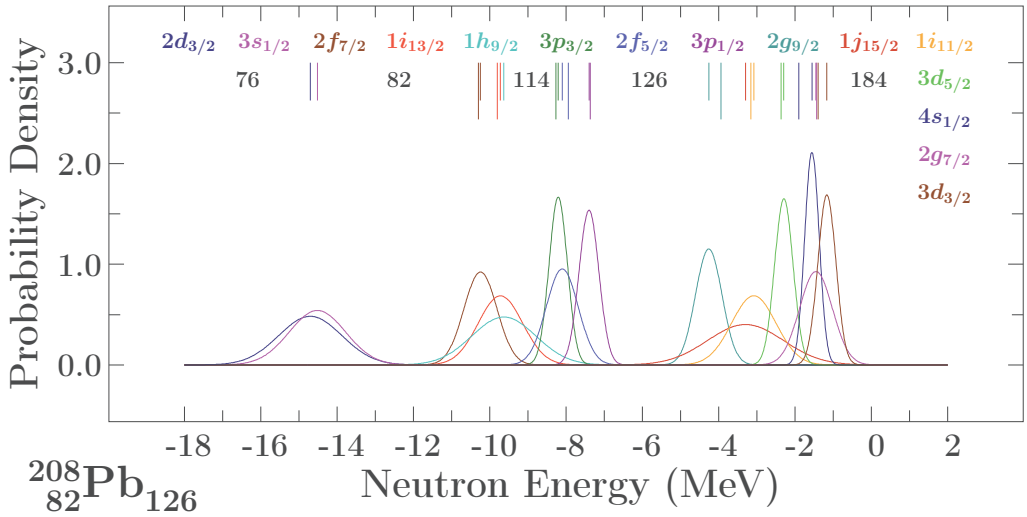

Figure 4.17 – Equivalent to Figure 4.15 but imposing $r^c_\nu = f(V^c_\nu)$, Eq. (4.3). The values of the FWHM of each distribution can be found in Table 4.7.

on the average, their original widths are preserved. This may possibly be due to the fact that these levels are more sensitive to the spin-orbit potential and the corresponding spin-orbit potential parameter correlations and therefore the changes in the central-potential parametric freedom has less impact on them.

Comparing Levels for $_{114}$Fl-Isotopes: Neutrons. Let us begin as before by analysing the low-ℓ levels but for heavier and heavier nuclei. Note that the widths of $3d_{5/2}$, $4s_{1/2}$ and $3d_{3/2}$ for $(Z = 114, N \leq 184)$ presented in Table 4.9 are systematically smaller as compared to the ones shown in Table 4.7, at least up to a neutron number $N = 184$. Emphasise

		$N_{\text{main}} = 5$						$N_{\text{main}} = 6$						
Z	N	$2f_{7/2}$	$1i_{13/2}$	$1h_{9/2}$	$3p_{3/2}$	$2f_{5/2}$	$3p_{1/2}$	$2g_{9/2}$	$1j_{15/2}$	$1i_{11/2}$	$3d_{5/2}$	$4s_{1/2}$	$2g_{7/2}$	$3d_{3/2}$
82	126	1.02*	1.37*	1.97	0.56*	0.99*	0.61*	0.82*	2.34	1.37*	0.57*	0.45*	1.01*	0.56*
114	164	1.41	1.51	2.54	0.99	1.29	0.98	0.92	1.77	1.71	0.59	0.52	0.99	0.69
114	170	1.57	1.53	2.65	1.15	1.45	1.14	0.81	1.53	1.67	0.35	0.24	0.86	0.48
114	172	1.64	1.56	2.70	1.24	1.53	1.22	0.82	1.47	1.69	0.34	0.20	0.87	0.47
114	180	1.99	1.80	2.96	1.62	1.91	1.61	1.06	1.38	1.86	0.62	0.51	1.07	0.69
114	184	2.18	1.96	3.11	1.83	2.12	1.82	1.23	1.42	2.00	0.83	0.73	1.24	0.88
114	196	2.80	2.52	3.63	2.48	2.77	2.47	1.82	1.76	2.51	1.47	1.37	1.83	1.48
114	214	3.72	3.42	4.47	3.41	3.71	3.40	2.72	2.55	3.37	2.36	2.22	2.73	2.34
114	228	4.40	4.09	5.12	4.08	4.39	4.07	3.37	3.20	4.03	2.99	2.80	3.36	2.90

Table 4.9 – Equivalent to Table 4.7 with which these results should be compared, but imposing $r^c_\nu = f(V^c_\nu)$. The ^{208}Pb neutron level distribution widths were extracted from the results in Figure 4.17.

that for $4s_{1/2}$ level, the distribution widths decreases for $N \leq 184$ in some cases by $\sim 63\%$ (!). The bigger-ℓ states have slightly improved, for example $2g_{9/2}$, whose distributions are $\sim 10\%$ narrower for $N \leq 184$.

> *Moreover: For states corresponding to $N > 184$, nearly no modifications can be signalled and this independently of the ℓ-value.*

Absolute Limits in Predicting: A New Manifestation of the NO-GO Property. Comparing the results in Table 4.9, we easily notice that the uncertainties of the levels grow extremely quickly with increasing neutron number in the super-heavy nuclei illustrated. In particular, for nuclei with $N > 184$, there is practically no difference in terms of uncertainty widths between Tables 4.7 and 4.9. In contrast to the lighter isotopes in which removing parametric correlations has lead to an improvement in terms of prediction uncertainties, for $N > 184$ the distribution peaks are extremely large and overlapping in an important manner. Figure 4.18 shows precisely this effect comparing the results obtained for ^{278}Fl and ^{342}Fl nuclei. Whereas for the case of ^{278}Fl uncertainty distributions can be still differentiated, for the case of ^{342}Fl distribution widths are very broad, making impossible to conclude something about the model prediction capacities at this zone.

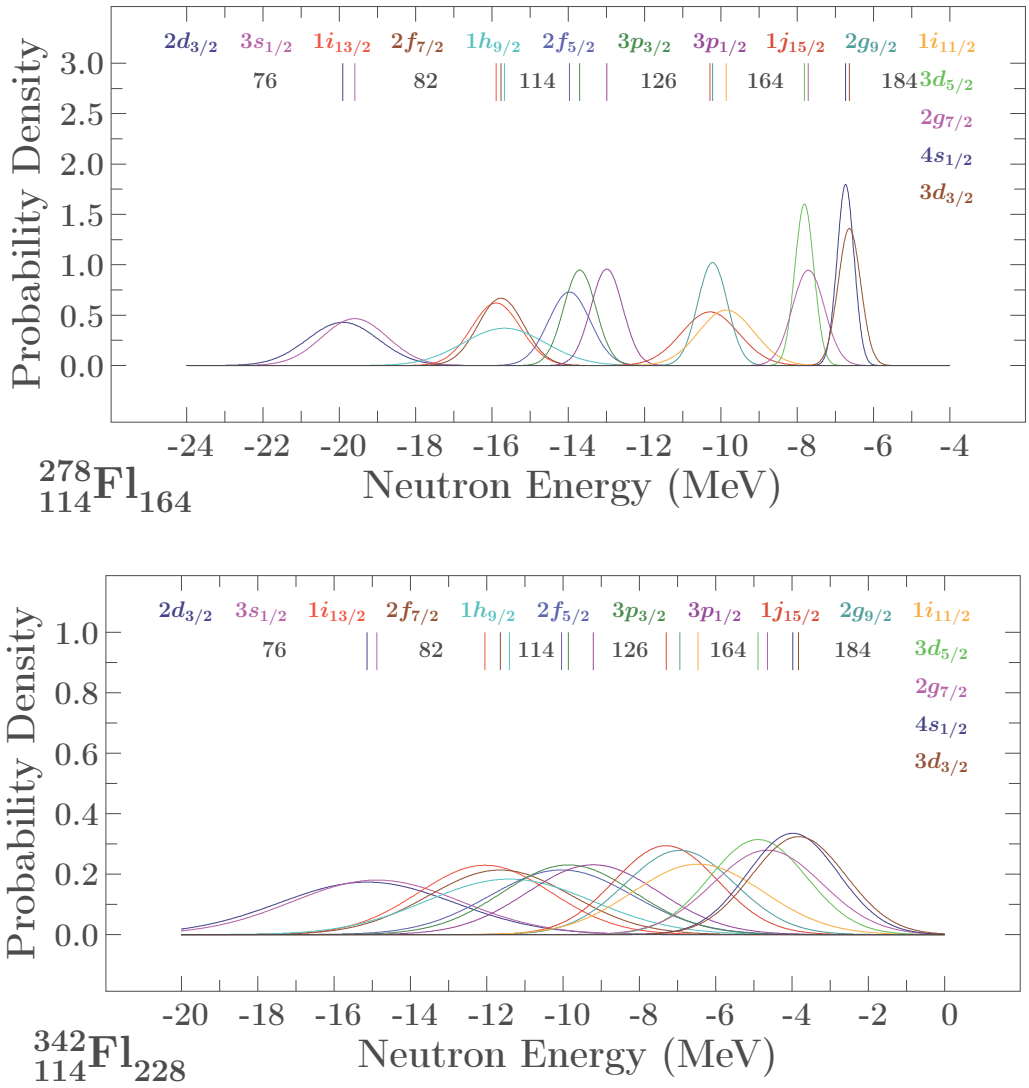

Figure 4.18 – Equivalent to Figure 4.17 but for the ^{278}Fl super-heavy nucleus (top) and ^{342}Fl (bottom). The values of the FWHM of each distribution can be found in Table 4.9. Let us emphasise that the distributions are extremely broad, especially for low-lying levels, with FWHM between 4 and 5 MeV in the N=5 shell.

Comparison for ^{208}Pb: Proton Levels. The results for the protons visible from Fig. 4.19 are similar to those for the neutrons discussed previously. In particular, for the low-ℓ levels we find systematically narrower uncertainty distributions. More specifically, for levels $3s_{1/2}$, $2f_{7/2}$, $2f_{5/2}$, $3p_{3/2}$ and $3p_{1/2}$ we find the uncertainties between 13% and 60% lower. Similarly to the neutron case – and as expected, the central-potential parameter correlation-removal has less impact on the high-ℓ orbital energies.

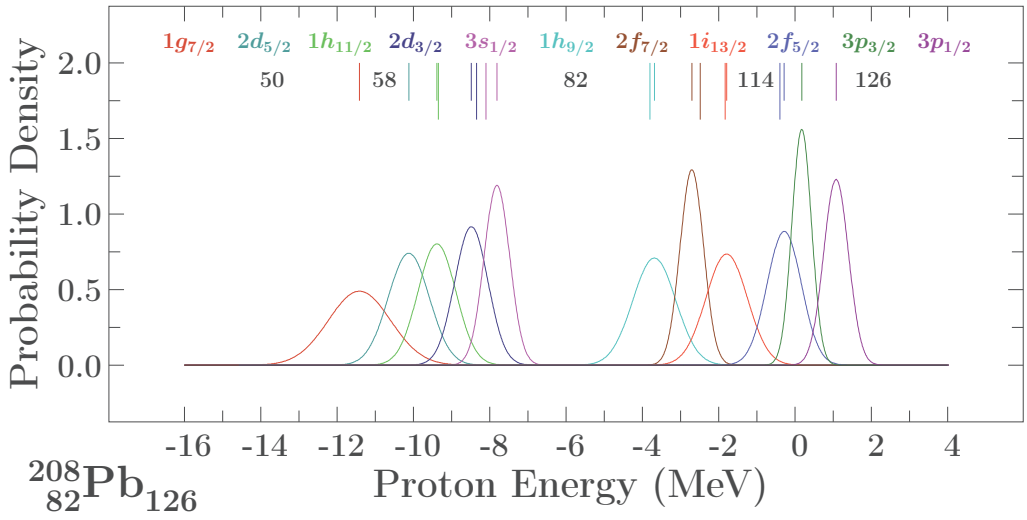

Figure 4.19 – Equivalent to Figure 4.16 but imposing $r^c_\pi = f(V^c_\pi)$, Eq. (4.3). The values of the FWHM of each distribution can be found in Table 4.10.

		$N_{\text{main}} = 4$					$N_{\text{main}} = 5$					
Z	N	$1g_{7/2}$	$2d_{5/2}$	$1h_{11/2}$	$2d_{3/2}$	$3s_{1/2}$	$1h_{9/2}$	$2f_{7/2}$	$1i_{13/2}$	$2f_{5/2}$	$3p_{3/2}$	$3p_{1/2}$
82	126	1.92	1.27	1.17*	1.03*	0.79*	1.32*	0.73*	1.28*	1.06*	0.60	0.76
114	164	1.79	1.10	1.19	0.95	0.73	1.36	0.83	1.20	1.12	0.86	0.99
114	170	2.00	1.34	1.34	1.11	0.91	1.31	0.68	0.99	0.86	0.48	0.64
114	172	2.08	1.43	1.42	1.19	1.01	1.34	0.69	0.96	0.81	0.39	0.54
114	180	2.49	1.87	1.80	1.62	1.46	1.57	0.95	1.03	0.83	0.40	0.44
114	184	2.72	2.10	2.01	1.86	1.70	1.75	1.15	1.16	0.97	0.61	0.60
114	196	3.42	2.81	2.68	2.59	2.44	2.40	1.82	1.73	1.59	1.32	1.28
114	214	4.47	3.85	3.68	3.66	3.50	3.46	2.84	2.71	2.63	2.37	2.33
114	228	5.26	4.61	4.42	4.45	4.28	4.26	3.60	3.45	3.42	3.15	3.10

Table 4.10 – Equivalent to Table 4.8 but imposing $r^c_\pi = f(V^c_\pi)$. The ^{208}Pb distributions were extracted from Figure 4.19.

Comparison for $_{114}$Fl-Isotopes: Proton Levels. In this case we find also that the widths decrease mainly in $3s_{1/2}$, $2f_{7/2}$, $2f_{5/2}$, $3p_{3/2}$ and $3p_{1/2}$ for $N \leq 184$ up to 66% in some cases (for example $3p_{3/2}$ with $N = 172$). Let us specifically notice that the uncertainty for $1i_{13/2}$, despite its big ℓ-value, decreases after central parametric removal and this by about $\sim 30\%$.

As in the case of neutrons, the NO-GO point is unavoidable.

4.3.3 Spin-Orbit Parametric Correlations and Uncertainties

In full analogy with the previous tests of the removal of correlations in the case of central potential we proceed to remove the spin-orbit parameter correlations with the help of the function $\lambda^{so} = g(a^{so})$, following Eq. (4.4) with the parameter values from Tables 4.5 and 4.6, for neutrons and protons, respectively. After verifications related to this particular couple of parameters we will turn to the effects specific to the dependence on the r^{so} parameter. We begin with the Monte-Carlo results for $\sigma_{exp} = 600$ keV.

Correlation $\boldsymbol{\lambda^{so} = g(a^{so})}$. In this case, since the strength-parameter of spin-orbit potential is no more considered as a minimisation variable, the χ^2 will be minimised over the following four parameters only

$$\{V^c, a^c, r^{so}, a^{so}\}_{\pi,\nu}. \tag{4.6}$$

Let us emphasise that in this case we removed two parametric correlations at the same time, namely $r^c = f(V^c)$ and $\lambda^{so} = g(a^{so})$. The results can be found in Tables 4.11 and 4.12 for neutrons and protons, respectively.

		$N_{\text{main}} = 5$						$N_{\text{main}} = 6$						
Z	N	$2f_{7/2}$	$1h_{9/2}$	$1i_{13/2}$	$3p_{3/2}$	$2f_{5/2}$	$3p_{1/2}$	$2g_{9/2}$	$1j_{15/2}$	$1i_{11/2}$	$3d_{5/2}$	$4s_{1/2}$	$2g_{7/2}$	$3d_{3/2}$
82	126	0.95*	1.82	1.31*	0.55*	0.76*	0.42*	0.42*	2.15	1.35*	0.38*	0.41*	0.85*	0.57*
114	164	1.34	2.44	1.61	1.00	1.21	0.92	0.86	1.76	1.75	0.58	0.56	0.93	0.68
114	170	1.44	2.46	1.58	1.09	1.30	0.98	0.73	1.51	1.67	0.33	0.25	0.67	0.33
114	172	1.50	2.49	1.60	1.15	1.36	1.04	0.75	1.45	1.66	0.31	0.20	0.64	0.25
114	180	1.82	2.66	1.79	1.50	1.68	1.39	1.01	1.36	1.76	0.62	0.49	0.77	0.43
114	184	2.01	2.79	1.94	1.70	1.88	1.59	1.20	1.41	1.87	0.84	0.71	0.93	0.64
114	196	2.62	3.26	2.48	2.34	2.50	2.23	1.82	1.79	2.33	1.50	1.34	1.52	1.28
114	214	3.55	4.08	3.38	3.27	3.43	3.16	2.75	2.61	3.17	2.40	2.20	2.42	2.15
114	228	4.24	4.72	4.07	3.94	4.11	3.82	3.42	3.27	3.83	3.03	2.79	3.07	2.76

Table 4.11 – Neutron case: Equivalent to Table 4.7, with which these results should be compared, but imposing $\lambda^{so}_\nu = g(a^{so}_\nu)$ in addition to $r^c_\nu = f(V^c_\nu)$.

		$N_{\text{main}} = 4$					$N_{\text{main}} = 5$					
Z	N	$1g_{7/2}$	$2d_{5/2}$	$1h_{11/2}$	$2d_{3/2}$	$3s_{1/2}$	$1h_{9/2}$	$2f_{7/2}$	$1i_{13/2}$	$2f_{5/2}$	$3p_{3/2}$	$3p_{1/2}$
82	126	2.09	1.43	1.15*	1.04*	0.89*	1.27*	0.70*	1.22*	0.92*	0.63	0.77
114	164	1.93	1.21	1.17	0.93	0.76	1.34	0.83	1.22	1.05	0.89	0.99
114	170	2.22	1.51	1.35	1.15	1.01	1.32	0.69	1.01	0.74	0.49	0.59
114	172	2.33	1.62	1.43	1.25	1.13	1.35	0.71	0.98	0.67	0.40	0.47
114	180	2.80	2.12	1.86	1.73	1.63	1.63	1.04	1.08	0.76	0.42	0.36
114	184	3.04	2.37	2.10	1.99	1.89	1.83	1.27	1.24	0.93	0.65	0.56
114	196	3.79	3.14	2.84	2.77	2.68	2.52	2.01	1.89	1.61	1.41	1.30
114	214	4.89	4.26	3.94	3.91	3.82	3.62	3.11	2.96	2.70	2.53	2.42
114	228	5.70	5.07	4.76	4.74	4.65	4.45	3.93	3.77	3.52	3.35	3.24

Table 4.12 – Similar to that in Table 4.11 but for the protons.

Correlation $\lambda^{so} = g(a^{so})$ – Neutrons: Observations and Discussion

Comparison for ^{208}Pb: Neutron Levels. Comparing the results of Table 4.11 with the ones in Table 4.9 we note that the uncertainty widths indeed decreased for some levels. This is mainly the case for $2f_{5/2}$, $3p_{3/2}$, $2g_{9/2}$, $3d_{5/2}$ and $2g_{7/2}$ orbitals. However, big-ℓ orbitals are almost not impacted by the removal of this particular parametric correlation. At this point we should recall that there still exists yet another, third parametric correlation which have been recognised in the form of two-centre correlation distributions nicknamed compact-vs.-non-compact spin-orbit solutions – and the removal of this one was not yet considered.

Comparison for $_{114}$Fl-isotopes: Neutron Levels. Concerning the results for these super-heavy elements, no major changes can be noticed as compared to the results in Table 4.9. In this case, only $2g_{7/2}$ and $3d_{3/2}$ orbitals seem to have been impacted by the parameter removal and once again the *NO-GO property* seems to be present for $N > 184$.

Correlation $\lambda^{so} = g(a^{so})$ – Protons: Observations and Discussion

Comparison for ^{208}Pb and $_{114}$Fl-isotopes: Proton Levels. In this case, it will be instructive to compare the results for ^{208}Pb and $_{114}$Fl at the same time. Results for the protons in Table 4.12 do not seem very encouraging. All the widths increased as compared to the results in Table 4.10. One may associate this effect with the fact, that the presence of the Coulomb potential influences significantly the shape of the WS central potential and in particular the effective diffusivity thereof.

Another difference between the neutrons and protons can be associated with the fact that we know experimentally the energies of 11 orbitals in the first case and only 7 in the second. Since we discovered empirically, as discussed earlier, that the level widths for the orbitals whose energies are not known experimentally have a tendency to be broader – some systematic effect of worsening in terms of the level widths in the protons is to be expected.

4.3.4 Comments – Diffusivity of the Central Potentials: ν-vs.-π

Figure 4.20 shows separately the profile of the WS-central and electrostatic potentials for the protons (green and purple solid lines, respectively), together with their sum (red solid line) which is to be compared with the neutron WS-central potential (blue). Large differences between the neutron (blue line) and the proton (red line) potentials visible from the right panel deserve noticing. They show that the proton-potential diffuseness-parameter should be systematically much bigger in order to provide finally similar profiles for the protons and neutrons – wherefrom an extra systematic impact.

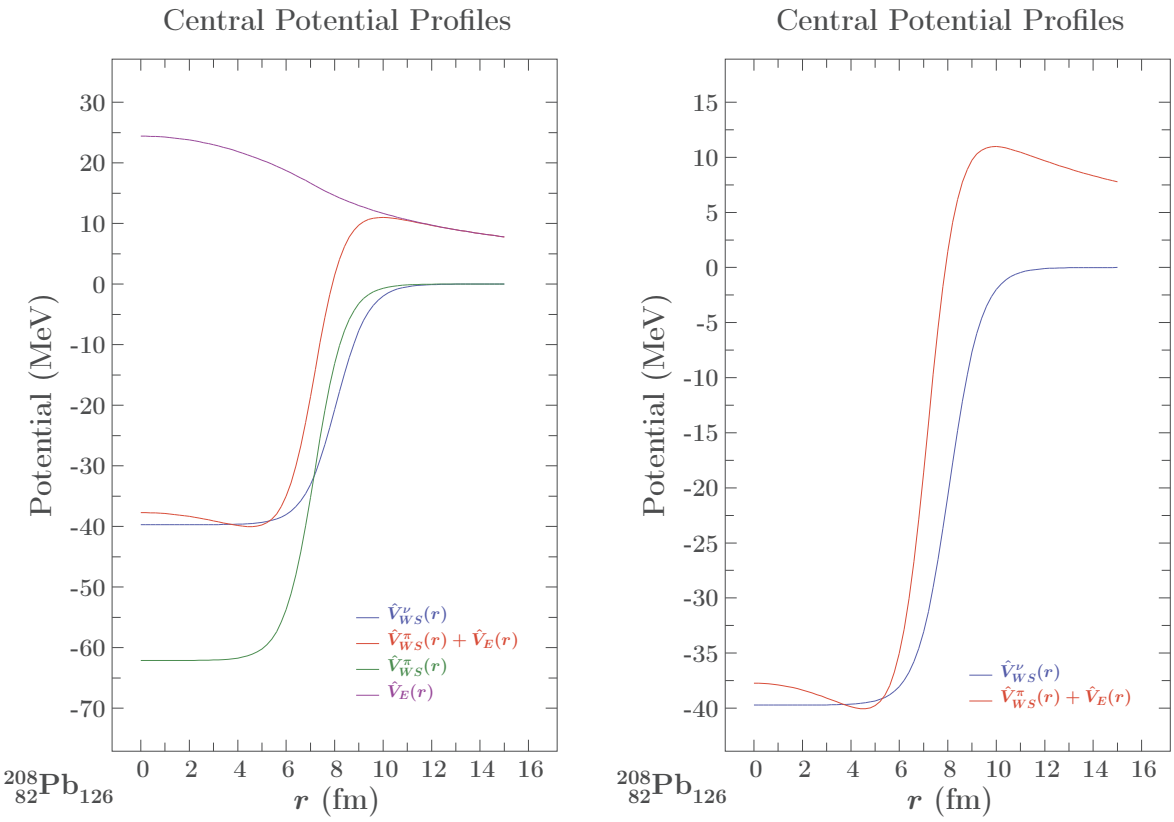

Figure 4.20 – Potential profiles as functions of r. Blue and green lines represent the Woods-Saxon central potential, cf. Eq. (2.4), for neutrons and protons, respectively. Purple line represents the Coulomb (electrostatic) potential for protons, cf. Eq.(2.10). Red curves represent the sum of the WS central potential and the electrostatic contribution for protons. Right panel is just an expansion on the y-axis of the left one. The parameter values used to obtain them come from Figures 4.1 and 4.2.

This clearly indicates that the Coulomb radius should be treated as an independent parameter, but it was not our priority at this time to enter this issue as commented earlier.

4.3.5 Correlation in the Form of Two-Center Distribution

When eliminating the parametric correlations as discussed so far we were confronted with the simplest possible position of the problem: We had the correlations in the 'one-to-one' functional form in terms of two couples of parameters, i.e. either $r^c = f(V^c)$ for the central-, or $\lambda^{so} = g(a^{so})$ for the spin-orbit potentials. However, the correlations involving parameters r^{so} and $\lambda^{\rm so}$ have a different structure of 'double-bubble bi-dimensional distributions' and cannot be treated in the same way. In this sense we encounter a new situation: parametric correlations which cannot be represented in a 'classical form' of the type $y = f(x)$ since the correlations are represented by two distributions centred around two distant points: Here in the (a^{so}, r^{so})-plane. Following the results in Figures 4.11-4.14 we can define the couples $(a^{so}, r^{so})_{\rm comp.}$ and $(a^{so}, r^{so})_{\rm non-comp.}$, whereas from Eq. (4.4) we determine in addition $\lambda^{so}_{\rm comp.}$ and $\lambda^{so}_{\rm non-comp.}$. The final combinations are given in Table 4.13.

Type/name	r^{so}_ν [fm]	λ^{so}_ν [MeV fm$^2/\hbar^2$]	a^{so}_ν [fm]
compact	0.93	30.0	0.46
non-compact	1.22	28.0	0.25

Table 4.13 – Compact and non-compact solutions for neutron spin-orbit parameters obtained from the Monte-Carlo results of Figures 4.11-4.14.

We have re-run the Monte-Carlo simulations two more times for the neutrons:

- Fixing the three spin-orbit parameters to their compact solution, and
- Fixing the three spin-orbit parameters to their non-compact solution.

Under these conditions, the final minimisation parameters are:

$$\{V^c, a^c\}_\nu. \tag{4.7}$$

In the next section we will discuss the results of the full parameter elimination taking into account the just presented two centre correlations in their 'compact' and 'non-compact' configurations.

4.4 Full Elimination of Parametric Correlations

In this section we discuss the effects of the complete removal of all the parametric correlations detected in the studied Hamiltonian. We begin by analysing the results for ^{208}Pb, extending the discussion for the super-heavy $_{114}$Fl-isotopes in the second step.

4.4.1 Monte Carlo Results for ^{208}Pb: Neutrons

In what follows we will present the results of the consecutive, step-by-step parametric correlation removal by testing the removal's impact on the neutron levels in ^{208}Pb. The results will be presented in the form of a series of tables, which will serve as the basis for comparisons. The structure of the tables is as follows:

- Row no. 1: Results of the Monte Carlo calculations with all the 6 parameters of the Hamiltonian considered independent and thus minimising the χ^2 in the full 6-dimensional space;
- Row no. 2: We impose $r^c_\nu = f(V^c_\nu)$ thus eliminating the central-potential radius-parameter from the minimisation which is performed in this case in a 5-dimensional subspace of the original space;
- Row no. 3: We keep the preceding condition activated and add an extra one by imposing $\lambda^{so}_\nu = g(a^{so}_\nu)$, in which case the minimisation is performed in the 4-dimensional space spanned by the remaining parameters;
- Row no. 4: We keep both preceding conditions simultaneously activated and add the first $(r^{\rm so}, \lambda^{\rm so})_{\max_{\rm left}}$ constraint from the 'double-bubble' distribution (compact solution); now, since $\lambda^{\rm so}$ is a function of $a^{\rm so}$ the χ^2 is minimised in a 2-dimensional space only;
- Row no. 5: The same as 4, but fixing the constraint as $(r^{\rm so}, \lambda^{\rm so})_{\max_{\rm right}}$ (non-compact solution).

Table 4.14 shows the ^{208}Pb results for the neutron levels around the $N = 126$ shell closure. In the present test we consider the levels which are in majority known experimentally – except for two; those known are marked with the asterisks. Results indicate that the uncertainty-widths decrease systematically for the big majority of levels presented in this Table (except for $2g_{9/2}$ and $4s_{1/2}$), down to the 'compact constraint', line no. 4. One may notice that whereas the widths of the levels corresponding to small ℓ-values decrease approximately by a factor of two, the similar variation associated with the higher ℓ-levels is much smaller – yet strictly speaking no general rule has been established.

Comparison of the results in the last two rows indicates strong irregularities for nearly a half of the considered levels, but the root-mean-square deviations remain nearly unchanged and always below 20 keV. The results for the two experimentally unknown levels in Table 4.14, i.e. $1h_{9/2}$ and $1j_{15/2}$, seem very encouraging: their uncertainty widths decrease by more than 50% (!) – a signal of a significant improvement of the predictive power.

Let us observe that the differences between the compact and the non-compact variants are important and far from systematic. This implies that the mechanism in question should be studied more in detail e.g. when extending the number of nuclei for which the present analysis is performed. Let us remark in passing that the two maxima of the 'double-bubble' structure correspond to two local χ^2-minima as tested in the PhD project of B. Szpak [25]; thus the presence of such two solutions can be seen as an opportunity to be explored especially when richer experimental information will allow for more advanced tests on the r.m.s. and R.M.S. level.

$N_{\rm main}=5$						$N_{\rm main}=6$								
$\mathbf{2f_{7/2}*}$	$\mathbf{1i_{13/2}*}$	$\mathbf{1h_{9/2}}$	$\mathbf{3p_{3/2}*}$	$\mathbf{2f_{5/2}*}$	$\mathbf{3p_{1/2}*}$	$\mathbf{2g_{9/2}*}$	$\mathbf{1j_{15/2}}$	$\mathbf{1i_{11/2}*}$	$\mathbf{3d_{5/2}*}$	$\mathbf{4s_{1/2}*}$	$\mathbf{2g_{7/2}*}$	$\mathbf{3d_{3/2}*}$	r.m.s.	Inv
1.09	1.38	1.99	0.76	1.04	0.77	0.98	2.39	1.39	0.88	0.79	1.13	0.83	0.16	1
1.02	1.37	1.97	0.56	0.99	0.61	0.82	2.35	1.37	0.57	0.45	1.02	0.56	0.16	0
0.95	1.31	1.82	0.55	0.76	0.42	0.42	2.15	1.35	0.38	0.41	0.85	0.57	0.16	0
0.50	1.18	0.96	0.28	0.54	0.36	0.44	0.98	1.34	0.32	0.40	0.09	0.38	0.18	0
0.79	1.27	1.85	0.56	0.41	0.10	0.25	1.88	1.02	0.26	0.41	0.98	0.72	0.29	0

Table 4.14 – The FWHM values [in MeV] associated with the neutron single particle uncertainty distributions for the main shells $N_{\rm main}=5$ and 6 in ^{208}Pb. The resulting r.m.s.-deviations [in MeV], cf. Eq. (3.30), are given in the last but 1 column. The last column controls the level ordering: except for the first variant, line no. 1, where one level inversion is reported, in all other cases all the theory levels respect the experimental order. The content of each row has been defined in the list of 5 items at the beginning of this section. The asterisks indicate the levels which are known experimentally, thus included when minimising the χ^2-test.

We continue the analysis with an extension to the deeply-bound neutron main shells for ^{208}Pb. These results are given in Tables 4.15 and 4.16. Notice that in both tables, the distribution-widths get narrower when all the parametric correlations are eliminated and the spin-orbit radius-parameter is fixed to its *compact* solution.

$N_{\rm main}=3$				$N_{\rm main}=4$				
$\mathbf{2p_{3/2}}$	$\mathbf{1f_{5/2}}$	$\mathbf{2p_{1/2}}$	$\mathbf{1g_{9/2}}$	$\mathbf{2d_{5/2}}$	$\mathbf{1g_{7/2}}$	$\mathbf{1h_{11/2}}$	$\mathbf{2d_{3/2}}$	$\mathbf{3s_{1/2}}$
3.11	4.07	3.07	2.87	2.02	3.14	1.82	1.96	1.76
3.11	4.12	3.09	2.83	2.01	3.16	1.80	1.94	1.74
2.82	3.55	2.77	2.70	1.81	2.78	1.78	1.73	1.57
1.85	1.79	1.60	1.85	1.20	1.13	1.50	1.01	1.00
2.31	3.20	2.59	1.45	1.45	2.56	1.02	1.62	1.34

Table 4.15 – The same as Table 4.14 but for the neutron levels within $N_{\rm main}=3$ and 4 shells.

$N_{\text{main}} = 0$	$N_{\text{main}} = 1$			$N_{\text{main}} = 2$		
$\mathbf{1s_{1/2}}$	$\mathbf{1p_{3/2}}$	$\mathbf{1p_{1/2}}$	$\mathbf{1d_{5/2}}$	$\mathbf{1d_{3/2}}$	$\mathbf{2s_{1/2}}$	$\mathbf{1f_{7/2}}$
6.28	5.53	5.50	4.73	4.79	4.24	3.86
6.31	5.53	5.57	4.70	4.86	4.26	3.81
5.75	5.09	4.94	4.38	4.21	3.86	3.59
3.47	3.02	3.09	2.59	2.51	2.38	2.21
3.70	4.15	4.36	3.29	3.80	3.29	2.33

Table 4.16 – The same as Table 4.14 but for the neutron levels within $N_{\text{main}} = 0$, 1 and 2 shells.

Preliminary Conclusions: We can summarise the results presented so far by saying that the removal of the parametric correlations diminishes the uncertainties of the predictions for the majority of the single nucleon levels and that *the effect is particularly strong for the deeply bound states* for which (no experimental information available there) the uncertainty widths are particularly big to start with. Within this average trend there are important fluctuations what implies that when it comes to discussing particular problems, e.g. in relation any given experiment, the analysis must be performed on the case-by-case basis. Results presented in Table 4.14 show that the spin-orbit compact configuration gives a better description in terms of r.m.s.-deviation than the non-compact one as well as in terms of uncertainty widths. The latter conclusion holds not only for the results presented in Table 4.14 but also for the low energy levels in Tables 4.15 and 4.16.

4.4.2 Results for the Single ^{208}Pb Nucleus Tests: Summary

We find it instructive to compare the calculated and experimental single nucleon energies when minimising the χ^2 in the space of the only two remaining independent parameters[4], cf. eq. (4.7). The results are given Figure 4.21. Even though the r.m.s.-deviation is slightly worse when working with really independent parameters only, $r.m.s = 0.20\,\text{MeV}$ instead of 0.16 MeV, nevertheless:

> *We arrive at reducing the global R.M.S.-deviation for the 8 known spherical nuclei from 1.86 MeV to 1.56 MeV, an encouraging measure of improvement of the predictive power.*

Moreover, we arrived at eliminating the inversion originally present in Figure 4.1 between levels $4s_{1/2}$ and $2g_{7/2}$.

Control Test of Parametric Elimination. We may expect that if the parametric correlations present in the original central potential have been successfully removed, the remaining free parameters should present no correlations in the final parameter-adjustment test. Figure 4.22 shows the corresponding test for the neutrons. The related Pearson coefficient being very close to zero informs us that there are no linear correlations left among the two parameters what allows us, for aesthetic reasons, to select the axis units in such a way that the final 'dot-plot' represents radial symmetry – just better visualising the fact that there are all originally present correlations removed in this case.

[4]Recall that the correlation of the form $y = f(x)$ can usually also be expressed in the form $x = x(y)$, and it is up physicist to select one of the two alternative forms according to some convenience criteria.

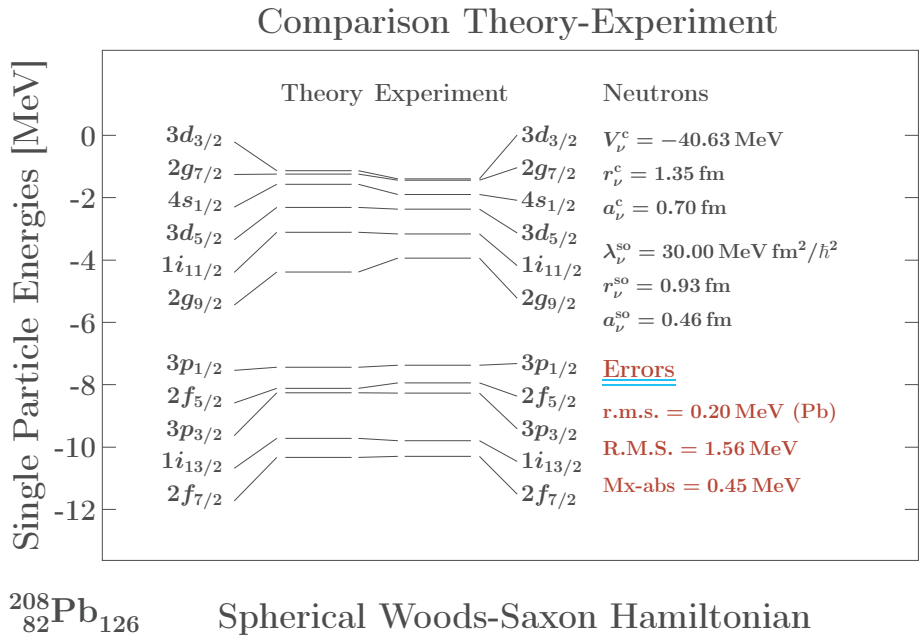

Figure 4.21 – Calculated neutron single particle energies, left column, resulting from the fit of the parameters of the WS Hamiltonian while imposing the removal of all the parametric correlations. One finds, from top to bottom: r.m.s.-deviation from Eq. (3.30), R.M.S.-deviation from Eq. (3.32) and the maximum absolute error, Mx-abs.

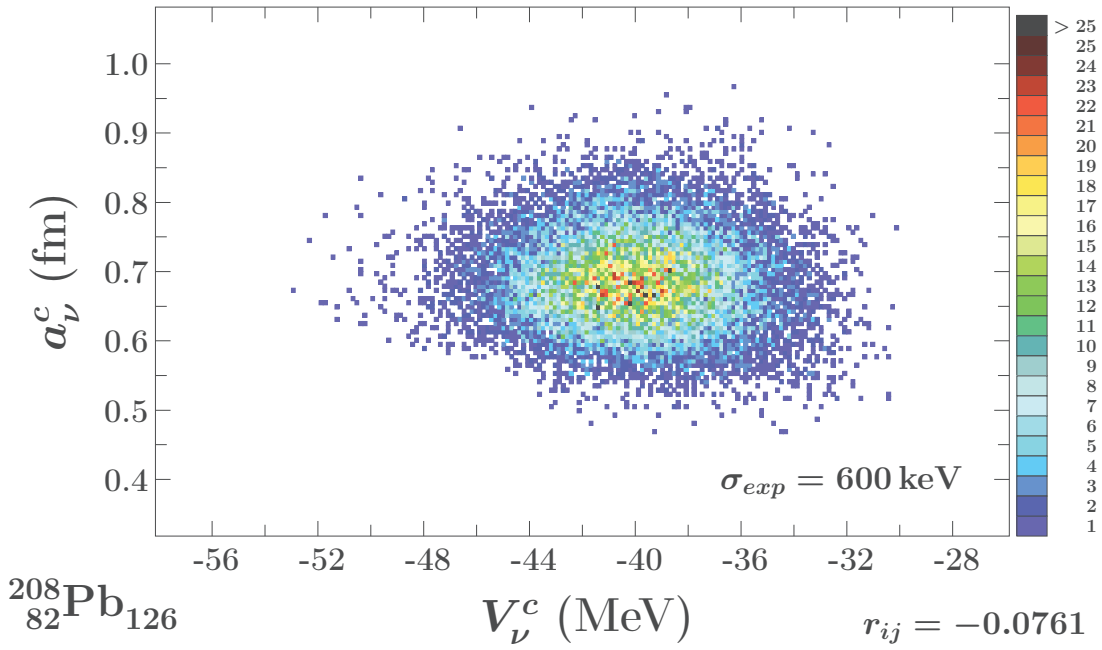

Figure 4.22 – Dot-plots illustrating the parametric correlations between the two neutron parameters indicated at $\sigma_{exp} = 600$ keV; It shows that there are no correlations left.

The Differences with the Proton Case. An analogous test for the protons shows that according to Pearson coefficient, whose value remains at the level of 0.5, the parametric correlations have not been eliminated. This confirms our earlier conjecture that by fixing the Coulomb potential as parameter-free, we also impact rigidly the diffusivity properties of the full (nuclear plus Coulomb) potential. In other words, the diffusivity of the full potential is influenced "by an external element" *viz.* the fixed Coulomb term, and thus 'diffusivity coupling' with the remaining parameters of the Hamiltonian is different as compared the neutrons. As mentioned earlier, taking this mechanism fully into account would require either a new extra parameter related to the Coulomb part or changing the definition of the Coulomb potential and calculating it out of the single-proton wave functions. Such techniques are discussed separately in the next Chapter and we intend to focus on those as much more promising ones for the large scale nuclear structure calculations – as compared to the fully phenomenological (traditional Woods-Saxon) approach.

4.5 Prediction Results for Neutrons in $_{114}$Fl-Isotopes

In this section we present the results of our predictions for the isotopes of $_{114}$Fl using the full-scale parameter-correlation removal-techniques discussed in the preceding sections – thus with the effective parametric freedom of the Hamiltonian reduced to two parameters: V_0^c and a_0^c. The corresponding uncertainty distribution-widths are presented in Table 4.17 and Table 4.18 for compact and non-compact solutions, respectively.

In the preceding sections we arrived at the conclusion that for the ^{208}Pb nucleus the most stable predictions are obtained for the compact variant of the spin-orbit potential parametrisation. The similar conclusion will be reached in the case of neutrons in various isotopes of Flerovium.

Comparing the results in Tables 4.17 and 4.18 with results in Table 4.7, one notices that the levels widths for $2f_{7/2}$, $1h_{9/2}$, $2f_{5/2}$, $3p_{3/2}$, $3p_{1/2}$, $1i_{11/2}$, $3d_{5/2}$, $4s_{1/2}$ and $3d_{3/2}$ are narrower for the compact solution. Specifically one finds that for the $1h_{9/2}$ level the results differ by about 50% between the two solutions. At the same time the results for the level $1i_{13/2}$ seem to be comparable with a slight preference for the non-compact solution.

Finally, let us mention a certain specificity noticed for $2g_{9/2}$, $1j_{15/2}$ and $2g_{7/2}$ levels. As it turns out, for $N \leq 184$ these levels are narrower in the case of the non-compact solution whereas the tendency is inverted for $N > 184$.

		$N_{\text{main}} = 5$						$N_{\text{main}} = 6$						
Z	N	$2f_{7/2}$	$1i_{13/2}$	$1h_{9/2}$	$2f_{5/2}$	$3p_{3/2}$	$3p_{1/2}$	$2g_{9/2}$	$1i_{11/2}$	$1j_{15/2}$	$3d_{5/2}$	$4s_{1/2}$	$2g_{7/2}$	$3d_{3/2}$
114	164	0.92	1.42	1.14	0.89	0.72	0.76	0.71	1.39	1.23	0.51	0.48	0.61	0.48
114	170	0.90	1.43	1.02	0.88	0.68	0.74	0.49	1.18	1.17	0.23	0.22	0.51	0.23
114	172	0.93	1.46	1.01	0.91	0.70	0.77	0.45	1.13	1.17	0.16	0.17	0.53	0.18
114	180	1.11	1.63	1.06	1.11	0.90	0.98	0.50	1.00	1.29	0.32	0.33	0.73	0.38
114	184	1.24	1.74	1.15	1.24	1.04	1.12	0.63	1.00	1.40	0.49	0.50	0.89	0.54
114	196	1.69	2.17	1.52	1.72	1.52	1.60	1.09	1.21	1.82	1.00	0.97	1.39	1.04
114	214	2.41	2.88	2.20	2.45	2.23	2.32	1.80	1.77	2.53	1.69	1.63	2.12	1.71
114	228	2.93	3.43	2.72	2.99	2.75	2.84	2.31	2.25	3.08	2.17	2.08	2.65	2.18

Table 4.17 – Realistic Monte Carlo results for the FWHM [in MeV] of the probability distributions of the neutron levels within main shells $N_{\text{main}} = 5$ and 6 for different super-heavy $_{114}$Fl-isotopes. They have been obtained imposing $r_\nu^c = f(V_\nu^c)$ and compact spin-orbit parameters.

		$N_{\text{main}} = 5$						$N_{\text{main}} = 6$						
Z	N	$2f_{7/2}$	$1h_{9/2}$	$1i_{13/2}$	$3p_{3/2}$	$2f_{5/2}$	$3p_{1/2}$	$2g_{9/2}$	$1j_{15/2}$	$1i_{11/2}$	$3d_{5/2}$	$4s_{1/2}$	$3d_{3/2}$	$2g_{7/2}$
114	164	1.03	2.16	1.31	0.90	1.12	0.77	0.67	1.90	1.58	0.50	0.50	0.77	0.74
114	170	1.11	2.32	1.10	0.96	1.22	0.79	0.60	1.59	1.69	0.39	0.23	0.44	0.47
114	172	1.16	2.38	1.06	1.02	1.27	0.83	0.63	1.50	1.75	0.42	0.18	0.34	0.42
114	180	1.46	2.69	1.03	1.32	1.57	1.13	0.91	1.23	2.04	0.71	0.42	0.21	0.45
114	184	1.64	2.86	1.09	1.50	1.74	1.31	1.10	1.18	2.21	0.90	0.61	0.36	0.60
114	196	2.21	3.40	1.45	2.06	2.29	1.87	1.70	1.28	2.76	1.46	1.17	0.91	1.17
114	214	3.07	4.22	2.19	2.90	3.11	2.69	2.56	1.81	3.61	2.26	1.92	1.67	2.00
114	228	3.69	4.84	2.78	3.50	3.72	3.29	3.18	2.31	4.24	2.83	2.45	2.20	2.57

Table 4.18 – Similar to Table 4.17 but for non-compact spin-orbit parameters.

• For the final summary-comparison, Figures 4.23, 4.24 and 4.25 below illustrate the results of Tables 4.7 and 4.17 for $^{278}_{114}\mathrm{Fl}_{164}$, $^{298}_{114}\mathrm{Fl}_{184}$ and $^{342}_{114}\mathrm{Fl}_{228}$, respectively.

• Results in Figures 4.23 - 4.25 show that the removal of the parametric correlations (bottom panels) leads to a decrease of the $N = 114$ gap. This result shows that predictions for the $N = 114$ gap are sensitive to details in the present-day experimental information and, consequently, a new experimental input may play a decisive role at the present status of the analysis.

• In reference to the results in Fig. 4.25 one can remark that we are at the NO-GO limit: even if the distribution-widths decrease, their sizes are still so large that there exist big overlaps among them.

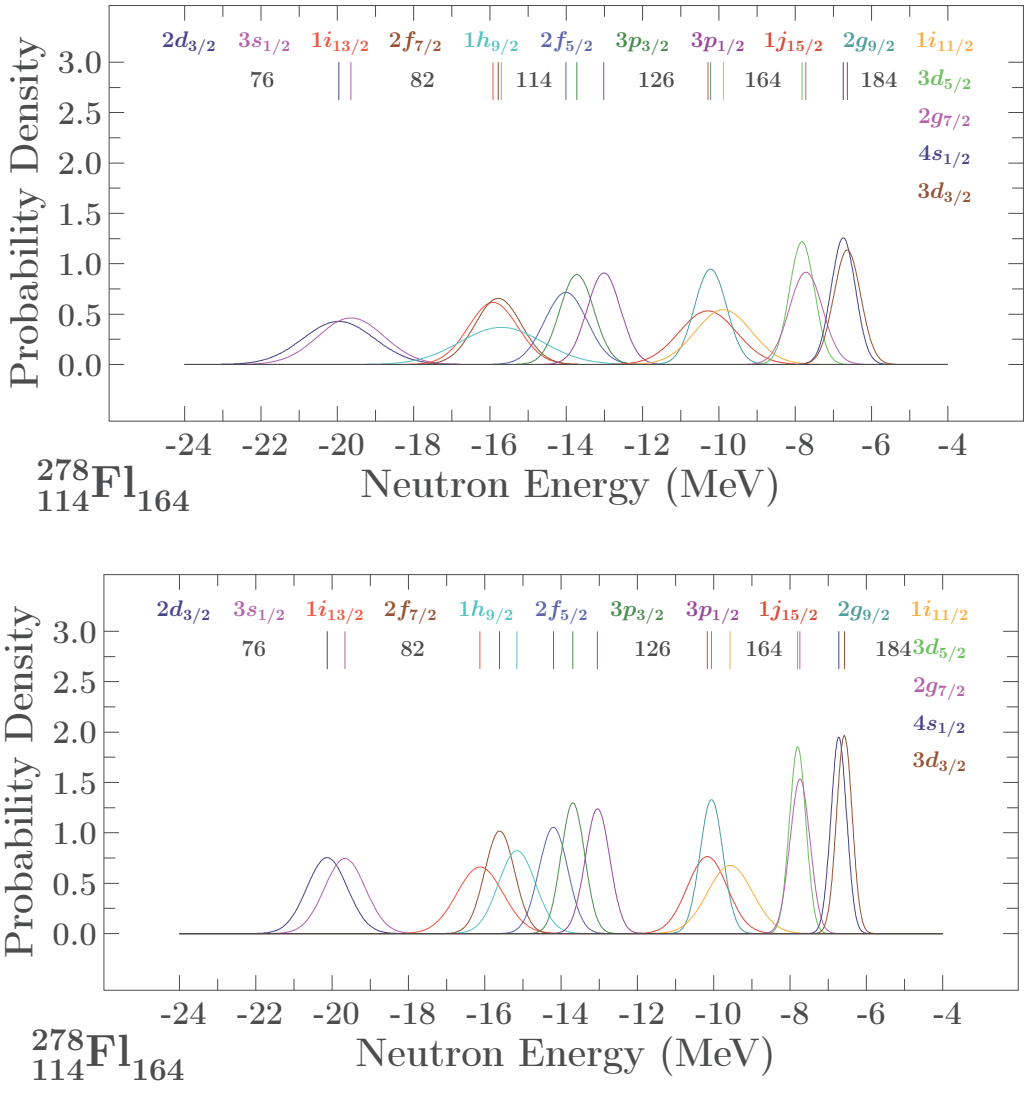

Figure 4.23 – Neutron probability density distributions for ^{278}Fl fitting with full parametric freedom (top) and after full parametric correlation removal, imposing compact spin-orbit solution (bottom). The values of the corresponding FWHM can be found in Tables 4.7 and 4.17 for top and bottom results, respectively.

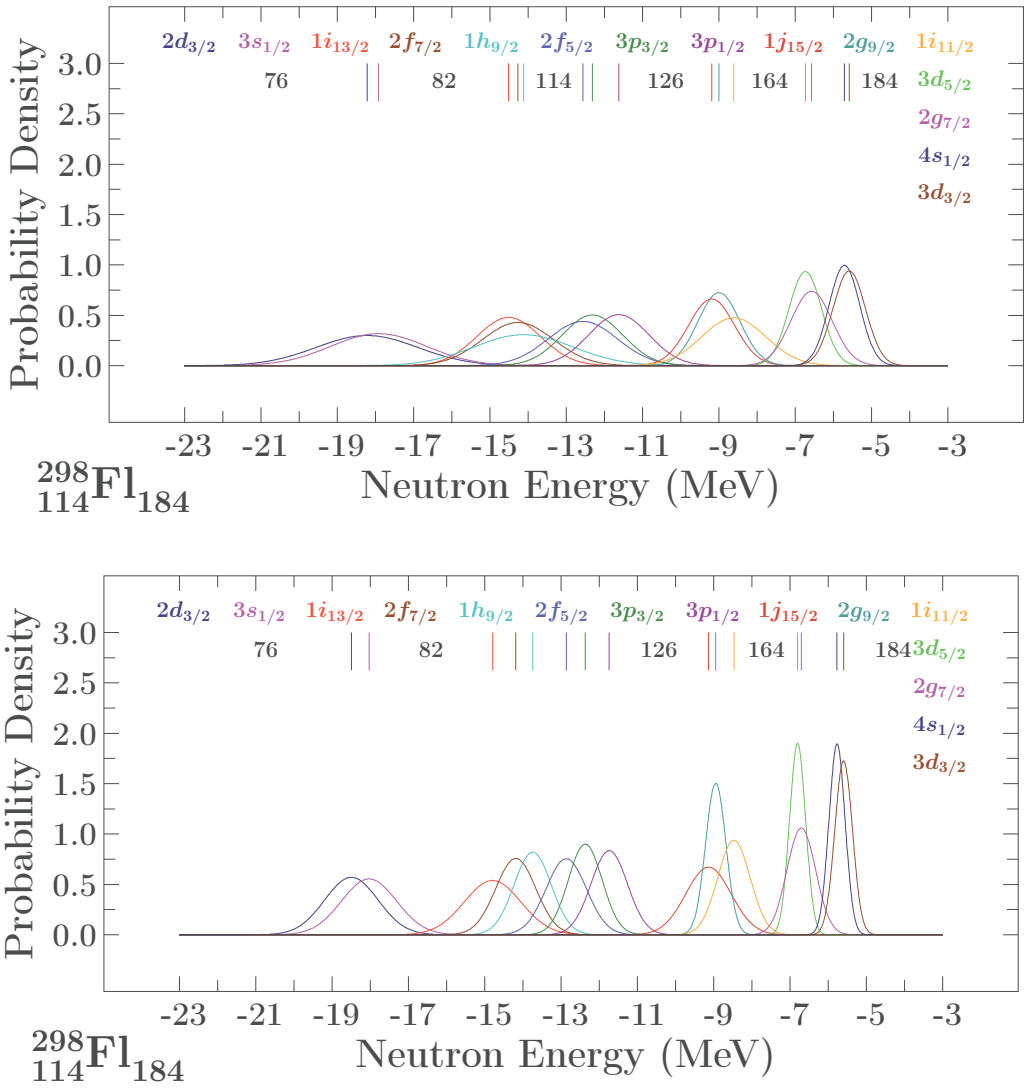

Figure 4.24 – Similar to Figure 4.23 but for ^{298}Fl.

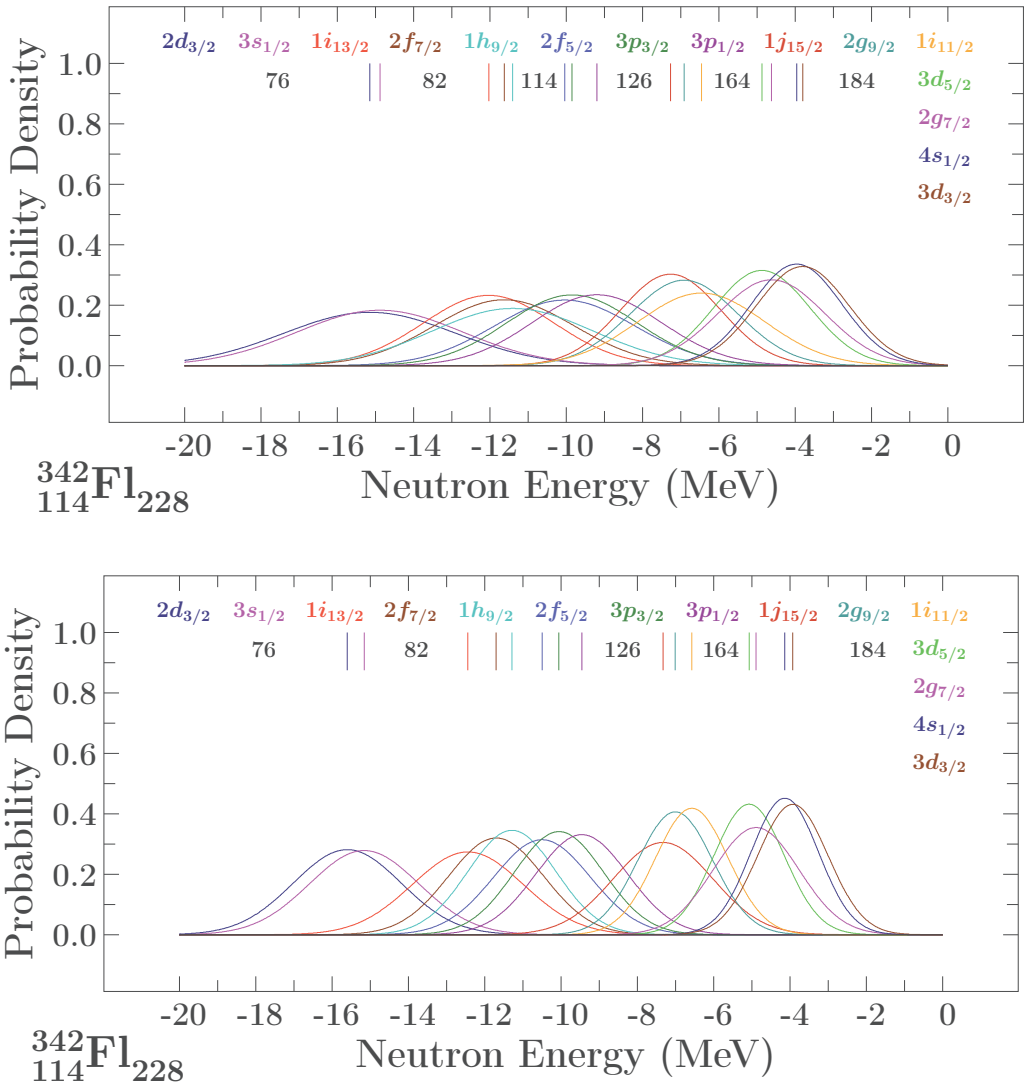

Figure 4.25 – Similar to Figure 4.23 but for ^{342}Fl.

4.6 Experimental Errors and Modelling Uncertainties

In the previous sections we have discussed the uncertainty distributions of single-nucleon energy-levels. They were obtained using Monte-Carlo method assuming a common error of 600 keV for all the experimentally known levels. We have shown that the uncertainty distributions resemble very closely the Gaussian form and that their widths decrease significantly when correlations are removed. The strongest improvement was obtained when the correlations including the spin-orbit radius parameter were eliminated.

It can be expected, and our preliminary results confirmed this expectation, that when the experimental error bars decrease, certain alternative forms of the uncertainty distributions appear thus revealing possibly interesting new stochastic features generated by the realistic Hamiltonians. This part of the research program is important since the ultimate goal of the instrumental progress is to increase the precision – thus to decrease the error bars. Should the stochastic features of the inverse-problem based modelling – like ours – change importantly, when the precision increases, to study such stochastic effects should be one of the first goals. Therefore it will be instructive to focus now on the limiting case of very small experimental error bars. We will take as a model of an excellent experimental precision the $\sigma_{exp} = 50\,\mathrm{keV}$ case and illustrate in detail the forms of the uncertainty distributions the goal being to focus on the possibly non-Gaussian structures.

Figure 4.26 illustrates the uncertainty distributions for the neutron single particle energies in ^{208}Pb around $N = 126$. These distributions where generated using Monte-Carlo simulation with the experimental errors represented by $\sigma_{exp} = 50$ keV. Minimisation over the full set of the six Hamiltonian parameters has been employed in this case. A clear appearance of the double-hump structure histograms deserves emphasising. Such an effect may be induced by parametric correlations but if real – it may cause serious complications of the stochastic interpretation of the theory predictions. Indeed, strictly speaking a double hump structure of the probability distribution implies that two theoretical energy levels with the same quantum number characteristics, e.g. $2f_{7/2}$, are possible within the model. Similar mechanism has been signalled in the PhD thesis of B. Szpak [25], and was attributed to the parametric correlations among in the spin-orbit parameters of the Hamiltonian but it was not investigated further. Let us also remark that the appearance of these double-hump structures does not depend on whether the predicted level is or not experimentally known.

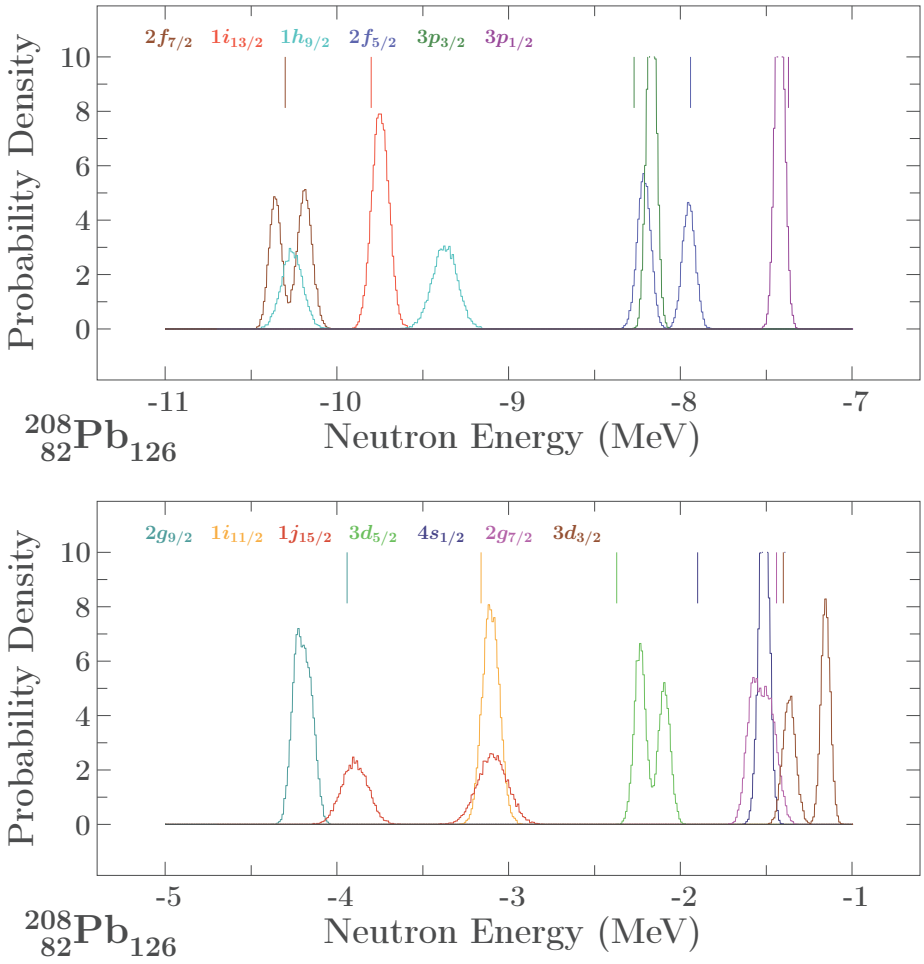

Figure 4.26 – Realistic Monte-Carlo calculations showing the probability density distributions for the neutron levels of ^{208}Pb within the main shells $N_{\text{main}} = 5$ (top) and 6 (bottom). The simulations have been run imposing $\sigma_{exp} = 50$ keV to the neutron single particle energies experimentally known (solid vertical bars) for ^{208}Pb and minimising the χ^2 over the full set of Hamiltonian parameters. The surface under each curve is equal to 1.

In what follows we will investigate the evolution of these relatively complex stochastic structures with the removal of various forms of parametric correlations.

Imposing $r_\nu^c = f(V_\nu^c)$ Removal: Results with Five Independent Parameters. As demonstrated with the results in Figure 4.3, the parabolic dependence between the central-depth and the central-radius parameters does not depend on σ_{exp}, at least in any important manner. Figure 4.27 illustrates the results obtained when imposing $r_\nu^c = f(V_\nu^c)$ showing that the double-hump structures become markedly asymmetric. In Figure 4.27 the right peak of $2f_{7/2}$, $1h_{9/2}$, $1j_{15/2}$ and $3d_{3/2}$ is narrower than in the case of Figure 4.26. On the other hand, $2f_{5/2}$ and $3d_{5/2}$ seem to narrow their right peak. This may help us understand why there was no much difference between Table 4.7 and Table 4.9.

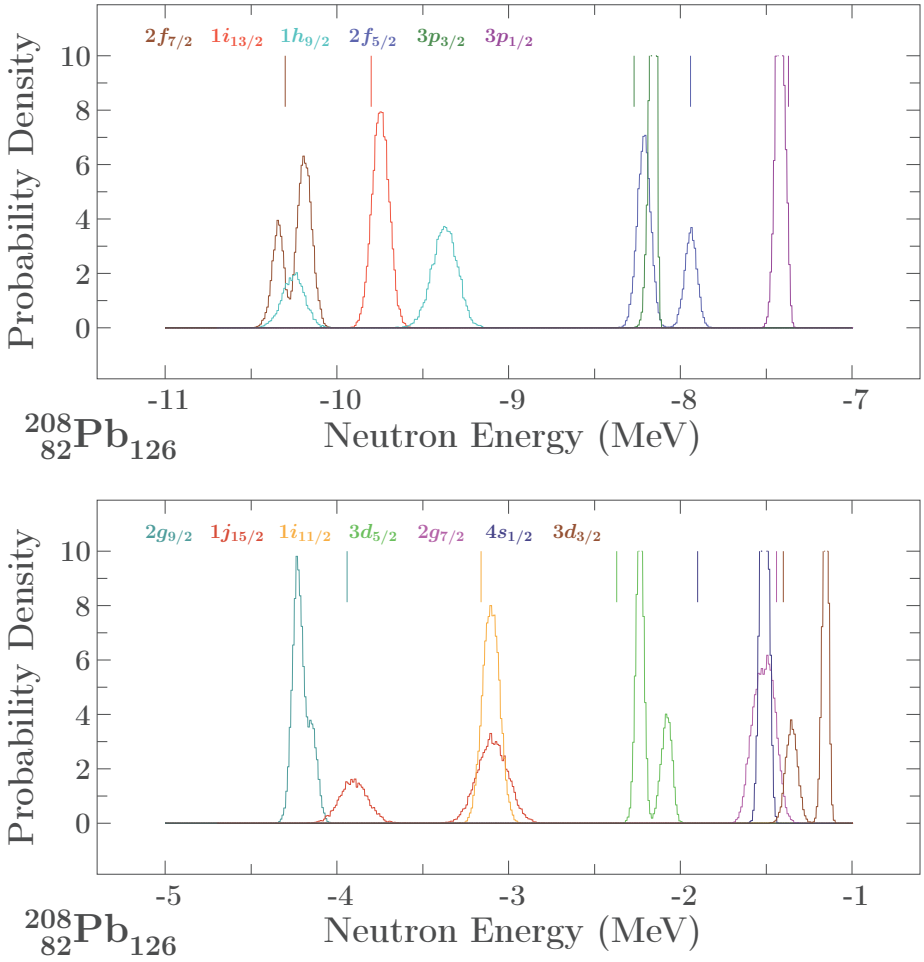

Figure 4.27 – The same as Figure 4.26 but imposing $r_\nu^c = f(V_\nu^c)$

The above simple comparison suggests that the parameter-correlation removal may have important impact on the for of the corresponding profiles thus encouraging to proceed with the removal of the remaining parametric correlations related to the spin-orbit term in the Hamiltonian; this will be done as before using the following information.

Type/name	r_ν^{so} [fm]	λ_ν^{so} [MeV fm$^2/\hbar^2$]	a_ν^{so} [fm]
compact	0.93	30.0	0.60
non-compact	1.22	28.0	0.35

Table 4.19 – Compact and non-compact solutions for neutron spin-orbit parameters obtained from the Monte-Carlo results with $\sigma_{exp} = 50$ keV of Figures 4.11-4.14.

In what follows, we will present the Monte-Carlo result when minimising the χ^2 over

$$\{V_\nu^c, a_\nu^c\} \tag{4.8}$$

Removing All Parametric Correlations: Compact Solution. Figure 4.28 shows the neutron energy distributions when in addition the central correlation, the spin-orbit correlations are removed imposing the compact solution. one notices that the double-hump structures have completely disappeared whereas all the peaks take the form resembling a single-Gaussian. The widths of the distributions are now much narrower as compared to the ones in Figure 4.26.

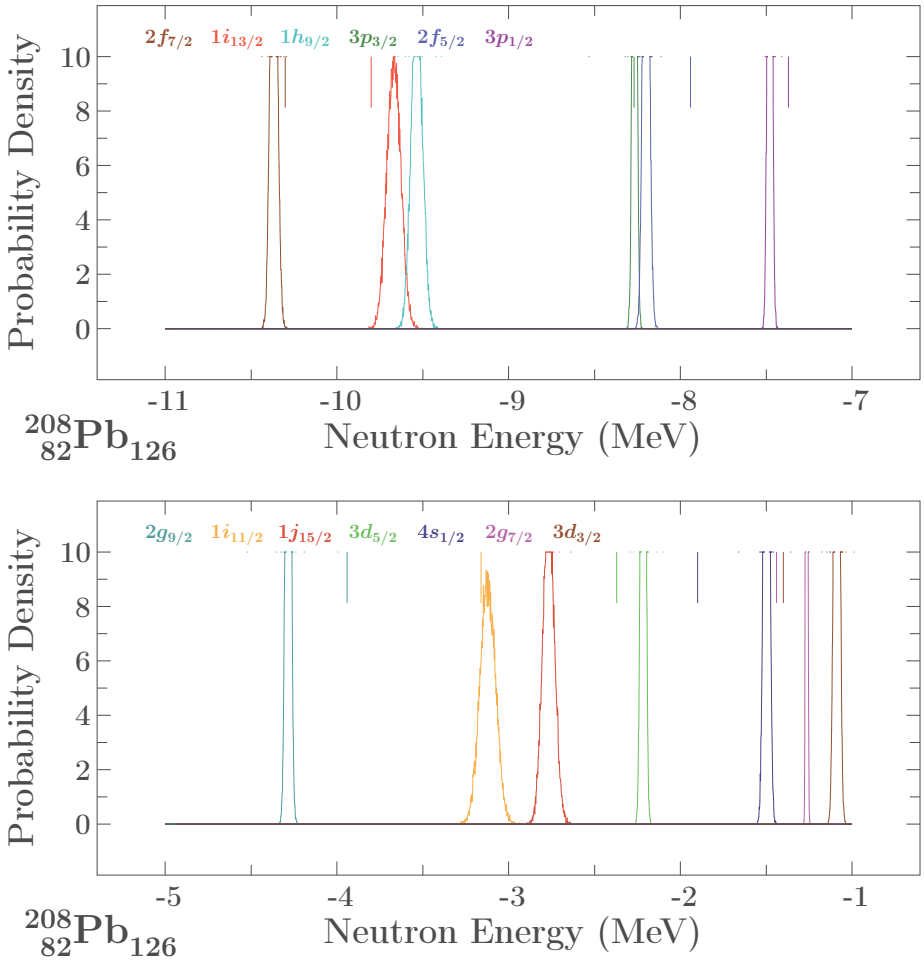

Figure 4.28 – The same as Figure 4.26 but imposing $r_\nu^c = f(V_\nu^c)$ and compact spin-orbit solution, cf. Table 4.19.

Removing All Parametric Correlations: Non-Compact Solution. In the case of the non-compact variant of the parameter removal the double-hump structure disappears as well – even though the details of the characteristics of each distribution as well as the centre-positions of the distributions differ.

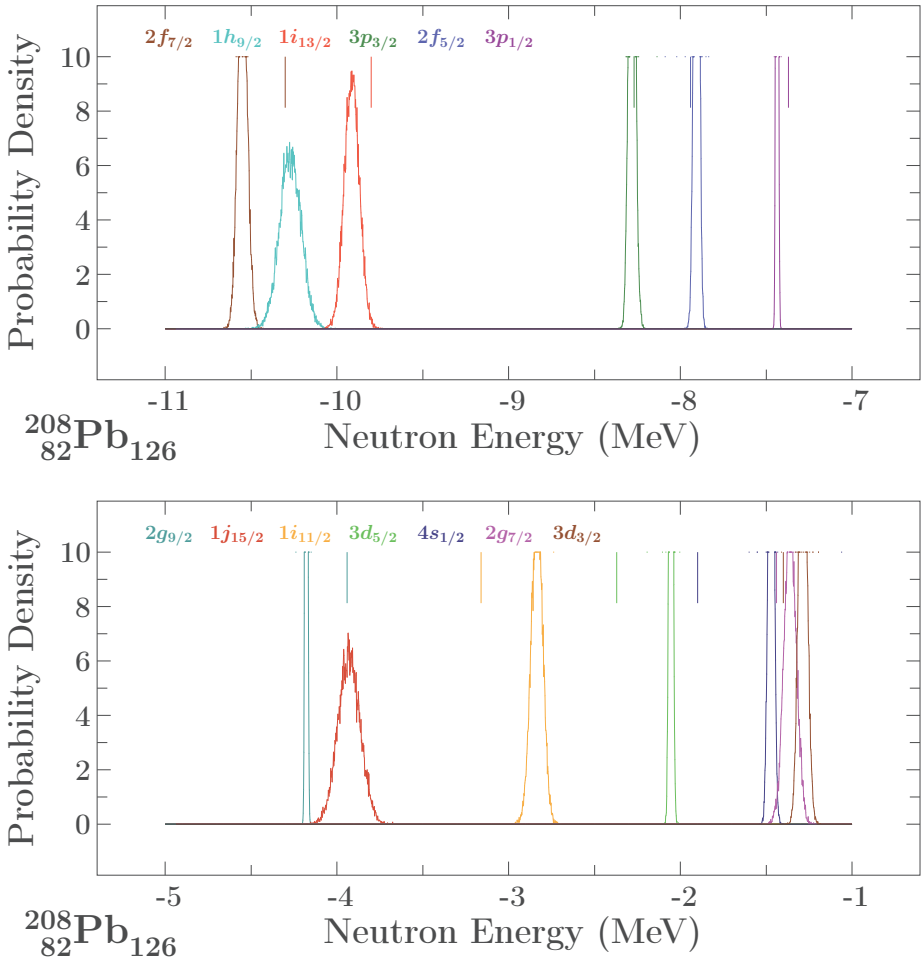

Figure 4.29 – The same as Figure 4.26 but imposing $r^c_\nu = f(V^c_\nu)$ and non-compact spin-orbit solution, cf. Table 4.19.

In the present approach to the parametric-correlation removal the two *viz.* compact and non-compact variants are permitted by the model: Both serve efficiently the mathematical goal 'of removing correlations' and are mathematically both equally acceptable.

It is then up to the physicist to choose between one of the two according to some 'physics based' criteria. Let us remark in passing that the compact configuration seems to give better results in terms of the root-mean-square deviations; however, these predictions may depend on the sampling what evidently encourages the search of new observables possible to include.

4.7 Annexe A: Synthetic 'Quick-Look' Comparison

In what follows we present a series of graphical illustrations which essentially repeat the information already presented in the preceding Sections. The purpose here is to change the scale and putting the right diagrams next to each other in order to allow for a quick conclusive comparison:

- *Disappearance of the double-hump distributions,*
- *Narrowing of single-Gauss-type distributions when correlations are removed.*

^{208}Pb: Parametric Correlation Removal Effect – A Summary for $N_{\text{main}} = 5$

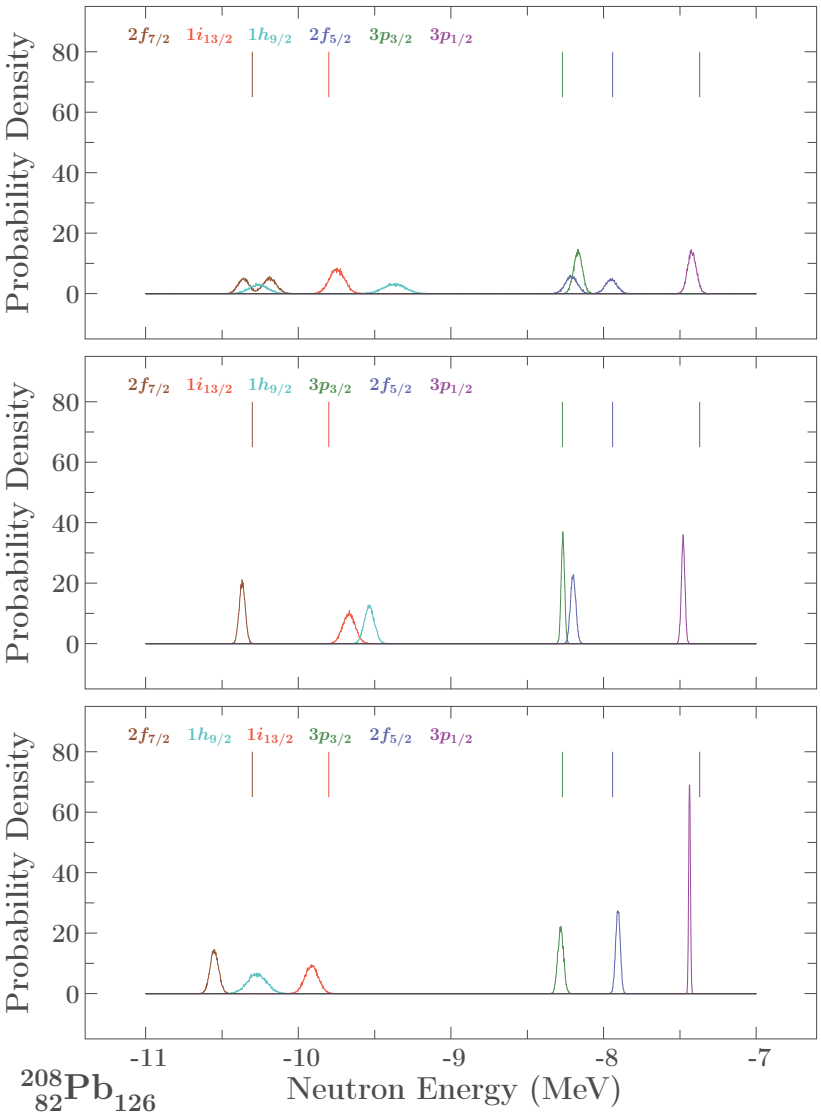

Figure 4.30 – Neutron probability distributions for ^{208}Pb in main shell $N_{\text{main}} = 5$ for $\sigma_{exp} = 50$ keV. Top: full parametric freedom (six parameter minimisation); Middle: removing all possible parametric correlation, imposing compact spin-orbit solution (two parameter minimisation); Bottom: removing all possible parametric correlation, imposing non-compact solution (two parameter minimisation). The solid vertical lines indicate the experimental position the corresponding level. The surface under each curve is equal to 1.

^{208}Pb: Parametric Correlation Removal Effect – A Summary for $N_{\text{main}} = 6$

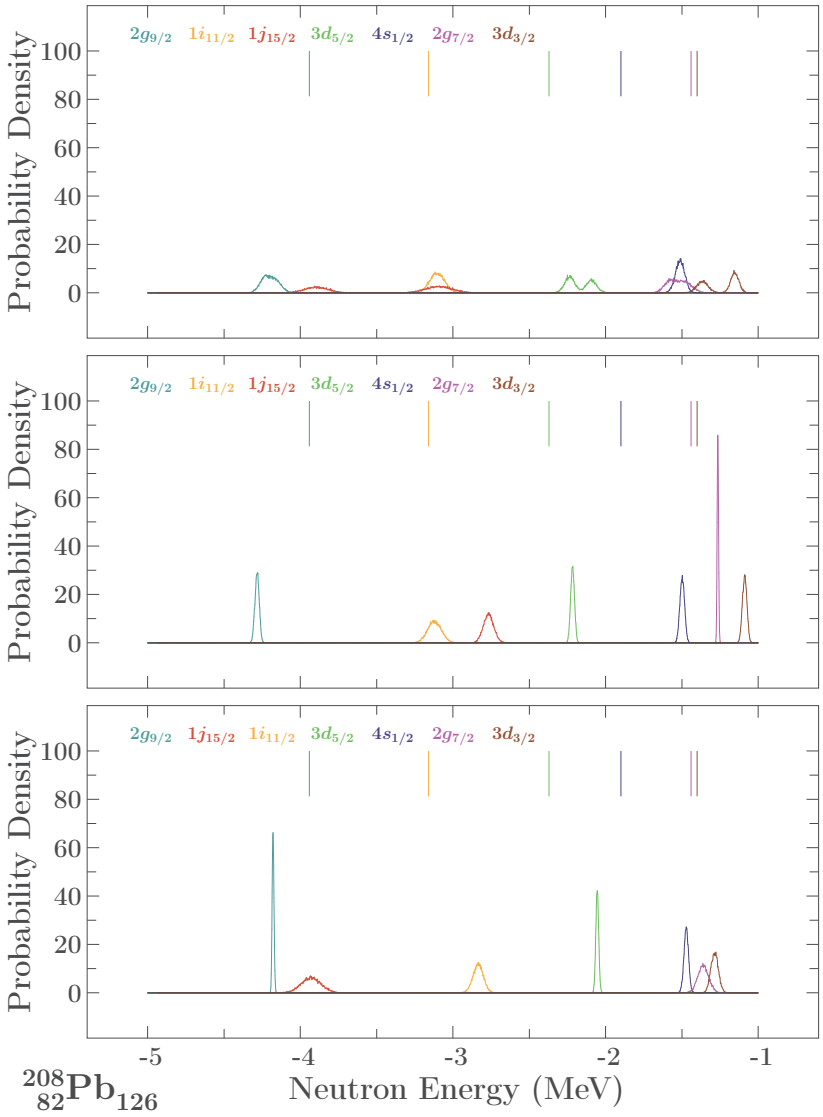

Figure 4.31 – The same as Figure 4.30 but for the neutron levels corresponding to the main shell $N_{\text{main}} = 6$.

$^{278}_{114}$Fl: Parametric Correlation Removal Effect – A Summary for $N_{\text{main}} = 5, 6$

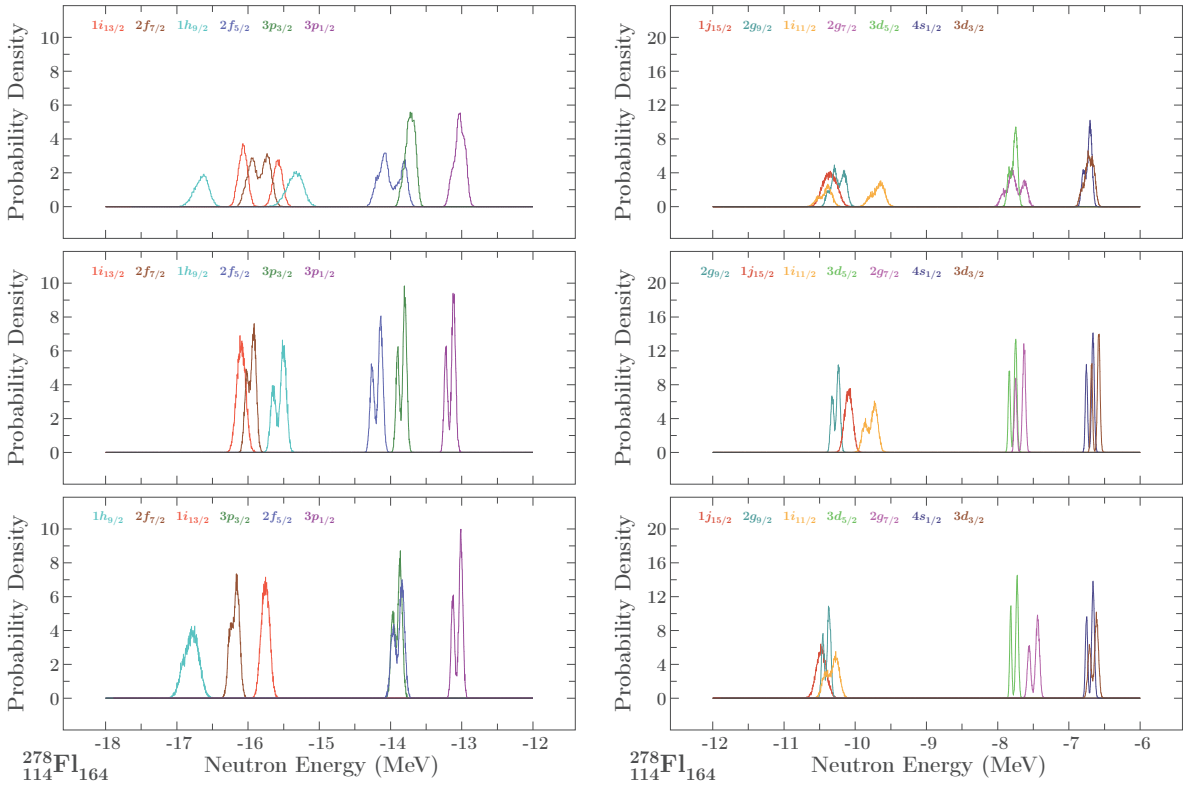

Figure 4.32 – Realistic Monte-Carlo calculations showing the probability density distributions for the ^{278}Fl neutron levels within the main shells $N_{\text{main}} = 5$ (left column) and 6 (right column), applying $\sigma_{exp} = 50$ keV. Top row: full parametric freedom (six parameter minimisation; middle row: all parametric correlations removed, imposing compact spin-orbit solution (2 parameter minimisation); bottom row: equivalent to middle row but imposing non-compact spin-orbit solution.

$^{298}_{114}$Fl: Parametric Correlation Removal Effect – A Summary for $N_{\text{main}} = 5, 6$

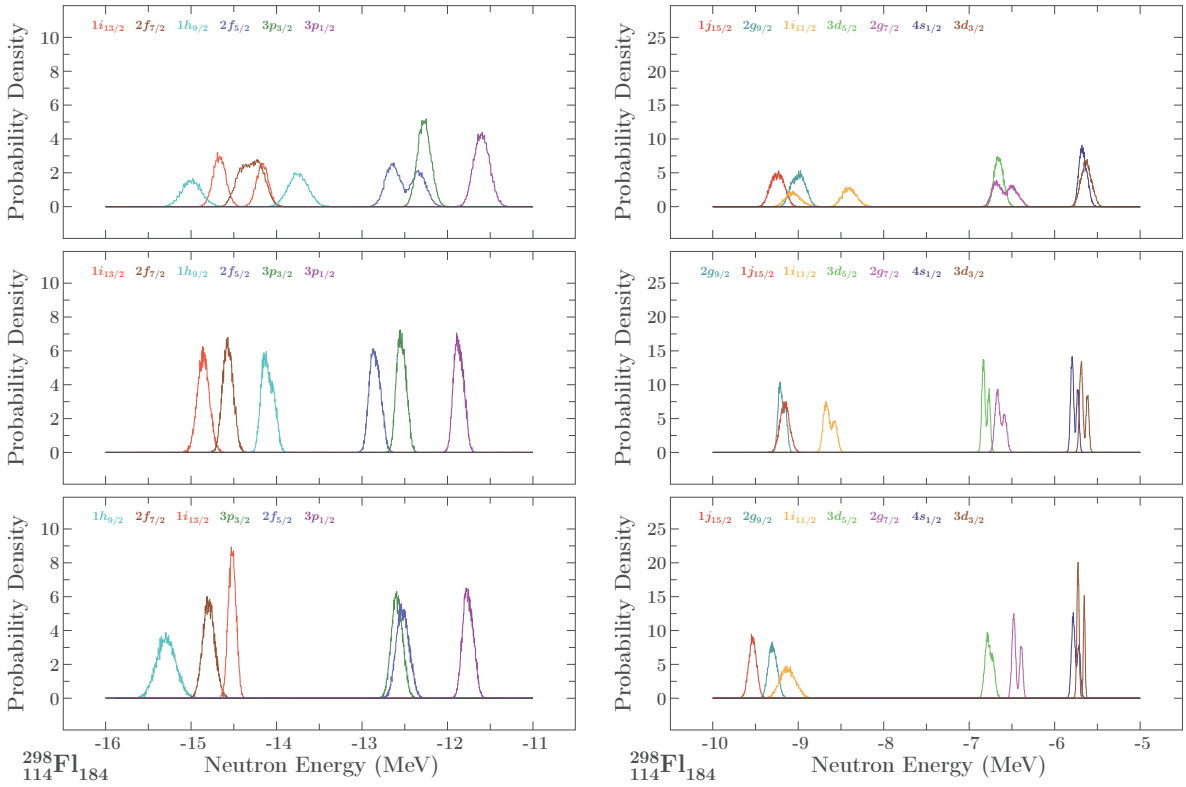

Figure 4.33 – Similar to Figure 4.32 but for ^{298}Fl.

$^{242}_{114}$Fl: Parametric Correlation Removal Effect – A Summary for $N_{\text{main}} = 5, 6$

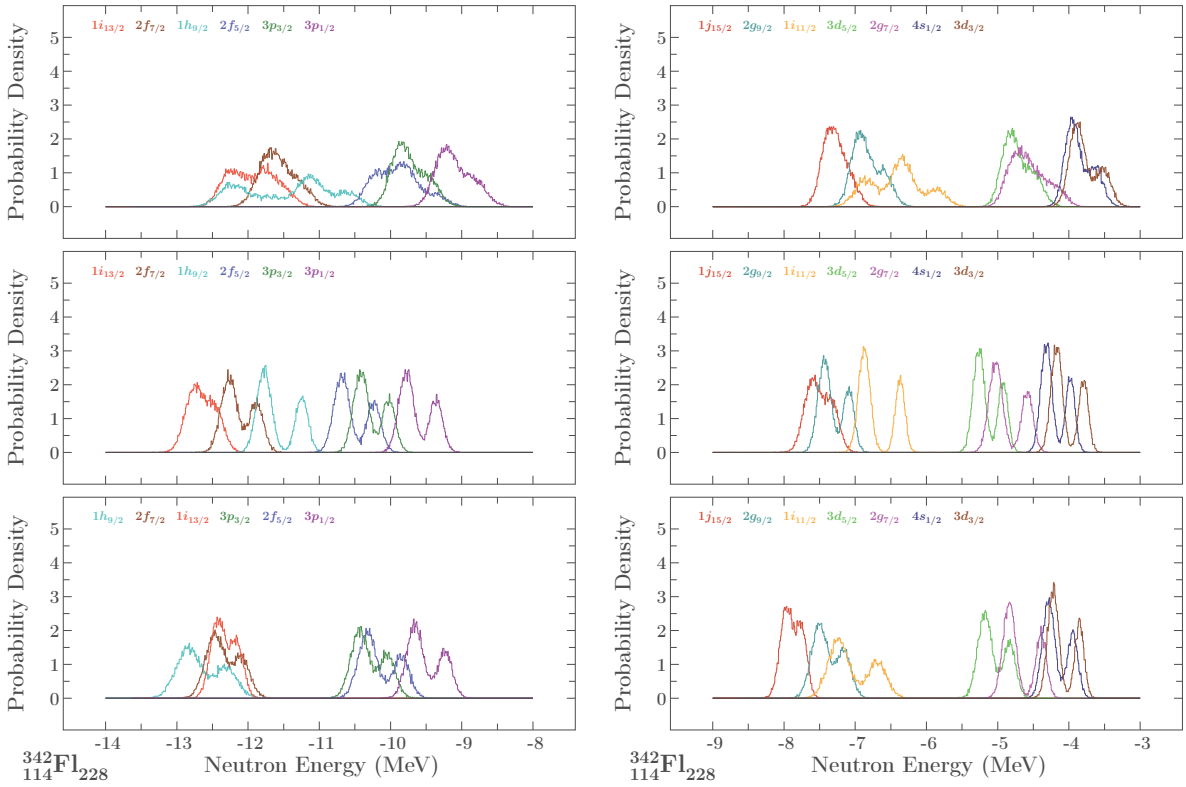

Figure 4.34 – Similar to Figure 4.32 but for ^{342}Fl.

4.8 Annexe B: Comments About Detecting Correlations

Concerning the techniques of studying parametric correlations, we have presented and employed one of the methods of detecting their presence and their form using Monte Carlo approach. Such an approach is based on collecting the statistics: 'The longer the CPU simulation time the more viable the resulting information'. The advantage of this technique consists in the fact that the experimental input errors are taken into account 'naturally': Their presence is an essential element of this stochastic approach.

An alternative approach consists in constructing the projection of the r.m.s.-deviation onto parameter planes (p_i, p_j). For this purpose, one tabulates the χ^2 using these two parameters as independent variables, while minimising the χ^2 at each (p_i, p_j)-point over the remaining ones. The input consists in the experimental energy spectra where no information about the uncertainties (error-bars) is present.

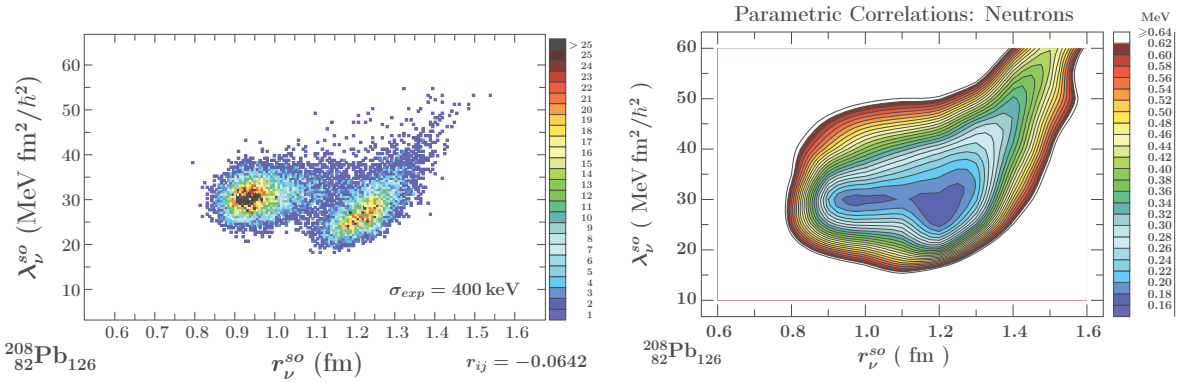

Figure 4.35 – Parametric correlation between spin-orbit radius and spin-orbit strength for the neutrons. Left panel shows realistic Monte Carlo simulations with the colour scale indicating the concentration of data points. Right panel: Projection of the r.m.s.-deviations onto the two dimensional plane with the colour scale representing the r.m.s.-values.

Figure 4.35 compares the two, in principle non-equivalent ways of testing for the presence of parametric correlations. On the left panel, the colour scale represents the concentration of points. On the right panel, the colour scale indicates the actual value of the r.m.s.-deviation. As it can be seen from this comparison the 'double-bubble' structure is present in both representations – yet graphical differences are visible. In particular, the bigger concentration of black dots around r_ν^{so}-compact solution on the left panel translates into a steeper valley for the compact solution on the right panel – whereas in the case of the non-compact solution the flatter distribution of points translates into a flatter energy landscape.

Chapter 5

Density-Dependent Spin-Orbit Potential: Parameter Optimisation

Let us briefly remind the reader about the definitions of the spin-orbit interaction potentials used in this project. It will be instructive to re-introduce the definition of the traditional form first in order to appreciate clearly the mathematical similarities and differences between the traditional and the new one, referred to as microscopic – or density dependent – spin-orbit interaction.

5.1 Short Summary of Mathematical Details

Let us recall first the mathematical form of the spin-orbit interaction in the framework of the analytical expressions of the potentials according to the traditional formulation of the Woods-Saxon Hamiltonian.

5.1.1 Traditional Form of the Spin-Orbit Potential

It is by definition proportional to the scalar product of the orbital angular momentum and the intrinsic spin operators (where from its name):

$$\hat{V}_{SO}(\vec{r}) \rightarrow \hat{V}_{SO}(r) \stackrel{df.}{=} \frac{1}{r}\frac{dv_{so}(r)}{dr}\,\vec{\ell}\cdot\vec{s} \tag{5.1}$$

where the radial nucleonic-position dependent form-factor is defined by

$$v_{so}(r) \stackrel{df.}{=} \frac{\lambda^{so}}{1+\exp\left[(r-R^{so})/a^{so}\right]}. \tag{5.2}$$

Adjustable parameter λ^{so} represents the strength of the spin-orbit interaction potential, r^{so} in $R^{so} = r^{so}A^{1/3}$ is the spin-orbit radius parameter and a^{so}, the spin-orbit diffuseness parameter. The operators of the intrinsic spin $\vec{s}$ and of orbital angular-momentum $\vec{\ell}$ give the total angular momentum $\vec{j}$ represented by the simple sum:

$$\vec{s}+\vec{\ell}=\vec{j}, \tag{5.3}$$

wherefrom

$$\vec{\ell}\cdot\vec{s}=\frac{1}{2}(\vec{j}^{\,2}-\vec{s}^{\,2}-\vec{\ell}^{\,2}). \tag{5.4}$$

Acting with $\vec{\ell}\cdot\vec{s}$ on the eigenstates of $\hat{j}^2$, $\hat{\ell}^2$ and $\hat{s}^2$ we find the result of its action in the form

$$\vec{\ell}\cdot\vec{s} \equiv \frac{1}{2}\left[j(j+1) - \ell(\ell+1) - s(s+1)\right]. \tag{5.5}$$

This latter form of the considered expression will be common for both the traditional and for the microscopic formulation; the latter will be briefly presented next.

5.1.2 Density-Dependent Form of the Spin-Orbit Potential

Recall that according to the microscopic background of the mean-field theory the elementary building blocks of the one-body potential are provided by the effective two-body interaction $\hat{v}_{N-N}(\vec{r}-\vec{r}\,')$. The mean-field interaction $V(\vec{r})$ originating from the two-body interaction[1] has the form introduced already in Chapter 2:

$$V(\vec{r}) \sim \sum_i \int \Psi_i^*(\vec{r}\,')\hat{v}_{N-N}(\vec{r}-\vec{r}\,')\Psi_i(\vec{r}\,')\,d^3\vec{r}\,', \tag{5.6}$$

where $\Psi_i(\vec{r}\,')$ are the single-nucleon wave functions. In what follows we use the isospin-conservation property which allows to represent the full nucleonic density as a sum of the proton and neutron contributions

$$\rho(\vec{r}) \to \rho\,(r) = \sum_i |\Psi_i(r)|^2 = \rho_\pi(r) + \rho_\nu(r). \tag{5.7}$$

Above, $\rho_{\pi/\nu}(r)$ refer to the proton/neutron density functions, respectively. Details of the mathematical derivation of the final expression for the density-dependent spin-orbit potential can be found in [29], where it is shown that introducing Taylor expansion

$$\rho(r') \simeq \rho(r) + (r-r')\cdot\nabla\rho|_{r=r'}, \tag{5.8}$$

one obtains the spin-orbit interaction potential in the form:

$$\hat{V}_{SO}(r) = \lambda\frac{1}{r}\frac{d\rho(r)}{dr}\,\vec{\ell}\cdot\vec{s}. \tag{5.9}$$

Above, λ is the spin-orbit interaction strength parameter. Since the nucleonic density is the sum of the proton and neutron contributions, we obtain the following final form of the spin-orbit potential: The one acting on the protons:

$$\hat{V}^{\pi}_{SO}(r) = \frac{1}{r}\left[\lambda_{\pi\pi}\frac{d\rho_\pi(r)}{dr} + \lambda_{\pi\nu}\frac{d\rho_\nu(r)}{dr}\right](\vec{\ell}\cdot\vec{s})\Big|_\pi, \tag{5.10}$$

and the one acting on the neutrons:

$$\hat{V}^{\nu}_{SO}(r) = \frac{1}{r}\left[\lambda_{\nu\pi}\frac{d\rho_\pi(r)}{dr} + \lambda_{\nu\nu}\frac{d\rho_\nu(r)}{dr}\right](\vec{\ell}\cdot\vec{s})\Big|_\nu. \tag{5.11}$$

[1] Let us mention in passing that at this point we wish to summarise a schematic approach used in Ref. [29] to justify the microscopic extension of the phenomenological spin-orbit Woods-Saxon Hamiltonian into the form of Eqs. (5.9-5.11). This can in no way pretend addressing the formal solution of the many-body problem with any, so-called realistic assumptions about the mathematical representation of such interactions [the presence of the hard-core and healing distance mechanisms, diagrammatic techniques, etc.].

With this new formulation we describe the spin-orbit potential with 4 parameters for protons and neutrons $\{\lambda_{\pi\pi}, \lambda_{\pi\nu}, \lambda_{\nu\nu}, \lambda_{\nu\pi}\}$, instead of 6 parameters within the traditional formulation.

Since the numerical calculation of the spin-orbit potential depending on the density requires an iterative procedure towards auto-reproduction and that, for this new formulation, the protons and neutrons need to be taken into account at the same time, the CPU demand in this case it is considerably higher than in the traditional version.

5.2 Density-Dependent S-O: Parametric Correlations

Similarly to the presentation scheme introduced in the preceding Chapter we will begin by analysing the ill-posedness of the problem with the density-dependent description of the spin-orbit potential with the help of the condition number.

5.2.1 About Ill-Posedness: S.V.D. Theorem, Condition Number

In order to obtain the 'first glance' estimates of the quality of the description capacities of the new formulation vs. experimental data we adjust simultaneously the ten parameters of the new Hamiltonian

$$\{V_\pi^c,\, r_\pi^c,\, a_\pi^c,\, V_\nu^c,\, r_\nu^c,\, a_\nu^c,\, \lambda_{\pi\pi},\, \lambda_{\pi\nu},\, \lambda_{\nu\nu},\, \lambda_{\nu\pi}\} \tag{5.12}$$

to the experimentally known neutron and proton single particle energies in ^{208}Pb, cf. Tables 2.2 and 2.3. Figures 5.1 and 5.2 show the results. The optimal parameter values are given inside the frames together with the root-mean-square deviations, defined in Eqs. (3.30)–(3.32). The r.m.s.-deviations for neutrons and protons are 0.16 MeV and 0.08 MeV, respectively (cf. Figures 4.1 and 4.2 for the traditional case) showing that the new description (with two parameters less) is of the same quality as the traditional one. Notice that the global R.M.S.-deviation is also comparable to the previous case.

As before we will employ the S.V.D.-theorem, cf. Eq. (1.53) and calculate the condition number as the first indicator for the degree of ill-posedness of the inverse problem. We find

$$\mathrm{cond}(\mathcal{A})_{\pi\nu} = \frac{5.10 \times 10^2}{4.30 \times 10^{-3}} = 1.18 \times 10^5. \tag{5.13}$$

This result is two orders of magnitude worse as compared to the results obtained in the traditional variant, cf. Eqs. (4.1) and (4.2) what implies that the inverse problem here is strongly ill-posed. Therefore, the issue of the parametric-correlation removal can be considered of even more importance as compared to the previously discussed cases.

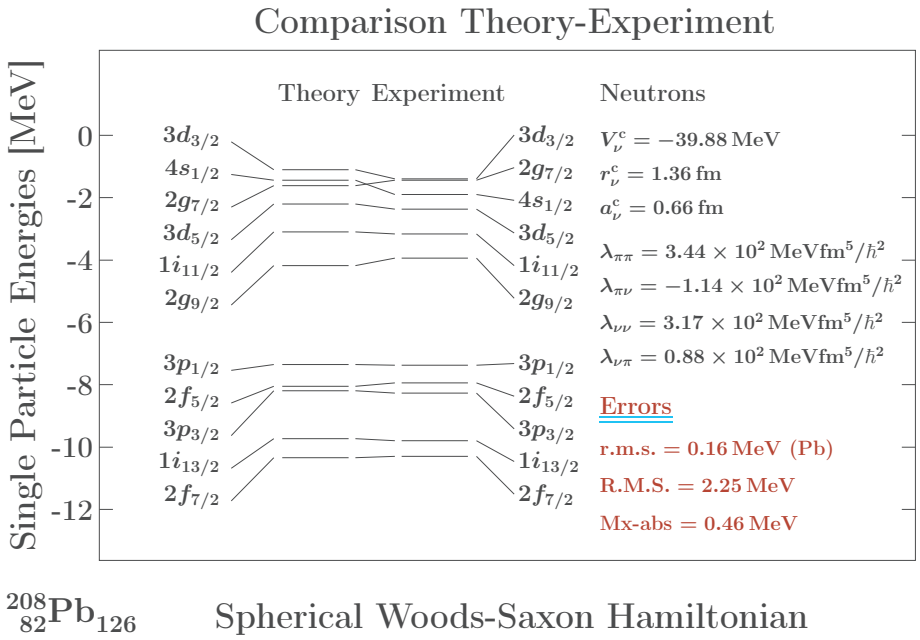

Figure 5.1 – Calculated ^{208}Pb neutron single particle energies, left column, resulting from the fit of the density-dependent-WS Hamiltonian parameters. The experimental energies are given in the left column and the parameters on the right side of the figure. One finds, from top to bottom: r.m.s.-deviation from Eq. (3.30), R.M.S.-deviation from Eq. (3.32) and the maximum absolute error, Mx-abs.

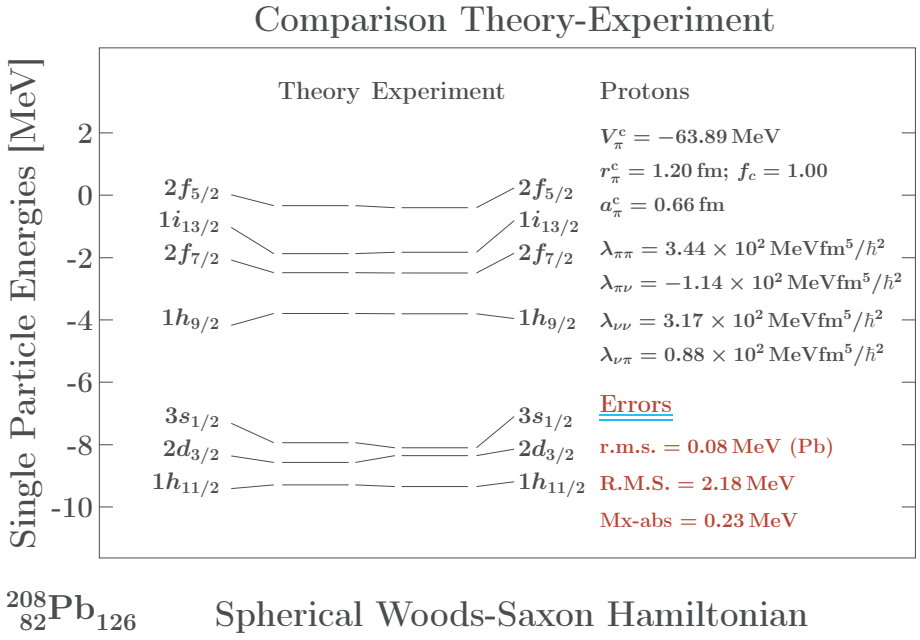

Figure 5.2 – The same as in Fig. 5.1 but for the protons.

5.2.2 Parametric Correlations Studied by χ^2-Projection

Since the present-case density-dependent formulation of the spin-orbit potential is more CPU time consuming, in the present case it will be practical to attempt detecting the existence of parametric correlations using directly the χ^2-test as described in Annex 4.8 of the preceding Chapter rather than employing the Monte-Carlo simulations. Recall that the information of interest is obtained in this case through projections of the $\{p_k\}$-minimised $\chi^2(p_k; k \neq i, k \neq j)$ onto the planes (p_i, p_j). In what follows we present the parametric correlations between the four spin-orbit coupling constants: $\{\lambda_{\pi\pi}, \lambda_{\pi\nu}, \lambda_{\nu\nu}, \lambda_{\nu\pi}\}$.

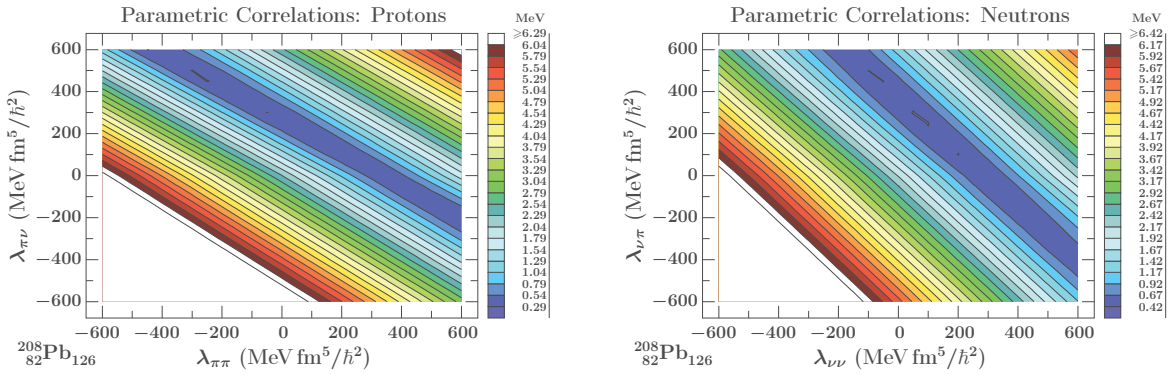

Figure 5.3 – Left: Proton r.m.s.-deviation in MeV projected onto the $(\lambda_{\pi\pi}, \lambda_{\pi\nu})$-plane. For this introductory test the central potential parameters were kept fixed at the values obtained from the single fit minimisation, cf. Figs. 5.1 and 5.2. At each $(\lambda_{\pi\pi}, \lambda_{\pi\nu})$ value the χ^2 was minimised over $\lambda_{\nu\nu}$ and $\lambda_{\nu\pi}$. The coloured vertical space indicates the value of the proton-r.m.s. in MeV. Right: Analogous illustration for the neutrons.

Separate Treatment of Parameters $(\lambda_{\pi\pi}, \lambda_{\pi\nu})$ of $\hat{V}^{\pi}_{SO}$, and $(\lambda_{\nu\pi}, \lambda_{\nu\nu})$ of $\hat{V}^{\nu}_{SO}$. Figure 5.3 shows the results for the proton and neutron r.m.s.-projections onto the planes $(\lambda_{\pi\pi}, \lambda_{\pi\nu})$ and $(\lambda_{\nu\nu}, \lambda_{\nu\pi})$, respectively. The two illustrations show clearly linear dependencies between the couples of parameters in question. This type of the dependence can be parameterised using the expression of the form

$$\lambda_{qq'} = \alpha \cdot \lambda_{qq} + \beta\,;\ \alpha > 0\,,\ \beta < 0 \tag{5.14}$$

where $q, q' = \pi, \nu$ and $q \neq q'$.

Couples of Parameters Entering Equations One For $\hat{V}^{\pi}_{SO}$, and One For $\hat{V}^{\nu}_{SO}$.

Having detected the correlations present between the parameters entering $\hat{V}^{\pi}_{SO}$ and $\hat{V}^{\nu}_{SO}$ separately, let us continue by analysing the cross-selections, *viz.* those combining one parameter of $\hat{V}^{\pi}_{SO}$ with another one in $\hat{V}^{\nu}_{SO}$. These results are shown in Figure 5.4.

Top-left panel illustrates the neutron-r.m.s. projection onto the $(\lambda_{\pi\pi}, \lambda_{\pi\nu})$-plane forming a horizontal valley. This illustration carries an important physical message: $\lambda_{\pi\pi}$ and $\lambda_{\nu\nu}$ can be considered independent. The top-right panel shows an analogous result for the proton-r.m.s. projection, and confirms again the independence of these two concerned parameters. These two results indicate that the parameter elimination procedures which we will enter next will not need to involve the two relations.

Similar results are shown on the bottom panels of Figure 5.4 for the plane of projection

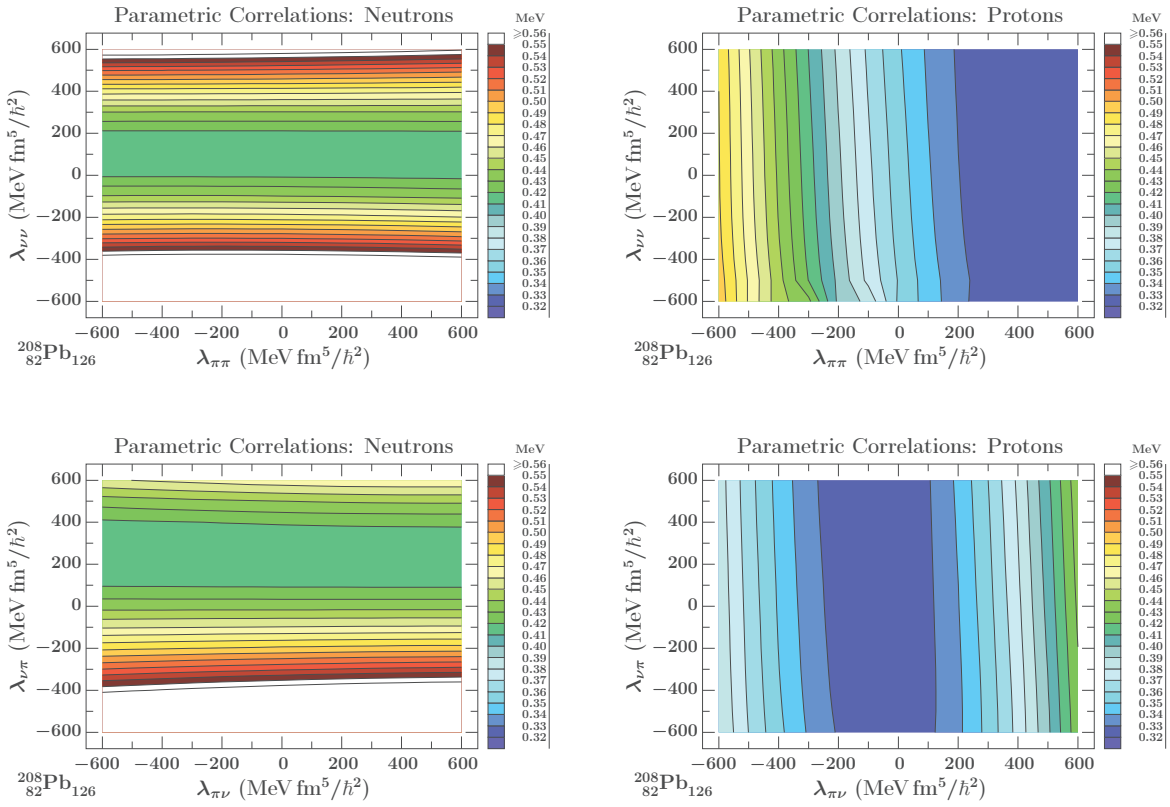

Figure 5.4 – Left column: Neutron r.m.s.-deviation projections onto the $(\lambda_{\pi\pi}, \lambda_{\nu\nu})$-plane (top) and $(\lambda_{\pi\nu}, \lambda_{\nu\pi})$-plane (bottom). The central potential parameters are fixed, cf. caption to Figure 5.3, and the minimisation performed over $\lambda_{\pi\nu}$ and $\lambda_{\nu\pi}$. Right column: Analogous illustration for the protons.

$(\lambda_{\pi\nu}, \lambda_{\nu\pi})$. The results take the same form of horizontal and vertical valleys indicating that $\lambda_{\pi\nu}$ and $\lambda_{\nu\pi}$ are mutually independent, and therefore de-correlated.

Conclusions. We may conclude this part of the discussion as follows. The four parameters

$$\{\lambda_{\pi\pi},\ \lambda_{\pi\nu},\ \lambda_{\nu\nu},\ \lambda_{\nu\pi}\} \tag{5.15}$$

may a priori present 4*3/2 = 6 one-to-one parametric correlations. After examining the r.m.s.-projection onto planes-(p_i, p_j), we have determined that the four among six couples are uncorrelated. The linear correlations are present between $\lambda_{\pi\pi}$ and $\lambda_{\pi\nu}$ on the one-hand side, and $\lambda_{\nu\nu}$ and $\lambda_{\nu\pi}$ on the other. In other words $\hat{V}^{\pi}_{SO}$ and $\hat{V}^{\nu}_{SO}$ may be considered independent – and this – despite the fact that the proton and neutron densities are determined using a simultaneous self-consistency algorithm.

5.3 Microscopic Justification of Linear Correlations

In this Section we are going to construct a microscopic justification scheme for the presence of the linear correlations between the coupling constants of the spin-orbit interaction potential used in this Chapter.

$\lambda_{\pi\pi}$	$\lambda_{\pi\nu}$	$\lambda_{\nu\nu}$	$\lambda_{\nu\pi}$
−400	600	600	−200
−200	400	400	0
0	200	0	200
200	0	−200	400
600	−200	−400	600

Table 5.1 – Five selections of parameters $\{\lambda_{\pi\pi}, \lambda_{\pi\nu}, \lambda_{\nu\nu}, \lambda_{\nu\pi}\}$ from the bottoms of the valleys in Figure 5.3. They have been used to calculate the density gradients in Figure 5.5.

For the sake of an illustration, let us focus on the $(\lambda_{\pi\pi}, \lambda_{\pi\nu})$ and $(\lambda_{\nu\nu}, \lambda_{\nu\pi})$ valley-patterns in Figure 5.3. Their forms indicate that independently of the particular choice of the pair of parameters along the straight line connecting the points at the bottom of the valley, the results for the χ^2 stay constant or nearly constant and very close to the optimal value.

For testing purposes we selected a sequence of pairs of coordinates of equidistant points along the two valleys. They are presented in Table 5.1. In our tests the attribution of pairs between the first two columns and the last two is completely arbitrary and we could have made another choice between 25 of all possible combinations. This independence between the pairs selection is as a matter of fact the central point of the following discussion addressing the issue of the 'independence of the choice'.

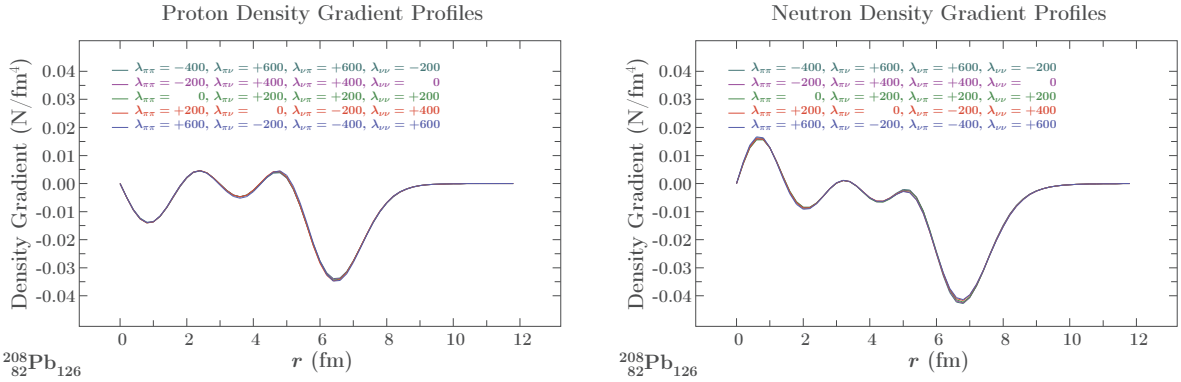

Figure 5.5 – Proton density gradient (left) and neutron density gradient (right) obtained considering 5 arbitrary selections of the $\{\lambda_{\pi\pi}, \lambda_{\pi\nu}, \lambda_{\nu\pi}, \lambda_{\nu\nu}\}$ parameter-sets from Table 5.1. Two properties deserve emphasizing. Firstly, within the scale of the illustration the curves corresponding to various and very different parameter choices are not distinguishable. Secondly, at the small distances from the centre of the nucleus, for, approximately, $r \in [0, 3]$ fm, the gradient of the density of the neutrons and the one of the protons are essentially of opposite signs whereas at relatively large r-values the two functions behave similarly.

Each selection of parameter values from Table 5.1 was used to calculate the density

gradient profiles for protons and neutrons. These profiles are presented in Figure 5.5, which shows that the resulting curves are not distinguishable within the scale of the diagram. Furthermore, in the nuclear interior, more precisely for $r \in [0, 4.5]$ fm, approximately, the density gradients oscillate remaining close to zero, thus contributing relatively little to the matrix elements of the spin-orbit interaction potential. Moreover, for $r \in [0, 2.5]$ fm, approximately, the proton and neutron gradients fluctuate keeping opposite signs. This implies that whatever relatively small contributions to the integrals in the matrix elements the protons and the neutrons separately may provide in this part of the nuclear volume, a bulk of these contributions will cancel out as the result of summations of the proton and neutron terms.

At the same time, for big-r values corresponding to the vicinity of the nuclear surface, Σ, both profiles have a similar structure so that one may write

$$\text{Close to } \Sigma: \quad \nabla\rho_\pi(r) \propto \nabla\rho_\nu(r) \;\leftrightarrow\; \nabla\rho_{q'}(r) \propto \nabla\rho_q(r) \;\leftrightarrow\; \nabla\rho_{q'}(r) \approx \mu\nabla\rho_q(r), \tag{5.16}$$

where μ is a certain constant, and we find

$$\begin{aligned} \hat{V}_q^{so} &= \left(\lambda_{qq}\frac{1}{r}\frac{d\rho_q}{dr} + \lambda_{qq'}\frac{1}{r}\frac{d\rho_{q'}}{dr}\right)\hat{\ell}\cdot\hat{s} \\ &\approx \underbrace{(\lambda_{qq} + \mu\lambda_{qq'})}_{\equiv\eta}\frac{1}{r}\frac{d\rho_q}{dr}\hat{\ell}\cdot\hat{s} = \eta\frac{1}{r}\frac{d\rho_q}{dr}\hat{\ell}\cdot\hat{s}, \end{aligned} \tag{5.17}$$

where η is yet another constant. It then follows that:

$$\lambda_{qq'} = \frac{1}{\mu}(\eta - \lambda_{qq}) \;\leftrightarrow\; \lambda_{qq'} = \alpha\cdot\lambda_{qq} + \beta. \tag{5.18}$$

The above argumentation leads to the same result as the one conjectured in Eq. (5.14) and can be seen as the microscopic justification of the latter. Thus the fully microscopic origin of the linear correlations between $\lambda_{\pi\pi}$ and $\lambda_{\pi\nu}$ on the one hand-side and $\lambda_{\nu\nu}$ and $\lambda_{\nu\pi}$ on the other can be considered 'discovered' for the generalised Woods-Saxon Hamiltonian studied in this Chapter.

The property of the independence of the parameters illustrated in Figure 5.4 suggests the simplest realisation of such a condition for the parameter optimisation procedure, *viz.* choosing the spin-orbit parametrisation in the form

$$\boxed{\lambda_{\pi\pi} \approx \lambda_{\pi\nu} \approx \lambda_{\nu\pi} \approx \lambda_{\nu\nu} \equiv \lambda,} \tag{5.19}$$

at least for ^{208}Pb. To convince ourselves that the proposed relation can be used more generally, we carried out equivalent r.m.s.-projection tests for other nuclei studied in this document, and it turns out that solutions in Eq. (5.14) and (5.17-5.18) are also justified, cf. Annexe A.

5.4 Results of Monte Carlo Simulations

After detecting the shape of the parametric correlations in the present form of the Hamiltonian, we proceed with the Monte Carlo simulations to study the dependence of the single particle level uncertainties on σ_{exp} as well as on the parameter-correlation removal.

In the previous chapter we showed that the central diffuseness parameter does not correlate with the other parameters what suggests the possibility of fixing it – for simplicity, at least in the exploratory phase – at a certain plausible value. We selected here the values used as usual with the universal-parameter set of the traditional Woods-Saxon Hamiltonian:

$$a_\nu^c = a_\pi^c = 0.7 \text{ fm}. \tag{5.20}$$

With this *ad hoc* assumption the minimisation parameter set reduces to

$$\{V_\pi^c, V_\nu^c, r_\pi^c, r_\nu^c, \lambda_{\pi\pi}, \lambda_{\pi\nu}, \lambda_{\nu\nu}, \lambda_{\nu\pi}\}. \tag{5.21}$$

Following the structure of the presentation in the previous Chapter, we begin with the $\sigma_{exp} = 600$ keV case, since this value can be considered representative for the present-day experimental uncertainties of the mean-field single-nucleon energies.

5.4.1 Central Potential Parametric Correlations

Figure 5.6 shows the results of our Monte-Carlo simulations demonstrating a parabolic dependence between the central-depth and the central-radius parameters, similar to the one obtained in the case of the traditional Woods-Saxon Hamiltonian. Table 5.2 presents the values of the coefficients of the two parabolas fitted, for protons and neutrons, cf. Eq. (4.3).

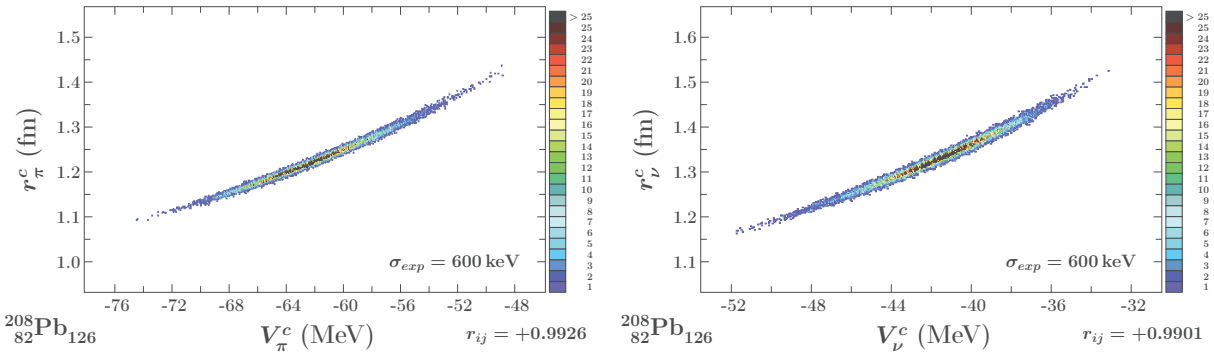

Figure 5.6 – Dot-plot representations of the realistic Monte Carlo simulations showing the projections on the (V_π^c, r_π^c)-plane (left) and (V_ν^c, r_ν^c)-plane (right). They have been obtained imposing $\sigma_{exp} = 600$ keV.

	α [fm MeV^{-2}]	β [fm MeV^{-1}]	γ [fm]
protons π	0.0001893	0.0361974	2.7404277
neutrons ν	0.0003844	0.0515710	2.8095715

Table 5.2 – Parabola coefficients, cf. Eq. (4.3), fitted to the diagrams presented in Figure 5.6, for protons and neutrons.

Having determined the form of the central-potential parametric correlations we will proceed, as in the previous Chapter, to analysing the effect of the spin-orbit parametric correlations.

5.4.2 Spin-Orbit Linear Parametric-Correlations: Monte-Carlo

We proceed by showing the dot-plot representation of the correlations for those two combinations among the density-dependent spin-orbit parameters which were originally showing the linear correlations. The results are given in Figure 5.7. They are fully analogous to those in Figure 5.3, apart from the scales on the x-, and y-axes, here adapted to the distributions of the 'dots' on the 'dot-plots'. A careful comparison of Figures 5.7 and 5.3 (taking into account the scale differences) shows that they are fully equivalent: Both show the same linear parametric correlation. Using the results in Figure 5.7 we calculate the Pearson coefficient $r_{ij} \approx -0.9$, thus confirming the strongly linear correlations between the pairs of parameters studied.

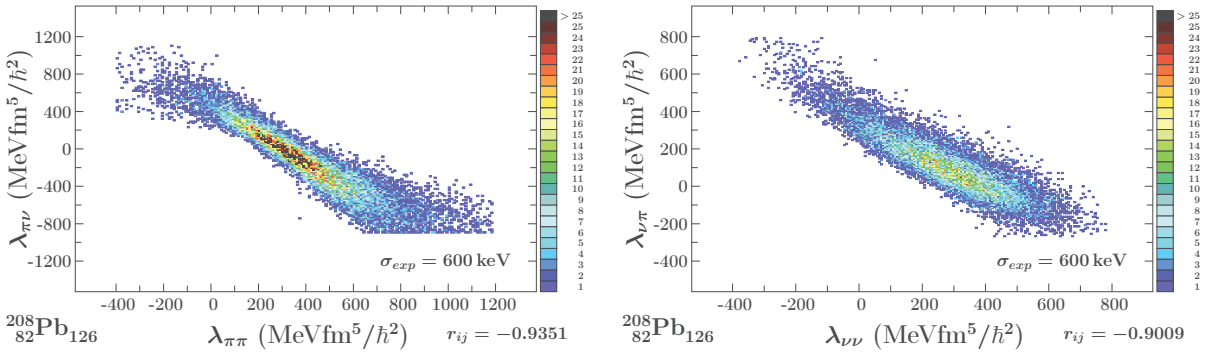

Figure 5.7 – Dot-plot representations of the realistic Monte Carlo calculations on the $(\lambda_{\pi\pi}, \lambda_{\pi\nu})$-plane (right) and $(\lambda_{\nu\nu}, \lambda_{\nu\pi})$-plane (left). The results were obtained imposing $\sigma_{exp} = 600$ keV and show a clear linear dependence between the pairs of parameters considered [see the text for more details].

Conclusion. We obtain a fully consistent image of

$$\text{Linear correlations present between :} \quad \lambda_{\pi\pi} \text{ and } \lambda_{\pi\nu}, \tag{5.22}$$

$$\lambda_{\nu\nu} \text{ and } \lambda_{\nu\pi}, \tag{5.23}$$

via both χ^2-test and and Monte-Carlo simulations.

5.4.3 Signs of No-Correlation Patterns: Monte-Carlo

After presenting the case of the detected parametric correlations in the preceding Section, we will switch now to the case of four other combinations of pairs of parameters showing originally the horizontal or vertical valley-pattern, thus parametric independence.

Figure 5.8 address this situation. Notice that Figs. 5.8 and 5.4 are equivalent even though showing the same information in a different manners. Indeed, the dot-plot representation of the non-existing correlations should manifest radial symmetry which is indeed the case, whereas the Pearson coefficients, nearly zero, fully confirm this expectation.

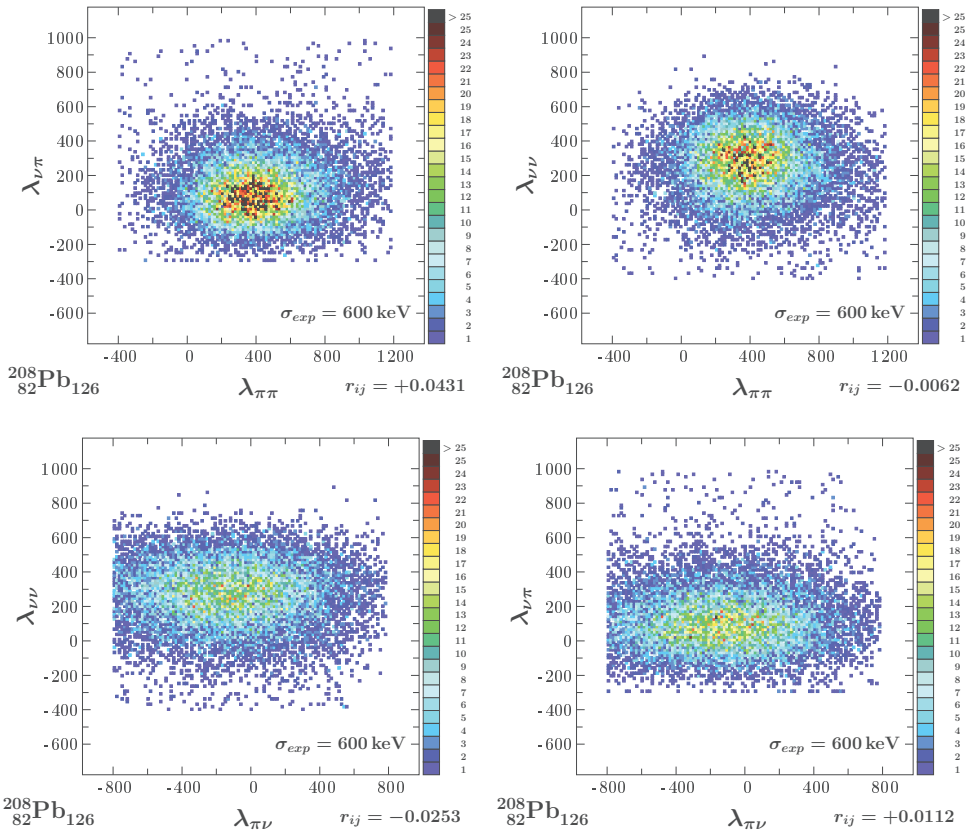

Figure 5.8 – The same as in Figure 5.7 but for projections on the planes $(\lambda_{\pi\pi}, \lambda_{\nu\pi})$ (top-left), $(\lambda_{\pi\pi}, \lambda_{\nu\nu})$ (top-right), $(\lambda_{\nu\nu}, \lambda_{\pi\nu})$ (bottom-left) and $(\lambda_{\pi\nu}, \lambda_{\nu\pi})$ (bottom-right). Let us emphasise that all the figures manifest *consistently parametric independence* both 'graphically' and via Pearson coefficients. Certain small deviations from the radial symmetry may result both form the insufficient statistics in the Monte-Carlo runs and from the Coulomb term whose contribution influences diffusivity 'rigidly' (no Coulomb parameter adjustment).

Conclusion. We obtain a consistent (χ^2-test, Pearson, Monte-Carlo) image of

$$\text{Linear correlations absent between :} \quad \lambda_{\pi\pi} \text{ and } \lambda_{\nu\pi}, \tag{5.24}$$
$$\lambda_{\pi\pi} \text{ and } \lambda_{\nu\nu}, \tag{5.25}$$
$$\lambda_{\nu\nu} \text{ and } \lambda_{\pi\nu}, \tag{5.26}$$
$$\lambda_{\pi\nu} \text{ and } \lambda_{\nu\pi}, \tag{5.27}$$

via both χ^2-test and and Monte-Carlo simulations.

5.5 Uncertainties Within Full Parametric Freedom

To keep as much as possible the analogy between the structure of the presentations in the preceding Chapter 4 and in this one, we will introduce here the results of the uncertainty distributions for the neutron and proton mean-field energies obtained from the Monte-Carlo simulations. Table 5.3 and Figure 5.9 refer to the neutron solutions, Table 5.4 and Figure 5.10 to the proton ones.

5.5.1 Properties of the Neutron Levels

Let us observe that there is a systematic difference between the results with the phenomenological description of the spin-orbit interaction and the actual one: The density dependent variant produces systematically narrower uncertainty widths. This can be seen comparing Tables 5.3 and 4.7, the latter copied below[2] as Table 5.4.

		$N_{\text{main}} = 5$						$N_{\text{main}} = 6$						
Z	N	$2f_{7/2}$	$1h_{9/2}$	$1i_{13/2}$	$3p_{3/2}$	$2f_{5/2}$	$3p_{1/2}$	$2g_{9/2}$	$1j_{15/2}$	$1i_{11/2}$	$3d_{5/2}$	$2g_{7/2}$	$4s_{1/2}$	$3d_{3/2}$
82	126	0.89*	1.34	1.13*	0.65*	0.92*	0.67*	0.95*	1.71	1.20*	0.56*	1.06*	0.39*	0.52*
114	164	1.16	1.88	1.29	0.99	1.13	1.00	0.92	1.39	1.60	0.64	0.92	0.58	0.63
114	170	1.23	1.93	1.28	1.04	1.19	1.06	0.86	1.28	1.57	0.58	0.89	0.50	0.58
114	172	1.27	2.10	1.37	1.08	1.18	1.11	0.86	1.38	1.76	0.57	0.90	0.49	0.60
114	180	1.45	2.20	1.49	1.22	1.34	1.21	0.93	1.35	1.77	0.66	0.94	0.57	0.73
114	184	1.57	2.34	1.71	1.32	1.42	1.30	1.06	1.58	1.95	0.74	1.03	0.65	0.81
114	196	1.87	2.49	1.87	1.65	1.69	1.65	1.27	1.55	1.95	1.03	1.19	0.96	1.18
114	214	2.42	2.89	2.37	2.20	2.28	2.14	1.84	1.98	2.27	1.49	1.82	1.46	1.64
114	228	2.84	3.34	2.86	2.59	2.67	2.58	2.25	2.43	2.75	1.86	2.19	1.81	2.06

Table 5.3 – Realistic Monte Carlo calculations of the FWHM [in MeV] of the neutron single particle energy uncertainty distributions for ^{208}Pb and several Fl-isotopes, within the main shells $N_{\text{main}} = 5$ and 6. The results have been obtained using the density-dependent spin-orbit potential, minimising the χ^2 over the parameters in Eq. (5.21) and imposing the condition in Eq. (5.20). The asterisk indicates that the level is experimentally known.

		$N_{\text{main}} = 5$						$N_{\text{main}} = 6$						
Z	N	$2f_{7/2}$	$1i_{13/2}$	$1h_{9/2}$	$3p_{3/2}$	$2f_{5/2}$	$3p_{1/2}$	$2g_{9/2}$	$1j_{15/2}$	$1i_{11/2}$	$3d_{5/2}$	$4s_{1/2}$	$2g_{7/2}$	$3d_{3/2}$
82	126	1.09*	1.38*	1.99	0.76*	1.04*	0.77*	0.98*	2.37	1.39*	0.88*	0.79*	1.10*	0.82*
114	164	1.43	1.53	2.55	1.05	1.31	1.03	0.99	1.77	1.73	0.77	0.75	1.02	0.83
114	170	1.59	1.54	2.63	1.22	1.49	1.20	0.91	1.53	1.69	0.63	0.59	0.91	0.67
114	172	1.66	1.58	2.68	1.30	1.57	1.28	0.92	1.48	1.70	0.62	0.59	0.92	0.67
114	180	2.00	1.81	2.91	1.67	1.93	1.65	1.14	1.39	1.85	0.84	0.78	1.11	0.84
114	184	2.19	1.96	3.06	1.87	2.14	1.85	1.30	1.42	1.98	1.01	0.94	1.27	1.00
114	196	2.78	2.51	3.55	2.48	2.76	2.47	1.85	1.74	2.46	1.57	1.47	1.83	1.53
114	214	3.66	3.38	4.35	3.37	3.67	3.36	2.70	2.48	3.28	2.39	2.25	2.69	2.33
114	228	4.31	4.04	4.96	4.01	4.33	4.00	3.32	3.10	3.91	2.98	2.80	3.31	2.86

Table 5.4 – The same as the preceding Table but for the traditional Woods-Saxon Hamiltonian [reproduced from the preceding Chapter for the reader's convenience].

[2] Let us remark, nevertheless, that in the present case the central diffuseness parameter is kept fixed. This will have no impact on the present analysis since our interest is focussed on the variation of uncertainties induced by elimination of parametric correlations.

Concerning the NO-GO mechanism discussed in the preceding Chapter in the context of the $_{114}$Fl predictions for $N > 184$, the present results remain analogous: The widths of the uncertainty distributions remain very large in certain cases so that one can hardly speak about the quality in predicting and/or predictive power.

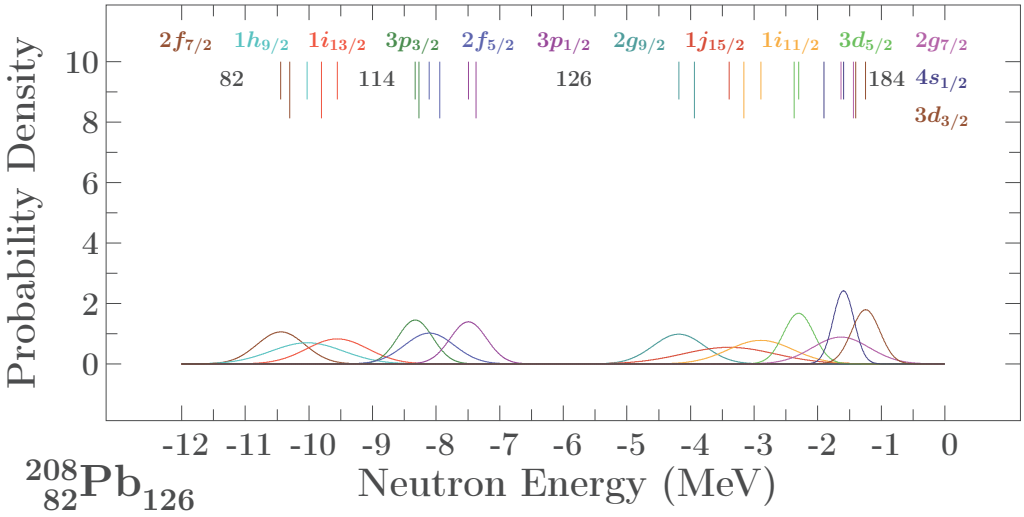

Figure 5.9 – Uncertainty probability distributions for the neutron single particle energies within the main nuclear shells $N_{\text{main}} = 5$ and 6. They have been obtained using realistic Monte Carlo simulations with $\sigma_{exp} = 600$ keV using the density-dependent spin-orbit and minimising over the set of parameters in Eq. (5.21), keeping $a^c_\pi = a^c_\nu = 0.7$ fm. The FWHM of each distribution can be found in Table 5.3. The surface under each curve is equal to 1.

5.5.2 Properties of the Proton Levels

Proton results, analogous to the neutron results discussed in the preceding Section are shown in Table 5.5; they can be compared to the analogous results obtained with the traditional Woods-Saxon Hamiltonian, reproduced here for the reader's convenience as Table 5.6. On the average, the widths obtained with the density-dependent spin-orbit potential are narrower, but fluctuations are non-negligible.

		$N_{\text{main}} = 4$					$N_{\text{main}} = 5$					
Z	N	$1g_{7/2}$	$2d_{5/2}$	$1h_{11/2}$	$2d_{3/2}$	$3s_{1/2}$	$1h_{9/2}$	$2f_{7/2}$	$1i_{13/2}$	$2f_{5/2}$	$3p_{3/2}$	$3p_{1/2}$
82	126	1.19	1.22	0.98*	1.03*	0.99*	1.15*	1.05*	1.18*	1.09*	0.74	0.79
114	164	1.59	1.12	1.30	1.24	0.95	1.62	0.67	1.45	0.86	0.65	0.97
114	170	1.69	1.30	1.40	1.23	1.10	1.59	0.76	1.40	0.77	0.67	1.17
114	172	2.05	1.35	1.81	1.32	1.16	2.08	0.72	1.88	0.77	0.82	0.94
114	180	2.13	1.65	1.89	1.54	1.44	1.94	0.94	1.76	0.87	0.78	0.71
114	184	2.13	1.81	2.02	1.68	1.58	1.72	1.06	1.94	0.98	0.87	0.80
114	196	2.57	2.25	2.32	2.16	2.05	2.10	1.42	2.03	1.34	1.27	1.13
114	214	3.03	2.96	2.77	2.75	2.73	2.23	2.16	2.26	1.82	1.85	1.83
114	228	3.69	3.47	3.46	3.26	3.25	3.02	2.65	3.16	2.34	2.38	2.25

Table 5.5 – Equivalent to Table 5.3 – density-dependent spin-orbit potential – but for the protons, within main shells $N_{\text{main}} = 4$ and 5.

		$N_{\text{main}} = 4$					$N_{\text{main}} = 5$					
Z	N	$1g_{7/2}$	$2d_{5/2}$	$1h_{11/2}$	$2d_{3/2}$	$3s_{1/2}$	$1h_{9/2}$	$2f_{7/2}$	$1i_{13/2}$	$2f_{5/2}$	$3p_{3/2}$	$3p_{1/2}$
82	126	1.96	1.28	1.20*	1.03*	1.01*	1.38*	1.11*	1.26*	1.22*	1.46	1.43
114	164	1.82	1.14	1.24	0.99	0.95	1.38	1.10	1.20	1.21	1.40	1.41
114	170	2.02	1.34	1.37	1.11	1.06	1.33	0.96	1.02	0.98	1.20	1.17
114	172	2.10	1.43	1.44	1.18	1.13	1.35	0.96	0.99	0.94	1.17	1.11
114	180	2.49	1.82	1.79	1.56	1.50	1.57	1.10	1.07	0.95	1.08	1.03
114	184	2.70	2.04	1.98	1.77	1.71	1.74	1.25	1.20	1.06	1.14	1.08
114	196	3.37	2.71	2.61	2.46	2.37	2.36	1.82	1.73	1.59	1.55	1.48
114	214	4.38	3.69	3.55	3.48	3.37	3.37	2.76	2.65	2.55	2.40	2.35
114	228	5.12	4.42	4.25	4.23	4.10	4.14	3.47	3.35	3.28	3.09	3.05

Table 5.6 – The same as in table 5.5 but for the protons, results with the traditional spin-orbit potential, covering the nuclear main shells $N_{\text{main}} = 4$ and 5.

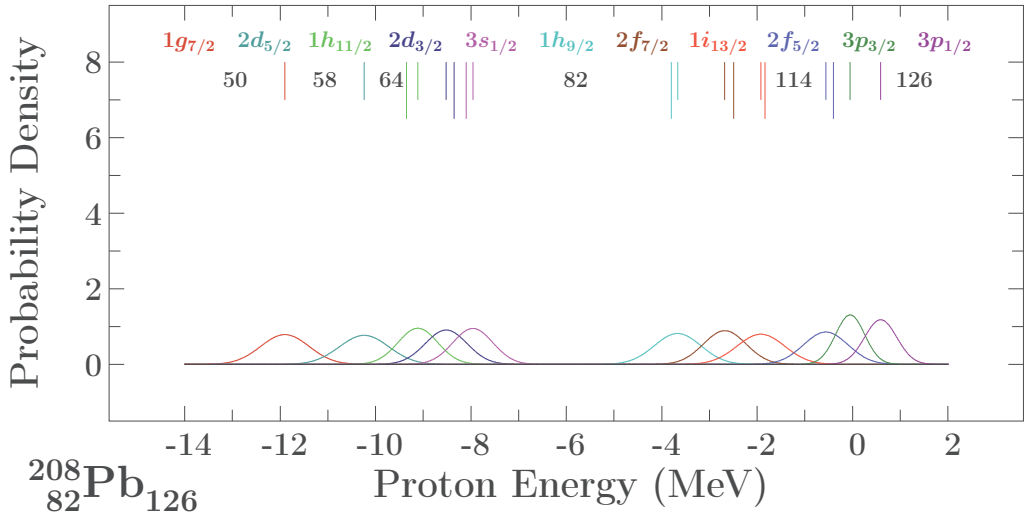

Figure 5.10 – Similar as in Figure 5.9 but for the proton levels within the main shells $N_{\text{main}} = 4$ and 5. The FWHM of each distribution can be found in Table 5.4.

5.5.3 Central Correlation: $r^c = f(V^c)$ – Impact on Uncertainties

Similarly to the presentation scheme adopted in Chapter 4, the first parametric correlation eliminated in the series is the one between the central-depth and the central-radius parameters, cf. Figure 5.6. In this case, the remaining parameters taken into account for the χ^2-minimisation are:

$$\{V^c_\pi, V^c_\nu, \lambda_{\pi\pi}, \lambda_{\pi\nu}, \lambda_{\nu\nu}, \lambda_{\nu\pi}\}. \tag{5.28}$$

Tables 5.7 and 5.8 show the corresponding results obtained for the level distributions widths for neutrons and protons, respectively.

^{208}Pb Neutron Orbitals. The widths in Table 5.7 are systematically smaller as compared to the ones of Table 5.3. As noticed previously, the decrease rate depends on the value of the orbital angular momentum, ℓ, of the state. The uncertainty widths of the levels $3p_{3/2}$, $3d_{5/2}$ and $3d_{3/2}$ become smaller by about 30% with the density-dependent Hamiltonian. On the other hand, levels $1i_{13/2}$, $3p_{1/2}$, $2g_{9/2}$, $1i_{11/2}$ and $2g_{7/2}$ improved between 10% and 20% their distribution widths. The $4s_{1/2}$ orbital deserves special attention: its width improved by 67%. Characteristically, the experimentally unknown levels $1h_{9/2}$ and $1j_{15/2}$, barely improve when passing to the density-dependent variant in full analogy to the phenomenological spin-orbit description, cf. comparison between Tables 4.7 and 4.9.

$_{144}$Fl Isotope Neutron-Orbitals. The uncertainty widths of the levels in the superheavy nuclei are also systematically smaller, cf. Table 5.7 as compared to Table 5.3, and similarly as before the best improvements are observed for the neutron levels with $N < 184$.

		$N_{\text{main}} = 5$						$N_{\text{main}} = 6$						
Z	N	$2f_{7/2}$	$1h_{9/2}$	$1i_{13/2}$	$3p_{3/2}$	$2f_{5/2}$	$3p_{1/2}$	$2g_{9/2}$	$1j_{15/2}$	$1i_{11/2}$	$3d_{5/2}$	$2g_{7/2}$	$4s_{1/2}$	$3d_{3/2}$
82	126	0.73*	1.33	0.99*	0.45*	0.86*	0.55*	0.79*	1.67	1.08*	0.35*	0.96*	0.13*	0.35*
114	164	1.06	1.87	1.18	0.90	1.09	0.92	0.73	1.31	1.51	0.42	0.81	0.37	0.45
114	170	1.14	1.94	1.17	0.96	1.17	0.97	0.68	1.17	1.50	0.31	0.80	0.21	0.39
114	172	1.22	2.17	1.29	0.98	1.22	1.01	0.74	1.27	1.79	0.34	0.89	0.20	0.50
114	180	1.39	2.32	1.43	1.15	1.36	1.18	0.82	1.25	1.89	0.47	0.96	0.35	0.66
114	184	1.50	2.39	1.51	1.26	1.44	1.28	0.89	1.27	1.92	0.57	1.01	0.48	0.79
114	196	1.82	2.53	1.76	1.61	1.68	1.64	1.18	1.39	1.93	0.94	1.14	0.87	1.17
114	214	2.38	2.93	2.30	2.16	2.28	2.10	1.79	1.86	2.28	1.42	1.81	1.40	1.60
114	228	2.79	3.21	2.62	2.56	2.66	2.54	2.17	2.14	2.51	1.81	2.11	1.77	2.01

Table 5.7 – Realistic Monte Carlo calculations of the FWHM [in MeV] of the neutron single particle energy uncertainty distributions for ^{208}Pb and several Fl-isotopes, within the main shells $N_{\text{main}} = 5$ and 6. The results have been obtained using the density-dependent spin-orbit potential, minimising χ^2 over the parameters in Eq. (5.28), imposing $r^c_\nu = f(V^c_\nu)$ and $a^c_\pi = a^c_\nu = 0.7$ fm. The asterisk indicates that the level is experimentally known.

^{208}Pb Proton Orbitals. Similarly to the neutron case, the uncertainty widths in Table 5.8 are systematically smaller than the ones in Table 5.5 where the results with the full parametric freedom are collected. The decrease rates are mainly between 20% and 30%, following the trend: 'The lower the ℓ, the better the improvement'. In this case the best improvement is obtained for $3p_{3/2}$-orbital, with the distribution width over 60% narrower.

Proton $_{144}$Fl-Isotope levels. Again we observe an important improvement in Table 5.8 as compared to Table 5.5. In the present case, even the widths for the orbitals with $N > 184$ increase significantly, even though at least some distributions remain rather broad. As for ^{208}Pb, the level which obtains the best improvement is $3p_{3/2}$, narrowing its width down to $\sim 70\%$ of the original value at $N = 172$.

		$N_{\text{main}} = 4$					$N_{\text{main}} = 5$					
Z	N	$1g_{7/2}$	$2d_{5/2}$	$1h_{11/2}$	$2d_{3/2}$	$3s_{1/2}$	$1h_{9/2}$	$2f_{7/2}$	$1i_{13/2}$	$2f_{5/2}$	$3p_{3/2}$	$3p_{1/2}$
82	126	0.93	1.05	0.89*	0.92*	0.79*	0.82*	0.73*	1.11*	1.08*	0.33	0.73
114	164	1.28	1.04	1.25	0.95	0.77	1.17	0.38	1.40	0.56	0.43	0.65
114	170	1.40	1.17	1.33	0.96	0.93	1.11	0.48	1.32	0.56	0.55	0.89
114	172	1.79	1.24	1.94	1.01	1.00	1.78	0.61	2.01	0.64	0.25	0.50
114	180	2.04	1.54	2.21	1.33	1.29	1.90	0.76	2.23	0.63	0.46	0.59
114	184	2.13	1.69	2.26	1.48	1.45	1.87	0.87	2.21	0.68	0.60	0.65
114	196	2.37	2.16	2.30	2.06	1.93	1.73	1.30	2.02	1.10	1.07	1.00
114	214	2.91	2.87	2.74	2.63	2.64	2.03	2.03	2.26	1.67	1.73	1.68
114	228	3.43	3.38	3.19	3.15	3.15	2.54	2.55	2.56	2.21	2.27	2.15

Table 5.8 – Realistic Monte Carlo calculations of the FWHM [in MeV] of the proton single particle energy uncertainty distributions for ^{208}Pb and several Fl-isotopes, within the main shells $N_{\text{main}} = 4$ and 5. The results have been obtained using the density-dependent spin-orbit potential, minimising χ^2 over the parameters in Eq. (5.28), imposing $r^c_\pi = f(V^c_\pi)$ and $a^c_\pi = a^c_\nu = 0.7$ fm. The asterisk indicates that the level is experimentally known.

5.6 Full Elimination of Parametric Correlations

In this section we analyse the results obtained after full removal of the parametric correlations in the density-dependent Hamiltonian what leads to the parametric freedom of three remaining parameters

$$\{V_\pi^c, V_\nu^c, \lambda\}. \tag{5.29}$$

We will begin by analysing the final results of ^{208}Pb and then we will focus our discussion on the $_{114}$Fl-isotope predictions.

5.6.1 Monte Carlo Results for ^{208}Pb

In what follows, to facilitate the interpretation of the results obtained in this section and corresponding to the full correlation removal we will also recall the results of the partial correlation removal form preceding sections. We begin with ^{208}Pb neutron orbitals. The results are collected in the tables which contain:

- Row no. 1: Results of the Monte Carlo simulations under the condition that the parameters in Eq. (5.21), i.e., $\{V_\pi^c, V_\nu^c, r_\pi^c, r_\nu^c, \lambda_{\pi\pi}, \lambda_{\pi\nu}, \lambda_{\nu\nu}, \lambda_{\nu\pi}\}$ are considered independent, and both proton and neutron central diffuseness are kept fixed at 0.7 fm.
- Row no. 2: Similar to the previous case, but we impose $r_{\pi,\nu}^c = f(V_{\pi,\nu}^c)$ thus eliminating the correlation between the central depth and central radius parameters. This corresponds to minimisation over parameters $\{V_\pi^c, V_\nu^c, \lambda_{\pi\pi}, \lambda_{\pi\nu}, \lambda_{\nu\nu}, \lambda_{\nu\pi}\}$ cf. Eq. (5.28).
- Row no. 3: Full elimination of the correlations minimising over parameters $\{V_\pi^c, V_\nu^c, \lambda\}$, cf. Eq. (5.29) under the assumption of all λ-coefficients equal, cf. Eq. (5.19).

$N_{\text{main}} = 5$						$N_{\text{main}} = 6$								
$\mathbf{2f_{7/2}*}$	$\mathbf{1h_{9/2}}$	$\mathbf{1i_{13/2}*}$	$\mathbf{3p_{3/2}*}$	$\mathbf{2f_{5/2}*}$	$\mathbf{3p_{1/2}*}$	$\mathbf{2g_{9/2}*}$	$\mathbf{1j_{15/2}}$	$\mathbf{1i_{11/2}*}$	$\mathbf{3d_{5/2}*}$	$\mathbf{2g_{7/2}*}$	$\mathbf{4s_{1/2}*}$	$\mathbf{3d_{3/2}*}$	r.m.s. [MeV]	Inv
0.89	1.34	1.13	0.65	0.92	0.67	0.95	1.71	1.20	0.56	1.06	0.39	0.52	0.21	1
0.73	1.33	0.99	0.45	0.86	0.55	0.79	1.67	1.08	0.35	0.96	0.13	0.35	0.21	1
0.74	1.33	0.81	0.53	0.49	0.45	0.32	1.64	0.80	0.26	0.60	0.12	0.20	0.26	1

Table 5.9 – Uncertainty widths, FWHM [in MeV], calculated using Monte-Carlo simulations with the density-dependent Hamiltonian for the main shells $N_{\text{main}} = 5$ and 6 in ^{208}Pb. The resulting r.m.s.-deviations [in MeV], cf. Eq. (3.30), are given in the last but 1 column. The last column controls the level ordering of the theoretical results with respect to the experimental ordering. The content of each row is defined at the beginning of this section. The asterisks indicate the levels which are known experimentally, thus included when minimising the χ^2-test.

^{208}Pb Neutron Orbitals. Table 5.9 shows the results for the neutron levels of ^{208}Pb around $N = 126$. Comparing the first with the last rows of the Table, one notices that all values are systematically smaller when the density-dependent Hamiltonian is used. The widths of the orbitals $2f_{5/2}$, $2g_{9/2}$, $3d_{5/2}$, $2g_{7/2}$, $4s_{1/2}$ and $3d_{3/2}$ are narrower by more than 40%, the width of $2g_{9/2}$ is 66% smaller, the one of $4s_{1/2}$ is 70% smaller. On the other hand, levels $1i_{13/2}$, $3p_{1/2}$, $1i_{11/2}$, $2f_{7/2}$ and $3p_{3/2}$ also improved, even though less, by about 20-30%; even the widths of $1h_{9/2}$ and $1j_{15/2}$ orbitals improved slightly.

^{208}Pb Neutron Orbitals – Graphical Comparison. Figure 5.11 shows the numerical results from row no. 1 and row no. 3 transformed into the uncertainty distributions.

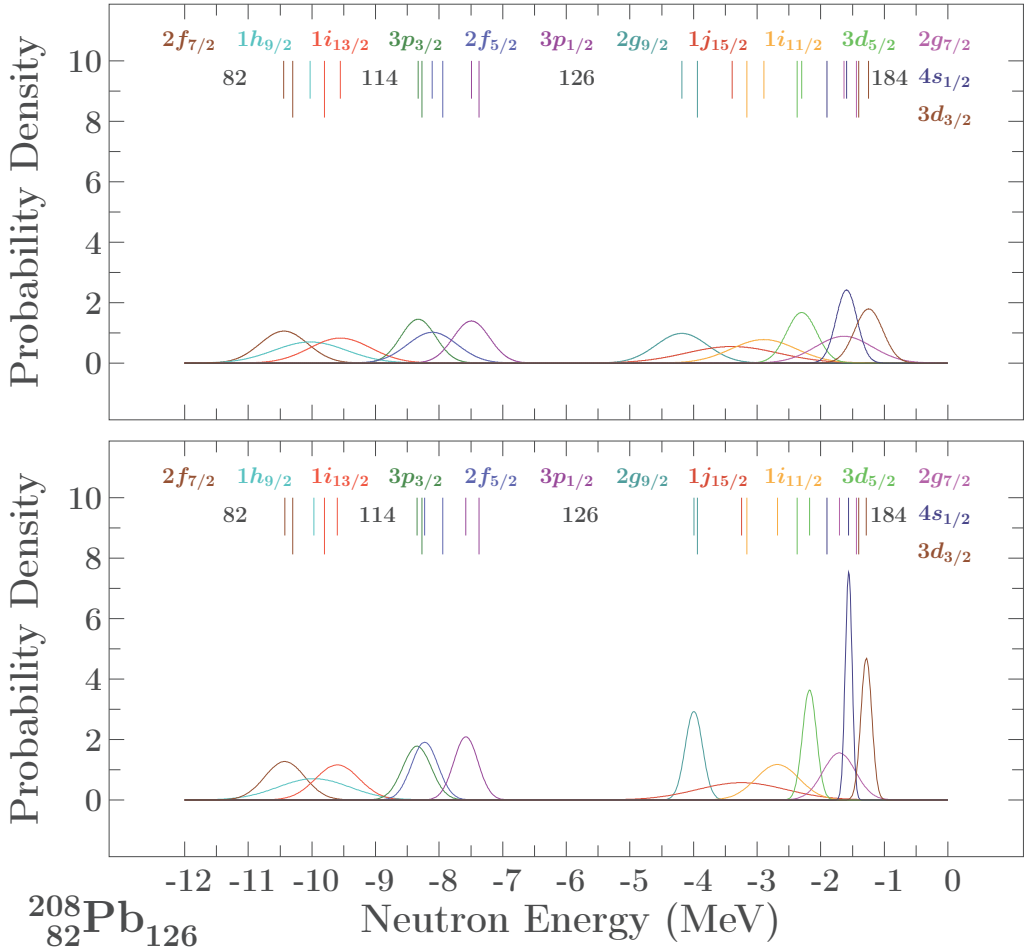

Figure 5.11 – Probability density distributions of the neutron single particle energies of ^{208}Pb within the main nuclear shells $N_{\text{main}} = 5$ and 6. They have been obtained with realistic Monte Carlo simulations with $\sigma_{exp} = 600$ keV using the density-dependent spin-orbit potential and minimising over the full set of parameters $\{V_\pi^c, V_\nu^c, r_\pi^c, r_\nu^c, \lambda_{\pi\pi}, \lambda_{\pi\nu}, \lambda_{\nu\nu}, \lambda_{\nu\pi}\}$ in Eq. (5.21) (top panel), and using parameters $\{V_\pi^c, V_\nu^c, \lambda\}$ from Eq. (5.29) (bottom panel). In both cases $a_\pi^c = a_\nu^c = 0.7$ fm. The FWHM of each distribution can be found in Table 5.9. The surface under each curve is equal to 1. Notice that the widths of the majority of levels decrease significantly when parametric correlations are fully elliminated.

^{208}Pb Proton Orbitals. Table 5.10 shows the results for the ^{208}Pb proton levels around $Z = 82$. Similarly to the neutron case, the full elimination of the parametric correlations leads to systematic and occasionally significant decrease in the uncertainty widths. The only level that seems to stay unchanged is $1g_{7/2}$ (not know experimentally). There are three remarkable orbitals for which the decrease in the uncertainty widths are very significant. These are $2f_{7/2}$ (78%), $2f_{5/2}$ (63%), $3p_{3/2}$ (77%) and $3p_{1/2}$ (61%). Levels $1h_{11/2}$ and $1h_{9/2}$ narrowed they distributions by over 50%. The widths of $2d_{5/2}$, $2d_{3/2}$ and $3s_{1/2}$ orbitals are improved by about 15%, and finally $1i_{13/2}$ had a tiny decrease of 7%.

$N_{\text{main}} = 4$						$N_{\text{main}} = 5$						
$\mathbf{1g_{7/2}}$	$\mathbf{2d_{5/2}}$	$\mathbf{1h_{11/2}*}$	$\mathbf{2d_{3/2}*}$	$\mathbf{3s_{1/2}*}$	$\mathbf{1h_{9/2}*}$	$\mathbf{2f_{7/2}*}$	$\mathbf{1i_{13/2}*}$	$\mathbf{2f_{5/2}*}$	$\mathbf{3p_{3/2}}$	$\mathbf{3p_{1/2}}$	r.m.s. [MeV]	Inv
1.19	1.22	0.98	1.03	0.99	1.15	1.05	1.18	1.09	0.74	0.79	0.17	0
0.93	1.05	0.89	0.92	0.79	0.82	0.73	1.11	1.08	0.33	0.73	0.16	0
1.19	1.03	0.53	0.90	0.85	0.51	0.23	1.09	0.40	0.17	0.31	0.32	0

Table 5.10 – Similar to Table 5.9 but for the protons, main shells $N_{\text{main}} = 4$ and 5. Since in the present calculations the parametric correlations have been removed, some parametric freedom has been removed as well what implies less freedom in approaching the experimental data and consequently the r.m.s.-values may increase.

^{208}Pb Proton Orbitals – Graphical Comparison. Figure 5.12 shows the corresponding proton level Gaussian distributions from Row no.1 and Row no.3.

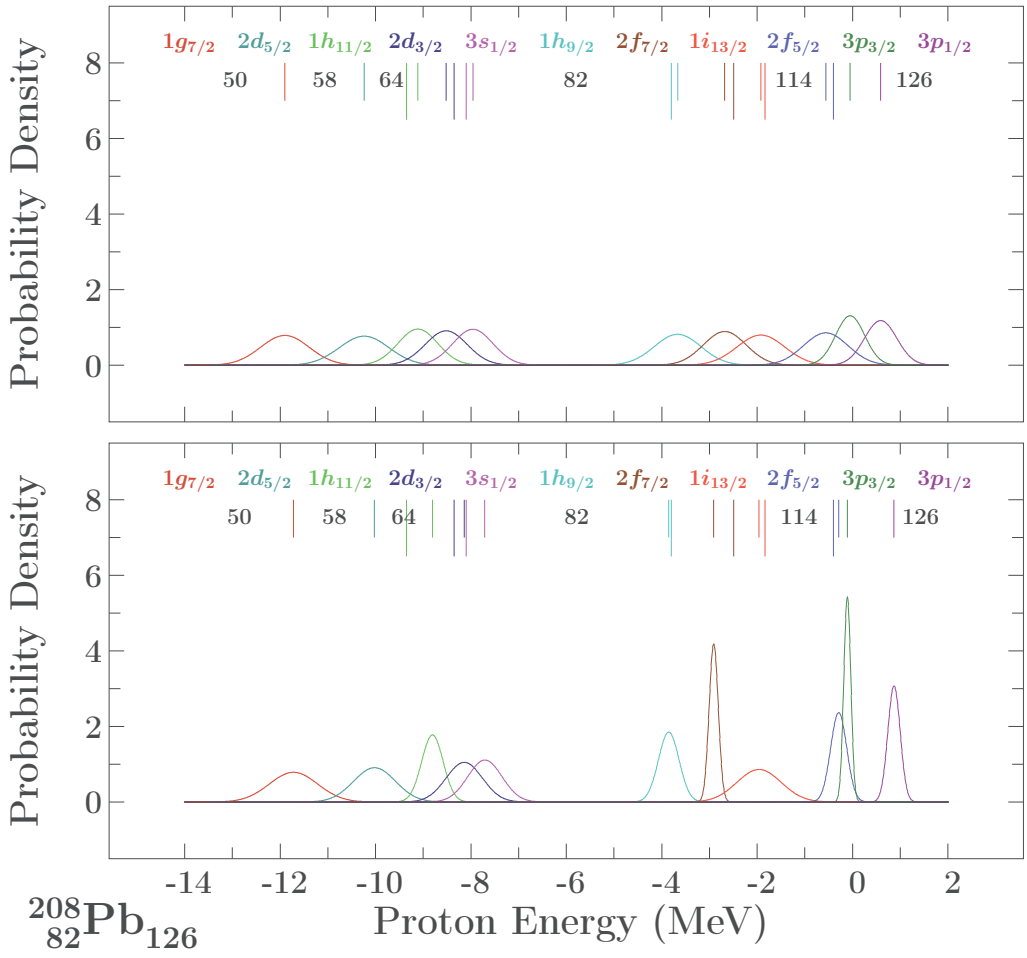

Figure 5.12 – Similar to Figure 5.11 but for the protons, main shells $N_{\text{main}} = 4$ and 5. The values of the distribution widths are contained in Table 5.10.

5.7 Monte Carlo Uncertainty-Widths for Fl-Isotopes

In this section we present the results for the uncertainty widths obtained with the density-dependent Hamiltonian for super-heavy isotopes of $_{114}$Fl – after the complete elimination of the parametric correlations.

5.7.1 Uncertainty Widths for Neutron Levels

Table 5.11 shows the results for the neutron levels in Fl-isotopes indicated, within the main shells around $N = 126$, after full parametric elimination. These results should be compared to the ones presented on Table 5.3, the latter copied below as Table 5.12, for reader's convenience. The use of the density-dependent spin-orbit potential has a positive impact on the levels in the $N_{\text{main}} = 6$ shell, whose widths significantly decrease as compared to the case when the Hamiltonian parameters where considered independent. Levels $2g_{9/2}$, $3d_{5/2}$, $2g_{7/2}$, $4s_{1/2}$ and $3d_{3/2}$ have decrease rates between 50% to 60% for the nuclei with $N \leq 184$.

		$N_{\text{main}} = 5$						$N_{\text{main}} = 6$						
Z	N	$2f_{7/2}$	$1h_{9/2}$	$1i_{13/2}$	$3p_{3/2}$	$2f_{5/2}$	$3p_{1/2}$	$2g_{9/2}$	$1j_{15/2}$	$1i_{11/2}$	$3d_{5/2}$	$2g_{7/2}$	$4s_{1/2}$	$3d_{3/2}$
114	164	1.07	1.62	1.13	0.90	1.00	0.87	0.47	1.56	0.79	0.44	0.69	0.45	0.54
114	170	1.22	1.91	0.92	1.01	1.10	0.96	0.40	1.18	1.05	0.25	0.45	0.22	0.29
114	172	1.29	2.05	0.87	1.07	1.16	1.02	0.46	1.07	1.20	0.25	0.42	0.20	0.25
114	180	1.64	2.48	0.85	1.41	1.45	1.30	0.83	0.71	1.64	0.57	0.48	0.47	0.43
114	184	1.84	2.69	0.94	1.60	1.62	1.47	1.05	0.62	1.85	0.77	0.61	0.66	0.61
114	196	2.42	3.29	1.51	2.20	2.20	1.98	1.66	0.92	2.43	1.34	1.16	1.22	1.16
114	214	3.32	4.15	2.43	3.08	3.00	2.73	2.57	1.77	3.26	2.10	1.93	1.98	1.93
114	228	3.96	4.76	3.11	3.69	3.58	3.31	3.20	2.45	3.86	2.68	2.51	2.52	2.49

Table 5.11 – Realistic Monte Carlo simulations showing the FWHM [in MeV] of the neutron levels within main shells $N_{\text{main}} = 5$ and 6 for different $_{114}$Fl-isotopes after imposing full parametric correlation elimination: $r^c = f(V^c)$ and $\lambda_{\pi\pi} = \lambda_{\pi\nu} = \lambda_{\nu\pi} = \lambda_{\nu\nu}$. The input experimental error is $\sigma_{exp} = 600$ keV.

		$N_{\text{main}} = 5$						$N_{\text{main}} = 6$						
Z	N	$2f_{7/2}$	$1h_{9/2}$	$1i_{13/2}$	$3p_{3/2}$	$2f_{5/2}$	$3p_{1/2}$	$2g_{9/2}$	$1j_{15/2}$	$1i_{11/2}$	$3d_{5/2}$	$2g_{7/2}$	$4s_{1/2}$	$3d_{3/2}$
114	164	1.16	1.88	1.29	0.99	1.13	1.00	0.92	1.39	1.60	0.64	0.92	0.58	0.63
114	170	1.23	1.93	1.28	1.04	1.19	1.06	0.86	1.28	1.57	0.58	0.89	0.50	0.58
114	172	1.27	2.10	1.37	1.08	1.18	1.11	0.86	1.38	1.76	0.57	0.90	0.49	0.60
114	180	1.45	2.20	1.49	1.22	1.34	1.21	0.93	1.35	1.77	0.66	0.94	0.57	0.73
114	184	1.57	2.34	1.71	1.32	1.42	1.30	1.06	1.58	1.95	0.74	1.03	0.65	0.81
114	196	1.87	2.49	1.87	1.65	1.69	1.65	1.27	1.55	1.95	1.03	1.19	0.96	1.18
114	214	2.42	2.89	2.37	2.20	2.28	2.14	1.84	1.98	2.27	1.49	1.82	1.46	1.64
114	228	2.84	3.34	2.86	2.59	2.67	2.58	2.25	2.43	2.75	1.86	2.19	1.81	2.06

Table 5.12 – Realistic Monte Carlo calculations of the FWHM [in MeV] of the neutron single particle energy uncertainty distributions for several Fl-isotopes, within the main shells $N_{\text{main}} = 5$ and 6. The results have been obtained using the density-dependent spin-orbit potential, minimising the χ^2 over the parameters in Eq. (5.21) and imposing the condition in Eq. (5.20) - full parametric freedom. [Copied here for reader's convenience.]

		$N_{\text{main}} = 5$						$N_{\text{main}} = 6$						
Z	N	$2f_{7/2}$	$1i_{13/2}$	$1h_{9/2}$	$2f_{5/2}$	$3p_{3/2}$	$3p_{1/2}$	$2g_{9/2}$	$1i_{11/2}$	$1j_{15/2}$	$3d_{5/2}$	$4s_{1/2}$	$2g_{7/2}$	$3d_{3/2}$
114	164	0.92	1.42	1.14	0.89	0.72	0.76	0.71	1.39	1.23	0.51	0.48	0.61	0.48
114	170	0.90	1.43	1.02	0.88	0.68	0.74	0.49	1.18	1.17	0.23	0.22	0.51	0.23
114	172	0.93	1.46	1.01	0.91	0.70	0.77	0.45	1.13	1.17	0.16	0.17	0.53	0.18
114	180	1.11	1.63	1.06	1.11	0.90	0.98	0.50	1.00	1.29	0.32	0.33	0.73	0.38
114	184	1.24	1.74	1.15	1.24	1.04	1.12	0.63	1.00	1.40	0.49	0.50	0.89	0.54
114	196	1.69	2.17	1.52	1.72	1.52	1.60	1.09	1.21	1.82	1.00	0.97	1.39	1.04
114	214	2.41	2.88	2.20	2.45	2.23	2.32	1.80	1.77	2.53	1.69	1.63	2.12	1.71
114	228	2.93	3.43	2.72	2.99	2.75	2.84	2.31	2.25	3.08	2.17	2.08	2.65	2.18

Table 5.13 – The same as the preceding Table but for the traditional Woods-Saxon Hamiltonian imposing compact spin-orbit solution [reproduced from the preceding Chapter for the reader's convenience].

Partial Summary, Remarks and Comments. In the case of the density-dependent potential and for the very lightest isotopes we observe a slight improvement of uncertainty widths for $N = 5$ (not as good as in the ^{208}Pb case) and on the average much better for the $N = 6$ shell. However for $N > 184$, in majority of the cases the parameter removal does not improve the trend. This is very likely due to the fact that in these nuclei we approach the NO-GO regime according to which the uncertainty widths are very large to start with what causes a strong overlapping of the distributions and thus much smaller impact of the potential variations on the final calculated eigenstates.

Comparing with the results for the traditional potential we may notice that the results with the density dependent potential – thus depending on one spin-orbit potential parameter – are of comparable quality.

5.7.2 Uncertainty Widths, Neutrons, Graphical Comparisons

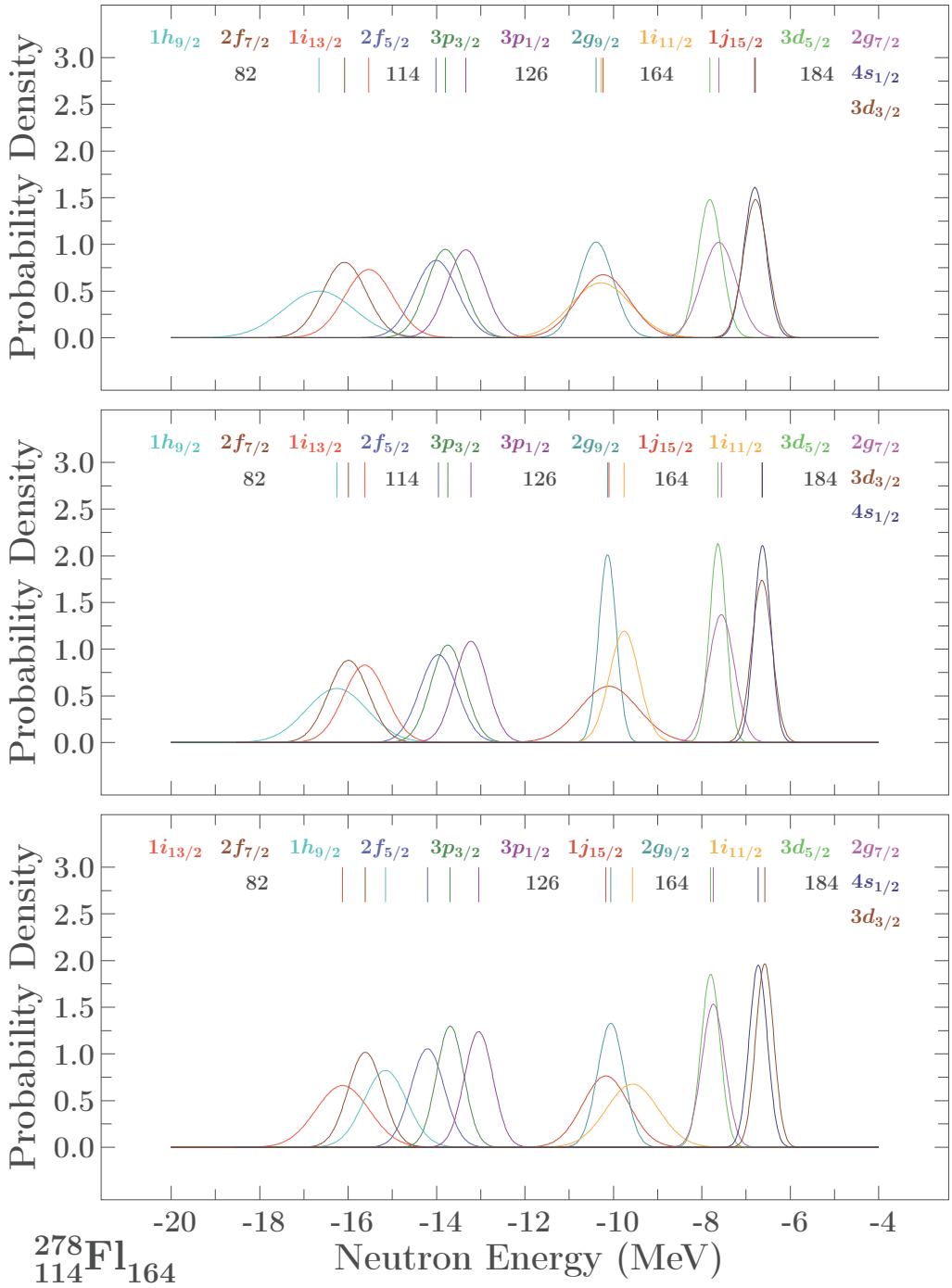

Figure 5.13 – Probability density distributions for neutrons within the main nuclear shells $N_{\text{main}} = 5$ and 6 from Monte Carlo simulations with $\sigma_{exp} = 600$ keV using the density-dependent spin-orbit potential, top and middle panels. Minimisation over parameters in Eq. (5.21) (top panel, full parametric freedom), and using parameters on Eq. (5.29) (centre panel, full elimination), keeping in both cases $a^c_\pi = a^c_\nu = 0.7$ fm. Bottom panel: Full parametric correlation elimination using traditional Woods-Saxon Hamiltonian and imposing compact solution for the spin-orbit parameters. The FWHM of each distribution can be found in Tables 5.3, Table 5.11 and 5.13, for top, middle and bottom panels, respectively. Cf. synthetic comments after Fig. 5.15.

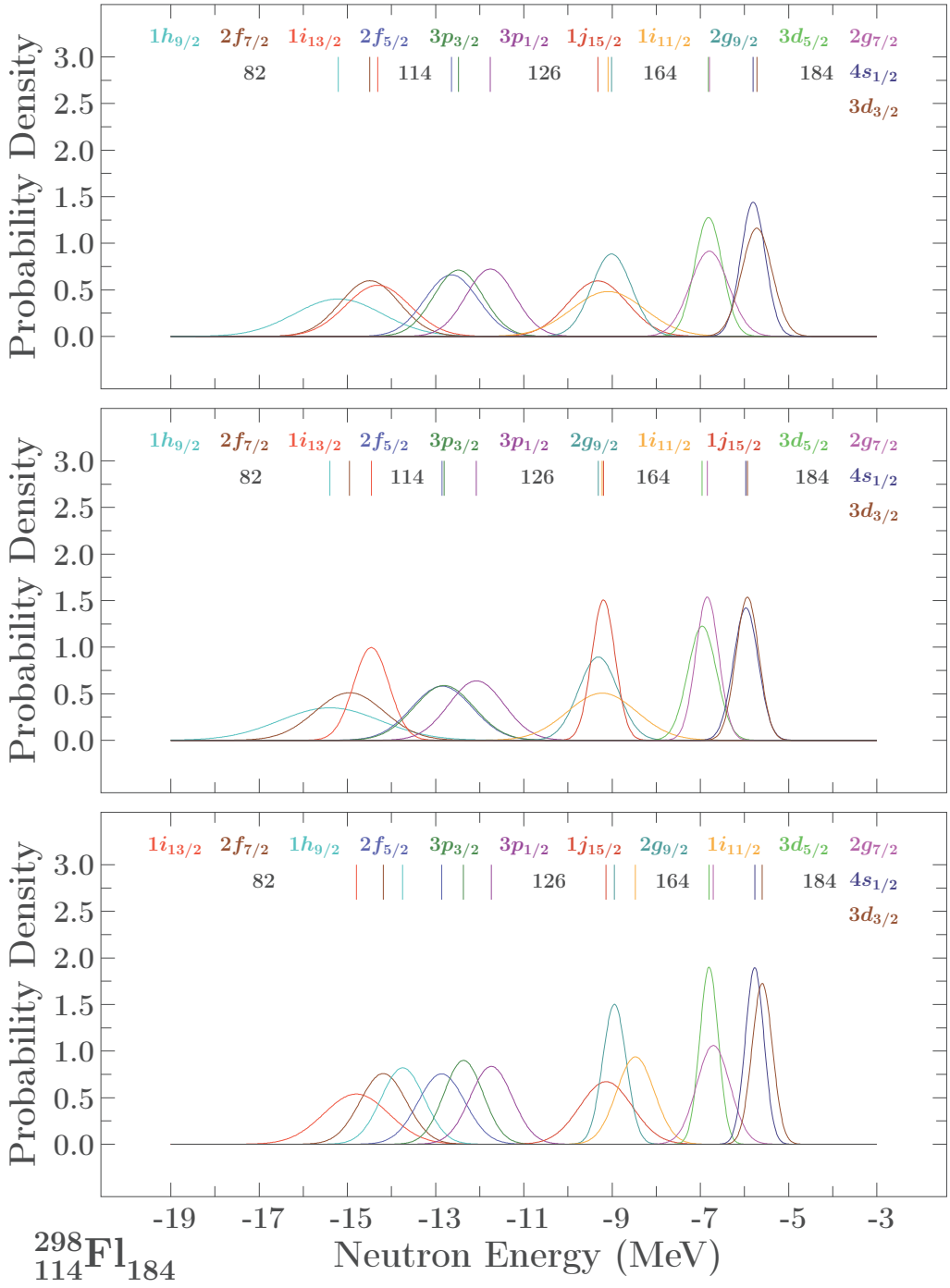

Figure 5.14 – Similar to Figure 5.13 but for ^{298}Fl.

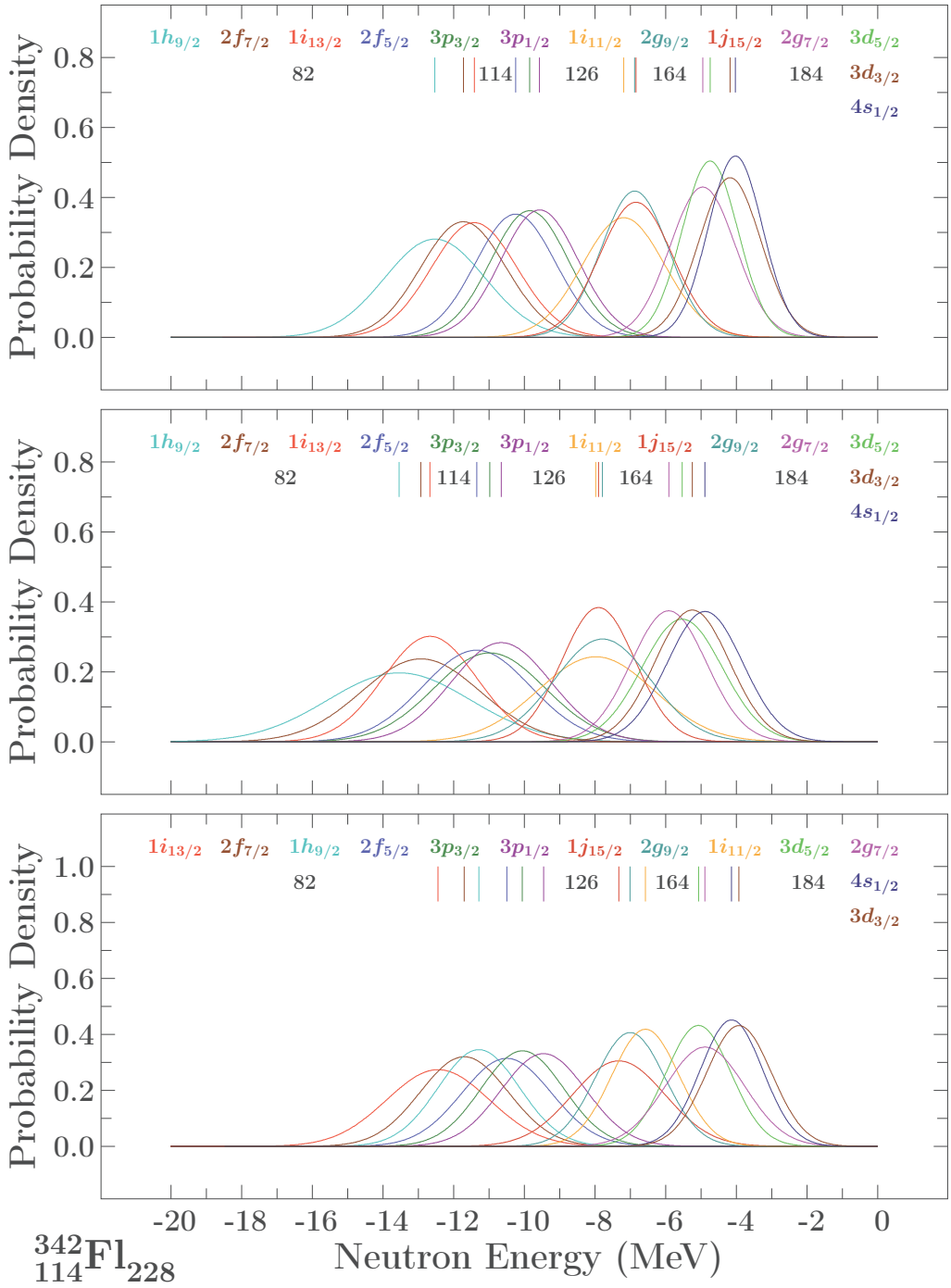

Figure 5.15 – Similar to Figure 5.13 but for ^{342}Fl.

Partial Summary and Comments. Let us observe that the results with the density-dependent Hamiltonian in which the spin-orbit term depends on one single parameter lead, after elimination of the parametric correlations, to the results for the uncertainty widths which are better or comparable with the traditional version results, the latter depending on 6 spin-orbit parameters. At the same time, the density-dependent algorithm allows naturally to include both the microscopically calculated Coulomb and the tensor terms, both expected to improve the description. The latter two options have been programmed but are not a part of this project.

5.7.3 Uncertainty Widths for Proton Levels

The uncertainty widths after full parametric correlation elimination are presented in Table 5.14. Comparing them to the results Table 5.5, here copied as Table 5.15 for reader's convenience, it can be seen that the results for $N < 184$ have improved with respect to the case with full parametric freedom.

For the heaviest isotopes the results are comparable in both cases considered. This confirms the earlier conclusions related to the neutrons i.e. of approaching the NO-GO regime with very large uncertainty widths from the very beginning (i.e. in the case of the full parametric freedom).

		$N_{\text{main}} = 4$					$N_{\text{main}} = 5$					
Z	N	$1g_{7/2}$	$2d_{5/2}$	$1h_{11/2}$	$2d_{3/2}$	$3s_{1/2}$	$1h_{9/2}$	$2f_{7/2}$	$1i_{13/2}$	$2f_{5/2}$	$3p_{3/2}$	$3p_{1/2}$
114	164	1.13	0.91	0.66	0.84	0.75	0.47	0.49	1.11	0.51	0.54	0.54
114	170	1.39	1.12	0.68	1.05	0.95	0.48	0.29	0.77	0.28	0.20	0.19
114	172	1.51	1.19	0.72	1.16	1.03	0.61	0.30	0.76	0.28	0.14	0.11
114	180	1.91	1.59	0.99	1.56	1.42	0.94	0.63	0.44	0.59	0.44	0.38
114	184	2.13	1.79	1.19	1.78	1.63	1.17	0.85	0.44	0.81	0.66	0.61
114	196	2.90	2.44	1.76	2.43	2.28	1.98	1.49	0.86	1.47	1.29	1.32
114	214	3.83	3.29	2.73	3.54	3.22	2.95	2.41	1.79	2.53	2.24	2.24
114	228	4.51	3.99	3.44	4.19	3.91	3.64	3.10	2.50	3.22	2.89	2.99

Table 5.14 – Similar to Table 5.11 (full parametric correlation elimination) but for the proton levels within main shells $N_{\text{main}} = 4$ and 5.

		$N_{\text{main}} = 4$					$N_{\text{main}} = 5$					
Z	N	$1g_{7/2}$	$2d_{5/2}$	$1h_{11/2}$	$2d_{3/2}$	$3s_{1/2}$	$1h_{9/2}$	$2f_{7/2}$	$1i_{13/2}$	$2f_{5/2}$	$3p_{3/2}$	$3p_{1/2}$
114	164	1.59	1.12	1.30	1.24	0.95	1.62	0.67	1.45	0.86	0.65	0.97
114	170	1.69	1.30	1.40	1.23	1.10	1.59	0.76	1.40	0.77	0.67	1.17
114	172	2.05	1.35	1.81	1.32	1.16	2.08	0.72	1.88	0.77	0.82	0.94
114	180	2.13	1.65	1.89	1.54	1.44	1.94	0.94	1.76	0.87	0.78	0.71
114	184	2.13	1.81	2.02	1.68	1.58	1.72	1.06	1.94	0.98	0.87	0.80
114	196	2.57	2.25	2.32	2.16	2.05	2.10	1.42	2.03	1.34	1.27	1.13
114	214	3.03	2.96	2.77	2.75	2.73	2.23	2.16	2.26	1.82	1.85	1.83
114	228	3.69	3.47	3.46	3.26	3.25	3.02	2.65	3.16	2.34	2.38	2.25

Table 5.15 – Realistic Monte Carlo calculations of the FWHM [in MeV] of the proton single particle energy uncertainty distributions for several Fl-isotopes, within the main shells $N_{\text{main}} = 4$ and 5. The results have been obtained using the density-dependent spin-orbit potential, minimising the χ^2 over the parameters in Eq. (5.21) and imposing the condition in Eq. (5.20) - full parametric freedom. [Copied here for reader's convenience.]

5.7.4 Uncertainty Widths, Protons, Graphical Comparisons

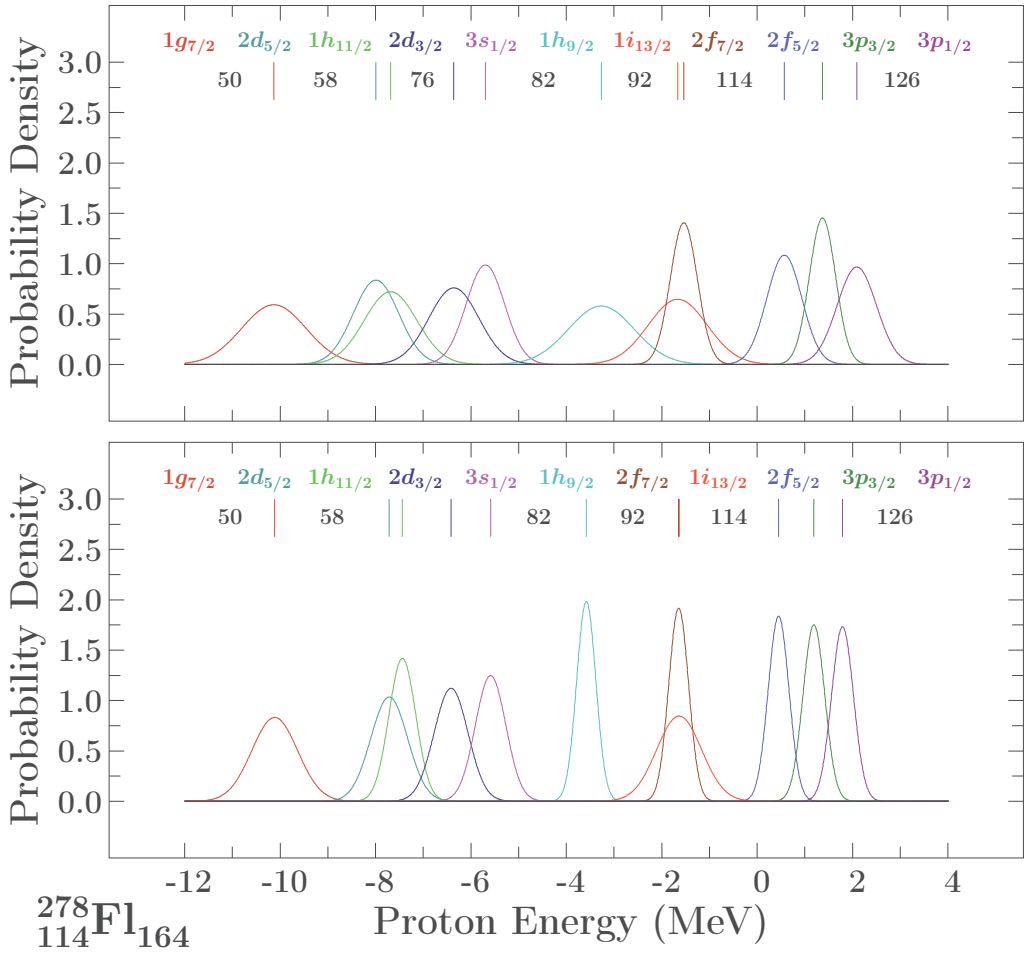

Figure 5.16 – Uncertainty probability density distributions of the proton single particle energies within the main nuclear shells $N_{\text{main}} = 4$ and 5 for ^{278}Fl. They have been obtained from realistic Monte Carlo simulations with $\sigma_{exp} = 600$ keV using the density-dependent spin-orbit and minimising over the set of parameters in Eq. (5.21) (top panel), and using parameters on Eq. (5.29) (bottom panel), keeping in both cases $a_\pi^c = a_\nu^c = 0.7$ fm. The FWHM of each distribution can be found in Table 5.5 and Table 5.13, for top and bottom results, respectively. The surface under each curve is equal to 1. Observe systematic and significant improvements accompanying the parametric-correlation removal.

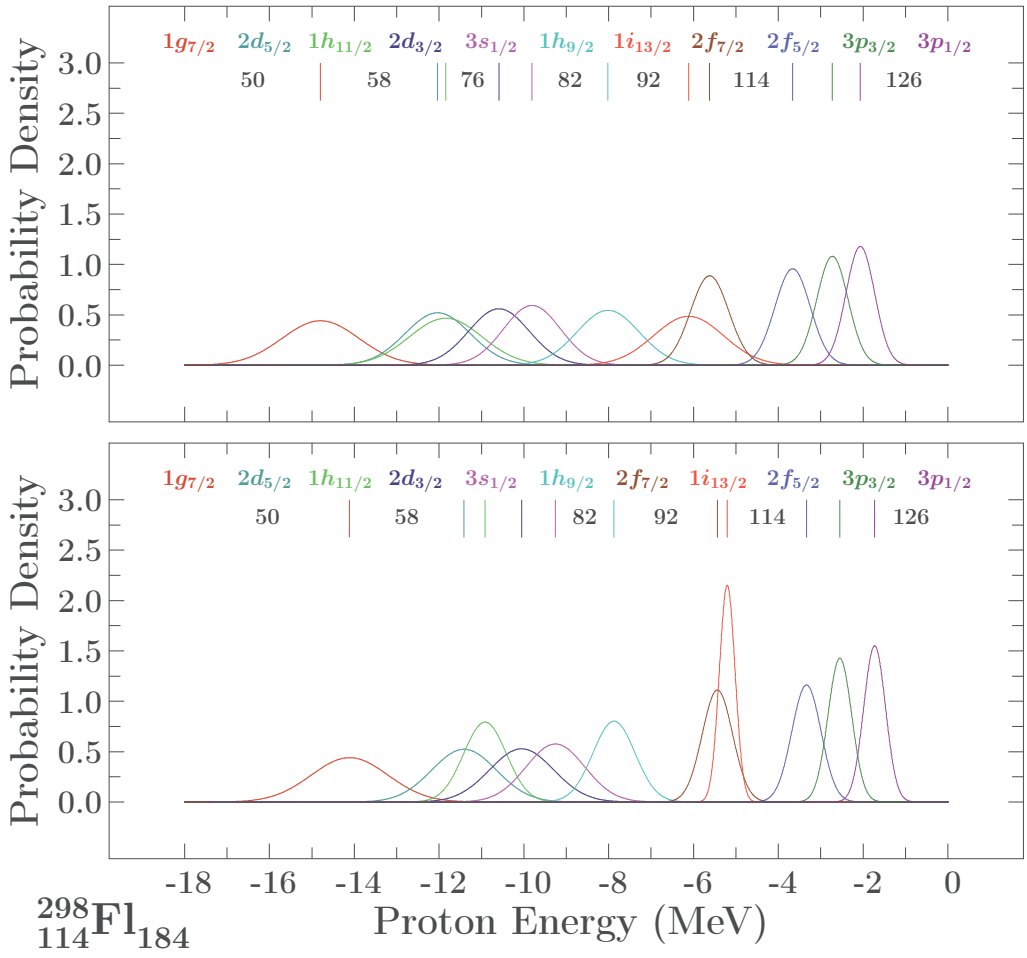

Figure 5.17 – Similar to Figure 5.16 but for ^{298}Fl. Improvements in terms of the uncertainty widths are rather systematic but less pronounced as compared to the previous case.

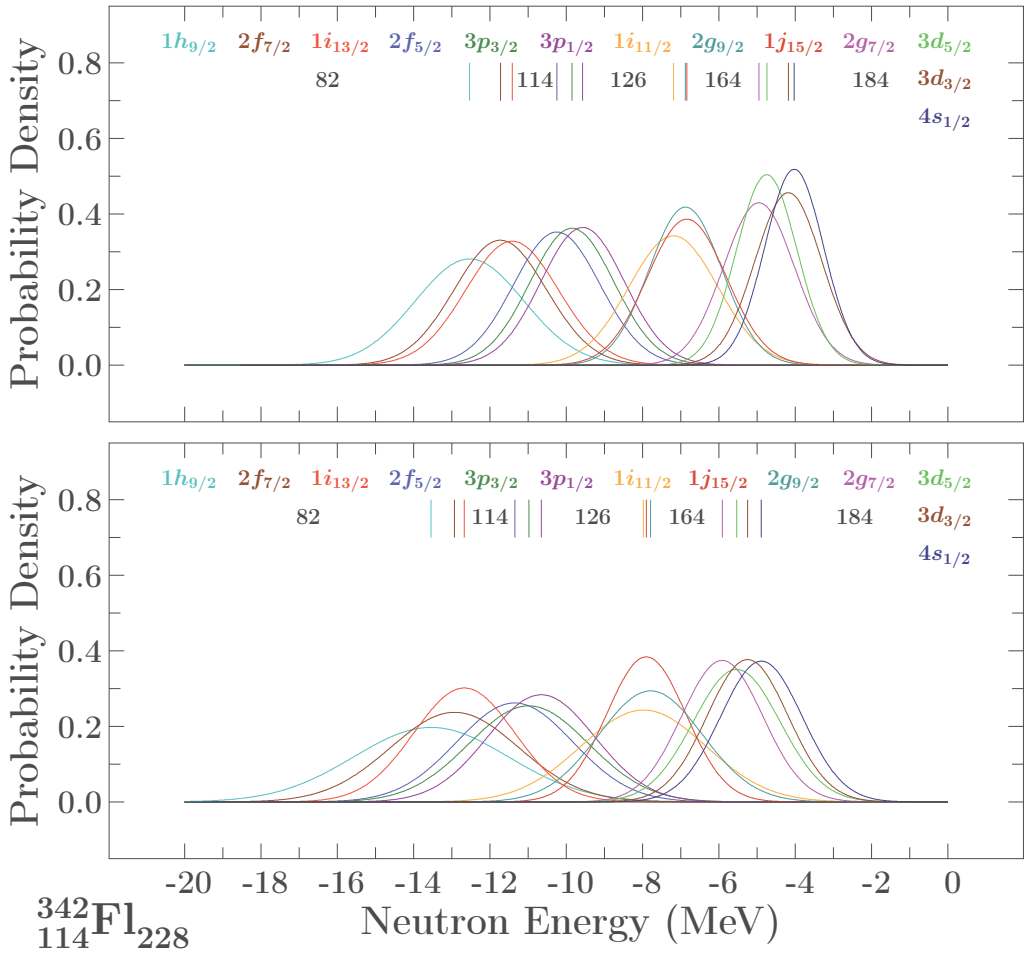

Figure 5.18 – Similar to Figure 5.16 but for ^{342}Fl. In this case the very broad starting point distributions [compare the vertical scales in this and the preceding Figures] get on the average even broader as compared to the full parametric freedom case in the top panel.

5.8 Increase in Sampling and the Predictive Power

In the preceding sections we have demonstrated the improvement of the model performance after removal of the parametric correlations from the density-dependent Hamiltonian by imposing:

- The parabolic dependence between the central radius and the central depth, and:
- Reducing the number of independent spin-orbit coupling constant from four to one.

Indeed, both have a positive impact on the uncertainty distributions of the predictions by reducing their widths in the great majority of the cases of interest. Our analysis so far was focused on the sampling composed of one single nucleus: ^{208}Pb. In this Section we will extend our discussion related to the impact of the parametric correlation removal when more than one nucleus compose the experimental sample.

5.8.1 Increasing the Sampling: Neutrons in ^{132}Sn and ^{208}Pb

In this section we will present the results with the sampling extended to two nuclei: ^{208}Pb and ^{132}Sn. Since in the present case the sampling is composed of more than one nucleus, the potential depth will be parameterised with the help of the isospin factor $(N-Z)/(N+Z)$ and the two parameters: V_o and κ_c, see Chapter 2 and the full parameter space is composed of

$$\{V_o, \kappa_c, r^c_{\pi,\nu}, a^c_{\pi,\nu}, \lambda_{\pi\pi}, \lambda_{\pi\nu}, \lambda_{\nu\nu}, \lambda_{\nu\pi}\}. \tag{5.30}$$

Figure 5.19 shows the impact of just increasing the sampling (top: single nucleus fit, bottom two nuclei fit) when acting with full parameter-correlation removal. Whereas the local r.m.s. values are getting slightly worse, the predictive power increase since the R.M.S. values decrease from 1.65 MeV to 1.39 MeV. One possibility of illustrating the predictive power and the impact of the sampling would be to fix one nucleus, e.g. the highest in the sample - and tabulate the r.m.s. of this particular nucleus for various variants of increasing sampling by taking ^{208}Pb, ^{132}Sn etc.; we prefer a global estimate as presented here.

Figure 5.20 compares one of the diagrams from the preceding Figure (complete correlation removal while fitting two nuclei) with the results for the full parametric freedom case, again with two nuclei in the fit:

> *Let us emphasise the confirmation of the expected mechanism: The R.M.S. is worse in the case of the using of the full parametric freedom (since parameters are correlated what destabilises the predictions) and is being improved when the parametric correlations are eliminated, the change being from R.M.S.=1.58 MeV to R.M.S.=1.39 MeV. And this can be considered as a good starting point, the tensor interactions and the microscopic calculations of the Coulomb potential being the next steps on the list.*

For this reason, some conclusion is somehow clear at this point: whereas the sampling will always remain as a subjective choice mainly depending on the physical context, the parametric correlation elimination can be seen as an 'absolute need' required by mathematically formulated criteria which remain an indisputable part of the mathematical posing of the inverse problem.

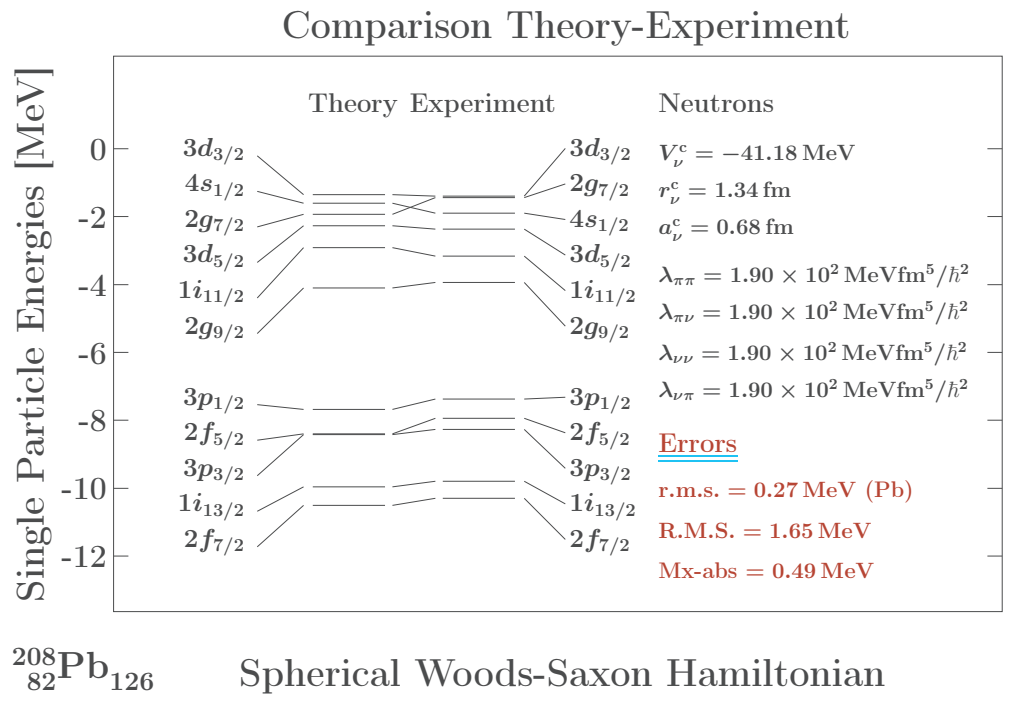

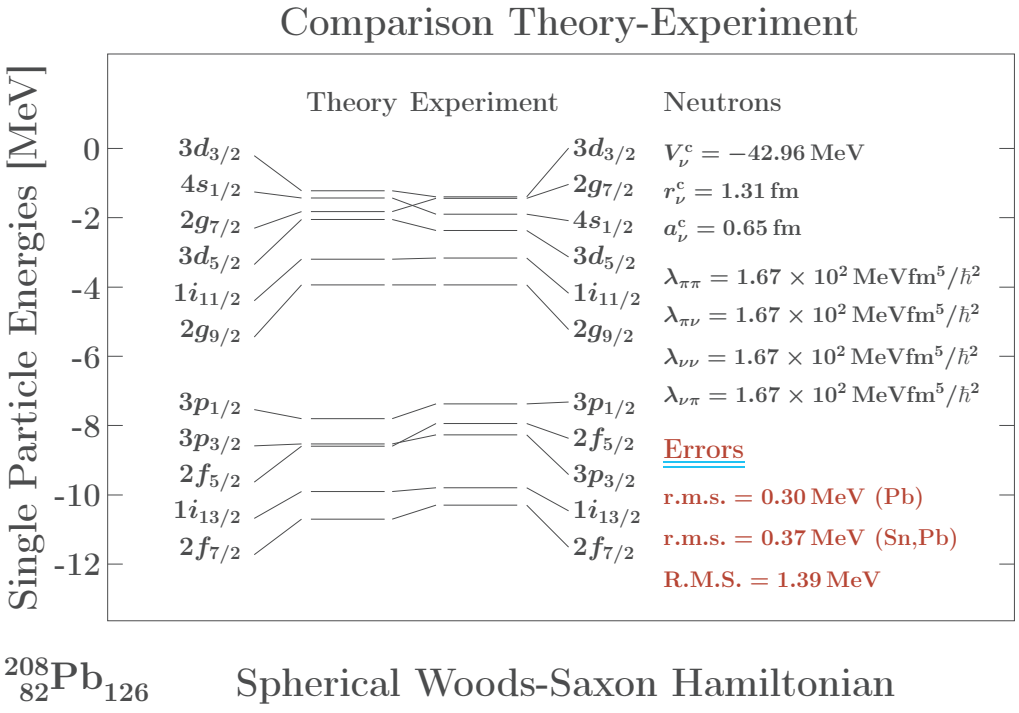

Figure 5.19 – Top: Calculated ^{208}Pb neutron single particle energies, resulting from the fit of the density-dependent-WS Hamiltonian parameters after full parametric correlation removal. Bottom: Similar to the preceding one but fitting to the experimental levels of ^{208}Pb and ^{132}Sn simultaneously. Notice that increasing of the sampling resulted in decreasing of the R.M.S. from 1.65 MeV to 1.39 MeV.

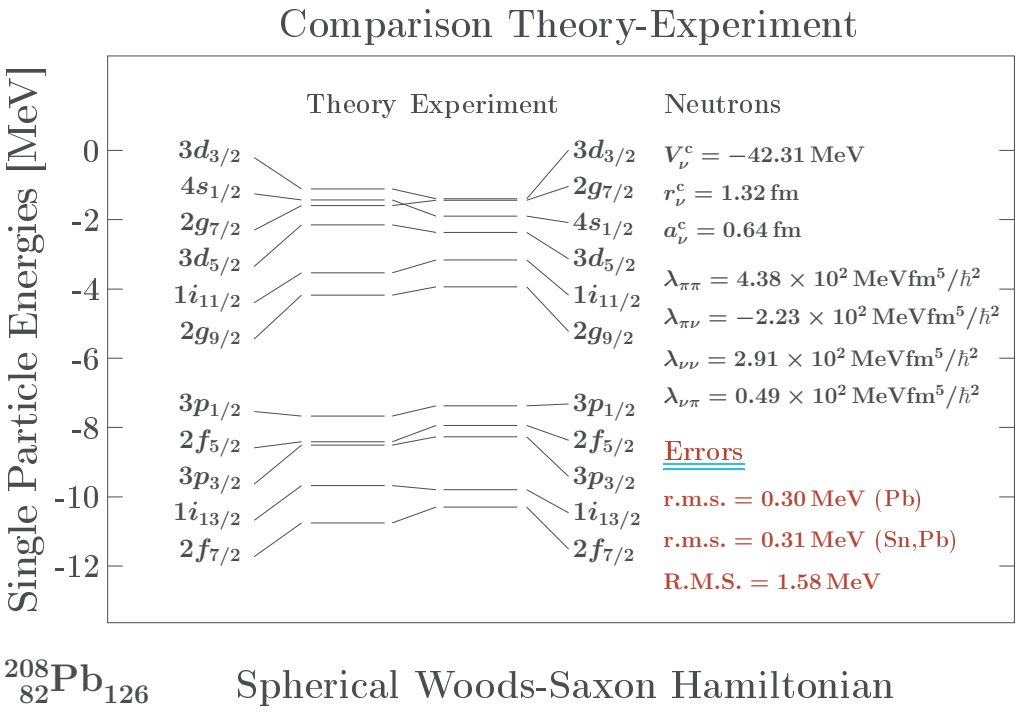

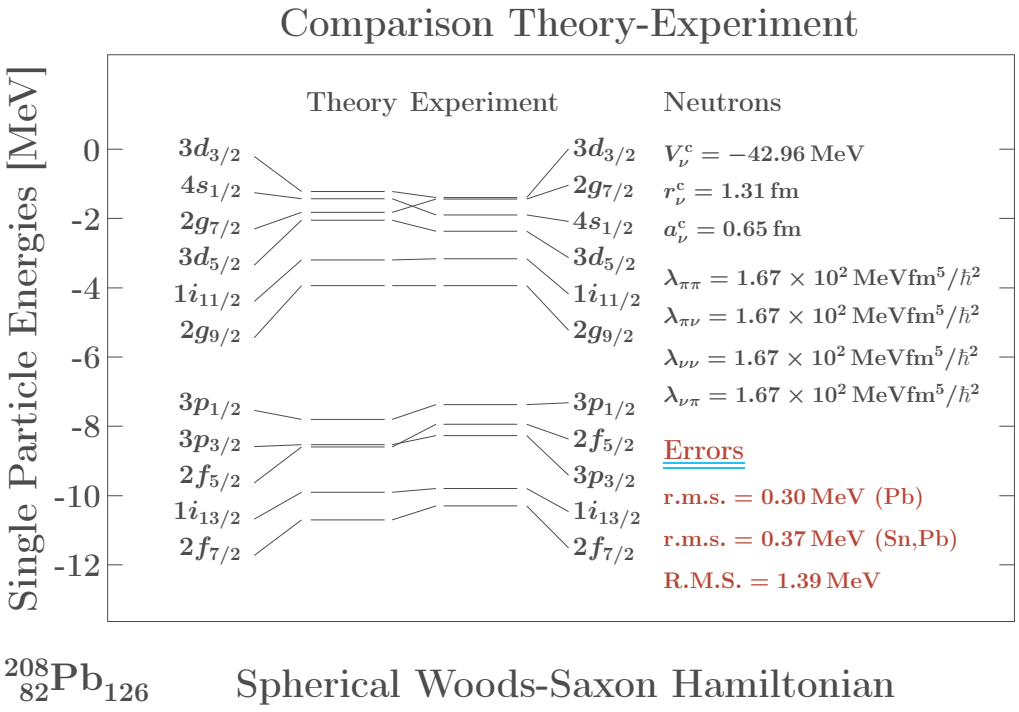

Figure 5.20 – Top: Calculated ^{208}Pb neutron single particle energies, while to the experimental levels of ^{208}Pb and ^{132}Sn simultaneously – here employing the full parametric freedom of the Hamiltonian. Bottom: Similar to the preceding one but with the full removal of the parametric correlations. Notice that increasing of the sampling resulted in decreasing of the R.M.S. from 1.65 MeV to 1.39 MeV. Let us notice that the results for ^{208}Pb remain unchanged whereas the results for the Pb-Sn r.m.s. change from 0.31 MeV to 0.37 MeV, i.e. not significantly. Interestingly, the predictive power for all the 8 nuclei, R.M.S. is improved (as it should be) from 1.58 MeV to 1.39 MeV.

5.8.2 Increasing the Sampling: Protons in ^{132}Sn and ^{208}Pb

Figures 5.21 and 5.22 present results analogous to those in Figures 5.19 and 5.20, but for the protons. The tendencies represented in the figures are strictly analogous. In particular, in reference to Figure 5.21, we notice that the global R.M.S. deviation is improved (variation from 1.55 MeV to 1.31 MeV) when increasing the sampling by considering ^{132}Sn together with ^{208}Pb. This improvement is accompanied by just a slight deterioration of the local description in the case of ^{208}Pb. Figure 5.22 compares the results before and after parametric correlation elimination, when the sampling is composed of ^{132}Sn and ^{208}Pb. As it was expected, global R.M.S.-deviations improve when parametric correlations are removed, here from 1.67 MeV to 1.31 MeV [about 20% improvement].

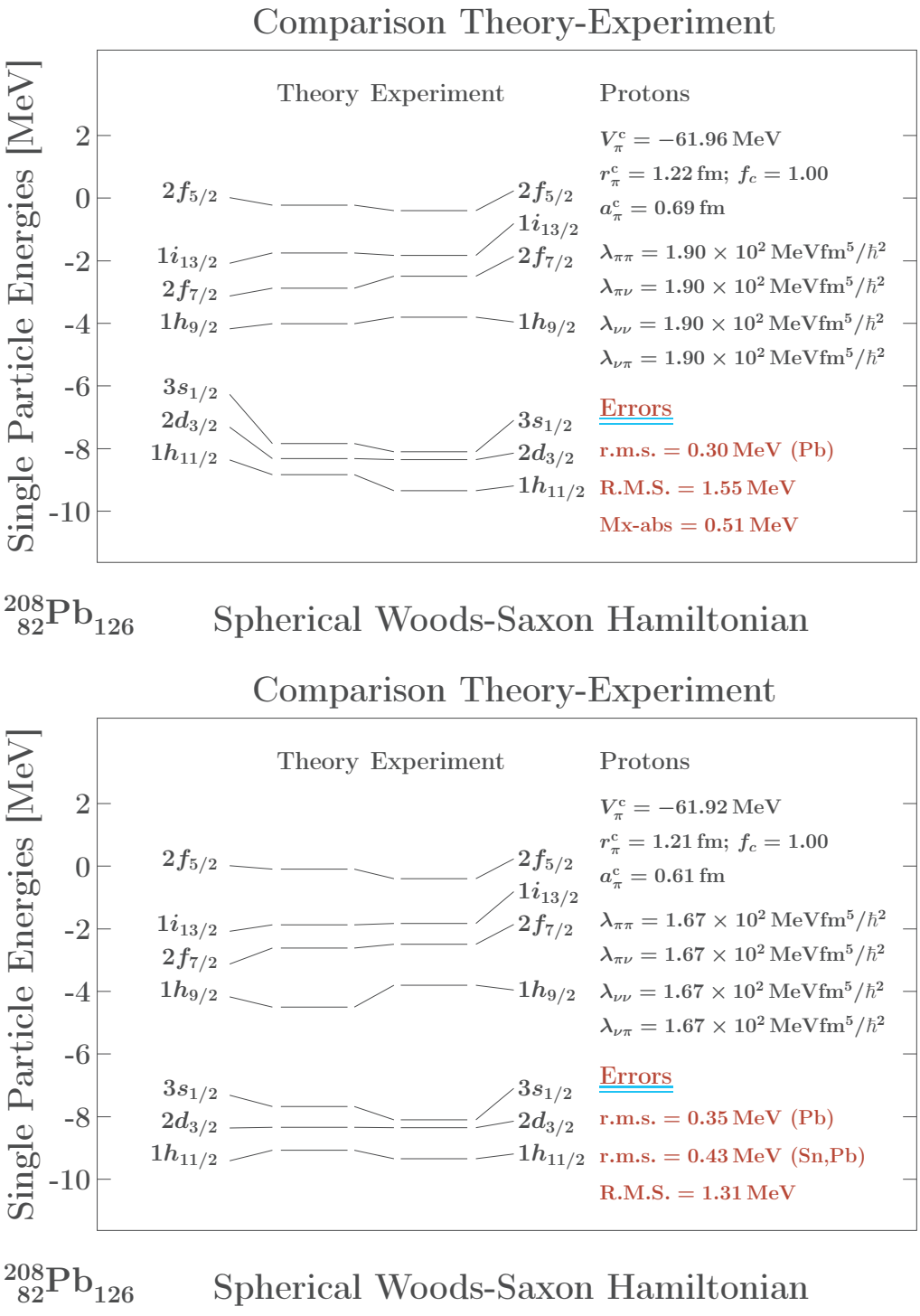

Figure 5.21 – Top: Calculated ^{208}Pb proton single particle energies, resulting from the fit of the density-dependent-WS Hamiltonian parameters after full parametric correlation removal. Bottom: Similar to the preceding one but fitting to the experimental levels of ^{208}Pb and ^{132}Sn simultaneously. Notice that increasing of the sampling resulted in decreasing of the R.M.S. from 1.55 MeV to 1.31 MeV.

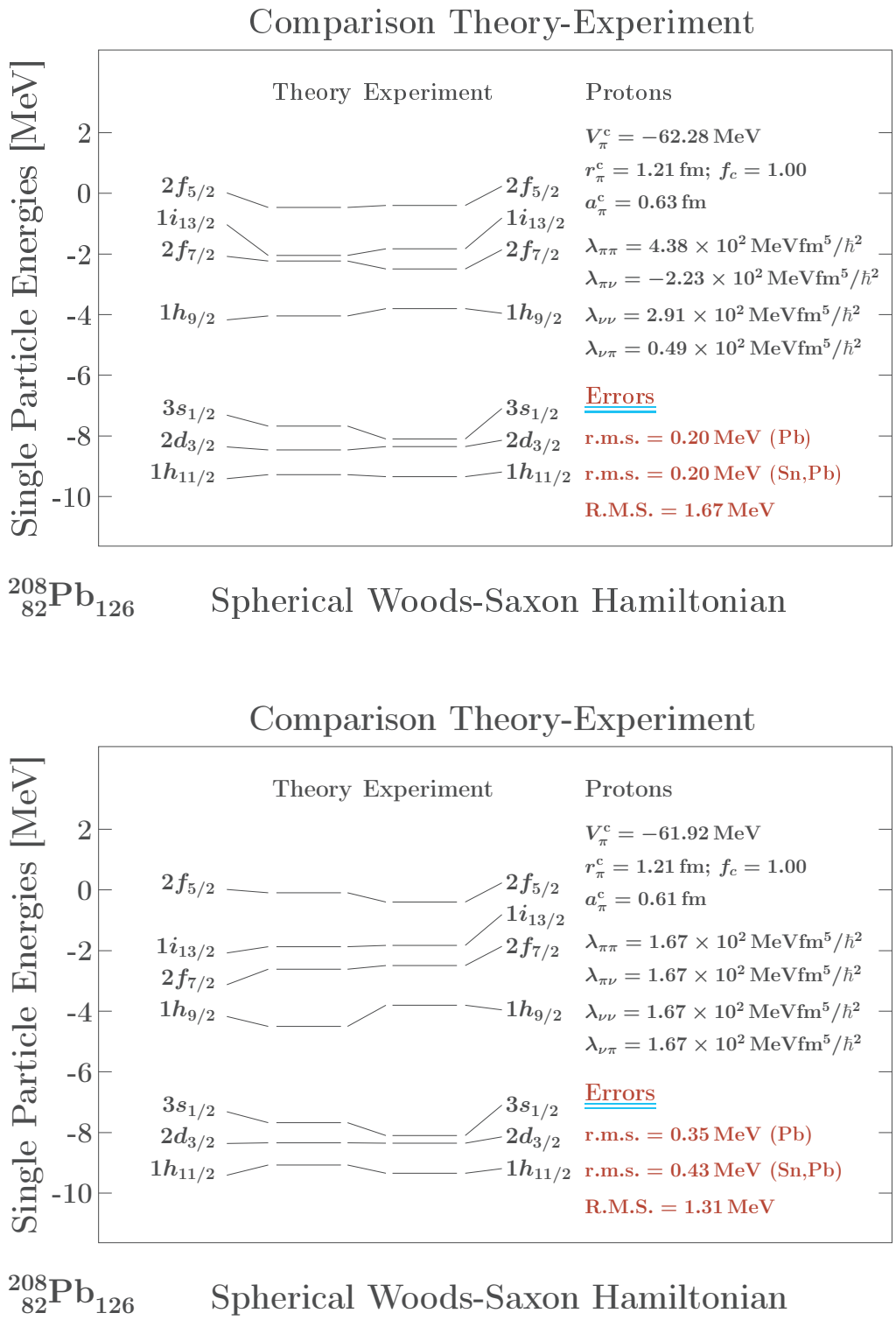

Figure 5.22 – Top: Calculated ^{208}Pb proton single particle energies, while to the experimental levels of ^{208}Pb and ^{132}Sn simultaneously – here employing the full parametric freedom of the Hamiltonian. Bottom: Similar to the preceding one but with the full removal of the parametric correlations. Notice that increasing of the sampling resulted in decreasing of the R.M.S. from 1.67 MeV to 1.31 MeV.

5.8.3 A Short Summary

Calculations show that in the case of ^{208}Pb there is a clear improvement in terms of the uncertainty widths for the great majority of orbitals when the parametric correlations are eliminated. It also should be noted that in this case the uncertainty widths are generally small or at least not very large, of the order of 1 MeV. However, in the test case of the superheavy Flerovium nuclei the situation is different in that the widths quickly approach 3-to-4 MeV limits at the heaviest isotopes considered.

As it turns out, the presence of the very large widths imposes a certain loss of the sensitivity of the reaction: Parameters of the Hamiltonian vs. eigenvalue properties. When this happens the impact of the removal of the parametric correlations gets weaker and weaker and finally disappears for the heaviest isotopes.

We are learning in this way that the model imposes its own limitations as far as the extraneous predictions are concerned – in full agreement with the exact models studied in Chapter 2. We refer to it as the NO-GO property or NO-GO Command. This allows to formulate strong warning statements as far as the predictions for the superheavy nuclei are concerned:

> *The present model (probably the most parameter-stable 'on the market') does not provide stochastically significant predictions for isotopes with $N > 184$ - as long as the experimental input uncertainties are characterised by $\sigma_{exp} = 600\,keV$.*
>
> *Two improvement paths are envisaged.*
>
> • *Firstly, by differentiating among the experimental errors individually, level-after-level, taking into account the detailed information rather than employing an average ($\sigma_{exp} = 600\,keV$) we may improve the initial sampling conditions and thus cause narrowing the initial uncertainty widths provided by the model.*
>
> • *Secondly, by introducing explicitly the tensor interaction terms (programmed and tested but not applied systematically yet) together with the microscopic calculations of the Coulomb potential with the help of the wave functions (like density-dependent spin-orbit term) rather than using a rather primitive approximation based on the uniform charge density we should be able to improve the microscopic quality of the description*[3]*.*
>
> • *Final observation: Recall that by applying this very approach to the spin-orbit interaction we were able to obtain the same quality of the description with the help of one parameter rather than six. This allows to hope that further improvements in the form of the Hamiltonian together with the more careful experimental error estimates will improve the prediction capacities.*

[3] Obviously the appropriately chosen spectroscopic observables in the form of new single-particle level-energies would be welcome as indicators of the spectroscopic information; it is not clear at this point whether – and to what extent – adding global 'observables' such as experimental diffusivity or radii spoil the r.m.s. features.

5.9 Annexe A: Spin-Orbit Parametric Correlations for Nuclei other than ^{208}Pb

In what follows we present a series of illustration demonstrating that the correlations between the pairs of parameters $(\lambda_{\pi\pi}, \lambda_{\pi\nu})$ and $(\lambda_{\nu\nu}, \lambda_{\nu\pi})$ are also linear for the other nuclei used in the present thesis, similarly to ^{208}Pb, the latter shown in Figure 5.3.

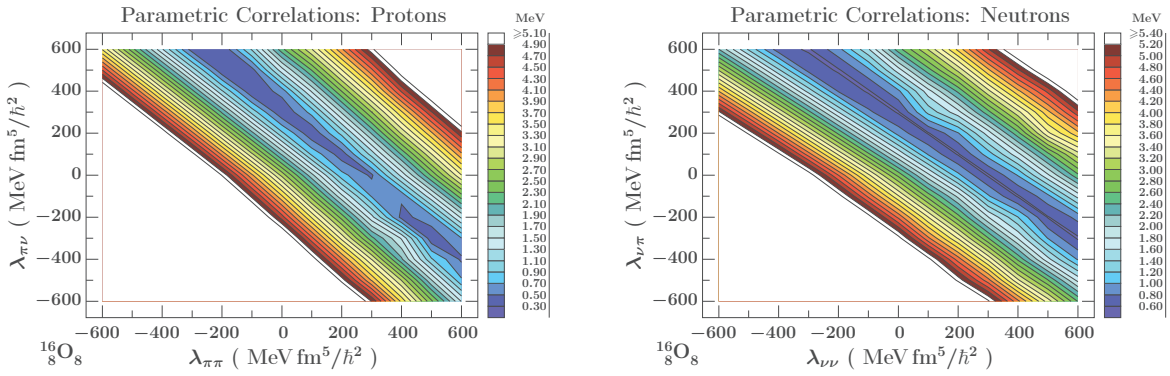

Figure 5.23 – Left: Proton r.m.s.-deviation in MeV projected onto the $(\lambda_{\pi\pi}, \lambda_{\pi\nu})$-plane for ^{16}O nucleus. The central potential parameters were kept fixed at the optimal values for ^{16}O. At each $(\lambda_{\pi\pi}, \lambda_{\pi\nu})$ value the χ^2 was minimised over $\lambda_{\nu\nu}$ and $\lambda_{\nu\pi}$. The colour scale gives the proton-r.m.s. deviation in MeV. Right: Analogous illustration for the neutrons.

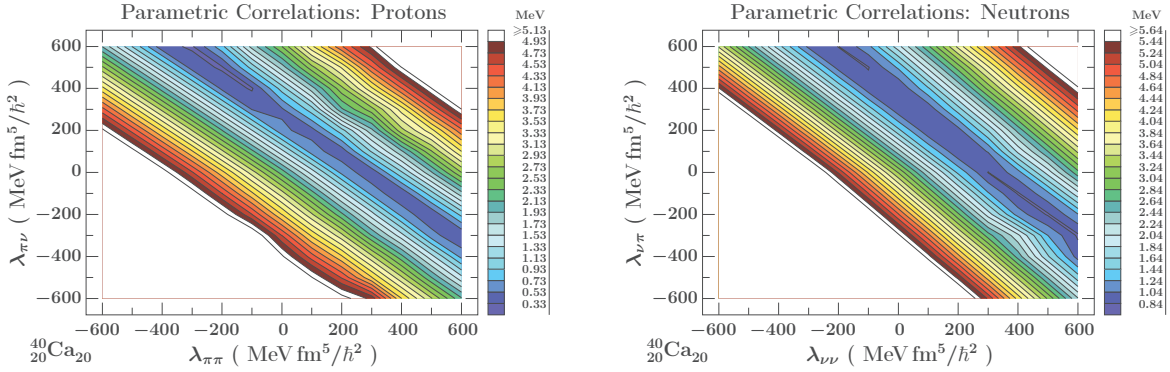

Figure 5.24 – Equivalent to Figure 5.23 but for ^{40}Ca.

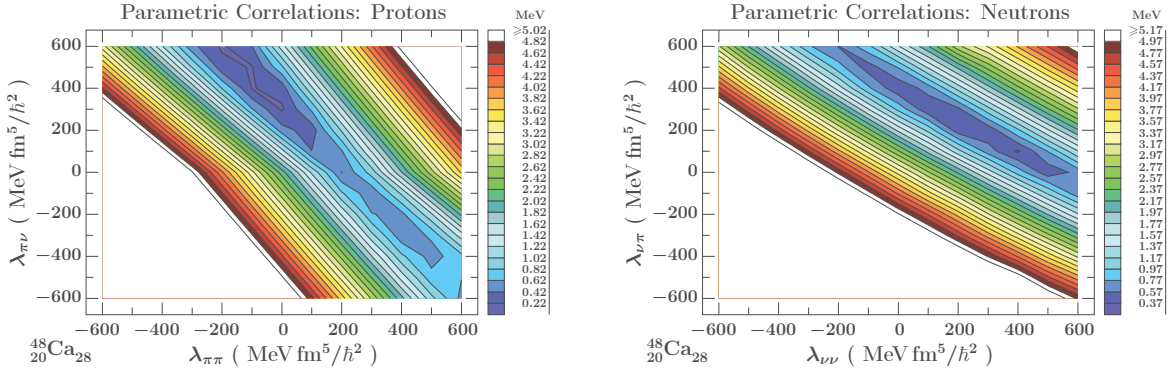

Figure 5.25 – Equivalent to Figure 5.23 but for ^{48}Ca.

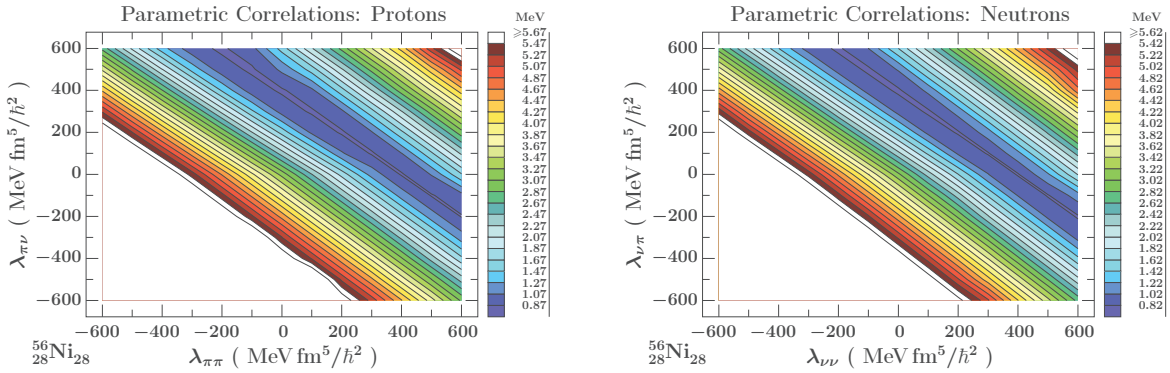

Figure 5.26 – Equivalent to Figure 5.23 but for ^{56}Ni.

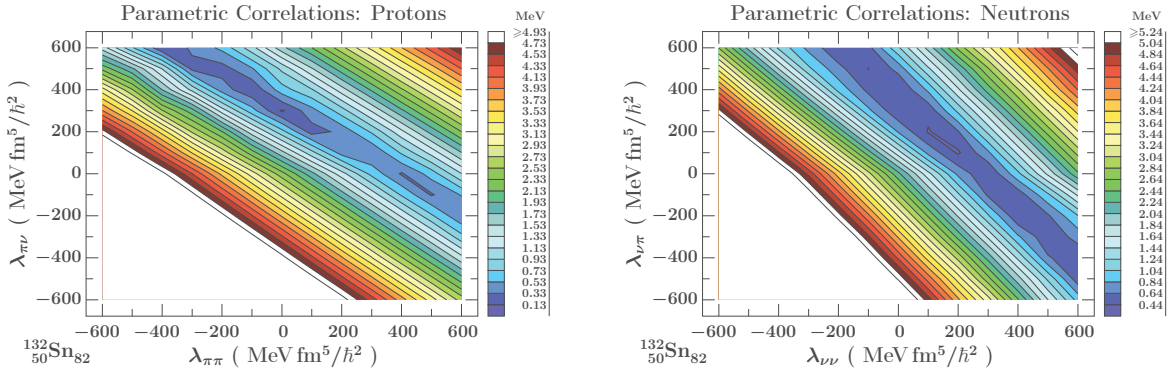

Figure 5.27 – Equivalent to Figure 5.23 but for ^{132}Sn.

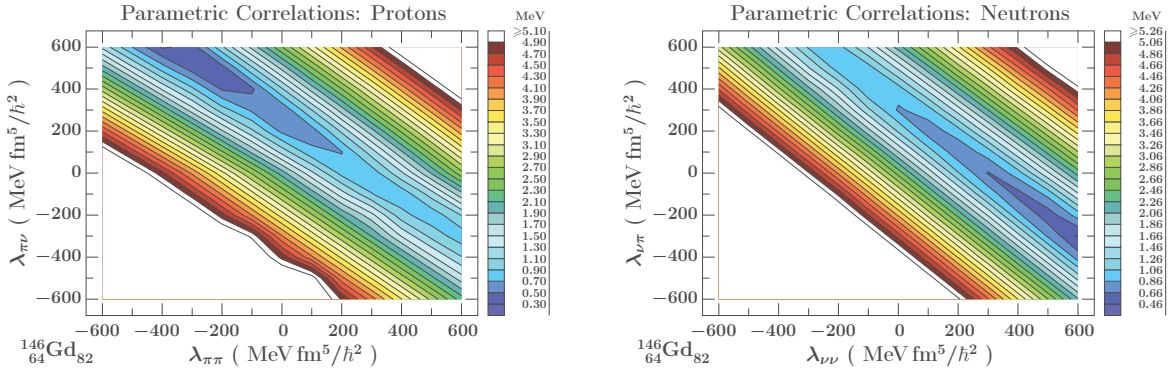

Figure 5.28 – Equivalent to Figure 5.23 but for ^{146}Gd.

Chapter 6

Summary, Conclusions and Perspectives

The present doctor-thesis project belongs to the field of theoretical nuclear physics within the sub-field of nuclear structure theory. Its particularity lies in the fact that even though we model the experimental phenomena reproducing selected observables, the main purpose lies not so much in reproducing them as well as possible – but rather in using this information in order to be able to *predict the today unknown facts* in a way that satisfies certain criteria of stability and stochastic reliability.

Specificity of the Project. We follow the above guideline in the present research project employing methods of nuclear structure theory combined with the mathematical methods of strongly developed today a branch of *Applied Mathematics* called *Inverse Problem Theory*. The latter mathematical theory is sometimes nicknamed the 'mathematics of modelling'. It combines in an abstract manner the mathematical tools that are common to all mathematical models of certain realities, no matter the particular model or (e.g. physical) reality. In a great majority of modelling approaches used in physics, the central role is played by an appropriate determination of the model's optimal parameter values. According to the Inverse Problem Theory, any optimal parameterisation to become acceptable must be first tested, employing certain mathematical criteria, to verify a number of conditions, among others the conditions of stability and continuity.

The application of such criteria is one of the central issues in the present project.

The Present Project: Selection of the Nuclear Model. The goal of the present project is to study prediction capacities of a selected nuclear structure theory. Therefore the selected for this purpose nuclear theory together with its Hamiltonian must not only be realistic, but, optimally, also applicable to all the nuclei throughout the Periodic Table. Only under these conditions we will be able to profit from the information e.g. about the existing nuclei to 'sharpen the tools' in preparation for the predictions for the exotic nuclei, especially since studying the latter is one of the frontier tasks in our domain today. For this purpose we have chosen the nuclear mean-field theory which satisfies such criteria. Indeed it is 'universally applicable' to atomic nuclei with all combinations of the proton and neutron numbers throughout the Periodic Table. It appears in two realisations. The first one will be qualified as phenomenological since it uses the pre-defined phenomenological mean-field potentials, whereas the second one is usually qualified as microscopic even though, strictly speaking both are phenomenological. (We avoid here terms such as e.g. "macroscopic" since

the latter one has a reserved meaning in the macroscopic-microscopic method of Strutinsky referring to the Liquid-Drop-Model energy part only). The latter uses a parametrisation of the nucleon-nucleon interactions as the input and provides the mean-field potentials with the help of the Hartree-Fock type selfconsistent approaches.

We had a choice of selecting between both of the two realisations of the nuclear mean-field theory, since both were used for a long time in our group and there exist advanced numerical programs using both[1] strategies. For reasons which are justified in what follows we decided to use the *phenomenological variant of the nuclear mean-field theory* and in particular focusing on the analysis of the mean-field single-nucleon energies in spherical nuclei. This choice allows to straightforwardly extend the use of the newly tested parameterisations in the framework of the large scale total energy calculations for the deformed nuclei – in particular exotic and superheavy ones.

The Present Project: Selection of the Mathematical Tools. One of the main results of the Inverse Problem Theory pertinent for the present project is that the determination of the optimal parameters of any model is hurt (or made impossible) by what is called parametric correlations. As it very often happens not all parameters of the model can be considered independent from one another. This mechanism depends on two elements: the mathematical structure of the model itself and the choice of the experimental data employed to optimise the parameters. Thus it is a condition *since qua non* to determine the presence (or absence) of parametric correlations within any project which aims at parameter optimisation – before attempting any predictions and/or interpretations within the model in question.

One of the most powerful and elegant a method of determining the parametric correlations as well as the uncertainty probability distributions for the predictions – suggested in *Applied Mathematics* – is the Monte-Carlo technique. It is based on repetitive solutions of the Schrödinger equation under stochastically controlled variation of the input, and this – a very large number of times, N_{M-C}. The best conditions correspond to $N_{M-C} \to \infty$. It then follows that the CPU time needed for each solution plays a very crucial role. As it is well known, the phenomenological variants of the mean-field theory require negligible CPU program execution times compared to the Hartree-Fock approaches. Moreover, it has been found out in another PhD project obtained in collaboration with our group[2] that the Skyrme-Hartree-Fock iteration processes very often fail and need to be treated 'manually case-by-case' making the automatic data collection nearly impossible. Since the main goal of this project was defined as the study of the model-prediction stability and the methods of stabilisation of the ill-posed modelling, the problems with the iteration convergence would have been an unnecessary complication for the main goals. Thus we decided against using the Skyrme-Hartree-Fock approach for this project and selected the

[1] One of the early versions of phenomenological Woods-Saxon related computer programs has been published in:

1) *Single-Particle Energies, Wave-Functions, Quadrupole-Moments and g-Factors in Axially Deformed Woods-Saxon Potential with Applications to the 2-Center-Type Nuclear Problems*; S. Ćwiok, J. Dudek, W. Nazarewicz, J. Skalski and T. Werner, *Comp. Phys. Comm.* **46 (3)** *(1987) 379*,

but much more advanced unpublished versions of the code exist. The infrastructure of the Woods-Saxon code has been used to produce the full series of the Skyrme-Hartree-Fock type codes:

2) *Solutions of the Skyrme-Hartree-Fock Equations in the Cartesian Deformed Harmonic-Oscillator Basis. (I) The Method*;
J. Dobaczewski and J. Dudek, *Comp. Phys. Comm.* ***102 (1)*** *(1997) 166-182*;

3) *Solutions of the Skyrme-Hartree-Fock Equations in the Cartesian Deformed Harmonic-Oscillator Basis. (II) The Program HF_ODD;*
J. Dobaczewski and J. Dudek, *Comp. Phys. Comm.* ***102 (1)*** *(1997) 183-209*

4) *Solution of the Skyrme-Hartree-Fock Equations in the Cartesian Deformed Harmonic-Oscillator Basis (III): A New Version of the Program*;
J. Dobaczewski and J. Dudek, *Comp. Phys. Comm.* ***131 (1)*** *(2000) 164-186*

. . .

9) *Solution of the Skyrme-Hartree-Fock-Bogolyubov Equations in the Cartesian Deformed Harmonic-Oscillator Basis – (VIII) HF_ODD (v2.73y): A New Version of the Program*; N. Schunck, J. Dobaczewski, W. Satuła, P. Bączyk, J. Dudek, Y. Gao, M. Konieczka, K. Sato, Y. Shi, X. B. Wang and T. R. Werner; *Comp. Phys. Comm.* **216** (2017) 145-174

[2] B. Szpak, PhD-thesis, Institute of Nuclear Physics, Polish Academy of Sciences, Cracow 2012.

phenomenological solution with the Woods-Saxon potential.

Woods-Saxon Mean-Field Hamiltonian: choices with 'Incidental Advantages'. As it turns out, for this particular project the traditional parametrisation of the phenomenological mean field in terms of the three-parameter Woods-Saxon potential has several advantages, which make out of the implied Hamiltonian an ideal *academic test case*. Indeed, all the three of them: The potential radius, diffusivity and depth parameters lead to experimental one-to-one test possibilities by measuring directly or indirectly anyone of the three geometrical properties, thus offering extremely precious control opportunities. Moreover it has been known for some time that the Woods-Saxon potential depth and radius parameters are quadratically correlated for any experimental data input, whereas the corresponding spin-orbit potential leads to a linear correlation between the spin-orbit strength and the spin-orbit diffusivity (all discussed in the thesis). With this information at hand one can focus the research of the unknown inverse problem mechanisms under simplified and well understood extra conditions – all that would have been impossible with alternative mean-field approaches.

Exact Model With Exact Solutions: Learning about the tools. After having introduced the methods related to the nuclear structure model used in this document and to the principles of the inverse problem together with its stochastic elements in the parameter optimisation – in Chapters 1 and 2 – we have formulated an exact mathematical toy model allowing to study various mechanisms within the inverse problem approach in Chapter 3. The exact model in question allows to examine all the elements which appear in the realistic problems such as sampling, its choice, control, possible optimisation, studying what we refer to as intraneous and extraneous model-prediction regimes, existence of the parametric correlations within the model, etc. In Chapter 3 we discuss in detail the meaning and the role of the 'exact models/theories' arriving at a number of instructive – not to say surprising – conclusions:

a. Any exact theory depending on parameters becomes inexact since there always exist experimental errors related to the experimental data employed to optimise the parameters,

b. When the experimental data become less and less precise, at a certain point even an exact model becomes useless since, after by-passing certain critical error-values, the data do not constrain the model anymore. We refer to this mechanism a NO-GO condition for the exact models, but even more dramatic realisations of it occur within non-exact ones.

c. There exists in general a great difference between the quality of performance of the model within its intraneous regime ('predictions in between the data points', alternatively 'within the fitting zone') and the extraneous regime (predictions for the zones farther and farther away from the fitting zone). More precisely, a possibly good quality of a fit in the intraneous area does not imply at all anything about the quality of the extraneous predictions. Assuming to the contrary without any proof – as often found in the literature – seems to be committing a grave error.

d. We learned in particular that the so called 'good description' within the intraneous zone may still occur with the parameter values outside of the physical regime what is equivalent to playing with random numbers when describing physical observables.

e. To avoid all these 'surprises' physicists should carefully analyse at least the issue of the parametric correlations and follow the rules known in the Inverse Problem Theory of Applied Mathematics. [The Inverse Problem Theory offers a selection of approaches which allow for going beyond "just pure" χ^2-fitting; some of them are used in the present project,

but the richness of possibilities bypasses the framework of a single project like this one and includes e.g. Bayesian techniques, various techniques called "regularisation methods" etc.]

All these and several more effects and results are discussed in Chapter 3.

Realistic Studies of Parameter Optimisation: Traditional Woods-Saxon Case. In Chapter 4 we present the systematic analysis of the problem of parametric correlations in a realistic nuclear context as well as the impact of the experimental errors on the uncertainties of the theory predictions. We focus the discussion on the properties of the data in relation to the ^{208}Pb nucleus (which provides an example of an intraneous zone) and on the superheavy nuclei selected as isotopes of Flerovium ($Z = 114$) – extraneous zone.

We found out as the result of calculations that the uncertainty widths are systematically larger for the orbitals not known experimentally – and thus not used by the adjustment procedures. We confirmed via numerical calculations the parabolic correlation between the central potential depth- and radius-parameters and a linear one between the spin-orbit strength and diffusivity parameters. However we also found out that there exists a new class of correlations which take the form of two (rather than a unique) distributions centred around spin-orbit radius parameter $r_{so} \approx 0.8\,\mathrm{fm}$, called compact, and $r_{so} \approx 1.2\,\mathrm{fm}$, called non-compact. This forces us to introduce two full classes of solutions called compact and non-compact, analogously. From the mathematics point of view they should be treated as equivalently acceptable but they are not physically equivalent and it is up to a physicist to take decisions. For instance, including extra observables, may help in defining the choice more favourable in a given context, e.g. taking into account the rotational properties of deformed nuclei N. Schunck, in his PhD project [47], was able to establish that the compact solution works systematically better.

We were able to eliminate the parametric correlations reducing the original space of six independent parameters for each kind of nucleons to two only, selected as the central depth and the central diffusivity parameters. We have shown by direct verification that the parameter elimination reduces the condition number by two orders of magnitude thus improving the stability of the final predictions accordingly. At the same time we were able to show that the widths of the level uncertainty distributions are systematically diminished when the parametric correlations are eliminated. This mechanism is not straightforward: different levels react differently and the corresponding detailed information is provided.

Applying the method to Flerovium isotopes show a very quick increase in the uncertainty widths of the single particle orbital energies which approach the limit of FWHM $\approx$ 4-to-5 MeV at the neutron number $N = 228$. This leads to a very strong overlap between various levels and implies that the Hamiltonian parameter changes do not translate into any strong changes of the level uncertainties. In this sense we arrive at the NO-GO property in the realistic problem of superheavy nuclei.

Towards Woods-Saxon Hamiltonian of New Generation: Density Dependence. It has been demonstrated in one of the earlier studies performed by our group that the traditional Woods-Saxon Hamiltonian can be transformed into a more microscopic version involving the density-dependent spin-orbit potential. For this purpose the Hartree-Fock microscopic techniques are used and the spin-orbit potential form is derived which depends on the gradients of the nucleonic densities - with the reduced number of parameters: The traditional spin-orbit potential depends on six parameters, three for the protons and three for the neutrons, whereas the new one on four. Within this (still phenomenological) for-

mulation we profit from the exemplary robustness of the Woods-Saxon central-potential properties while improving the realistic description of the spin-orbit coupling considerably.

We have found out using both analytical and numerical methods that among 4·3/2=6 possible binary correlations among those four spin-orbit potential parameters there exist only two relations which are strictly linear whereas all other parameters are uncorrelated. This – as discussed in detail in the document – allows us to introduce the specific condition: All the four spin-orbit potential parameters being equal.

We have demonstrated that the new (so-called second generation) Woods-Saxon Hamiltonian provides nearly the same performance in terms of the comparison with the experimental data *with five independent parameters less*! – as compared to the traditional formulation.

We have eliminated the parametric correlations and shown that the uncertainty widths are systematically smaller after correlation removal – under the condition of working outside of the NO-GO zone. Within the NO-GO zone there is no visible impact of the parametric correlation removal and, as we have discovered, one enters the zone of a limited impact of the parameter variation on the final result.

Synthetic Comments Related to this Research Project. Whereas the previous conclusions were grouped according to their chronological appearance in this document, i.e. 'chapter after chapter' addressing various elements of the progress such as lessons from the exact mathematical model, their applications to the most elementary form of the Hamiltonian[3], generalisation to the Hamiltonian said 'of the new generation' – we will terminate this series with a few global and/or synthetic comments and conclusions.

To our knowledge we have for the first time analysed systematically the parametric correlations focussing on their detection, elimination, impact on the final results compared case by case via testing various orbitals with various quantum characteristics, on various nuclei and sets of nuclei etc., all that with concrete numerical results and within a realistic environment ('real nuclei and data'). We have applied for the first time the cross-checking of the prediction stability using simultaneously the Pearson-matrix test, SVD and condition number tests and extensive Monte-Carlo tests. Our results and conclusions are fully consistent, qualitatively and quantitatively, and convergent independently of the variant of the model used and we believe that this provides a solid starting point for the more advanced steps (see below).

We believe that the results of the project provide a new light towards the universality issue[4] and within the more microscopic and thus more realistic realisation of the mean-field:

> *Indeed, a very successful Universal Woods Saxon Hamiltonian in use also today employs 12 adjustable 'universal' parameters selected once for all the nuclei; at the time of their optimisation no attention was played to the destabilising role of the parametric correlations. With the arrival of the density dependent spin-orbit potential and with the full removal of the parametric correlations we arrive*

[3] *Let us mention in passing that the traditional form of the Woods-Saxon Hamiltonian in its 'universal realisation', be spherical or deformed, is being used in a big number of nuclear structure publications every year despite the fact that the original articles on that subject appeared long ago in the previous century. As a matter of example, only in one Journal (we selected for this test Physical Review C) and only within one year (our choice 2013) there appeared about 10 articles using the 'Universal Woods Saxon' approach in various nuclear structure calculations. The authors choose this realistic model just because of its remarkable predictive power and a single choice of parameters for all the nuclei in the Periodic Table.*

at the new universal parameterisation involving only 3 numbers (parameters) fixed once for all to describe all the nuclei in the Periodic Table. To complete this research with the final, global test, the large scale calculations of the nuclear properties for the spherical and deformed nuclei should be envisaged[4].

Perspectives and Challenges. As it often happens, completed-research results bring light to certain anterior issues but usually contribute to the progress by challenging with the new questions. We have shown that assuming an average experimental input uncertainty of the order of 600 keV we impose limits on the predictive power in terms of increasing nucleon numbers in superheavy nuclei which are synonymous in this project with extreme extraneous prediction zones: Beyond $N = 184$, the stochastic uncertainties seem to be too large to be trustworthy. Similar can be said about the deeply bound states in all heavy nuclei studied.

The question arises: What can be done to improve the situation?

We can envisage a number of scenarios which can be seen as relatively straightforward prolongation of this research.

• Firstly, the error estimates can be treated in a finer manner by using the error estimates adapted to each experimental level rather than employing the average estimate.

• Secondly, it is known that an important source of uncertainties, when working with the mean-field single particle levels in spherical nuclei, originates from the coupling of the individual nucleons with the collective surface vibrations. It is straightforward to include in our codes a Random Phase Approximation (RPA) subprogram for treating this type of coupling in a dedicated manner, estimate the vibration-coupling corrections to the individual levels us use the corrected ones for the parameter optimisation.

• Another improvement can be guided by the success with the density-dependent spin-orbit potential. Indeed, we have noticed at several occasions that the electrostatic Coulomb potential calculated from the fixed in space uniform charge distribution poses problems in that it influences the coupling with the nuclear diffusivity and via the latter one, introduces an extra coupling with the other parameters thus destabilising the prediction scheme. In the new realisation of the project such a potential would be calculated directly from the proton microscopic density distribution.

• Yet another improvement on the list would consist in introducing explicitly the tensor-interaction corrections to the mean-field central and spin orbit potentials. The importance of such corrections increases with the spin-unsaturation within the nucleus and these effects are expected to play an increasing role in superheavy nuclei. The corresponding sub-programs have been written and tested and are ready for the follow-up projects.

• Another point to take into account is the pairing between nucleons by solving the BCS Equations. The program code is already prepared for this, allowing us to calculate the occupation probabilities of the different nucleon energy states.

[4] *We were informed recently that the challenge of running the large scale calculations for hundreds of nuclei throughout the Periodic Table was convincing for one of the Funding Agencies which accepted financing the related three year project involving a number of senior researchers and postdoctoral fellows.*

Chapter 7

Computer Programs Written for the Present Project

The programming charge within the present project consisted in writing three principal computer codes and a number of minor ones, all programmed using Fortran77 for reasons of compatibility with certain existing codes. The biggest of them, of the volume of about 90 000 lines of the FORTRAN instructions contains a certain number of standard application subroutines downloaded form external libraries. However, nearly 80% of the code volume corresponds entirely to the parts conceived, programmed and tested for the purposes of this project. It solves of the Schrödinger equation with several variants of the interaction potentials using diagonalisation method and spherical harmonic oscillator basis. It controls also various other options related to minimisation, Monte-Carlo simulations, random number generation etc., see the next sections.

The typical versions of the fortran programs and the typical versions of the test-outputs, cf. especially graphical ones, are given for the quick reference of the reader in the annex file:

WSPHER-15-PROGRAMS_Annex-package

It contains the fortran source `wspher_15.f`, the corresponding standard input data file `wspher_15.d` and the standard output example-file `wspher_15_WSUNIV.out`.

The other two programs served the graphical purposes as needed for the project. They were created by us in Fortran77 using the free access standard *graphical interface package* called `Xfig`. The first of the two programs, `figlat_pl19.f`, plots various types of the one-dimensional diagrams including curves or energy levels ('ladder plots') – with identification labelling. Another one, `Xfig_Map_17.f`, plots the two-dimensional diagrams ('geographical maps'). The graphical programs and examples of the illustrations produced by them can be found in the annex directory:

WSPHER-15-PROGRAMS_Annex-package/Xfig_Plotting

In the rest of this chapter we include a number of comments about the functioning of the related programs and associated algorithms.

7.1 Parameter Optimisation Structure

The central line in the present thesis project consists in the parameter optimisation analysis and the statistical significance of the optimisation results. The associated computer program has been constructed around the minimisation (optimisation) package the latter downloaded from an external library. In terms of proportions of the necessary new programming to complete the code, the dominating part of the program had to be constructed 'from scratch'. The newly written parts contain not only the solution of the Schrödinger equation via diagonalisation within the spherical harmonic oscillator basis, but also control of various options of minimisation depending on the number of nuclei, including or not the condition on the experimental radii, using or not the tensor component, using or not the Monte-Carlo option etc.

The use of the Monte-Carlo algorithms requires various variants of the random-number generators; the corresponding subprograms have been downloaded from an external library.

The code contains various options which allow for testing the sampling and predictions e.g. via selecting a given subset of experimental data but calculating the implied r.m.s. deviations for the full set and/or required subset. All these option and the general flexibility of the program require quite some volume of extra coding instructions which needed to be conceived, programmed and tested. Specific complications are related to the programming of the Jacobian matrix and related partial derivatives, which need to be treated numerically using the finite difference methods within the cojugated gradient algorithms – and this – taking into account several variants of the principal algorithm. Needless to say, all these options with the requirement of the possibility of using anyone of the cross-combinations increases considerably the complexity of the code.

7.1.1 The χ^2-Test Definition

The forms of the χ^2-function needed for the sake of the present project have already been introduced in Eq. (1.21) but in a relatively compact manner. Let us begin by reminding in what follows the general definition of this function

$$\chi^2 = \sum_{i=1}^{n_d} w_i \left[e_i^{exp} - e_i^{th}(p) \right]^2 , \tag{7.1}$$

where we have introduced the experimental e^{exp} and theoretical e^{th} single particle energies. Whereas the differences in the square brackets are the standard element of the definition, the weights w_i depend on a subjective choice by physicist. In the case of the spherical single particle levels characterised by the angular momentum quantum number j the natural choice is:

$$w_i = (2j_i + 1). \tag{7.2}$$

This form of the weight factor is natural in the case of fitting the data for one single nucleus. However, when taking into account at the same time several nuclei, what implies e.g. combining the data for light and heavy nuclei at the same time, with the definition in Eq. (7.2) we favour the states with bigger total angular momentum j. Thus the heavier the nucleus, the higher j-states will be occupied giving the higher relative weight to the heavy nuclei. This type of the correlation is not necessarily what we may wish to accept in order not to loose the information coming from the light nuclei.

For example, the state with the highest j-value in ^{16}O is $j = 5/2$, whereas the highest j in ^{208}Pb is $j = 13/2$. Thus using Eq. (7.2) we give much higher importance to ^{208}Pb as compared to ^{16}O, which will hardly have any impact on the values of the final parameters. To achieve more freedom in controlling this mechanism we added an extra weight factor, $\tilde{w}$, depending on the relative mass of any given nucleus with respect to the mass of the heaviest nucleus under considerations:

$$\tilde{w}_\kappa = \frac{208}{A_\kappa} \tag{7.3}$$

where A_κ denotes the mass of any given nucleus No. κ, and 208 is the mass of ^{208}Pb, the heaviest nucleus for which we have experimental data. With these weight factors the final expression of the χ^2 to be minimised is

$$\chi^2 = \frac{\sum_{\kappa=1}^{\mathcal{N}} \tilde{w}_\kappa \sum_{i=1}^{n_\kappa} \left\{ (2j_{i\kappa}+1) \left[e_{i\kappa}^{exp} - e_{i\kappa}^{th}(p) \right]^2 \right\}}{\sum_{\kappa=1}^{\mathcal{N}} \tilde{w}_\kappa}, \tag{7.4}$$

where $\mathcal{N}$ is the number of nuclei we take into account and n_κ is the number of energy levels for the nucleus No. κ. This is the function to be minimised using the Levenberg-Marquardt algorithm, cf. Section 1.6. The optimal values of the parameters $\{p\}$ are expected to define a minimum of χ^2 in which case

$$\frac{\partial \chi^2}{\partial p} = 0. \tag{7.5}$$

The minimisation routine will need the partial derivatives and particular the Jacobian matrix generated by χ^2. Calculating the derivatives of χ^2 according to (7.5) reduces to calculating the derivatives of $e^{th}(p)$. Since these energies are generated numerically as the solutions of the Schrödinger equation they are calculated numerically using the finite difference method.

Finite Differences: Definition. Knowing that the classical definition of the derivative $f'(x)$ of a certain function $f(x)$ is

$$f'(x) = \lim_{h\to 0} \frac{f(x+h) - f(x)}{h}\,, \tag{7.6}$$

one can define what it is called the *forward derivative* for $e^{th}(p)$

$$\frac{\partial e^{th}(p)}{\partial p} = \frac{e^{th}(p+\delta p) - e^{th}(p)}{\delta p}, \tag{7.7}$$

The above equation can be used to calculate the derivative of $e^{th}(p)$ with respect to p what requires increasing the number of diagonalisations by one to calculate $e^{th}(p+\delta p)$ for each component of the parameter-vector p.

However, as one shows in the elementary lecture courses of numerical methods the so-called *centred derivative*

$$\frac{\partial e^{th}(p)}{\partial p} = \frac{e^{th}(p+\delta p) - e^{th}(p-\delta p)}{2\,\delta p}. \tag{7.8}$$

offers the quadratic precision, error $\sim \delta p^2$, whereas the preceding one offers the precision only up to a linear term, error $\sim \delta p$, thus Eq. (7.8) is the one programmed in our codes.

7.1.2 The Fitting Procedure

At this place we wish to limit ourselves to a few words of precision about the differences between the fitting procedure when using the traditional (phenomenological) definition of the spin-orbit, cf. Eq. (2.5), as compared to density-dependent definition, cf. Eq. (2.51).

The main difference is the self-consistency requirement used in the density-dependence case. The first step for the iterative process is to calculate the c^N_{nlj} coefficients, cf. Eq. (2.56), using the traditional description of the spin-orbit potential. Next, we use these to calculate the nuclear density and density gradient and we diagonalise again the Hamiltonian but this time using the density-dependent formulation. With the new c^N_{nlj}, one can recalculate the density and its gradient, and therefore diagonalise once more the Hamiltonian. This iterative precess finishes when the single particle energies obtained from the Hamiltonian diagonalisation of the latest iteration and the preceding one are less than a certain ε given as the input value to the programme:

$$\sqrt{\sum_i \left[e_i^{(k)} - e_i^{(k-1)}\right]^2} \leq \varepsilon, \tag{7.9}$$

where k indicates the iteration. It turns out that, typically, for $\varepsilon \sim 10^{-3}$ the number of necessary iterations is around $k \approx 6$.

Another difference between the two variants of the Hamiltonian becomes visible when comparing the calculation for one nucleus and for several nuclei simultanously. On the one hand, since the density-dependent description depends at the same time on the proton and neutron densities, in the process of fitting one needs to take into account both the proton energies and the neutron energies simultaneously, therefore we need to minimise at the same time over the proton and the neutron parameters. This makes the parametric optimisation procedure slower because there are more partial derivatives to calculate using the finite differences at each step.

7.2 Numerical Integration

A very important aspect of the solution of the Schrödinger equation using the diagonalisation method is the calculation of the matrix elements of the Hamiltonian, which have an explicit integral form; these are calculated numerically using Gauss-Laguerre quadrature theorem. This algorithm is combined with the package of subroutines calculating the Laguerre-functions and their derivatives to express the densities and calculate numerically the matrix elements.

The numerical integration of the matrix elements of the Hamiltonian involves the integrals for any given operator $\hat{\mathcal{O}}$, cf. Eq. (2.46)

$$\langle n'\ell|\hat{\mathcal{O}}|n\ell\rangle = \frac{a}{2}\,\mathcal{N}_{n'\ell}\mathcal{N}_{n\ell}\int_0^\infty dz\, e^{-z} z^{\ell+\frac{1}{2}}\, L_{n'}^{(\ell+\frac{1}{2})}(z)\,\hat{\mathcal{O}}(z)\,L_n^{(\ell+\frac{1}{2})}(z)\,. \tag{7.10}$$

The numerical integration expression using the so-called generalised Gauss-Laguerre quadrature theorem is given by

$$\int_0^\infty e^{-x} f(x) dx = \sum_i w_i f(x_i) \tag{7.11}$$

cf. [27] Eq. (25.4.45).

Due to the presence of $z^{\ell+\frac{1}{2}}$ in Eq. (7.10), we could have chosen the integration weights w_i proportional to it. However, we chose the w_i to be proportional to $z^{\ell-\frac{1}{2}}$ because of the form of the kinetic energy matrix elements, cf. Eq. (2.47). Consequently, Eq. (7.10) takes the form

$$\begin{aligned}\langle n'\ell|\hat{\mathcal{O}}|n\ell\rangle &= \frac{a}{2}\mathcal{N}_{n'\ell}\mathcal{N}_{n\ell}\int_0^\infty dz\, e^{-z}z^{\ell-\frac{1}{2}}\, z\, L_{n'}^{(\ell+\frac{1}{2})}(z)\,\hat{\mathcal{O}}(z)\,L_n^{(\ell+\frac{1}{2})}(z)\\ &= \frac{a}{2}\mathcal{N}_{n'\ell}\mathcal{N}_{n\ell}\sum_{i=1}^{N_{GL}} w_i\, z_i\, L_{n'}^{(\ell+\frac{1}{2})}(z)\,\hat{\mathcal{O}}(z)\,L_n^{(\ell+\frac{1}{2})}(z)\,, \end{aligned} \tag{7.12}$$

where N_{GL} is the number of integration points.

7.3 Code Variants

The essential skeleton of the code is the parameter optimisation block taking into account one or more nuclei at the same time. One may also chose which parameters are optimised and which stay constant during the process of the minimisation.

Since we were interested in different aspect of the modelling and model predictive power, different variants of the code were developed in order to have as much as possible a detailed analysis of the problem.

Variant 1 - Direct Diagonalisation. This is the simplest calculation variant. After introducing the required parameter values the code provides the single particle energies for the nuclei specified.

Variant 2 - Simple Fit. This is the parameter optimisation variant where one chooses the number of nuclei and the parameters over which the minimisation needs to be performed. The results are the values of the optimal parameters and the single particle energies of the desired nuclei calculated from these parameters.

Variant 3 - Single Particle Energies as Functions of One Parameter. In this case we perform the calculations for a single nucleus. Defining the sequence of the parameter values, we tabulate the single particle energies. The parameters over which we do not tabulate can either remain fixed or they can be optimised via χ^2-minimisation.

Variant 4 - Mapping of χ^2. This is one of the techniques developed to detect parametric correlations. In this case, the χ^2 is projected onto a plane. In this case, the χ^2 is tabulated as a function of the two parameters, whereas the remaining parameters are either kept fixed or are optimised via minimisation.

Variant 5 - Monte Carlo Simulations. This variant was already discussed in Sect. 1.8. The goal of this variant is to obtain occurrence histograms of the parameters and single particle energies. For this purpose, a Gaussian noise is defined according to some standard deviation, σ_{exp}, defined via input. The experimental data are introduced, they are transformed into 'noisy' data and the χ^2-minimisation is performed. Repeating this operation a large number of times, say N_{MC}, allows us to obtain N_{MC} sets for the fitted parameters. Next, with each set of so obtained parameters we can calculate the single particle energies for the desired nuclei, and/or to construct the occurrence histograms.

Acknowledgements

The paradox in the thesis Acknowledgements lies in the fact that they are usually written at the end of the whole work, whereas my experienced colleagues tell me that this is the first 'thing' one reads in a thesis. This is where the young researcher recapitulates her/his years as a PhD student.

First of all, I would like to express my most sincere gratitude to my thesis supervisor Professor J. Dudek, for his exceptional guidance during all these three years. I would like to thank him for his strong dedication he devoted to my work from the very first day, his passion in teaching me the new concepts and (on some occasions) for his patience. His motivation and conviction in the importance of the project kept me going on, being everyday more and more motivated and ready to find the new things and, to think about the next steps within the project. The fruitful discussions each time we had after obtaining new results, which were often surprising to us and which we had to interpret and understand, contributed to my learning research and getting more and more interested in it. I adored very much the discussions during which both of us we were proposing possible explanations of what we had in front of us. I really appreciated being under his supervision all this time, it was a real pleasure.

I would like also to thank all the researchers with whom I shared corridor these years for their welcome: They quickly made me feel comfortable treating me as one more member in the team. We had nice conversations and discussing talking about everything, not only discussing physics. For this, I would like particularly thank all the PhD students I met in the institute, Mateo (my funny and encouraging office mate), Markéta, Damien, Guillaume, Michaël, Jakub, Rémy, Nicolas, Daniel, Bart, Nicolas, Pierre, with who I shared really nice moments during the coffee breaks - in short – all those who I consider now being good friends. I would also like to thank my office neighbour David Rouvel for the nice discussions we had and for learning me very useful coding tools.

During these three years I also met many persons outside the institute. I would like to thank my perfect flatmate, Aurélie, for sharing with me the apartment, teaching me French, both the language and the lifestyle. I am also very thankful for her support every evening after work.

I also met Maria, Johanna, Camille, Loïc, Romain, who became very important for me during my stay in Strasbourg and with who, together with the other friends, we had incredible and fantastic moments. They made me feel as one more of the group immediately, the feeling which I deeply appreciated.

During these years I took part in the 'Les ReBelles' volleyball team. I would like to thank my coach Jacques and my team-mates Maria, Sakina, Cristina, Sabrina, Marie, Séverine, Manue, Valentine, Coralie, Sophie, Marie Pierre, Hélène and Laura, placing sporty Thursday evenings among the best moments of the week.

It is said that one should never forget her/his origins, so a huge Thank You goes to my friends in Barcelona: Maria, Adriana, Raquel, Carles, Judith, Maria Paz, Xavier, Marc, Jordi, Eduard, Aina, Laura, Néstor, Ignasi, Aleix, Maria, Núria, Lluís, Marc, Adrià and Oriol. The distance was not a problem to keep our nice friendship.

Usually one ends the Acknowledgements with thanking the family. This is why I would like to start thanking all members from Zacharatou family, Makis, Rena, Sophia and Charitini for their continuous encouragement and believing in me, always.

Thanks also to my uncle Jaume, my aunts Maria Isabel and Marie, and my cousin Sophia for their nice hugs every time I was going back home.

And the final huge, one of the most important Thank You goes to my parents Christos and Maria Lourdes, to my brothers Yorgos and Manolis, and their families Laura, Raquel, Júlia, Bruna, Bruno and Sofia. Their unconditional love, their hugs, their advices gave me all the strength needed to nicely complete this project. I thank them for always being there, next to me, even at the long distance.

As you set out for Ithaka
hope the voyage is a long one,
full of adventure, full of discovery...
K.P. Kavafis

Résumé

Le présent document décrit un projet de recherche de doctorat dans le domaine de la physique nucléaire théorique - plus précisément dans le domaine de la structure nucléaire théorique. Dans ce projet, nous présentons de nombreux résultats de calculs réalistes qui peuvent être et seront comparés aux données expérimentales. Cependant, l'intérêt principal de ce projet ne sera *pas tellement* de seulement

reproduire des données expérimentales existantes

mais plutôt de

reproduire des données expérimentales existantes
et surtout
prédire d'une manière aussi fiable que possible les résultats dans les zones inconnues.

Notre point de départ est l'observation selon laquelle tous les modèles théoriques réalistes de la structure nucléaire dépendent de paramètres réglables. Comme le montrent d'autres auteurs, une grande attention a été portée dans la littérature passée sur les développements des *modèles eux-mêmes*, alors qu'une attention bien moindre a été accordée au rôle des *procédures d'ajustement des paramètres*.

On accorde une attention croissante à ce deuxième aspect dans notre cadre de recherche suite à un progrès très rapide dans le domaine spécialisé de la science consacré à ce sujet :

la théorie du problème inverse dans les *mathématiques appliquées*.

1 Pouvoir de prédiction et problème inverse dans les théories quantiques

En discutant la théorie du pouvoir prédictif, on a généralement peu de doute à propos de ce que l'on veut dire. Nous supposons souvent sans le dire que la théorie en question peut prédire et produire de manière fiable des résultats qui traitent de la région expérimentalement inconnue. Mais dès que nous tentons de poser des questions plus précises de sérieuses difficultés sont susceptibles de se produire, déjà au niveau sémantique. Ci-dessous, nous donnerons quelques exemples avant d'aborder plus précisément le résultat de la définition des incertitudes de prédiction et du pouvoir prédictif.

Prédiction du modèle : que signifie « prédire » ?

Considérons un modèle mathématique donné, ou « théorie » expression que préfèrent les théoriciens. Tout calcul effectué avec cette théorie et s'intéressant à des informations encore inconnues peut être appelé une prédiction. Ce n'est qu'après la vérification expérimentale correspondante que nous pouvons dire si le résultat prédit, autrement dit la prédiction, est ou n'est pas acceptable. En d'autres termes, s'il s'agit d'une prédiction bonne ou mauvaise. Par conséquent, puisque l'exécution de tout calcul avant que les expériences soient effectuées peut toujours être appelée *une prédiction*, chaque prédiction a toujours *une puissance prédictive*. Subséquemment celle ci ne délivre à elle seule aucune qualité du modèle et pour devenir utile, elle doit être complétée par quelques qualificatifs. Par exemple, nous devrons peut-être spécifier ce que nous appelons *bon* pouvoir prédictif. Mais être bon pour quelqu'un peut ne pas être assez bon pour quelqu'un d'autre. Par conséquent, la terminologie discutée (nous éviterons à ce stade le mot « définition ») comporte une dose de jugement subjectif et arbitraire. C'est pourquoi nous devrons aborder la question de certains critères objectifs ou, si ce n'est pas possible de certains critères relatifs, qui permettront d'examiner les capacités de prédiction de la théorie, et donc le pouvoir prédictif, en minimisant l'effet d'un jugement subjectif explicite ou implicite.

1.1 Problème inverse : poser le problème et les stratégies de résolution

Considérons un opérateur $\hat{O}$ qui, agissant sur un ensemble de paramètres $\{p\}$, génère un ensemble de résultats habituellement appelés données $\{d\}$. Nous écrivons symboliquement :

$$\hat{\boldsymbol{O}}(\{\boldsymbol{p}\}) = \{\boldsymbol{d}\}. \tag{13}$$

La réalisation de l'opération dans l'Eq. (13) s'appelle la résolution d'un *problème direct*. Cependant, une telle opération peut être faite si, et seulement si, les valeurs des paramètres sont connues. Dans les applications réalistes, afin de pouvoir commencer à utiliser notre théorie, nous devons d'abord trouver l'ensemble des paramètres optimaux $\{p^{\text{opt}}\}$. Pour cela, nous aurons besoin *en principe* de construire l'inverse de l'opérateur $\hat{O}$ dans l'Eq. (13) :

$$\{\boldsymbol{p}^{\mathbf{opt}}\} = \hat{\boldsymbol{O}}^{-\mathbf{1}}(\{\boldsymbol{d}^{\mathbf{exp}}\}). \tag{14}$$

La réalisation de cette tâche s'appelle la résolution du *problème inverse*. Les solutions formelles d'un tel problème mathématique avec la correspondance $\hat{O} \leftrightarrow \hat{H}$, où $\hat{H}$ est dans notre cas le hamiltonien d'un système nucléaire, n'existent tout simplement pas.

Nous disons que le problème est *bien-posé* si pour chaque d il **existe** une solution p qui est **unique** et **continue**. Si l'une de ces conditions n'est pas satisfaite, nous disons que le problème est *mal-posé*. Dans ce cas, l'opérateur $\hat{O}$ n'a pas d'inverse, ce qui implique que les données expérimentales ne limitent pas les paramètres du modèle et par conséquent ils *ne peuvent pas* être déterminés. De plus l'existence ou non de l'opérateur inverse dépend non seulement du problème mathématique lui-même, mais aussi de l'ensemble des données $\{d\}$.

Si l'opérateur n'a pas d'inverse ou si son inverse est inconnu, une approche couramment appliquée consiste à *contourner la résolution* du problème inverse. Pour cela, l'une des méthodes les plus souvent utilisées est *la minimisation du* χ^2. En suivant une telle approche,

on minimise la distance entre les prédictions théoriques $\{e^{\text{th}}\}$ et les données expérimentales $\{e^{\text{exp}}\}$ en minimisant la fonction test χ^2 :

$$\boldsymbol{\chi^2(\{p\}) \sim \sum_{i=1}^{n_d} \left[e_i^{\text{exp}} - e_i^{\text{th}}(\{p\})\right]^2 .} \tag{15}$$

Ci-dessus, n_d est le nombre de données expérimentales à notre disposition et les données $\{d\}$ sont les énergies $\{e\}$ du système. En minimisant la fonction χ^2 dans l'Eq. (15) sur l'ensemble des paramètres $\{p\}$ nous pouvons trouver les paramètres optimaux qui peuvent être utilisés pour simuler les données expérimentales de manière réaliste.

Si le problème inverse est mal-posé, l'utilisation de la minimisation de la fonction χ^2 à la place de la véritable résolution du problème inverse conduit à des déviations entre la théorie et l'expérience qui «semblent acceptables», malheureusement les paramétrisations ainsi obtenues sont totalement instables. Ce problème a récemment été reconnu comme bien réel et de grande importance - du moins en physique nucléaire - et il existe des conférences internationales sur ce sujet organisées ces dernières années[1]. La présente thèse peut être replacée dans le cadre des études de solutions de ce type de problèmes dans le contexte de la physique de la structure nucléaire, et plus précisément, les approches de champs moyens nucléaires reconnues comme empiriquement parmi les plus efficaces dans notre domaine.

Il arrive souvent qu'en tentant de résoudre le problème inverse d'une manière ou d'une autre, on détecte l'existence de *corrélations paramétriques* : les paramètres ne sont pas indépendants les uns des autres. La corrélation paramétrique est encore un autre signe de problème inverse mal-posé, auquel cas différentes méthodes de contournement de la difficulté appelées *méthodes de régularisation* doivent être considérées.

1.2 Incertitudes théoriques et erreurs expérimentales

Cette thèse utilise la *théorie stochastique du pouvoir prédictif* [2] à partir des hypothèses suivantes. Soit une théorie $\mathcal{T}$ d'un certain phénomène $\mathcal{P}$ utilisant les observables quantiques $\hat{\mathcal{F}}_1, \hat{\mathcal{F}}_2, \ldots, \hat{\mathcal{F}}_n$. Ces dernières devraient être caractérisées par leurs valeurs propres dont les ensembles sont notés à l'aide d'accolades

$$\boldsymbol{\left[\hat{\mathcal{F}}_1 \to \{f_1\},\ \ \hat{\mathcal{F}}_2 \to \{f_2\},\ \ldots\ \hat{\mathcal{F}}_n \to \{f_n\}\right]} \tag{16}$$

ainsi que par leur distribution de probabilité

$$\boldsymbol{\mathcal{P}_1 = \mathcal{P}_1(f_1),\ \ \mathcal{P}_2 = \mathcal{P}_2(f_2),\ \ldots\ \mathcal{P}_n = \mathcal{P}_n(f_n).} \tag{17}$$

Le fait que les valeurs propres des observables possèdent des incertitudes conformément aux distributions de probabilité est dû au fait que les données expérimentales sont connues avec des barres d'erreur et aussi à ce que les théories elles-mêmes introduisent des incertitudes en raison de termes négligés ou de termes inconnus.

Toutes les théories connues qui décrivent la structure des systèmes subatomiques peuvent être considérées comme incomplètes. Cela tient au fait que la connaissance actuelle de l'interaction nucléon-nucléon, même si elle progresse dans le temps, est encore

[1] Focus Issue : *Enhancing the interaction between nuclear experiment and theory through information and statistics (ISNET),* J. Phys. G : Nucl. Part. Phys. **42** (2015)

[2] formulé et discuté dans "Open Problems in Nuclear Theory", *article invité*, J. Dudek et collaborateurs, J. Phys. G : Nucl. Part. Phys. 37 (2010) 064031.

assez limitée. Un peu familièrement : en principe, ce que nous voulons connaître est ce qu'on appelle parfois la « vérité complète sur le système ». Comme le « vrai hamiltonien » reste inconnu, nous pouvons écrire notre hamiltonien de connaissance actuelle en utilisant la forme symbolique suivante

$$\hat{H} = \hat{H}_{\text{true}} + \delta\hat{H}_{\text{ignor}} \;\leftrightarrow\; \hat{H}_{\text{true}} = \hat{H} - \delta\hat{H}_{\text{ignor}}, \tag{18}$$

où $\delta\hat{H}_{\text{ignor}}$ représente notre ignorance. Il existe des moyens efficaces bien connus de limiter l'impact négatif de notre manque de connaissance à partir de l'incomplétude des informations. Ces moyens consistent à parametrer notre ignorance, autrement dit, trouver les probabilités relatives de ce que nous pensons que les bonnes réponses sont.

L'information expérimentale que nous avons utiliser pour obtenir les valeurs des différents paramètres de notre modèle contient des erreurs. Ce projet se concentre sur les propriétés sélectionnées des noyaux sphériques dits *doublement magiques*. Plus précisément, nous analyserons les propriétés des énergies à un seul nucléon du champ moyen nucléaire en utilisant les informations expérimentales disponibles pour les noyaux suivants :

$$^{16}_{8}\mathrm{O}_{8},\ ^{40}_{20}\mathrm{Ca}_{20},\ ^{48}_{20}\mathrm{Ca}_{28},\ ^{56}_{28}\mathrm{Ni}_{28},\ ^{90}_{40}\mathrm{Zr}_{50},\ ^{132}_{50}\mathrm{Sn}_{82},\ ^{146}_{64}\mathrm{Gd}_{82} \text{ and } ^{208}_{82}\mathrm{Pb}_{126}. \tag{19}$$

Dans la physique de la structure nucléaire, les énergies soi-disant expérimentales à un seul nucléon sont en fait des objets complexes et dépendants du modèle, cf. Ref. [2].

Gardant à l'esprit qu'à la fois les théories et les données expérimentales viennent avec des erreurs, ces incertitudes sont propagées par la modélisation aux paramètres. Ainsi, les valeurs optimales des paramètres $\{p\}$ sont des variables aléatoires et par conséquent sont caractérisées par des distributions de probabilité $\mathcal{P} = \mathcal{P}(p)$.

Quel que soit le calcul que nous effectuons après, cela implique que toutes les quantités calculées doivent être impérativement vues comme des variables aléatoires accompagnées par leur distribution de probabilité, comme par exemple pour les énergies propres

$$\Pi_\rho = \Pi_\rho(e_\rho). \tag{20}$$

1.3 Simulation Monte-Carlo

Les techniques de simulation de Monte-Carlo sont basées sur les algorithmes répétitifs qui permettent d'effectuer une certaine estimation en changeant certaines conditions, par exemple la minimisation d'un test χ^2 un grand nombre de fois, disons N_{MC}. Chaque répétition peut être considérée comme un test d'une nouvelle hypothèse suivant un certain protocole, par exemple tester les données d'entrée expérimentales en fonction de la distribution de probabilité générée numériquement. À ce stade, les méthodes de Monte-Carlo utilisent les générateurs de nombres aléatoires numériques permettant de modéliser toute distribution de probabilité donnée nécessaire. Par exemple, on peut utiliser les méthodes de Monte Carlo pour simuler les distributions d'incertitude gaussiennes des données expérimentales et étudier la propagation de l'information représentée par une telle distribution d'entrée jusqu'aux distributions de probabilité résultantes des paramètres «optimaux» finals résultants.

Analyse des corrélations paramétriques - Matrice de Pearson. Avec les résultats obtenus de la simulation Monte Carlo, on peut construire different outils d'analyse pour étudier les correlations paramétriques. Un de ces outils est la matrice de correlation de

Pearson, qui informe sur la possible corrélation linéaire existante entre les paramètres du modèle. Les elements de matrice r_{ij} sont définis de la façon suivante

$$r_{ij} = \frac{\sum_{k=1}^{n}(p_{i,k} - \bar{p}_i)(p_{j,k} - \bar{p}_j)}{\sqrt{\sum_{k=1}^{n}(p_{i,k} - \bar{p}_i)^2}\sqrt{\sum_{k=1}^{n}(p_{j,k} - \bar{p}_j)^2}} \tag{21}$$

où n est le nombres d'éléments, dans ce cas $n = N_{MC}$ et $\bar{p}_i$ est la moyen arithmétique du paramètre p_i. Ce coefficient r_{ij} peut prendre différentes valeurs dans l'interval $[-1, +1]$. Si $r_{ij} = \pm 1$, il existe une correlation parfaitement linéaire entre les deux paramètres p_i and p_j. En d'autres termes, plus r_{ij} s'approche des limites ± 1 plus forte est la corrélation linéaire entre les deux paramètres correspondants, voir la première ligne de la Figure 1.2 (p. 24). D'autre part, $r_{ij} \to 0$ signifie seulement qu'il n'y a pas de corrélation linéaire entre les paramètres p_i et p_j ; en d'autres termes, les informations possibles sur les corrélations non linéaires doivent être recherchées en utilisant des moyens différents. Les techniques Monte-Carlo adaptées de manière appropriée constituent l'un des outils les plus puissants à cet égard ; ce seront les diagrammes que nous désignerons par *diagrammes à points (dot-plots)*, dont des exemples sont donnés dans la Figure 1.2 (p. 24). Ces diagrammes sont des distributions bidimensionnelles obtenues à partir des résultats de simulation de Monte Carlo projetés sur le plan (p_i, p_j) - où les axes représentent les p_i et p_j paramètres, respectivement.

Données pseudo-expérimentales. Les données expérimentales dont nous disposons et que nous utilisons pour ajuster les valeurs des paramètres du modèle sont limitées et ne sont généralement pas suffisantes pour divers types de considérations de test. Pour cette raison, on peut introduire le concept de *données pseudo-expérimentales*. Le principe de base de cette idée est le suivant. Pour commencer, nous utilisons le meilleur ensemble de données expérimentales existant pour ajuster l'ensemble optimal de ce que nous appelons *paramètres de référence*. Un tel ensemble assure que le modèle fonctionne à son meilleur regime ce que l'on peut attendre avec des données expérimentales limitées. Avec les paramètres de référence connus, nous calculons l'ensemble complet des résultats théoriques, par exemple tous les niveaux d'énergie qui peuvent être fournis par le modèle, généralement beaucoup plus que ce qui est connu expérimentalement. Après ces préliminaires, les données expérimentales réelles peuvent être remplacées par les données pseudo-expérimentales calculées. Ces dernières peuvent être utilisées pour effectuer différents tests. Par exemple, puisque les données pseudo-expérimentales reproduisent exactement les paramètres de référence du modèle, elles peuvent être utilisées pour une modélisation exacte avec les propriétés de performance proches de ce qui est nécessaire pour décrire les données *réelles*.

2 Modèle du champ moyen nucléaire sphérique

Nous nous concentrons sur l'étude du pouvoir prédictif d'un hamiltonien nucléaire réaliste impliquant un potentiel central de Woods-Saxon avec deux variantes pour l'interaction de spin-orbite : i) d'abord un potentiel spin-orbite en sa representation traditionnelle phénoménologique et ii) un potentiel spin-orbite dépendant de la densité.

Dans le présent projet, nous avons souhaité implémenter et tester les puissants algorithmes de Monte-Carlo pour détecter et supprimer les corrélations paramétriques. Pour cela, le temps d'exécution de c.p.u. ultra-court des algorithmes de résolution de l'équation

de Schrödinger est primordial. Nous avons donc décidé d'utiliser la réalisation phénoménologique de l'algorithme de champ moyen avec le hamiltonien de Woods-Saxon, d'autant plus que B. Szpak [25] a démontré dans sa thèse que le choix du hamiltonien sous la forme de l'approche sphérique de Skyrme-Hartree-Fock conduit à un mécanisme pathologiquement complexe de corrélations paramétriques. B. Szpak a montré que, dans de nombreuses situations, le hamiltonien de Skyrme conduit aux corrélations paramétriques sous la forme « tout le monde corrélé avec tout le monde », voir Figure 2.1 (p. 28).

2.1 Hamiltonien de Woods-Saxon sphérique

Commençons par introduire le hamiltonien qui sera utilisé pour décrire les énergies de particule individuelle de champ moyen dans ce projet. La structure générale du hamiltonien considérée ici a la forme

$$\hat{H}(\vec{r}) = \hat{t} + \hat{V}_C(\vec{r}) + \hat{V}_{SO}(\vec{r}) + \left[\hat{V}_E(\vec{r}) \leftrightarrow \text{potentiel électrostatique pour les protons}\right], \quad (22)$$

où $\vec{r}$ est le vecteur position d'un nucléon et $\hat{t}$, l'opérateur d'énergie cinétique du nucléon.

On a choisi le potentiel central, $\hat{V}_C(\vec{r}) \to \hat{V}_C(r)$ sous la forme de Woods-Saxon

$$\hat{V}_C(r) = \frac{V^c}{1 + \exp[(r - R^c)/a^c]} \quad (23)$$

où V^c est le paramètre de profondeur du puits de potentiel, r^c dans $R^c = r^c A^{1/3}$ est le paramètres de rayon, et a^c le paramètres de diffusion. Le troisième terme à droite dans Eq. (22) représente le potentiel spin-orbite. Dans sa représentation traditionnelle (contrairement à la réalisation auto-cohérente dépendant de la densité, qui sera introduite plus tard) elle a la forme suivante :

$$\hat{V}_{SO}(\vec{r}) \to \hat{V}_{SO}(r) = \frac{1}{r}\frac{dv_{so}(r)}{dr}\,\vec{\ell}\cdot\vec{s} \quad (24)$$

où par définition

$$v_{so}(r) \stackrel{df.}{=} \frac{\lambda^{so}}{1 + \exp\left[(r - R^{so})/a^{so}\right]}. \quad (25)$$

Par analogie à V^c dans le potentiel central, λ^{so} représente la force de l'interaction phénoménologique spin-orbite, r^{so} in $R^{so} = r^{so}A^{1/3}$ est le paramètre de rayon spin-orbite et a^{so} le paramètre de diffusion spin-orbite.

Enfin, le dernier terme du hamiltonien de l'Eq. (22) est le potentiel coulombien électrostatique agissant uniquement sur les protons. Pour la densité de charge uniforme, il prend la forme :

$$\hat{V}_E(\vec{r}) \to \hat{V}_E(r) = \hbar c\alpha(Z-1)\begin{cases}\frac{3-(r/R^{coul})^2}{2R^{coul}}, & \text{for } r \le R^{coul}\\ \frac{1}{r}, & \text{for } r > R^{coul}\end{cases} \quad (26)$$

où c est la vitesse de la lumière, α est la constante de structure fine et, comme dans le cas du potentiel central et spin-orbite, $R^{coul} = r^{coul}A^{1/3}$ est le paramètre de rayon de Coulomb. Dans le présent travail, nous supposons que le rayon de Coulomb est proportionnel au rayon central :

$$r^{coul} = f_c \cdot r^c, \quad (27)$$

où f_c est une constante positive. Cependant, dans ce qui suit nous travaillons la plupart du temps avec l'approximation $f_c = 1$, laissant des raffinements possibles pour plus tard.

Les paramètres profondeur du potentiel central et force du potentiel spin-orbite peuvent être définies séparément pour chaque noyau et type de particules, mais ici nous avons choisi de les paramétrer en termes de nombres de protons Z et de neutrons N et d'introduire deux paramètres auxiliaires pour chacun d'eux. Ainsi, pour la profondeur du potentiel central nous avons

$$V^c = V_o\left(1 \pm \kappa_c \frac{N-Z}{N+Z}\right), \tag{28}$$

et pour la force du potentiel spin-orbite

$$\lambda^{so} = \lambda_o\left(1 \pm \kappa_{so} \frac{N-Z}{N+Z}\right). \tag{29}$$

Dans les deux cas, le signe plus $(+)$ représente les protons et le signe moins $(-)$ pour les neutrons.

À ce stade, nous avons complètement défini notre hamiltonien qui dépend de douze paramètres, six pour les protons et six pour les neutrons :

$$\{V_o, \kappa_c, r^c_{\pi,\nu}, a^c_{\pi,\nu}, \lambda_o, \kappa_{so}, r^{so}_{\pi,\nu}, a^{so}_{\pi,\nu}\}. \tag{30}$$

Les indices π, ν se réfèrent aux ensembles de paramètres pour les protons et les neutrons, respectivement.

2.2 Potentiel spin-orbite dépendant de la densité

L'interaction spin-orbite introduite dans l'Eq. (24) est une pure construction phénoménologique et ne prend pas explicitement en compte les interactions nucléon-nucléon qui ont lieu dans le noyau. Dans cette section, nous présentons un choix alternatif de la définition du potentiel spin-orbite en utilisant le formalisme d'approche de Hartree-Fock. Après la généralisation microscopique de WS-Universal dans [29], nous obtiendrons une approche généralisée Woods-Saxon avec l'interaction spin-orbite dépendante de la densité qui impliquera une condition d'auto-cohérence dans son algorithme.

Il est hors de portée de ce document de donner tous les détails de la dérivation de l'interaction spin-orbite dépendante de la densité. Pour plus de détails sur la dérivation mathématique «pas à pas», voir [29]. La nouvelle forme correspondante de l'interaction spin-orbite est [29]

$$\hat{V}_{SO}(r) = \lambda \frac{1}{r}\frac{d\rho(r)}{dr}\,\vec{\ell}\cdot\vec{s}, \tag{31}$$

où λ est le paramètre de force. Puisque la densité nucléonique est la somme des contributions des protons et des neutrons, il sera instructif d'introduire la dépendance en isospin dans l'expression précédente. On obtient la forme suivante du potentiel spin-orbite, celui qui agit sur les protons :

$$\hat{V}^{\pi}_{SO}(r) = \frac{1}{r}\left[\lambda_{\pi\pi}\frac{d\rho_\pi(r)}{dr} + \lambda_{\pi\nu}\frac{d\rho_\nu(r)}{dr}\right]\vec{\ell}\cdot\vec{s}, \tag{32}$$

et celui qui agit sur les neutrons :

$$\hat{V}^{\nu}_{SO}(r) = \frac{1}{r}\left[\lambda_{\nu\pi}\frac{d\rho_\pi(r)}{dr} + \lambda_{\nu\nu}\frac{d\rho_\nu(r)}{dr}\right]\vec{\ell}\cdot\vec{s}. \tag{33}$$

Avec cette nouvelle formulation, nous décrivons le potentiel spin-orbite avec quatre paramètres pour les protons et les neutrons $\{\lambda_{\pi\pi}, \lambda_{\pi\nu}, \lambda_{\nu\nu}, \lambda_{\nu\pi}\}$, au lieu de six paramètres avec la formulation traditionnelle.

3 Incertitudes des prédictions théoriques

Dans ce chapitre, nous avons présenté le cadre conceptuel et les propriétés mathématiques liées à la solution du problème inverse en vue de l'optimisation et de la stabilisation des procédures d'ajustement des paramètres par des illustrations directes. Bien que nous cherchions à modéliser les propriétés réalistes du champ moyen nucléaire en se concentrant sur les énergies à un seul nucléon, nous souhaitons d'abord présenter les procédures et les propriétés assez complexes en utilisant un modèle simple exactement soluble.

Il s'avère que presque tous les mécanismes et propriétés de la modélisation mathématique, qui peuvent être nécessaires aux physiciens dans la théorie du problème inverse, peuvent être testés et illustrés jusqu'à un certain détail arbitraire avant de les appliquer dans un contexte physique réaliste. Pour illustrer cette section, nous allons discuter un «modèle-jouet» à quatre paramètres exactement soluble. La discussion complète et détaillée peut être trouvée dans le Chapitre 3, ici nous nous concentrerons uniquement sur les conclusions importantes et les implications trouvées.

Incertitudes : paramètres, prédictions internes et externes. Nous allons mettre ensemble, dans les observations finales, les résultats indiquant que les excellentes prédictions dans la zone interne, Tableau 3.3 (p. 58), sont obtenues avec des paramètres qui sont très incertains, Tableau 3.1 (p. 54) et ce sont les mêmes paramètres qui ont conduit à des prédictions externes inacceptables, voir Tableau 3.2 (p. 57).

Un physicien peut choisir de retenir à ce stade que, même si la performance détaillée du modèle peut dépendre du contexte particulier, il faut généralement accepter comme règle que si la qualité de l'ajustement et celle des prédictions internes est assurée cela n'implique pas nécessairement la qualité des predictions externes, qui sont au centre de l'attention. Lorsque les données expérimentales deviennent de moins en moins précises, il existe un seuil où le modèle exact choisi ici n'a plus aucun qualité de prédiction. En effet, après avoir dépasser une certaine valeur critique d'erreur, les données ne limitent plus le modèle. Nous appelons ce mécanisme une «condition NO-GO» pour les modèles exacts, mais des réalisations encore plus spectaculaires se produisent dans des modèles non exacts.

Enfin, soulignons que la notion même de zones de prédiction intrinsèques et étrangères introduite dans la Réf.[40] joue un rôle central dans la formulation de la distinction entre les deux concepts et la performance implicite très différente du modèle dans les deux cas.

Nous avons fourni une analogie directe du «modèle-jouet» exact, nous avons testé les mêmes caractéristiques avec notre modèle réaliste Woods-Saxon en construisant ce que nous appelons modèle exact induit par le concept de *données pseudo-expérimentales*, précédemment défini.

4 Détection des instabilités du modèle et stabilisation des prédictions de la modélisation

Une conséquence non désirée de la présence de corrélations paramétriques est que, selon leur forme précise, elles peuvent transformer le problème inverse en un problème inverse mal posé, c'est-à-dire que la solution n'est pas unique si elle existe ou elle ne change pas continument avec la modification de données d'entrée. En d'autres termes - dans le meilleur des cas, c'est-à-dire, si une solution peut être obtenue - toute petite variation de l'entrée

peut provoquer une très forte variation des résultats finals. Il existe différentes façons de détecter une mauvaise posture et son «degré d'intensité». Dans cette section, nous nous concentrerons sur la détection de la présence de corrélations paramétriques et examinerons les méthodes basées sur une simulation Monte-Carlo pour leur élimination.

4.1 Détection des correlations paramétriques

Dans ces simulations exploratoires, les barres d'erreur expérimentales seront définies à l'aide d'un seul paramètre σ_{exp} fixé pour tous les niveaux expérimentaux. La dépendance des résultats sur le choix de ce paramètre sera testée plus tard. Nous commencerons les tests de présence/absence de corrélations paramétriques, en utilisant la matrice de corrélation, Eq. (21) également appelée matrice de Pearson. Nous montrerons comment les corrélations paramétriques dépendent de la valeur de σ_{exp} et de la taille et du type de l'échantillonnage afin d'établir un lien quantitatif entre l'entrée typique au problème inverse avec la sortie d'optimisation de paramètre - dans notre cadre d'intérêt.

Échantillonnage : niveaux de neutrons[3] du ^{208}Pb. Nous commençons avec les niveaux de neutrons et calculons la matrice de corrélation de Pearson pour l'hypothèse $\sigma_{exp} = 600\,\text{keV}$. Les résultats du Tableau 4.1 (p. 74) pour les paramètres neutroniques montrent qu'à part les termes diagonaux, un seul élément matriciel non diagonal dans cette table est proche de 1, à savoir le coefficient de corrélation pour (V^c, r^c). Le paramètre de la diffusion centrale ne semble pas être corrélé avec les autres paramètres. Dans le cas des paramètres spin-orbite, on peut en déduire que les paramètres des neutrons ne sont pas aussi fortement corrélés que la paire (V^c, r^c) du potentiel central. La matrice de corrélation de Pearson pour $(\lambda_\nu^{so}, a_\nu^{so})$ mérite quelques commentaires supplémentaires. Les valeurs correspondantes des coefficients de corrélation sont autour de 0.5 pour les neutrons. Cette corrélation peut être attendue et comprise à cause de la forme du potentiel spin-orbite dans Eq. (24). En effet, en calculant la dérivée du facteur de forme $v_{so}(r)$ analytiquement, on peut facilement voir que le potentiel spin-orbite dépend explicitement du ratio (λ^{so}/a^{so}). Il s'ensuit qu'il doit y avoir une compensation automatique entre les variations de ces deux paramètres au cours du processus de minimisation impliquant leur corrélation.

Cependant, il ne faut jamais arrêter l'analyse des corrélations paramétriques en étudiant les éléments matriciels de la matrice de corrélation de Pearson, car elle n'informe que sur les corrélations linéaires possibles existant entre les paramètres, mais pas sur les autres formes, cf. Figure 1.2 (p. 24). Par conséquent, il est nécessaire de poursuivre avec l'analyse bidimensionnelle de corrélation. Une discussion préparatoire des propriétés topologiques attendues de tels diagrammes a été donnée dans le Chapitre 1, où nous avons introduit ce que nous avons appelé *les diagrammes à points (dot-plots)*.

Les résultats de Monte-Carlo pour toutes les corrélations possibles entre les paires de paramètres central-central et de spin-orbite-spin-orbite sont présentés pour les neutrons et les protons sur les Figures 4.3 - 4.14 (p. 77 - 84). Chaque figure est composée de quatre panneaux différents, montrant la même corrélation mais pour différentes valeurs de σ_{exp}, définies comme 50 keV, 200 keV, 400 keV et 600 keV. De cette façon, on peut superviser l'évolution des corrélations paramétriques avec l'augmentation de l'erreur d'entrée. Étant donné que la structure des « diagrammes à points » ne représente aucun modèle universel/général, nous procéderons dans ce qui suit à l'examen des résultats au cas par cas.

Correlations entre les paramètres du potentiel central. En analysant les figures

[3] Dans ce résumé, nous nous concentrerons sur les résultats des neutrons.

mentionnées dans le paragraphe précédent, nous avons montré qu'il existe une dépendance quadratique entre les paramètres de la profondeur centrale et du rayon central, nous avons pu déterminer sa forme exacte en ajustant l'expression

$$r^c = \alpha \cdot (V^c)^2 + \beta \cdot V^c + \gamma \,. \tag{34}$$

Lorsque le diagramme arbore une symétrie radiale, on peut en conclure que les paramètres impliqués sur les axes ne sont pas corrélés. Cela se produit entre la profondeur centrale et la diffusion centrale d'une part, et le rayon central et la diffusion centrale, d'autre part.

Correlations entre les paramètres du potentiel spin-orbite. Pour les paramètres spin-orbite, on peut remarquer une tendance de corrélation linéaire approximative entre (a^{so}, λ^{so}) : si a^{so} augmente, λ^{so} augmente aussi. Cette tendance ne semble pas dépendre beaucoup de la valeur de σ_{exp}. En ce qui concerne les corrélations entre (r^{so}, a^{so}) et (r^{so}, λ^{so}) elles apparaissent comme des corrélations non linéaires manifestant une structure à deux centres. La présence de cette structure à « double bulle » indique qu'il existe deux « solutions optimales » pour le rayon spin-orbite. La solution de rayon plus petit s'appelle *configuration compact* et la solution de plus grand rayon est appelée *configuration non-compacte*. Cet effet a déjà été étudié dans la thèse de N. Schunk [47] et a été discuté et expliqué en termes de la forme spécifique du potentiel spin-orbite proportionnelle au gradient du potentiel Woods-Saxon, presque constant à l'intérieur du noyau, et variant fortement à la surface.

4.2 Incertitudes des niveaux d'énergie nucléonique

Dans cette section, nous discutons des distributions de probabilité d'incertitude des énergies de particules individuelles obtenues en utilisant les techniques de Monte Carlo dans la section précédente, à savoir pour chaque ensemble de paramètres, nous pouvons calculer toutes les énergies de particules individuelles d'un noyau désiré.

Construction des histogrammes de probabilité d'incertitude. Pour construire les histogrammes de probabilité d'incertitude, nous divisons l'abscisse en petits intervalles et comptons le nombre de fois où une valeur de notre choix, par exemple la valeur propre de l'énergie ou la valeur d'un paramètre-modèle donné, est dans l'intervalle prédéfini. On obtient ainsi une distribution sous la forme d'un histogramme (fonction pas-à-pas) qui, après normalisation, devient la distribution de probabilité d'incertitude pour un niveau nucléonique donné ou un paramètre du modèle. Enfin, en ajustant une distribution gaussienne continue à chacun des histogrammes normalisés ainsi obtenus, nous déduisons les caractéristiques gaussiennes μ et σ pour chaque niveau ou paramètre. Avec cela, nous avons pu construire les distributions d'incertitude de niveau d'énergie pour ^{208}Pb et différents isotopes du flérovium ($Z = 114$) ^{278}Fl, ^{298} Fl et ^{342}Fl.

Conclusions synthétiques pour la liberté paramétrique complète. Lorsque les six paramètres du hamiltonien sont traités indépendamment, le comportement des distributions de niveaux peut être résumé comme suit :

- premièrement, *en moyenne*, les incertitudes augmentent avec l'augmentation de le nombre quantique ℓ du niveau ;
- deuxièmement, et cependant, les *fluctuations* autour de cette tendance moyenne sont clairement visibles ;

- troisièmement, et à ce stade, seulement quelques symptômes du mécanisme peuvent être signalés :

  chaque fois que l'information expérimentale sur un niveau donné n'est pas connue, l'incertitude obtenue par le test de Monte-Carlo semble être plus grande ;

  cette tendance devra être vérifiée plus tard en utilisant des constructions de test mieux conçues ;

- les résultats pour les noyaux super-lourds donnés dans les Tableaux 4.7 (p. 87) et 4.8 (p. 88) révèlent une augmentation très rapide des incertitudes avec une augmentation du nombre de neutrons au nombre de protons fixé. Cependant, la dépendance en ℓ des largeurs de niveau montre ses propres tendances.

Elimination des corrélation paramétriques. La corrélation existant entre le paramètre rayon central et le paramètre profondeur centrale peut être supprimée en utilisant une fonction simple qui nous permet d'écrire $r^c = f(V^c)$, et comme on l'a déjà dit, est parabolique, cf. Eq. (34). De cette façon, r^c n'est plus considéré comme un paramètre de minimisation puisque sa valeur est donnée par V^c, et au lieu de minimiser le χ^2 sur six paramètres, nous le minimisons sur seulement cinq : $\{V^c, a^c, \lambda^{so}, r^{so}, a^{so}\}_{\pi,\nu}$.

Concernant les corrélations paramétriques spin-orbite, rappelons qu'elles sont présentées comme une structure à double bulles. Par conséquent, aucune fonction « habituelle » du type $y = f(x)$ ne peut être définie. Dans ce cas, notre solution est de sélectionner deux solutions séparées correspondant aux deux maxima de distributions. Les résultats sont donnés dans le Tableau 4.13 (p. 96).

Dans ces conditions, nous avons réexécuté les simulations de Monte-Carlo deux fois de plus pour les neutrons :

- en imposant $r^c = f(V^c)$ et en fixant les trois paramètres spin-orbite à leur solution compacte ;
- en imposant $r^c = f(V^c)$ et en fixant les trois paramètres spin-orbite à leur solution non-compacte.

Dans ces conditions, les paramètres de minimisation finals sont : $\{V^c, a^c\}$.

Conclusions. Après avoir éliminé toutes les corrélations paramétriques possibles, la réaction des distributions d'incertitudes de niveau peut être résumée comme suit :

- l'élimination des corrélations paramétriques *diminue* les incertitudes de prédiction (distributions d'incertitudes plus étroites) pour la majorité des niveaux du noyau ^{208}Pb ;
- les largeurs d'incertitude dépendent de la valeur ℓ de l'état nucléonique ;
- les corrélations paramétriques du potentiel centrale ont un impact plus fort sur les états avec ℓ faible ;
- les corrélations de paramètres du potentiel de spin-orbite ont un impact sur tous les niveaux, où la solution compacte semble donner de meilleurs résultats en termes de déviation R.M.S. que la solution non-compacte ;

- l'extrapolation des résultats de ^{208}Pb devient plus précise après élimination des corrélations paramétriques pour les noyaux pas trop lourds
- après avoir dépassé une certaine distance critique de la zone d'ajustement [ou pour $N > N_{\rm crit} \approx 184$ neutrons], les largeurs de distribution sont si larges que l'on ne peut rien dire des capacités de prédiction, une manifestation du **mécanisme de NO-GO**.

5 Potentiel spin-orbite dépendant de la densité : optimisation des paramètres

En variante, nous avons également considéré une interaction spin-orbite dépendante de la densité qui inclut la condition d'auto-cohérence itérative, voir Eq.(32) - (33).

Puisque la formulation du potentiel spin-orbite dépendante de la densité est plus longue en temps de C.P.U., dans le cas présent il sera pratique de tenter de détecter l'existence de corrélations paramétriques en utilisant directement le test χ^2 - comme décrit dans l'annexe 4.8 du chapitre 4 plutôt que d'utiliser les simulations de Monte-Carlo. Rappelons que l'information d'intérêt est obtenue dans ce cas par des projections sur le plan (p_i, p_j) du $\chi^2(p_k; k \neq i, k \neq j)$ minimisé. Les Figures 5.3 (p. 121) et 5.4 (p. 122) présentent les corrélations paramétriques entre les quatre constantes de couplage spin-orbite : $\{\lambda_{\pi\pi}, \lambda_{\pi\nu}, \lambda_{\nu\nu}, \lambda_{\nu\pi}\}$.

Ces figures montrent que parmi les $\frac{4\times3}{2}$ c'est-à-dire six corrélations paramétriques possibles entre les quatre paramètres spin-orbite, il n'y a que deux corrélations. En outre ces corrélations semblent parfaitement linéaires entre $\lambda_{\pi\pi}$ et $\lambda_{\pi\nu}$ d'une part et $\lambda_{\nu\nu}$ et $\lambda_{\nu\pi}$ d'autre part. En d'autres termes, on peut considérer que $\hat{V}^{\pi}_{SO}$ et $\hat{V}^{\nu}_{SO}$ sont independents - et ce malgré le fait que les densités de protons et de neutrons sont déterminées en utilisant un algorithme d'auto-cohérence simultanée.

5.1 Justification microscopique des corrélations linéaires

En analysant le profil de gradient de densité pour les protons et les neutrons, on peut observer que pour les petites valeurs de r, les gradients de protons et de neutrons fluctuent en gardant des signes opposés. Cela implique que, quelle que soit la contribution relativement faible aux intégrales dans les éléments matriciels que les protons et les neutrons peuvent fournir séparément dans cette partie du volume nucléaire, une partie de ces contributions s'annulera à la suite des sommations des termes proton et neutron.

Dans le même temps, pour les grandes valeurs de r correspondant au voisinage de la surface nucléaire, Σ, les deux profils ont une structure similaire pour que l'on puisse écrire

$$\text{Proche de } \Sigma: \quad \nabla\rho_{\pi}(r) \propto \nabla\rho_{\nu}(r) \;\leftrightarrow\; \nabla\rho_{q'}(r) \propto \nabla\rho_{q}(r) \;\leftrightarrow\; \nabla\rho_{q'}(r) \approx \mu\nabla\rho_{q}(r), \tag{35}$$

où μ est une certaine constante, et nous trouvons

$$\begin{aligned} \hat{V}^{so}_{q} &= \left(\lambda_{qq}\frac{1}{r}\frac{d\rho_q}{dr} + \lambda_{qq'}\frac{1}{r}\frac{d\rho_{q'}}{dr}\right)\hat{\ell}\cdot\hat{s} \\ &\approx \underbrace{(\lambda_{qq} + \mu\lambda_{qq'})}_{\equiv\eta}\frac{1}{r}\frac{d\rho_q}{dr}\hat{\ell}\cdot\hat{s} = \eta\frac{1}{r}\frac{d\rho_q}{dr}\hat{\ell}\cdot\hat{s}, \end{aligned} \tag{36}$$

où η est une autre constante. Il s'ensuit que :

$$\lambda_{qq'} = \frac{1}{\mu}\left(\eta - \lambda_{qq}\right) \;\leftrightarrow\; \lambda_{qq'} = \alpha \cdot \lambda_{qq} + \beta \tag{37}$$

ce qui justifie la corrélation paramétrique linéaire présentée dans la Figure 5.3 (p. 121).

La propriété de l'indépendance des paramètres illustrés dans la Figure 5.4 (p. 122) suggère la réalisation la plus simple d'une telle condition pour la procédure d'optimisation des paramètres, *viz.* en choisissant la paramétrisation spin-orbite sous la forme

$$\boxed{\lambda_{\pi\pi} \approx \lambda_{\pi\nu} \approx \lambda_{\nu\pi} \approx \lambda_{\nu\nu} \equiv \lambda,} \tag{38}$$

pour ^{208}Pb et les autres noyaux étudiés dans le présent projet.

5.2 Résultats des simulations Monte Carlo

Après avoir détecté la forme des corrélations paramétriques dans la forme actuelle du hamiltonien, nous procédons aux simulations de Monte Carlo pour étudier la dépendance des incertitudes des niveaux de particules individuelles sur σ_{exp} ainsi que sur l'élimination des corrélations de paramètres.

Dans le chapitre précédent, nous avons montré que le paramètre de la diffusion centrale n'est pas corrélé avec les autres paramètres ce qui suggère la possibilité de le fixer - pour la simplicité, au moins dans la phase exploratoire - à une certaine valeur plausible. Nous avons sélectionné ici les valeurs utilisées dans l'ensemble des paramètres universels du hamiltonien de Woods-Saxon traditionnel :

$$a^c_\nu = a^c_\pi = 0.7 \text{ fm}. \tag{39}$$

Avec cette hypothèse *ad hoc*, les paramètres de minimisation sont réduits à

$$\{V^c_\pi, V^c_\nu, r^c_\pi, r^c_\nu, \lambda_{\pi\pi}, \lambda_{\pi\nu}, \lambda_{\nu\nu}, \lambda_{\nu\pi}\}. \tag{40}$$

Les diagrammes à points de la Figure 5.6 (p. 125) confirment à nouveau la dépendance quadratique existant entre la profondeur centrale et le rayon central. Les Figures 5.7 (p. 126) et 5.8 (p. 127) montrent une image entièrement cohérente respectivement pour les paires linéairement corrélées et non corrélées des paramètres spin-orbite.

Éliminer les corrélations paramétriques. Comme nous l'avons fait dans le chapitre 4, la corrélation paramétrique existant entre la profondeur centrale et le rayon central peut être facilement supprimée en définissant $r^c = f(V^c)$ et en utilisant la fonction parabolique. Concernant les corrélations paramétriques spin-orbite dans ce cas, nous les éliminons en imposant la condition sur Eq. (38). Cela conduit à la liberté paramétrique des trois paramètres restants

$$\{V^c_\pi, V^c_\nu, \lambda\}. \tag{41}$$

Résultats des distributions d'incertitude. En ce qui concerne les résultats de prédiction de Monte Carlo pour le noyau ^{208}Pb, toutes les largeurs d'incertitude sont systématiquement plus petites lorsque les corrélations paramétriques sont supprimées. Encore une fois, l'amélioration dépend de la valeur de ℓ de l'état : d'une manière générale, plus la valeur de ℓ est petite, plus l'amélioration est importante en termes de largeur de distribution.

En ce qui concerne les résultats pour les éléments super-lourds, pour les isotopes les plus légers, on observe une légère amélioration des largeurs d'incertitude pour $N_{main} = 5$ et en moyenne beaucoup mieux pour $N_{main} = 6$. Cependant pour $N > 184$, dans la majorité des cas, l'elimination des correlations paramétriques n'améliore pas la tendance. Ceci est très probablement dû au fait que dans ces noyaux nous approchons au régime NO-GO selon lequel les largeurs d'incertitude sont très grandes, ce qui provoque un fort chevauchement des distributions et donc un impact beaucoup plus faible sur les variations des états d'énergie propres.

5.3 Augmentation de l'échantillonnage : neutrons dans ^{132}Sn et ^{208}Pb

Notre code est préparé pour considérer les énergies de particules individuelles provenant de plus d'un noyau. Cela nous permet d'augmenter l'échantillonnage d'entrée pour notre procédure d'ajustement. Dans ce cas, nous avons décidé de considérer en même temps les énergies des neutrons à une seule particule de ^{132}Sn et ^{208}Pb. À partir des résultats des Figures 5.19 - 5.22 (p. 147 - 151) nous concluons que la deviation r.m.s. se dégradent légèrement pour ^{208}Pb, cependant nous avons une amélioration en termes de puissance prédictive parce qu'en augmentant l'échantillonnage et en éliminant les corrélations paramétriques la deviation R.M.S. diminue.

6 Conclusions et Perspectives

Le projet de doctorat actuel appartient au domaine de la physique nucléaire théorique dans le sous-domaine de la théorie de la structure nucléaire. Sa particularité réside dans le fait que même si nous modélisons les phénomènes expérimentaux reproduisant des observables sélectionnées, l'objectif principal n'est pas tant de les reproduire aussi bien que possible - mais plutôt d'utiliser ces informations pour *pouvoir prédire des faits aujourd'hui inconnus* d'une manière qui satisfait certains critères de stabilité et de fiabilité stochastique.

Nous avons effectué une analyse détaillée des corrélations paramétriques du hamiltonien de Woods-Saxon traditionnel et du hamiltonien de Woods-Saxon dependant de la densité. En utilisant les calculs de Monte-Carlo, nous avons identifié les paramètres corrélés et leur corrélation. Ainsi nous avons réussi à les éliminer toutes dans le potentiel de spin-orbite dépendant de la densité et dans le potentiel central. Ce faisant, nous avons observé comment les distributions de probabilité pour les niveaux individuels de nucléon ont été rétrécies, améliorant ainsi le pouvoir prédictif du modèle.

En utilisant un modèle mathématique simple qui contient toutes les caractéristiques génériques de toute théorie, nous avons démontré la « propriété NO-GO » : il existe une valeur critique de l'erreur expérimentale au delà de laquelle même les modèles exacts deviennent inutilisables puisque leurs paramètres ne sont plus récupérables.

Perspectives et défis. Comme il arrive souvent, les résultats de recherche complétés apportent de la lumière à certains problèmes antérieurs, mais contribuent habituellement au progrès en remettant en cause des nouvelles questions. Nous avons montré qu'en supposant une incertitude d'entrée expérimentale moyenne de l'ordre de 600 keV, cela induit une limite sur la puissance prédictive lors de l'augmentation du nombre de nucléons dans les noyaux super lourds qui se situent dans ce projet dans des zones de prédiction externes extrêmes :

au delà de $N = 184$, les incertitudes stochastiques semblent trop grandes pour être dignes de confiance. Une conclusion similaire peut être énoncée sur les états profondément liés dans tous les noyaux lourds étudiés.

La question se pose : que peut-on faire pour améliorer la situation ?

Nous pouvons envisager un certain nombre de scénarios qui peuvent être considérés comme un prolongement relativement simple de cette recherche.

- Tout d'abord, les estimations d'erreur peuvent être traitées de manière plus fine en utilisant les estimations d'erreur adaptées à chaque niveau expérimental plutôt qu'en utilisant l'estimation moyenne.
- Deuxièmement, on sait qu'une source importante d'incertitudes, lorsqu'on travaille avec les niveaux de particules individuelles dans les noyaux sphériques, provient du couplage des différents nucléons avec les vibrations collectives de surface. Il est simple d'inclure dans nos codes un sous-programme de *Random Phase Approximation (RPA)* pour traiter ce type de couplage de manière dédiée, d'estimer les corrections de couplage de vibration aux niveaux de particules individuelles et d'utiliser les corrections pour l'optimisation des paramètres.
- Une autre amélioration peut être guidée par le succès du potentiel spin-orbite dépendant de la densité. En effet, nous avons remarqué à plusieurs reprises que le potentiel coulombien électrostatique calculé à partir de la distribution uniforme de charge dans l'espace pose des problèmes en ce qu'il influence le couplage avec la diffusion du potentiel central nucléaire et par le second introduit un couplage supplémentaire avec les autres paramètres déstabilisants le schéma de prédiction. Dans la nouvelle réalisation du projet, un tel potentiel serait calculé directement à partir de la distribution de densité microscopique des protons.
- Une autre amélioration consisterait à introduire explicitement les corrections de l'interaction tenseur aux potentiels central et spin-orbite en champ moyen. L'importance de ces corrections augmente avec l'insaturation du spin dans le noyau et ces effets devraient jouer un rôle croissant dans les noyaux super-lourds. Les sous-programmes correspondants ont été écrits et testés et sont prêts pour les projets de suivi.

Bibliography

[1] W. H. Press, B. P. Flannery, S. A. Teukolsky, and W. T. Vetterling, *Numerical Recipes in FORTRAN: The Art of Scientific Computing*, vol. 1 (Press Syndicate of the University of Cambridge, 1992).

[2] J. Dudek, B. Szpak, M.-G. Porquet, H. Molique, K. Rybak, and B. Fornal, Journal of Physics G: Nuclear and Particle Physics **37**, 64031 (2010).

[3] M. Baranger, Nuclear Physics A **149**, 225 (1970).

[4] A. Bohr and B. R. Mottelson, *Nuclear Structure:(In 2 Volumes) Volume I: Single-Particle MotionVolume II: Nuclear Deformations* (World Scientific, 1998).

[5] P. Ring and P. Schuck, *The Nuclear Many-Body Problem* (Springer-Verlag Berlin Heidelberg, 1980), 1st ed.

[6] A. Tarantola, *Inverse Problem Theory: Methods for Data Fitting and Model Parameter Estimation* (Elsevier Science, 1987).

[7] R. Schmidt, *Advances in Nonlinear Parameter Optimization*, vol. 37 (Springer-Verlag Berlin Heidelberg, 1982).

[8] A. Bakushinskiy and A. Goncharsky, *Ill-Posed Problems: Theory and Applications* (Springer Netherlands, 1994).

[9] K. Mosegaard and A. Tarantola, International Geophysics **81** (2002).

[10] C. R. Vogel, *Computational methods for inverse problems* (Society for Industrial and Applied Mathematics, 2002).

[11] A. Tarantola, *Elements for Physics: Quantities, Qualities, and Intrinsic Theories* (Springer, 2006), ISBN 9783540253020.

[12] D. Calvetti and E. Somersalo, *An Introduction to Bayesian Scientific Computing: Ten Lectures on Subjective Computing*, Surveys and Tutorials in the Applied Mathematical Sciences (Springer New York, 2007).

[13] A. A. Samarskii and P. N. Vabishchevich, *Numerical methods for solving inverse problems of mathematical physics*, vol. 52 (Walter de Gruyter, 2007).

[14] A. Tarantola and K. Mosegaard, *Mapping of Probabilities Theory for the Interpretation of Uncertain Physical Measurements* (2007).

[15] G. Chavent, *Nonlinear Least Squares for Inverse Problems* (Springer Netherlands, 2010).

[16] R. Aster, B. Borchers, and C. Thurber, *Parameter Estimation and Inverse Problems*, International Geophysics (Elsevier Science, 2011).

[17] A. Kirsch, *An Introduction to the Mathematical Theory of Inverse Problems*, Applied Mathematical Sciences (Springer New York, 2011).

[18] C. Groetsch, *Inverse Problems in the Mathematical Sciences* (Vieweg+Teubner Verlag, 2013).

[19] F.-D. Moura-Neto and A.-J. Silva-Neto-CNPq, *An Introduction to Inverse Problems with Applications* (Springer-Verlag Berlin Heidelberg, 2013).

[20] L. Beilina, *Inverse Problems and Applications*, vol. 120 of *Springer Proceedings in Mathematics & Statistics* (Springer International Publishing, 2015).

[21] M. Kern, *Numerical Methods for Inverse Problems*, Collection mathématiques et statistiques (John Wiley & Sons, 2016).

[22] M. Richter, *Inverse Problems* (Birkhäuser Basel, 2016).

[23] K. Levenberg, Quarterly of Applied Mathematics **2**, 164 (1944).

[24] D. W. Marquardt, Journal of the Society for Industrial and Applied Mathematics **11**, 431 (1963).

[25] B. Szpak, *Predictive Power of Nuclear Structure Models from Inverse Problem Theory: Significance of Experimental Data* (PhD Thesis, Institute of Nuclear Physics, Polish Academy of Sciences, Krakow, Poland, 2012).

[26] L. Landau and E. Lifshitz, *Quantum Mechanics: Non-relativistic Theory*, Butterworth-Heinemann (Butterworth-Heinemann, 1977).

[27] M. Abramowitz and I. Stegun, *Handbook of Mathematical Functions: with Formulas, Graphs, and Mathematical Tables* (Dover Publications, Inc., New York, 1965).

[28] D. Varshalovich, A. Moskalev, and V. Khersonskii, *Quantum Theory of Angular Momentum* (World Scientific Pub., 1988).

[29] B. Belgoumène, J. Dudek, and T. Werner, Physics Letters B **267**, 431 (1991).

[30] D. Vautherin and D. M. Brink, Phys. Rev. C **5**, 626 (1972).

[31] Y.-S. Shen and Z. Ren, Zeitschrift für Physik A Hadrons and Nuclei **356**, 133 (1996).

[32] D. M. Brink and F. Stancu, Phys. Rev. C **75**, 064311 (2007).

[33] F. Stancu, D. Brink, and H. Flocard, Physics Letters B **68**, 108 (1977).

[34] M. Wang, G. Audi, A. Wapstra, F. Kondev, M. MacCormick, X. Xu, and B. Pfeiffer, Chinese Physics C **36**, 1603 (2012).

[35] H. Langevin-Joliot, J. van de Wiele, J. Guillot, E. Gerlic, L. H. Rosier, A. Willis, M. Morlet, G. Duhamel-Chretien, E. Tomasi-Gustafsson, N. Blasi, et al., Phys. Rev. C **47**, 1571 (1993).

[36] S. Gales, G. M. Crawley, D. Weber, and B. Zwieglinki, Phys. Rev. C **18**, 2475 (1978).

[37] S. Gales, C. P. Massolo, S. Fortier, J. P. Schapira, P. Martin, and V. Comparat, Phys. Rev. C **31**, 94 (1985).

[38] P. Grabmayr, A. Mondry, G. J. Wagner, P. Woldt, G. P. A. Berg, J. Lisantti, D. W. Miller, H. Nann, P. P. Singh, and E. J. Stephenson, Journal of Physics G: Nuclear and Particle Physics **18**, 1753 (1992).

[39] T. Editors, Phys. Rev. A **83**, 040001 (2011).

[40] J. Dudek, B. Szpak, B. Fornal, and A. Dromard, Physica Scripta **2013**, 014002 (2013).

[41] J. Dudek and T. Werner, Journal of Physics G: Nuclear Physics **4**, 1543 (1978).

[42] J. Dudek, A. Majhofer, J. Skalski, T. Werner, S. Cwiok, and W. Nazarewicz, Journal of Physics G: Nuclear Physics **5**, 1359 (1979).

[43] J. Dudek, W. Nazarewicz, and T. Werner, Nuclear Physics A **341**, 253 (1980).

[44] J. Dudek, Z. Szymański, and T. Werner, Phys. Rev. C **23**, 920 (1981).

[45] S. Cwiok, J. Dudek, W. Nazarewicz, J. Skalski, and T. Werner, Computer Physics Communications **46**, 379 (1987).

[46] S. Kahane, S. Raman, and J. Dudek, Phys. Rev. C **40**, 2282 (1989).

[47] N. Schunck, *Champ moyen nucléaire dans le formalisme de Dirac* (PhD Thesis, Université Louis Paster de Strasbourg, Strasbourg, France, 2001).

[48] M. J. A. de Voigt, J. Dudek, and Z. Szymanski, Rev. Mod. Phys. **55**, 949 (1983).

[49] I. Dedes and J. Dudek, Acta Physica Polonica B Proceedings Supplement **10**, 51 (2017).

[50] H. Molique, J. Dudek, K. Rybak, and M. Porquet, in *Zakopane Conference on Nuclear Physics* (Jagellonian University, Cracow, Zakopane, Poland, 2008), vol. 40, p. 597.

[51] N. Schunck and J. Dudek, in *International Research Conference NATO. Advanced Research Workshop. High spin physics 2001* (Jagellonian University, Cracow, Varsovie, Poland, 2001), vol. 32, pp. 2639–2643.

[52] T. H. R. Skyrme, Proceedings of the Royal Society of London A: Mathematical, Physical and Engineering Sciences **260**, 127 (1961).

[53] R. Bhattacharya, Nuclear Physics A **913**, 1 (2013).

[54] J. Dudek, B. Szpak, A. Dromard, M.-G. Porquet, B. Fornal, and A. Gózdz, International Journal of Modern Physics E **21**, 1250053 (2012).

[55] H. Molique and J. Dudek, International Journal of Modern Physics E **21**, 1250037 (2012).

[56] J. Dudek, K. Rybak, B. Szpak, M.-G. Porquet, H. Molique, and B. Fornal, International Journal of Modern Physics E **19**, 652 (2010).

[57] B. Szpak, J. Dudek, M.-G. Porquet, K. Rybak, H. Molique, and B. Fornal, International Journal of Modern Physics E **19**, 665 (2010).

[58] R. F. Casten, Journal of Physics G: Nuclear and Particle Physics **42**, 034029 (2015).

[59] J. Erler and P.-G. Reinhard, Journal of Physics G: Nuclear and Particle Physics **42**, 034026 (2015).

[60] M. Kortelainen, Journal of Physics G: Nuclear and Particle Physics **42**, 034021 (2015).

[61] R. Navarro-Pérez, J. E. Amaro, and E. Ruiz-Arriola, Journal of Physics G: Nuclear and Particle Physics **42**, 034013 (2015).

[62] J. Piekarewicz, W.-C. Chen, and F. J. Fattoyev, Journal of Physics G: Nuclear and Particle Physics **42**, 034018 (2015).

[63] X. Roca-Maza, N. Paar, and G. Colò, Journal of Physics G: Nuclear and Particle Physics **42**, 034033 (2015).

[64] N. Schunck, J. D. McDonnell, J. Sarich, S. M. Wild, and D. Higdon, Journal of Physics G: Nuclear and Particle Physics **42**, 034024 (2015).

[65] A. W. Steiner, Journal of Physics G: Nuclear and Particle Physics **42**, 034004 (2015).

[66] S. M. Wild, J. Sarich, and N. Schunck, Journal of Physics G: Nuclear and Particle Physics **42**, 034031 (2015).

[67] A. Tarantola, *Inverse problem theory and methods for model parameter estimation* (Society for Industrial and Applied Mathematics, 2005).

[68] *Enhancing the interaction between nuclear experiment and theory through information and statistics (ISNET)*, vol. 42 (Journal of Physics G: Nuclear and Particle Physics, 2015).

[69] J. Friedrich and P.-G. Reinhard, Phys. Rev. C **33**, 335 (1986).

Université de Strasbourg

Irene DEDES NONELL

Approche stochastique du problème du pouvoir prédictif dans la modélisation du champ moyen

IPHC Institut Pluridisciplinaire Hubert Curien Strasbourg

Résumé

Les résultats de notre étude des capacités de modélisation théorique axées sur les approches phénoménologiques nucléaires dans le cadre de la théorie du champ-moyen sont présentés. On s'attend à ce qu'une théorie réaliste soit capable de prédire de manière satisfaisante les résultats des expériences à venir, c'est-à-dire avoir ce qu'on appelle un bon *pouvoir prédictif*. Pour étudier le pouvoir prédictif d'un modèle théorique, nous avons dû tenir compte non seulement des erreurs des données expérimentales, mais aussi des incertitudes issues des approximations du formalisme théorique et de l'existence de *corrélations paramétriques*. L'une des techniques centrales dans l'ajustement des paramètres est la solution de ce qu'on appelle le *Problème Inverse*. Les corrélations paramétriques induisent généralement un problème inverse mal-posé; elles doivent être étudiées et le modèle doit être régularisé. Nous avons testé deux types de hamiltoniens phénoménologiques réalistes montrant comment éliminer théoriquement et en pratique les corrélations paramétriques. Nous calculons les intervalles de confiance de niveau, les distributions d'incertitude des prédictions des modèles et nous avons montré comment améliorer les capacités de prédiction et la stabilité de la théorie.

Mots clés: structure nucléaire; théorie du champ-moyen nucléaire; energies single particule; problème inverse; incertitudes stochastiques des prédictions de modélisation

Abstract

Results of our study of the theoretical modelling capacities focussing on the nuclear phenomenological mean-field approaches are presented. It is expected that a realistic theory should be capable of predicting satisfactorily the results of the experiments to come, i.e., having what is called a good *predictive power*. To study the predictive power of a theoretical model, we had to take into account not only the errors of the experimental data but also the uncertainties originating from approximations of the theoretical formalism and the existence of *parametric correlations*. One of the central techniques in the parameter adjustment is the solution of what is called the *Inverse Problem*. Parametric correlations usually induce ill-posedness of the inverse problem; they need to be studied and the model regularised. We have tested two types of realistic phenomenological Hamiltonians showing how to eliminate the parametric correlations theoretically and in practice. We calculate the level confidence intervals, the uncertainty distributions of model predictions and have shown how to improve theory's prediction capacities and stability.

Keywords: nuclear structure; nuclear mean-field theory; single nucleon energies; inverse problem; stochastic uncertainties of modelling predictions